UNIVERSITAT DE BARCELONA

Synthesis and Characterization of Carbon Nanotubes and Hybrid Carbon Nanostructures grown on flexible electrodes for Supercapacitor Applications

Islam Alshaikh

Doctoral Thesis

Synthesis and Characterization of Carbon Nanotubes and Hybrid Carbon Nanostructures grown on flexible electrodes for Supercapacitor Applications

Author: Islam Alshaikh

Directors: Enric Bertran-Serra
Roger Amade-Rovira

UNIVERSITAT DE BARCELONA

UNIVERSITAT DE BARCELONA

Síntesi i Caracterització de Nanotubs de Carboni i Nanoestructures de Carboni Híbrides Crescudes sobre Elèctrodes Flexibles

Memòria presentada per optar al grau de doctor per la Universitat de Barcelona

Programa de doctorat en Nanociències

Autor: Islam Alshaikh

Directors: Prof. Enric Bertran-Serra
Dr. Roger Amade-Rovira

Tutor: Prof. Enric Bertran-Serra

Barcelona, desembre 2021

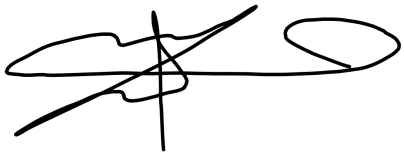

Dedicated to my loving parents and wife…

ACKNOWLEDGEMENT

First and foremost, praises and thanks to the God, the Almighty, for His showers of blessings throughout my research work to complete the research successfully.

I would like to express my deep and sincere gratitude to my research supervisors, Prof. Enric Bertran-Serra and Dr. Roger Amade-Rovira for giving me the opportunity to do the research in their group and providing invaluable guidance throughout this research. Their dynamism, vision, sincerity, and motivation have deeply inspired me. I benefited greatly from their scientific insight, ability to solve seemingly insoluble practical difficulties. It was a great privilege and honor to work and study under their guidance. I also thank Dr. Ester Pascual and Dr. José Luis Andújar for their pertinent comments, observations and recommendations that always contributed positively to my stay in the research group.

I am extremely grateful to my parents for their love, prayers, caring and sacrifices for educating and preparing me for my future. They were always the support in the good and difficult moments.

I am very thankful to my wife for her love, understanding, prayers and continuous support. Also, I express my thanks to my sister and brothers for their support and valuable prayers.

I also acknowledge the help of the scientific staff of the Scientific Technical Services of the UB (CCTiUB), without them most of the results described in this thesis would not have been obtained. Special thanks go to Dr. Tariq Jawhari for Raman analyses, Eva Prats Miralles and David Artiaga Torres for SEM measurements, Luis López for TEM analyses and Lorenzo Calvo for XPS analyses. I am also deeply thankful to the secretarial team of the Department, Ms. Maria Teresa Fraile Sanchez, Mr. Jordi Sola Antolin and Ms. Cristina Egusquiza. They have been always organizing everything in the best possible way.

I am grateful to all those with whom I have had the pleasure to work during writing this thesis. My special words of thanks for cooperation, motivation and support should also go to my past and present group members Fernando, Stefanos, Joan, Arevik, and Ash. Everyone of them had his kind touch to achieve this work successfully.

Many thanks to Prof. Davide Mariotti for accepting me to work in his laboratory at NIBEC-Ulster university in Northern Ireland. This opportunity had added a lot to my experience and knowledge. I also can't forget all My collegues at NIBEC Ruari and Paul for their help and support in the laboratory during my stay there.

It is my fortune to gratefully acknowledge all my friends who didn't stop supporting and encouraging me during my research work, Shahzad, Musab, Sayed, Tarik, Khader, Mohammed, Jenkidar, Ammar and Thomas. Thank you all for your support and generous care throughout the research journey. Special thanks to my dear friend Fuad who was always supporting me since my first minute in Barcelona until now.

Thanks to the Spanish Ministry of Education for the fund through the FPU scholarship for four years and for funding my research stay in the United Kingdom.

I also acknowledge the support for a 6 months contract, as a research collaborator during the final period of my thesis, from the project entitled "Textile Competence Centre Vorarlberg 2" (TCCV2) of the program COMET-PROJECTS (Competence Centres for Excellent Technologies) of Austria for the research on: 2.1 Next generation of electrodes and electrolytes for energy storage systems, and 2.2 Flexible circuits, sensors and e-textiles. This project is participated by the University of Innsbruck (UIBK, Austria), Research Institute of Textile Chemistry and Textile Physics, the Universitat de Barcelona and the company Advanced Nanotechnologies S.L. (Spain), together with up to 22 Companies and Public research Centres and Universities from Europe. The project activity will be developed in the period 2021-2025 and it is mainly co-granted by the State of Vorarlberg (Austria) with a total amount of 630,960 €.

Outline of the thesis

Nowadays, Nanotechnology is having an impact on practically every aspect of human life. It is a transformative technology that has influenced and will continue on electronics, computers, medicine, catalysis, energy, and transportation. It has changed the way materials are used in the future, improving their durability and reactivity. We have a lot of opportunities to make things smaller, lighter, and stronger. Carbon materials are one of the main materials that scientists have intensively studied their properties during the last three decades for their remarkable properties, which are still being investigated and new properties and applications being discovered till this moment. Carbon nanotubes (CNTs) and graphene are the main investigated and most important carbon materials since their discovery. The first discovery of CNTs was in 1991 by Dr. Sumio Iijima where they were multi-walled carbon nanotubes (MWCNTs) as he could produce them in his laboratory under stable conditions. Two years later, the same scientist could discover the first single-wall CNTs (SWCNTs). A decade later, the revolution of graphene started when Prof. Andre Geim and Prof. Constantine Novoselv could obtain a single layer of graphene by separating the graphite fragments repeatedly until they obtained a layer of carbon of one atom thick. Indeed, since the technology for producing CNTs and graphene on an industrial scale has been progressed, they can be found in a numerous number of applications, such as reinforcing polymers, acting as scaffolds for the artificial tissue growth, using them in many sensor devices such as electrical, optical, and biological, manufacturing the components of next-generation battery electrodes and supercapacitors. CNTs and graphene are ideal supporters for other materials especially when they are combined together with high capacitance materials. Researchers and companies all around the world are devoting significant efforts to developing electrodes with three-dimensional design at the nanoscale and a high specific surface area.

This thesis focuses on the optimization of CNTs synthesis parameters using different methodologies to obtain the CNTs on conductive and flexible substrates and without substrate to use them as electrodes for supercapacitors. The CNTs have been studied separately, combined with graphene nanowalls (GNWs), and combined with MnO_2 in order to increase the capacitance as much as possible. All the methodologies of CNTs and GNWs synthesis are CVD-related processes.

The studied technologies also offer a diversity of production methods of nanomaterials, which open other future developments of flexible electrodes for supercapacitors and batteries, sensors, photo and electrocatalysis, and other developments like biosensors for smart wear.

Chapter 1-Introduction

This chapter covers some basic principles of nanoscience and nanotechnology. Carbon materials take the rest of the chapter starting from carbon allotropes, explaining in detail concepts about carbon nanotubes, their properties, synthesis techniques, growth mechanism, and the catalyst and precursor gases effect on the growth. Then, graphene history and concepts are explained briefly in addition to its structure and thermal and mechanical properties.

Chapter 2 – Characterization techniques

The characterization techniques used during this thesis are described in detail in this chapter. Different spectroscopic, electrical and electrochemical measurements were carried out to characterize the carbon materials we synthesized, as well as their application as electrodes for supercapacitor devices. In this chapter, also there are the descriptions of electronic microscopies and surface analysis techniques used for the compositional, structural and morphological characterization of samples.

Chapter 3 – Experimental concepts and setups.

This chapter is the core for the ability to imagine how the work of synthesis material was carried out. It covers in detail the vacuum system concepts and the possible gas resources inside vacuum chambers, plasma concepts and the related processes of physical vapor deposition (PVD) and chemical vapor deposition (CVD). The three reactors that we used to synthesize the carbon materials are explained. In particular, their parts (working principle, pumps, vacuum gauges, etc…) and the importance of each part for a successful and safe use of the chambers. Finally, an atmospheric plasma technique for the synthesis of metal nanoparticles was explained as well.

Chapter 4 – Synthesis of Carbon-based composites on highly flexible Papyex® substrate

In this chapter, the optimization of the growth parameters of vertically aligned CNTs (VACNTs) and their GNWs composite on Papyex® graphite substrate using plasma enhanced CVD (PECVD) and inductively coupled plasma CVD (ICP-CVD) is presented in view to use them as electrodes for supercapacitors. The parameters were optimized one by one including the sample's plasma functionalization. The samples were characterized using different microscopic,

spectroscopic and X-ray techniques. The electrochemical properties of the CNTs and hybrid carbon structures were investigated before and after the electro-deposition of MnO_2.

Chapter 5 – Synthesis of Carbon-based composites directly on flexible SS310 alloys

In this chapter, we studied the growth of CNTs directly on SS310 stainless steel alloys using the catalyst particles present on the substrate itself in a single continuous process using PECVD. The optimization of the process parameters was carried out through Box-Wilson experimental design. The obtained CNTs were decorated with GNWs flakes in order to increase their specific surface area. The morphology and properties of CNTs and CNTs-GNWs composite were characterized by different microscopic and spectroscopic techniques. Manganese dioxide was deposited on the obtained structure and their electrochemical properties studied.

Chapter 6 – Synthesis of carbon nanotubes and metal oxide nanoparticles at atmospheric pressure.

This is the last chapter of results, which will present a different technique for the growth of CNTs. The CNTs synthesis was done without substrate using floating catalyst CVD (FC-CVD). This technique allows the continuous (scalable) synthesis of CNTs at atmospheric pressure in a free-oxygen environment inside a tubular furnace reactor. Another technique for the synthesis of metal oxide nanoparticles is presented in this chapter called plasma-liquid interaction. Through this technique, different metal oxides were synthesized but we used only the NiO_2. Through these techniques we could obtain a hybrid structure of CNTs and NiO_2 nanoparticles. Both were characterized by microscopic and spectroscopic techniques to finally use them for electrochemical applications. The most of this work was carried out during a short stay at Ulster University - Northern Ireland.

Conclusions

The exposition of results and discussion has been completed by a list of conclusions derived from the main results and achievements of the thesis.

Table of Contents

List of Figures

List of Table:

Chapter 1

Introduction

1.1. Nanoscience and Nanotechnology

The term ‘nano’ is commonly used in many science fields such as physics, chemistry, computer science reaching to the industrial products that we use in our daily life. ‘*Nanoscience*’ term was defined by the International Society for standardization (ISO) as: “study, discovery and understanding of matter where size and structure-dependent properties and phenomena manifest, predominantly in the nanoscale (up to 100 nm) (Dai 2006), distinct from those associated with individual atoms or molecules, or extrapolation from larger sizes of the same material”. Thus, the nanotechnology can be defined as the application of manipulating and controlling matter mostly in nanoscale in order to exploit size- and structure-dependent properties (ISO 2015). The ability of studying, understanding and manipulating the nanoscale matter allows the materials development by combining the physical optical and mechanical properties that aren’t provided by the bulk material. Graphene is considered as one of the most promising nanoscale material (Gupta 2017).

The properties of the materials at the nanoscale dimensions change such as energy due to quantum effects. As the size decreases, the ratio of the surface atoms increases. These high energy surface atoms are so reactive. Due to the high surface-to-volume ratio associated with nanometer-sized materials, a tremendous improvement in chemical properties is also achievable through a reduction in size (Hussain 2014).

The database of articles could identify four big groups of the nanoscience and nanotechnology (Stopar et al. 2016): (1) materials, physics, chemistry, computer sciences, engineering; (2) environmental sciences, geosciences, agriculture; (3) biological, medical sciences; (4) economics, social sciences and humanities. According with that research, the first group is the one that provides the most scientific information in the nanoscience area. The information that is then used by the areas included in the three remaining groups. In this work, the focus was on the first area which include the fields of physics, chemistry, material science to obtain and optimize the synthesis of carbon nanostructured materials.

1.2. Carbon materials

Carbon is the 6th element of the periodic table. Carbon based materials, clusters and molecules are unique in a lot of ways. One distinction relates to the many possible configurations of the electronic states of a carbon atom, which is known as the hybridization of atomic orbitals. Each carbon atom has six electrons which occupy $1s^2$, $2s^2$, and $2p^2$ atomic orbitals, making carbon the first element in Group IV. The $1s^2$ orbital contains two strongly bounded electrons, and they are called core electrons. Four electrons occupy the $2s^2$ $2p^2$ orbitals, and these weaker bound electrons are called valence electrons. In the crystalline phase the valence electrons give rise to 2s, 2px, 2py, and 2pz orbitals which are important in forming covalent bonds in carbon materials. Since the energy difference between upper 2p energy levels and the lower 2s level in carbon is small compared with the binding energy of the chemical bonds, the electron wave functions for these four electrons can readily mix with each other, therefore changing the occupation of the 2s and three 2p atomic orbitals so as to enhance the binding energy of the C atom with its neighboring atoms. The mixing between 2s and 2p atomic orbitals is called hybridization, where the mixing of a single 2s electron with n =1, 2, 3 electrons is called sp^n hybridization. There are three possible hybridizations in carbon: *sp*, sp^2, and sp^3; other group IV elements such as Si, Ge exhibit primarily sp^3 hybridization. Carbon differs from Si and Ge in so far as carbon does not have inner atomic orbitals except for spherical 1s orbitals, and the absence of near inner orbitals facilitates hybridization involving only valence s and p orbitals from carbon (Saito et al. 1998). (Figure 1.1) shows schematic image of *sp*, sp^2 and sp^3 hybridization (Hussain 2014).

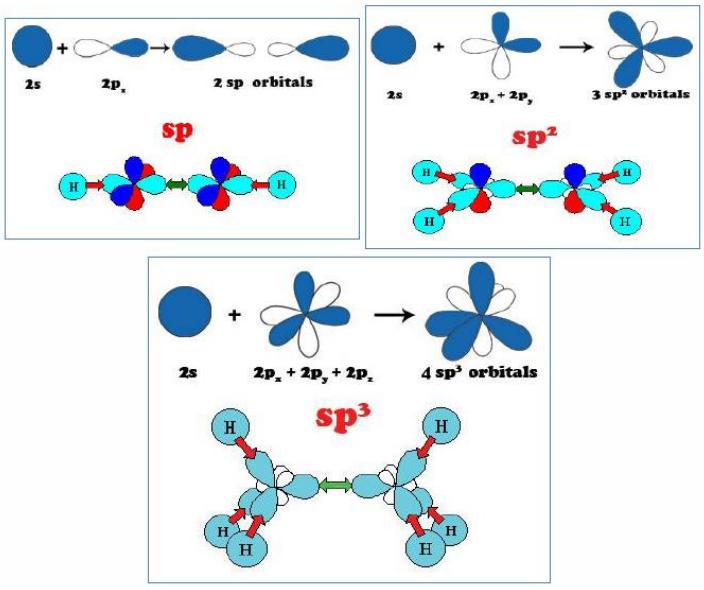

Figure 1.1: Schematic hybridization of carbon (Kiamahalleh et al. 2012).

In modern society carbon holds a much richer and complex meaning (Landau and Lifshitz 1980). This common material plays a singular role in chemical science and materials science. Carbon possesses a very large sphere of application, from drugs to synthetic materials. Specific industrial applications include areas such as oil and natural gas, food, pharmaceuticals, water treatment, hydrometallurgy, gold recovery and carbon-in-pulp process, which are widely used (Stillahn et al. 2008). The main feature of carbon is its ability to form a variety of allotropes and ability to combine with other elements. Carbon allotropes can be classified in terms of their spatial dimensionality: zero-dimensional are fullerenes, one dimensional are carbon nanotubes, three dimensional are graphite and diamond, two dimensional is graphene. The basic difference between 2D and 3D is considered by the number of layers of atoms. For example, a single layer of an atomic crystal is considered as 2D carbon, whereas 100 layers of carbon form the 3D graphite material (Wu et al. 2004). Elemental carbon existed for a long time only in two natural allotropes, diamond and graphite. Both allotropes show unique thermal and electrical properties. In 1985 Kroto et al. discovered the new form of the carbon fullerenes (Kroto et al. 1985). After this discovery a novel era of synthetic carbon allotropes started. In 1991 synthesis of carbon nanotubes was discovered (Iijima 1991) and in 2004, graphene was rediscovered (Novoselov et al. 2004). At present, more than 9 carbon modifications are known (Fig. 1.2).

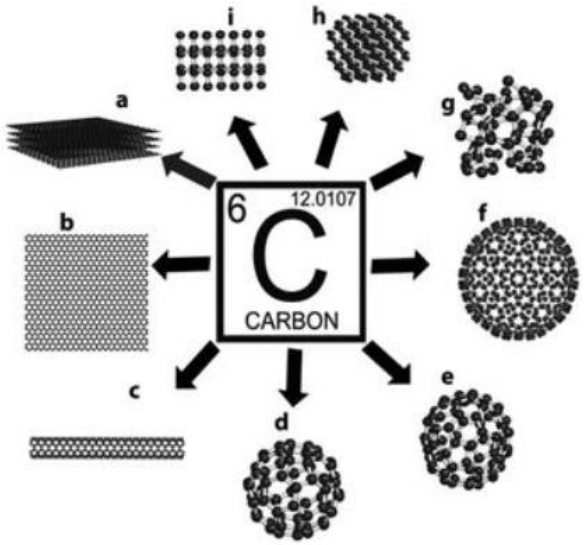

Figure 1.2. Different allotropes of carbon: (a) graphite; (b) graphene; (c) carbon nanotube; (d) C_{60} (Buckminsterfullerene); (e) C_{70} (Fullerene); (f) C_{540}(Fullerite); (g) amorphous carbon; (h) lonsdaleite and(i) diamond (Ravula et al. 2015).

Fullerenes

It is a zero dimensional allotrope of carbon. Fullerenes which are composed entirely of carbon were discovered in 1985 at Rice University by a group of scientists consisting of Richard Smalley, Robert Curl and Harry Kroto. As they shared a Nobel Prize for this discovery, they shared a Nobel Prize in 1996 (Kroto et al. 1985). The fullerene molecule is the fundamental building block of the crystalline phase. In addition, through doping and chemical reactions, they could form the basis of a large family of materials with interesting properties. Fullerenes include many structural variations, it can be found in spherical, elliptical tubes and many other shapes. Spherical form, so-called Buckminsterfullerene (C_{60}) consists of 60 carbon atoms, organized in 12 pentagons and 20 hexagons, in the same way as a spherical ball (Figure 1.3). The C_{60} fullerene is a well-known example of an ideal zero-dimensional structure. In the C_{60} molecule each carbon atom is bonded to three others by two longer bonds (0.145 nm) and one shorter bond (0.14 nm). They are conventionally referred to in the Fullerene's literature as two C-C single bonds, which link a hexagon to a pentagon and one C=C double bond, which lies between two hexagons. It follows that there is bonding anisotropy in the C_{60} molecule since bonds around a pentagon are all single bonds and bonds around a hexagon are alternately single bonds and double bonds. It appears, therefore that the bonding in C_{60} is mainly sp^2 with delocalized π electrons, but with some sp^3 character resulting from the the C-C curvature bonds (Honeychuck 1996).

Fullerenes are extremely strong molecules, they are harder than steel and diamond. The effective bulk modulus of C_{60} is 688 GPa. Some experiments show that fullerenes could withstand collisions of up to 15,000 mph against stainless steel and sustain their shape, thus indicating high stability of the fullerenes molecules. Fullerenes also have attractive chemical and optical properties. Nowadays fullerenes represent a big area of application and they are deemed like a hot topic in nanotechnology. Fullerenes can be used as photo resistant in certain photolithographic processes, in preparation of super-conductors, in electronic, microelectronic and optical devices, in batteries as charge conies, etc. (Ulloa 2013) Fullerenes are very useful in medical applications. In future it may be used in the drug delivery of small amounts for slow release, e.g., cancer treatment. Recently, applications of fullerene C_{60} and its derivatives in cosmetics have been intensively tested. Biological activity permits fullerene to be proper active compounds in the preparation of skin reconstruction cosmetic formulations (Lens 2009).

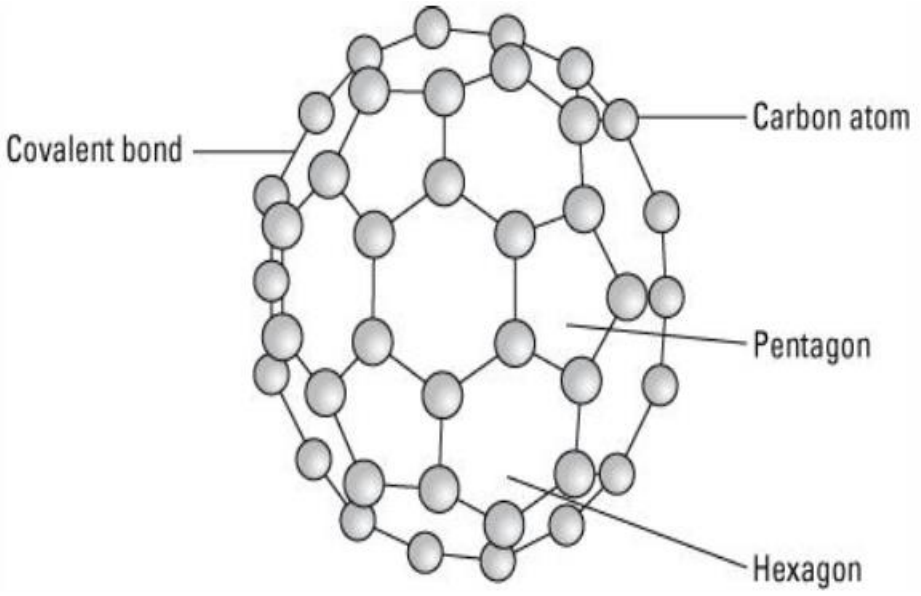

Figure 1.3: Fullerene molecule (Hussain 2014).

1.3 Carbon Nanotubes

1.3.1. Definition

Carbon nanotubes (CNTs) are a 2-D carbon allotrope and at present one of the most interesting members of the carbon family due to their physical, chemical, optical, mechanical, and electronic characteristics. The past two decades have witnessed their spread in a range of applications including building blocks in modern electronics, nonvolatile memory, field emission sources, photodetectors, ultrasensitive chemical and biosensors, and transparent
conductive membranes (An et al. 2017). This makes this topic a point of interest for many researchers as the number of publications only in the last ten years increased from 38,145 (2009) to 107,419 (2021) (Figure1.4). A single CNT (without a cap) is composed entirely of sp^2 bonds similar to the at structure of graphite. On the other hand, fullerenes and CNTs (with cap) have hybrid link orbitals between sp^2 and sp^3. However, CNTs that have a low percentage of sp^3 bonds are closer to graphite. The difference in chemical activity between the CNT caps and the sidewalls, as well as between the straight and bent CNTs, is determined by the sp^2-sp^3 bonding ratio (Kong et al. 2019). CNT name is taken from their long, hollow structure with the walls formed by one atomic layer sheets of carbon called graphene. These sheets are rolled at specific and discrete (chiral) angles, and the combination of rolling angle and radius determines the carbon nanotube properties (Figure 1.5). CNTs are categorized as single-walled (SWCNT) or multiple-walled nanotubes (MWCNTs) (Sagar et al. 2021).

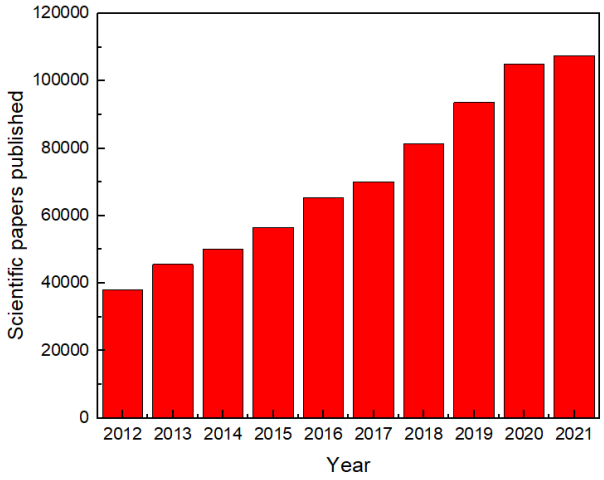

Figure 1.4. Scientific published papers related to the carbon nanotubes during the last 10 years (Dimentions 2021).

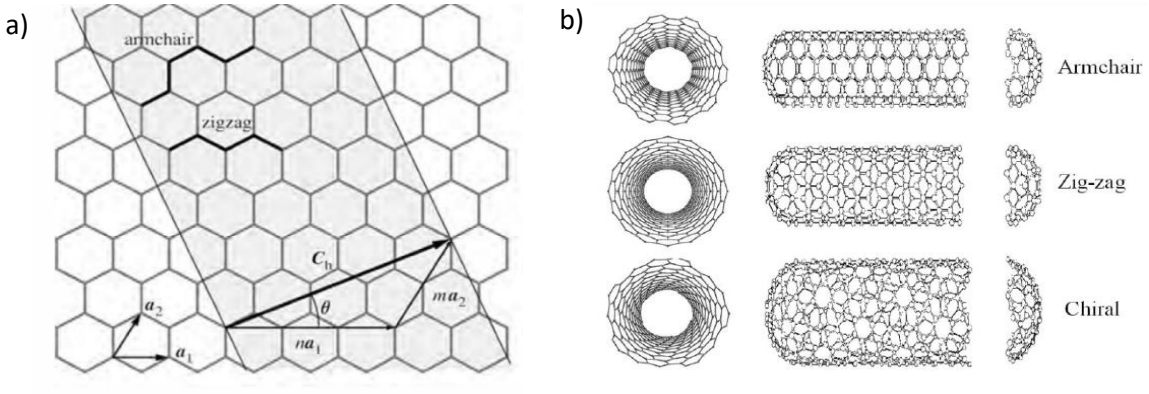

Figure 1.5 a) An illustration of the structures of an unrolled sheet of SWCNT, and (b) the three possibilities of its rolling up zigzag, armchair, and chiral SWCNTs (Avetisyan 2019).

Most SWCNTs have a diameter of approximately 1nm with a tube length that can be many millions of times longer (high aspect ratio). The structure of SWCNT can be hypothesized by wrapping a one atom thick layer of graphene into a seamless cylinder. The way the graphene sheet is folded is represented by a pair of indices (n, m). The integer n and m denote the number of unit vectors along two directions in honey-comb crystal lattice of graphene. If m = 0, the nanotube is called zigzag nanotube, and if n = m, it is called armchair; otherwise, the nanotube is called chiral (Odom et al. 1998; Chen et al. 2001). The diameter and helicity of a defect-free SWNTs are uniquely characterized by the vector:

$$c_h = na_1 + ma_2 = (n, m) \quad (1.1)$$

which connects crystallographically equivalent sites on a two-dimensional graphene sheet, where a_1 and a_2 are the graphene lattice vectors (Figure 1.9a). Electronic band structure calculations prove that the (n,m) indices define the metallic or semiconducting behaviour of SWNTs. Zigzag (n, 0) SWNTs should have two distinct types of behaviour: the tubes will be metals when n/3 is an integer, while otherwise semiconductors. As c_h rotates away from (n, 0), chiral (n, m) SWNTs are probably with electronic properties similar to the zigzag tubes; that is, when (2n + m/3) is an integer the tubes are metallic, and otherwise semiconducting. The gaps of the semiconducting (n, 0) and (n, m) tubes should be proportional in reverse with diameter. Finally, when c_h rotates 30° relative to (n, 0), then n = m. The (n, n) or armchair tubes are expected to be metallic with band crossings at k = $\pm\ 2/3$ of the one-dimensional Brilluoin zone (Odom et al. 1998). The diameter (d) of an individual nanotube can be calculated from its indices as follows:

$$d = (a/\pi)\sqrt{n^2 + nm + m^2} \quad (1.2)$$

where a = 0.246 nm.

1.3.2. Properties

Carbon nanotubes have been in interest as nanoscale materials due to their extraordinary physical properties such as their very high Young's modulus, their ultimate strength and their high thermal and electric conductivity. However, directly measuring the properties of these nanoparticles is very difficult by conventional methods. Therefore, several properties have been first evaluated using theoretical studies. The covalent bond sp^2 in the CNTs is one of the strongest bonds, which means a fiber formed by these axially oriented covalent bonds would be an extremely strong material. The mechanical parameter most commonly used to characterize a CNT is by determining its Young's modulus. Theoretical investigations have led to estimated Young's modulus of CNTs in the range of 1 TPa (Lu 1997). Different experimental methods have been established to measure the elastic properties of individual nanotubes. One method allows the determination of the CNT stiffness by the observation of their intrinsic thermal vibrations amplitude in a transmission electronic microscope (TEM). Average Young's modulus values of 1.8 TPa and 1.25 TPa were obtained for MWNTs and SWNTs, respectively (Treacy et al. 1996; Krishnan et al. 1998). Quantum mechanics calculations predict that defect-free single-walled carbon nanotubes possess Young's modulus values of 1 TPa, tensile strengths of 100 GPa, and multiwalled carbon nanotubes with a mean fracture strength >100 GPa [20]. For illustration, a

tensile strength of 200 GPa for MWNT relates the ability to sustain a weight of 20 tons on a cable with a cross-section of 1 mm². Carbon nanotubes thus represent the strongest and hardest materials in terms of tensile strength and elastic modulus. The above mechanical properties of CNTs refer to axial properties of the nanotube. Simple geometrical considerations propose that CNTs should be much softer in the radial direction than along the tube axis.

TEM observations of radial elasticity showing that even van der Waals forces can deform two adjacent nanotubes (Ruelle 2010). Nanoindentation experiments with AFM indicated Young's modulus of the order of several GPa in the radial Axis (Yu et al. 2000). In spite of these excellent mechanical properties, carbon nanotubes possess also a remarkable flexibility. Besides their experimental observations, the bending of nanotubes at large angles is completely reversible up to 100° despite the formation of complex kink shapes (Iijima et al. 1998). Moreover, the thermal conductivity of CNTs in the axial direction exceeds the best-known bulk heat conductors including diamond. The thermal conductivities of isolated SWNT and MWNT were experimentally measured, in the axial direction, were 3500 and 3000 $W.m^{-1}.K^{-1}$ respectively. Such exceedingly high thermal conductivity contributes to the effective heat removal, which is also assisted by the extremely high surface area of CNTs. All the above presented data shows that carbon nanotubes are actual interesting materials for electrical engineering applications as they have the characteristics of a seamless electrical conductor, current carrying capacity, strength, and thermal conductivity, adding to them the low mass (Lekawa-Raus et al. 2014; Pantoja-Suárez 2019).

The chemical reactivity of a CNT is compared with a graphene sheet, improved as a direct result of the curvature of the CNT surface. Carbon nanotube reactivity is directly related to the pi-orbital mismatch caused by an increased curvature. Therefore, a distinction must be made between the sidewall of the nanotubes and their end caps. For the same reason, a smaller nanotube diameter increases the reactivity. Covalent chemical modification of either sidewalls or end caps has shown to be possible. For example, the solubility of CNTs in different solvents can be monitored this way. However, direct investigation of chemical modifications on nanotube behavior is not easy as the crude nanotube samples are still not pure enough (Hussain 2014).

1.3.3. Synthesis techniques

Carbon nanotubes are generally produced by three main techniques, arc discharge, laser ablation and chemical vapor deposition. However, scientists are investigating more economic ways to produce these structures. In arc discharge, a vapor is created by an arc discharge between two carbon electrodes with or without catalyst, therefore, nanotubes self-assemble from the resulting

carbon vapor. In the laser ablation technique, a high-power laser beam imposes on a volume of carbon-containing feedstock gas (methane, acetylene or carbon monoxide). At the moment, laser ablation produces a small amount of clean nanotubes, while arc discharge methods generally produce large quantities of impure material. In general, chemical vapor deposition (CVD) results in MWCNTs or poor quality SWCNTs. The SWNTs obtained with CVD have a large diameter range, which can be poorly controlled. But on the other hand, this method is easy to scale up for commercial production (Hussain 2014).

Arc discharge

This method which can be operated either by alternating or direct current (AC/DC) is the one by which CNTs were produced by Iijima (Iijima 1991) (Figure 1.6). In this process a voltage of 10 to 20V and a current in the range of 20=100 A (approx.) is established between two cylindrical graphite electrodes separated by the order of 1 mm. The graphite electrodes (rods) used in the arc discharge systems are usually between 6 and 12 mm in diameter and are water-cooled. The chamber is kept at a sub-atmospheric pressure. Gram-scale synthesis of MWCNTs by arc discharge has been accomplished in the presence of helium (He) and CH4 gases at a pressure of _ 7 kPa. An arc current of 20A is applied to the anode with a diameter of 6mm (Ebbesen and Ajayan 1992). Other sub-products like amorphous carbon, fullerenes and nanoparticles are also obtained. The inert gas drags and cools the synthesized products, so the growth is affected by the speed of the existing ow, as well as by the thermal conductivity of the gas. CNTs are normally deposited on the cathode while the rest of the carbonaceous species are deposited mostly on the walls of the chamber. A graphite rod containing a metal catalyst (Fe, Co, etc.) is used as the anode with a pure graphite cathode to produce SWNTs in the form of soot (Bethune et al. 1993; Iijima et al. 1998). H2 use during the process results in better graphitization of CNTs as well as better process performance. This is due to the fact that hydrogen forms C-H bonds with the atoms at the ends of the CNT, which prevents the CNT from closing with a fullerene cap. (Y. Jiang et al. 2009) demonstrated that the use of NH3 during the arc discharge process improves the production efficiency of CNTs. Besides arc discharge, single-pulse arc discharge has been successfully applied in the production of near-vertically oriented MWCNTs on Ni/glass using a graphite counter-electrode in an ambient air (Parkansky et al. 2004; Prasek et al. 2011; Pantoja-Suárez 2019).

The growth of SWCNTs can be done by arc discharge method with or without the use of catalyst precursors. On the other hand, the MWCNTs are produced without a catalyst precursor. In

SWCNTs, the anode is made of graphite and a metal catalyst such as nickel (Ni), cobalt (Co), palladium (Pd), titanium (Ti), or platinum (Pt), or the mixtures of Co-Ni, Fe-Ni, Ni-Ti, etc. is used. The metal catalyst plays an important role in the process yield. The gap distance between the electrodes is held constant to ensure high efficiency. The production of CNTs is mostly affected by the presence of impurities. Calcination in air at 400 °C for 2 h is very effective in the removal of carbon nanoparticles deposited during DC arc discharge. Heating by IR irradiation in air at 500 °C is also being used to remove the unwanted carbon nanoparticles (Gupta 2017).

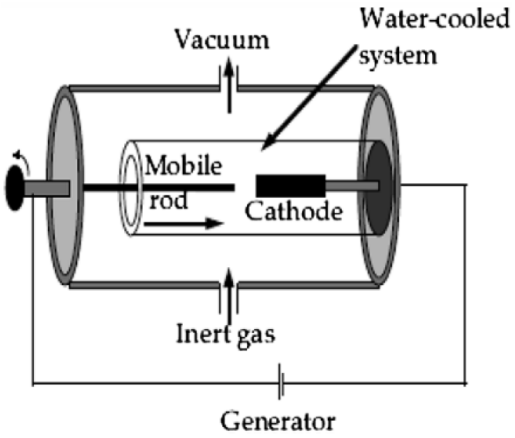

Figure 1.6: Experimental set-up of an arc discharge apparatus (Hussain 2014).

Laser ablation

A pulsed or continuous laser is used to vaporize a graphite target in an oven at 1200°C. The oven is filled with helium or argon gas in order to keep the pressure at 500 Torr (6.7×10^4 Pa). A hot vapor plume forms, then expands and cools rapidly. As the vaporized species cool, small carbon molecules and atoms quickly condense to form larger clusters, sometimes including fullerenes. The catalysts also begin to condense, but more slowly at first, and attach to carbon clusters and prevent their closing into cage structures. Catalysts may even open cage structures when they attach to them. From these initial clusters, tubular molecules grow into SWCNTs until the catalyst particles become too large, or until conditions have cooled sufficiently that carbon no longer can diffuse through or over the surface of the catalyst particles (Hussain 2014).

Chemical vapor deposition

Catalytic chemical vapor deposition (CCVD), either thermal or plasma enhanced (PECVD), is now the standard method for the CNTs production. Moreover, there are trends to use other CVD techniques, like water assisted CVD (Hussain 2014), alcohol assisted CVD (Li et al. 2018), oxygen assisted CVD (Hye et al. 2007), hot-filament (HFCVD) (Varshney et al. 2010), microwave plasma (MPECVD) (Brown et al. 2011) or radiofrequency CVD (RF-CVD) (Xu et al. 2011). CCVD is an economically viable process for large scale and quite pure CNTs production compared with laser ablation. The main advantage of this approach is the versatility to obtain CNTs on a multitude of different supports (conducting, semiconducting, and insulating materials) and geometries. In addition, in CVD processes it is possible to easily control the reaction course and the high purity of the obtained material. Chemical vapor deposition (CVD) is practiced in different formats. These formats generally differed in the means by which chemical reactions are performed. They are classified as follows (Pantoja-Suárez 2019):

- Atmospheric pressure CVD (APCVD), low-pressure CVD (LPCVD), and ultrahigh vacuum CVD (UHVCVD), when the operation depends on the chamber pressure.
- Aerosol-assisted CVD(AACVD), direct liquid injection CVD(DLICVD), when the operation depends on the physical characteristics of vapor.
- Plasma-enhanced CVD (PECVD), atomic layer CVD (ALCVD), microwave plasma assisted CVD (MPCVD), when the operation is controlled by plasmas.
- Hot filament CVD, rapid thermal CVD, and flame pyrolysis CVD in open air. All these operations are performed by following combustion technology.

CVD processes involve the catalytic decomposition of a solid, liquid or gaseous precursor rich in C atoms on nanometric-sized metal particles (catalyst) at temperatures between 600 and 1200 °C. The method involves passing a hydrocarbon gas (CH_n) (typically 15-60 min) through a tubular reactor in the presence of a catalyst material. The tube is heated to a high temperature to decompose the hydrocarbon. The function of the catalyst in the CVD process is the decomposition of the carbon source by applying heat (Gupta 2017).
Chemical vapor deposition (CVD) is the most prominent technique to synthesize the CNTs. It is also known as thermal CVD or catalytic CVD. As compared to arc-discharge and laser-ablation methods, CVD is a simple and economic technique for synthesizing CNTs at low temperature and ambient pressure. In crystallinity, arc- and laser-grown CNTs are superior to the CVD-grown ones (although CVD-grown MWCNTs possess inferior crystallinity, the crystallinity of SWCNTs grown

by CVD is close to that grown by arc or laser methods). However, in yield and purity, CVD beats the arc and laser methods. And, when it comes to structure control or CNT architecture, CVD is the only answer. Arc discharge and laser vaporization can be classified as high temperature (> 3000 °C) and short time reaction (μs to ms) techniques, whereas catalytic CVD is a medium temperature (500-1100°C) and longtime reaction (typically minutes to hours) technique. The CVD method uses a carbon source in the gas phase and a heated coil, to transfer the energy to the gaseous carbon molecule. Commonly used carbon sources are methane, carbon monoxide and acetylene. The energy source cracks the molecule into atomic carbon. The carbon then diffuses towards the substrate, which is heated and coated with a catalyst (usually a first-row transition metal such as Ni, Fe or Co) and binds to it (Rao and Govindaraj 2011). CVD is versatile in the sense that it offers harnessing plenty of hydrocarbons in any state (solid, liquid or gas), enables the use of various substrates, and allows CNT growth in a variety of forms, such as powder, thin or thick films, aligned or entangled, straight or coiled nanotubes, or a desired architecture of nanotubes on predefined sites of a patterned substrate. It also offers better control on the growth parameters (Kumar and Ando 2010).

Plasma enhanced chemical vapor deposition

The plasma enhanced chemical vapor deposition (PECVD) is a low temperature operation and can be also used in several different modes (radio frequency (RF), direct current (DC), diffusion (D), or microwave (MW)). The major difference between RF and DC mode PECVD is the higher concentration of reactive radicles in the former (Gupta 2017). Obtaining CNTs at lower temperatures than thermal CVD processes is vital when substrates sensitive to high temperatures are used (above 900 °C), especially in the manufacture of electronic devices. In comparison to the thermal CVD, with the PECVD it is possible (Pantoja-Suárez 2019):

- To have an extra contribution of precursor species due to the dissociation of the gases produced by the plasma.
- Obtain alignment perpendicular to the substrate of the CNTs, regardless of their density.
- Reduce the activation energy for the growth of CNTs.
- Lower growth rate with respect to thermal CVD.

The plasmatic energy efficiently dissociates gas molecules at lower temperatures, and the synthesis of carbon nanotubes might occur at lower temperature. PECVD has been investigated for its ability to produce vertically aligned nanotubes. It has been suggested that in PECVD only VACNTs grown from the tip are aligned specifically due to the presence of the plasma electric

field in the growth process, whereas VACNTs grown from the base are aligned mainly due to the crowding effect. The electrostatic force *F* creates a uniform tensile stress across the entire particle/CNT interface, regardless of where the particle is located tip or at base. The plasma is composed of electrons, charged species and ions, and neutral atoms and molecules. The plasma remains electrically neutral as the ion density is balanced by the electron density. The electron density in the radio frequency (RF) generated plasma is typically 10^8-10^9 cm^{-3} for a pressure range of 0.1- 133mbar. The electron temperatures are 1-11 eV, while the ion temperatures are lower at 50-100 meV. There is also a spontaneous but nonequilibrium conversion of neutral species into long lived radicals. The plasma forms \sheaths", dark regions of very low electron density, with the electrodes (Hussain 2014).

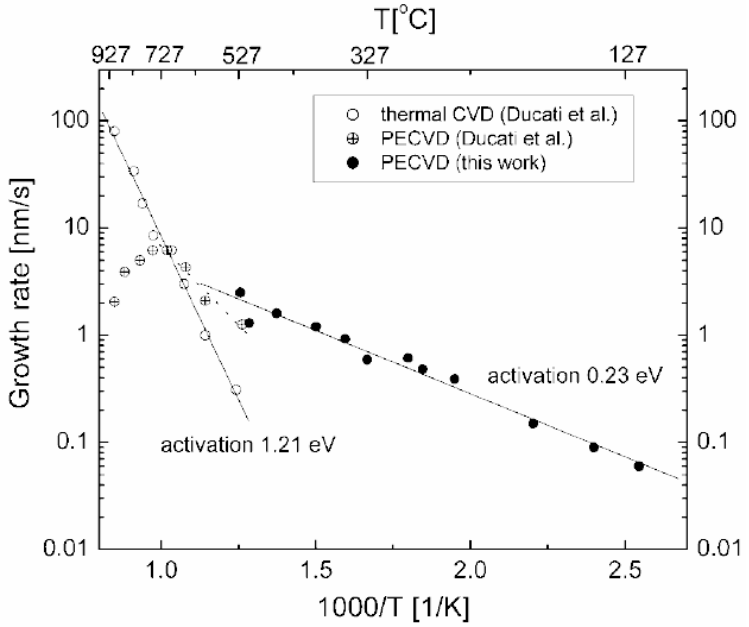

Figure 1.7: The growth rate variation with temperature for thermal CVD and PECVD (Hofmann et al. 2003).

Note that according to the VLS growth mechanism, the catalyst particles must be in liquid phase. Carbon nanotubes were precipitated from the supersaturated eutectic liquid (Grüneis et al. 2006). The activated energy for thermal CVD (≤700 °C) was reported to be about 1.21 eV, while in the case of PECVD, the activation energy is much lower (0.23 eV) (Hofmann et al. 2003). The differential fact that the PECVD technique allows such a low temperature for the synthesis of these nanostructures is the dissociation of species produced in the plasma, which increases the contribution of precursors to the catalyst. At high temperatures (> 700 °C approx.) CNTs grown by PECVD have a lower growth rate than their counterparts grown under thermal CVD conditions.

While at low temperatures, given that CNTs grown by PECVD present a lower activation energy, the growth rate is higher compared to thermal CVD Figure 1.7. Moreover, in general terms, the contribution of carbon atoms cannot be as high in PECVD as in thermal CVD, whose working pressure can be atmospheric. In a PECVD system, the technical difficulties in creating a stable discharge limits the working pressure to values below 5×10^3 Pa (Meyyappan et al. 2003; Pantoja-Suárez 2019)

1.3.4. Growth Mechanism

The mechanism known as vapor-liquid-solid (VLS) is widely accepted. VLS model was introduced for explaining the growth of silicon whiskers. For CNTs, this model was first adapted for explaining the formation of sea-urchin-like structures. According with this mechanism (Figures 1.8), the growth process includes the dissociation of gaseous hydrocarbon on the catalyst, the diffusion of adsorbed carbon atoms into the bulk of the nanoparticle, carbon precipitation, and the nucleation of cap structures of nanotubes (Chen and Zhang 2014). Since the caps that are initially formed around the catalyst define the diameter and the chirality of the growing nanotube, it is extremely effective to control the diameter and chirality by tuning the size, shape, and composition of the catalyst nanoparticles. It should be noted that CNTs can also be obtained using non-metallic particles. In this case, the growth of CNTs is explained by the mechanism known as vapor-solid-solid (VSS, illustrated in Figures 1.8) (Tessonnier and Su 2011). It was (Rümmeli et al. 2007) who noticed that oxide particles (which met certain requirements) could be used to obtain CNTs. This approach results in better diameter control and chirality control. The nonmetal catalysts, such as metal oxide and diamond, have high melting points so that their structure and morphology remain unchanged at high growth temperature. Such stable catalysts are superior templates for cap nucleation, thereby defining the diameter and chirality of the growing nanotube. Additionally, these solid nonmetal catalysts have little activity of carbon feed stock decomposition, resulting in the tendency of carbon atoms to diffuse along the particle surface (surface diffusion) instead of within the nanoparticle (bulk diffusion) (An et al. 2017; Pantoja-Suárez 2019).

The growth of CNTs by CVD ends when the catalyst loses its activity, which occurs when the diffusion of new C atoms into the particle becomes impossible. This may occur due to the formation of a stable carbide in the metal particle (Hernadi et al. 1996), or after total coverage of the metal particle by concentric graphitic shells (Guo et al. 2005; Li et al. 2015).

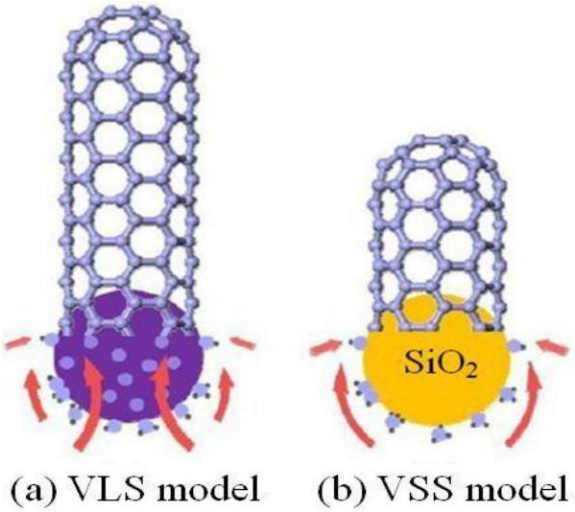

Figure 1.8. (a) The classical VLS mechanism during SWCNT growth by metallic catalyst. (b) The supposed VS mechanism during SWCNT growth from SiO2 nanoparticles as nucleation centers (Chen and Zhang 2011).

There are two different growth mechanisms in a CVD process, tip growth and root growth. When the catalyst-substrate interaction is weak hydrocarbon decomposes on the top surface of the metal, carbon diffuses down through the metal, and CNT precipitates out across the metal bottom, pushing the whole metal particle off the substrate. As long as the metal's cap is open for fresh hydrocarbon decomposition, the concentration gradient exists in the metal allowing carbon diffusion, and CNT continues to grow longer and longer. Once the metal is fully covered with excess carbon, its catalytic activity ceases and the CNT growth is stopped. This is known as "tip-growth model". In the other case, when the catalyst-substrate interaction is strong, initial hydrocarbon decomposition and carbon diffusion take place similar to that in the tip-growth case, but the CNT precipitation fails to push the metal particle up; so the precipitation is compelled to emerge out from the metal's apex (farthest from the substrate, having minimum interaction with the substrate). At first, carbon crystallizes out as a hemispherical dome (the most favorable closed-carbon network on a spherical nanoparticle) which then extends up in the form of seamless graphitic cylinder. Subsequent hydrocarbon decomposition takes place on the lower peripheral surface of the metal, and as-dissolved carbon diffuses upward. Thus, CNT grows up with the catalyst particle rooted on its base; hence, this is known as "base-growth model" (Kumar and Ando 2010). CNT synthesis involves many parameters such as hydrocarbon, catalyst, temperature, pressure, gas flow rate, deposition time, reactor geometry (Hussain 2014).

1.3.5. Properties of catalysts

Most important catalysts are transition metal alloys. Ni, Fe and Co are the most commonly used metals, because of their strong activity in catalyzing the decomposition of carbon feedstock and sufficient carbon solubility (Yan Li et al. 2010). However, other metals and their alloys can also be used: Mo, Pd, Cu, Au, Ag, Mn, Cr, Sn, and Al, and their combinations, have been employed as catalysts in the form of nanoparticles, nanoclusters, or single crystals (An et al. 2017).

In most of the cases a barrier layer could be metal (e.g. Al, Ti) or metal oxide, (e.g. Al2O3, SiO2) is deposited on the top surface of the substrate to avoid the catalyst diffusion upon annealing at higher temperature. The heating is performed in an inert atmosphere such as under hydrogen flow to reduce the catalyst to metallic form during heating. At a desired temperature the thin catalyst film collapse and converts into nanometric size particles. The size of nanoparticles tells the diameter of the growing nanotube. So starting from an oxide catalyst, a reduction of metal oxide takes place during decomposition of carbon precursor compound. As a result, a metallic particle forms through intermediate oxide states. Upon carbon dissolution, metal-carbon mixture or metal carbide is formed. Subsequent segregation results in the formation of graphitic carbon and metal particles. Bimetallic catalyst such as iron-cobalt alloy shows higher catalytic activity based on lower melting temperature and an increase in carbon solubility (Flahaut et al. 1999; Moisala et al. 2003). The size of metal particles explains the melting temperature of the metal, at a size of less than about 100 nm melting temperature can be lowered significantly and lower than 10 nm an exceptional decrease is observed. The reason is at nanometric size the ratio of surface atoms increase with respect to internal atoms. The surface atoms are electronically and coordinately unsaturated and thus are more reactive and mobile (Moisala et al. 2003). The melting temperature of a metal particle (*Tc*) with radius *r* can be approximated by following (equation 1.3) [24].

$$T_c = T_0 - \frac{2T_0}{\Delta H_{fusion}\rho_s r}\left[\sigma_{sl} + \left(1 - \frac{\rho_s}{\rho_l}\right)\sigma_l\right] \quad (1.3)$$

where T_0 is the bulk melting temperature, ΔH_{fusion} is the latent heat of fusion, ρ_s and ρ_l are the densities of solid and liquid metal respectively, σ_s is the surface energy associated to the interface solid/liquid and σ_l is the surface energy.

According with the iron-carbon phase diagram, the eutectic temperature for the Fe-C in the bulk phase is 1153 °C but it decreased down to 732 °C significantly at the nanometer scale (Harutyunyan et al. 2005). At higher temperature catalyst particle is more active and stay in liquid phase for longer time but it is important to grow the nanotubes at the temperature well below self-pyrolysis temperature and slightly above the eutectic point. The self-pyrolysis temperature depends on the stability of the carbon source used and the eutectic point decreases for all metals with the film thickness. The catalyst deactivation due to the amorphous carbon is a major problem which is the result of the self-pyrolysis of hydrocarbon or excessive carbon concentration (Hussain 2014). Figure 1.9 represents the iron-carbon phase diagram, and it shows the eutectic points of other two metals used commonly as catalysts (Co and Ni). Note that Fe is the metal with the lowest eutectic point. Indeed, eutectic means easy to melt. The carbon content at the eutectic points of cobalt-carbon and nickel carbon phases is approximately two times lower and the temperature significantly higher than for the iron-carbon phase. Additionally, the solidification of cobalt-carbon and nickel-carbon phases occurs at relatively low concentration of carbon, at a given temperature. These can terminate the growth of SWCNTs at early stages. Therefore, cobalt and nickel catalysts will require higher synthesis temperatures, as in the cases of laser ablation or arc-discharge methods (Harutyunyan et al. 2005). It is important to consider that the catalyst particle diameter largely determines the diameter of the CNTs formed from them. It is relatively easy to control the diameter and number of walls of the CNTs by tuning the size of the catalyst nanoparticles.

As shown in Figure 1.10, when iron is used as catalyst, the number of graphitic walls in a CNT is dependent on CNT diameter, which is dependent on catalyst thickness. The mean CNT diameter is proportional to the thickness of the Fe thin film, and thin CNTs have a strong tendency to be SWCNTs while thick CNTs tend to be double-walled carbon nanotubes (DWCNTs) or MWCNTs. SWCNTs occupied most of the nanotube population within a diameter range of 1.0 – 2.5 nm, and DWCNTs account for the majority of CNTs with a diameter in the range of 3.0-4.0 nm, while MWCNTs have a higher percentage for the diameter larger than 4.5 nm. Maximum DWCNT selectivity was reached at an Fe thin film thickness of 1.69 nm. It is generally believed that during catalyst annealing, thick metal thin films break up into smaller (larger) catalytic nanoparticles, which, in turn, produce smaller (larger) tubes. Empirically, it is well established that a thin catalytic metal film (around 1 nm) is required to grow SWNTs.

There are many other parameters affect the catalyst nanoparticles such as pressure, gas used, temperature, surface energy of the substrate, among others. (Dervishi et al. 2009) studied the

thermal effect from an MgO supported Fe-Co catalyst system. It was found that the diameter distribution was broadened when raising the growth temperature from 800 to 1000 °C. These results are normally explained by particle coalescence or Ostwald ripening (Wen et al. 1996). At the CNT growth temperatures, catalyst sintering by coalescence modifies the particle size distribution and consequently the CNT diameter distribution. Some supports, MgO and Al_2O_3, seem to keep the particles in a dispersed state. Another approach to solve the sintering problem is to embed the transition metal species in a matrix. Several groups showed that mixed oxide catalysts, that is, oxides with several elements present as cations in the structure, are efficient catalysts to grow MWCNTs. Mixed oxides with perovskite- and spinel-type oxide structures led to particularly interesting results (Tessonnier and Su 2011).

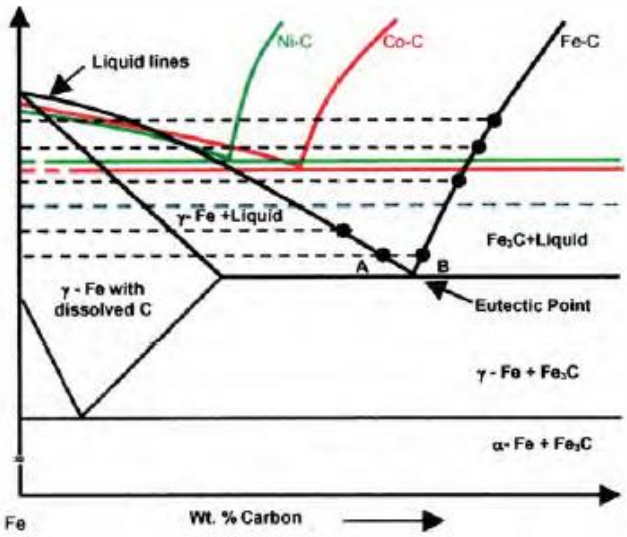

Figure 1.9: Scheme of the iron-carbon phase diagram (Harutyunyan et al. 2005).

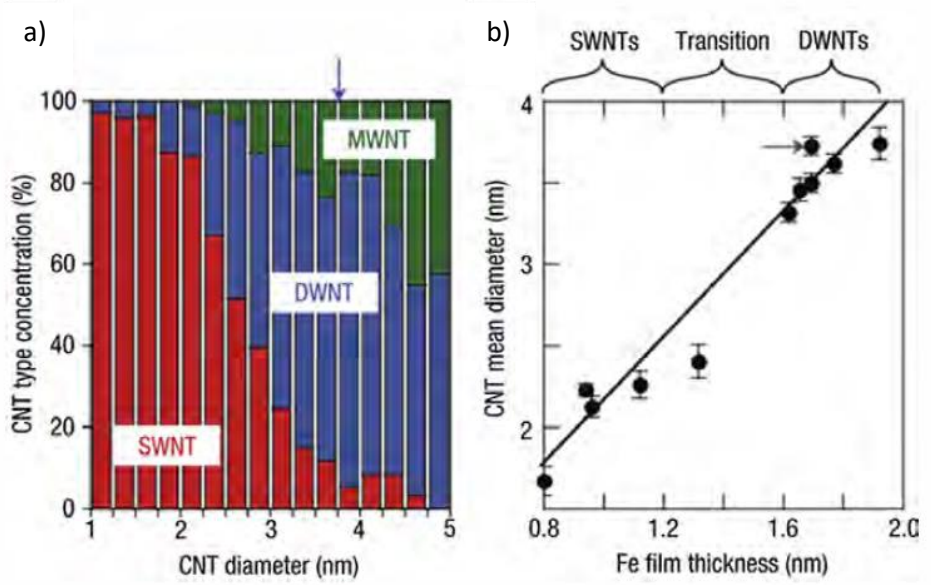

Figure 1.10: Trends in carbon nanotube (CNT) type and diameter. (a) Concentrations of single walled carbon nanotube (SWNT), double-walled carbon nanotube (DWNT), and multiwalled carbon nanotube (MWNT) as a function of the CNT diameter; (b) CNT mean diameter as a function of Fe film thickness (An et al. 2017).

1.3.6. Effect of Precursor gases

The selection of the gas(s) influences the characteristics of the CNTs. From the formation of the catalyst nanoparticles, through the orientation of the nanotubes, to the amount of amorphous carbon are strongly related to the gases used during the production of these carbon-based materials. Among the precursor materials of CVD growth of CNTs, a distinction can be made between those that are used as sources of carbon atoms, and those that have a catalytic, or simply carrier, function. The precursors traditionally used as sources of carbon are acetylene (C_2H_2) and methane (CH_4). However, there are many other gaseous precursors such as ethane (C_2H_6), ethylene (C_2H_4), 1,2-propandiene (C_3H_4), carbon monoxide (CO); solid C sources such as camphor ($C_{10}H_{16}O$); and liquid precursors such as benzene (C_6H_6), toluene ($C_6H_5CH_3$), iso-octane or ethanol (C_2H_5OH) or 2,2,4-trimethyl-pentane (C_8H_{18}) among others. The gas that can provide high quantity of CNTs, better crystallinity at low temperature with as low as possible of amorphous carbon is considered ideal for the growth of CNTs (Pantoja-Suárez 2019).

To prevent the deposition of amorphous carbon (“a-C”), which inhibits the formation of nanotubes by poisoning the growth catalyst and can also cause short circuits on the substrate surface, the

carbon source is combined with a hydrogen-rich gas (typically, NH_3 or H_2), which produces reactive species in the plasma to remove any excess carbon. The use of etch gas during the growth process of CNTs is important. It has been widely reported that atomic hydrogen is the active species for the removal of excess carbon. NH_3 has a key role in removing any excess carbon through the generation of reactive atomic hydrogen species, which combine with and carry away carbon atoms (Hussain 2014). At high NH_3 ratios, NH_3 decomposes preferentially over C_2H_2. This is because the chemical bonds that hold the NH_3 molecule together are weaker than those that hold C_2H_2 together. This allows the C_2H_2 to decompose slowly, generating the small amounts of carbon necessary for nanotube self-assembly. At high C_2H_2 ratios, there is insufficient NH_3 to effectively suppress C_2H_2 decomposition, resulting in higher levels of carbon generation and deposition of excess carbon as a-C.

NH_3 therefore has two key roles in the formation of carbon nanotubes: Not only does it generate atomic hydrogen species to remove any excess carbon, it also suppresses the decomposition of C_2H_2, limiting the amount of carbon generated in the first place. The gas-phase removal of carbon containing species results in the production of gaseous HCN, which is detected in the mass spectra (Bell et al. 2006)

1.4. Graphene

Graphene is a two-dimensional allotrope of carbon. The name 'graphene' was first mentioned in 1987 to describe the graphite layers that had various compounds inserted between them. Graphene prices drop in (euro/cm^2) during the last 10 years from 1000 to about 2 euros/cm^2 (Figure 1.11)

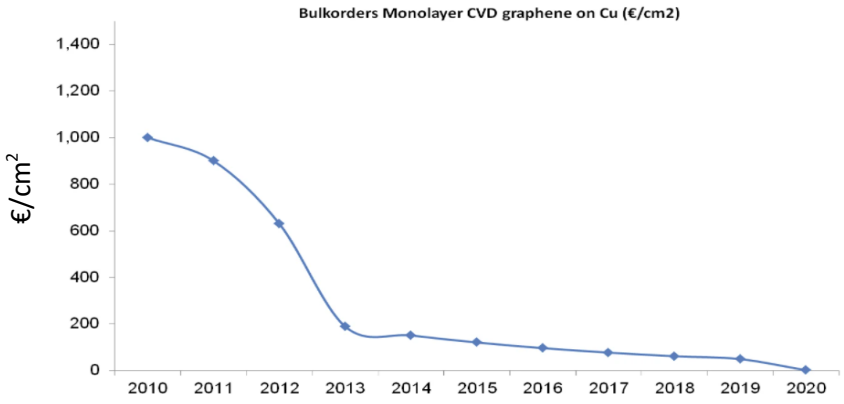

Figure1.11 : Graphene prices drop in (euro/cm^2) during the last 10 years from 1000 to about 2 euros/cm^2 (Graphenea 2020).

In 1948, with the advent of the first electron microscopy, images of several layers of graphite were first observed, followed by the observation of single graphene layers by Ruess and Vogt (Ruess and Vogt 1948). Since then, pursuit of “isolating graphene” started, and in 2004 two scientists from University of Manchester Andre Geim and Constantine Novoselov for the first time isolated a single atomic layer of carbon (graphene) layers from graphite. They noticed some flakes to be thinner than others. By separating the graphite fragments repeatedly, they managed to create flakes which were just one atom thick. They played with graphite cubes and Scotch tape, for pulling flakes of graphite. They had repeated the flaking-off graphite until they obtained a one atom thick layer. Geim and Novoselov had invented Wallace’s graphene. The ¨scotch tape¨ method was so simple and effective, that this area of science grew extremely quickly and nowadays many research institutes around the world use this technique for investigation of graphene, because it doesn’t require large investments or complicated equipment (Novoselov et al. 2004). In 2010 Andre Geim and Konstantin Novoselov were awarded Nobel Prize in physics for this work, becoming the 24th and 25th Nobel Laureates in history of the University's (Avetisyan 2019). The interest of studing the graphene has increased in last decades as the number of scientific published articles about studying its properties and applications reached to 144,485 articles during the year 2021 until the moment of writing this line (Figure 1.12).

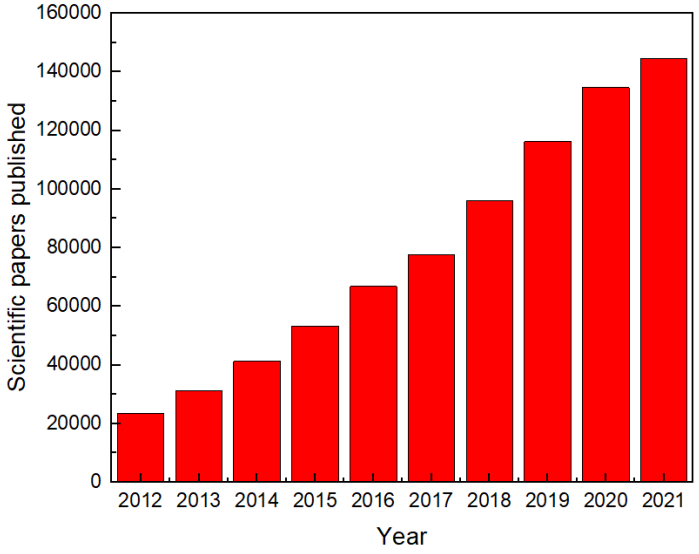

Figure 1.12. The increase of the number of publications of graphene during the past 10 years.

1.4.1. Graphene structure

Graphene is a single layer of carbon packed in a hexagonal (honeycomb) lattice, with a carbon-carbon distance of 0.142 nm that mimics a honeycomb structure. Out of graphene plane, the non-completely filled π orbitals forms weak π bonds and they are responsible for conductive properties. Its extended honeycomb network is the basic building block of other important allotropes; it can be stacked to form 3D graphite, rolled to form 1D nanotubes, and wrapped to form 0D fullerenes. Graphene sheets can stack in three main different ways: hexagonal (Order, AA), bernal (AB), and rhombohedral (ABC) stacking (Fig. 1.14). In Order stacking all the carbon atoms of each layer are well-aligned. For AB and ABC stacking, a cycle period is constituted by two layers and three layers of a non-aligned graphene, respectively (Koshino 2009; Jhang et al. 2011; Lui et al. 2011). In Order stacking, all the carbon atoms of each layer are well aligned. For AB and ABC stacking, a cycle period is constituted by two layers and three layers of a non-aligned graphene, respectively. A highly symmetrical structure occurs in Order stacking, while the structure in ABC stacking is relatively complicated. Graphene possesses many extraordinary properties and has been the subject of intense scientific interest. One of the interesting features of graphene is the edge effect. Graphene edges are typically far from ideal and suffer from atomic-scale defects, structural distortion, and unintended chemical functionalization, leading to unpredictable properties. The presence of edges strongly affects the electronic structure depending on their edge shape (zigzag and armchair edges).

Depending on the direction of the cutting line of a graphene sheet, there can be two types of edges created, as shown in figure 1.13, namely armchair edges and zigzag edges [Enoki T, 2007]. Manipulation of graphene edges at atomic level is very promising for exploiting graphene recognized potential in the next generation of electronic, optical, mechanical, and chemical devices.

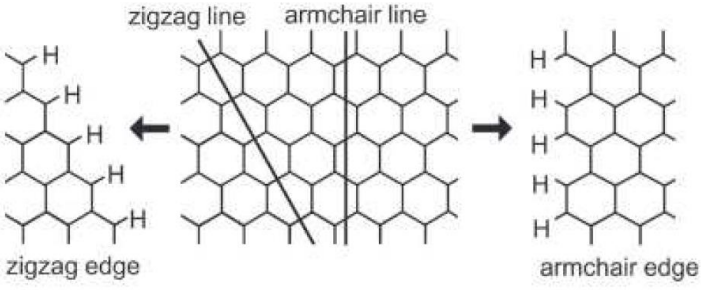

Figure 1.13 Zigzag and armchair lines and hydrogen-terminated zigzag and armchair edges in a graphene sheet (Enoki et al. 2007).

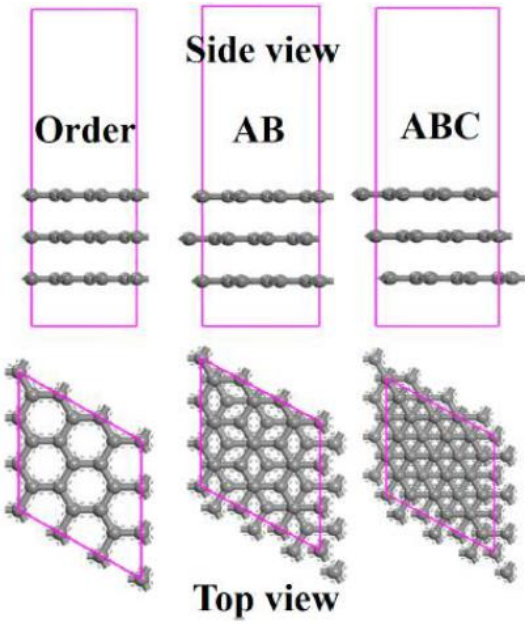

Figure 1.14 The side and top views of the stacked graphene layers with Order, AB, and ABC pattern (Yang et al. 2018).

1.4.2. Properties

The unique plane structure and geometry of monolayer graphene contribute its super properties, including high Young's modulus (~1100 GPa), high fracture strength (~125 GPa), excellent electrical (~106 S/cm) and thermal conductivity (~5000 W/(m·K)), fast mobility of charge carriers (2×105 cm2/(V·s)) and large specific surface area (theoretically calculated value, 2630 m2/g). Below described in some details the thermal and mechanical properties of graphene. (Avetisyan 2019)

Thermal Properties

The strong and anisotropic bonding and the low mass of the carbon atoms give graphene and related materials unique thermal properties. Therefore, recently, there has appeared a strong motivation to investigate thermal properties of graphene and related composite materials from the positions of practical applications. From the point of view of performance and reliability of new technologies, such as modern electronic, optoelectronic, photonic devices and systems, the efficient heat removal it is an important issue, which can be resolved by using optimal thermal interface materials (TIMs) between heat sources and heat sinks. Conventional TIMs filled with

thermally conductive particles require high volume of fractions filler (f ~ 50%) to achieve thermal conductivity *K* of the composite in the range of ~1-5 W/(m·K) at a room temperature (RT) (Shahil and Balandin 2012) There is a great demand of TIMs for electronic used in information processing and communications and also for used in the ¨green¨ technology (Photovoltaic solar cells) revolution.

Graphene is great material for using in TEMs. It is demonstrated in different researches that thermal conductivity of TIMs with enhanced graphene elements may lead to revolutionary increase in device and system performance not only in electronics but also in optoelectronics and

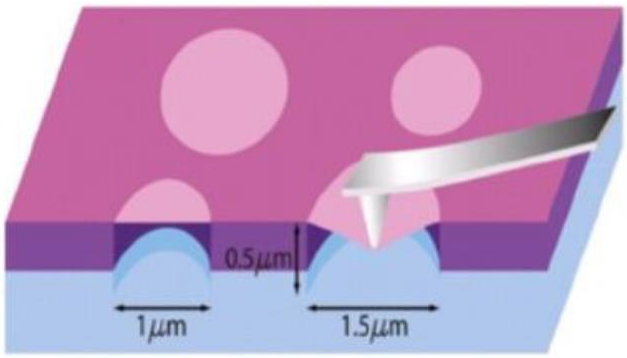

Figure 1.15. Mechanical testing of graphene. Schematic of nanoindentation on suspended graphene membrane [Lee C,2008].

renewable energy generation. In 2008, it was discovered that graphene has extremely high intrinsic thermal conductivity (*Ki*), which can exceed that of carbon nanotubes (CNTs) (Balandin 2011) The extraordinary thermal properties were discovered at the University of California-Riverside. Original non-contact optothermal technique was used for experiment based on Raman spectroscopy (Fig. 1.14). In this experiment the graphene layer was obtained by mechanical exfoliation from high quality bulk graphite. This technique was developed only for measuring thermal conductivity of the atomically thin materials. The value of *K* was found between 3000 W/(m·K) to 5300 W/(m·K), depending on the size of the graphene flakes, at a near room temperature. This number is among the highest of any known material. This result is clearly above the bulk graphite limit of 2000 W/(m·K) [Balandin, AA, 2008] and it exceeds the record values of diamond and carbon nanotubes, about 2000–4000 W·m–1·K–1 for freely suspended samples [Balandin, AA, 2011; Chen S, 2012]. This attractive thermal conductivity of graphene makes this material beneficial for electronic applications and establishes graphene as an excellent material for thermal management.

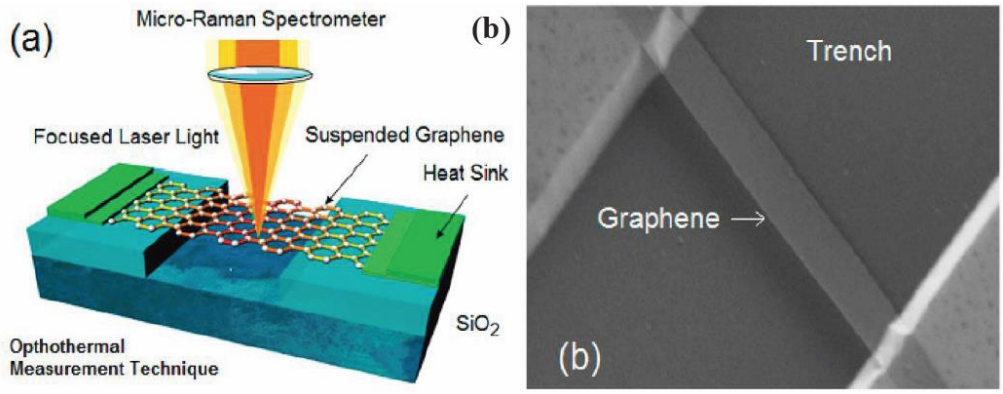

Figure 1.16 Schematic structure of the suspended grapheme used for measurements of the thermal conductivity. Graphene was heated with the laser light focused in the middle of the suspended part. The temperature rise was determined from the shift of the G peak position in graphene Raman spectrum; (b) Scanning electron image of the bilayer graphene ribbon suspended across the 3-μm trench in Si/SiO2 wafer for optothermal measurements [Balandin AA, 2011].

Mechanical properties

Graphene is one of the strongest materials, which provides a tensile strength of 130 GPa and is one of the stiffest known materials characterized by a remarkably high Young's modulus of ~ 1 TPa. In general, mechanical properties of a crystalline solid are controlled by characteristics of its pristine crystal lattice and structural defects such as dislocations and grain boundaries [Hirth JP, 1982; Veprek S, 2007]. In the case of graphene, the reason for the exceptional mechanical properties lies in the stability of the sp2 bonds that form the hexagonal lattice and oppose a variety of in-plane deformations [Lee C, 2008]. For the first time, mechanical measurements of free-standing monolayer graphene were carried out by using nanoindentation in an AFM [Lee C, 2008] (Figure 1.16). For measuring the mechanical properties of graphene, it was deposited onto a substrate with arrays of circular wells and loaded by a tip of an atomic force microscope. The force-displacement behavior was interpreted within a framework of nonlinear elastic stress strain response and yields second- and third-order elastic stiffnesses of 340 $N \cdot m^{-1}$ and 690 $N \cdot m^{-1}$, respectively. The breaking strength is 42 Nm^{-1} and represents the intrinsic strength of a defect free sheet. These quantities correspond to a Young's modulus of E = 1.0 TPa, third-order elastic stiffness of D = -2.0 TPa, and intrinsic strength of σ_{int} = 130 GPa for bulk graphite. They also

showed that atomically perfect nanoscale materials can be mechanically tested to deformations, which are well beyond the linear regime [Lee C,2008]. Then, graphene has strength 300 times more than that of steel. However, concept of the strength is something general, there are different types of strength: strength in tension, compression, hardness, toughness and fatigue just to name a few (Avetisyan 2019).

1.4.3. Graphene Nanowalls

Graphene nanowalls (CNWs) are two-dimensional carbon nanostructures consisting of walls that are constructed of aligned graphene layers on different substrates. Vertical graphene (VG) is intrinsically graphene with unique structural features, being arranged perpendicularly to the substrate surface. Individual VG nanostructure usually has lateral and vertical dimensions of 0.1 to tens of micrometers and a thickness of only few nanometers [Kondo S, 2008; Ni ZH, 2007]. As compared with the horizontally oriented graphene this type of graphene nanostructures attract attention due to its high surface-area-to-volume ratio. The most important features of multi-layeres GNWs are high aspect ratio, large surface area and sharp edges [Ni ZH, 2007].

MLGNWs were first discovered in 2001 by Yihong Wu. The vertical structure was found during the growth of carbon nanotubes in a microwave PECVD process. MLGNWs first deposit was carried out over NiFe (40 nm) coated sapphire substrate, under CH_4 and H_2 gas flow in the 650ºC-700ºC temperature range. Since then, a number of reports has been published using a variety of growth parameters for MLGNWs synthesis. For vertically oriented graphene growth, the plasma state has an essential role, as compared with planar graphene, which can be synthesized by mechanical and chemical exfoliation, thermal decomposition of carbon-terminated silicon carbide, epitaxial growth and chemical vapor deposition (CVD) [Wu YH, 2002]. Many researchers have used different types of plasma enhanced chemical vapor deposition methods (PECVD), such as DC, RF and microwave plasma discharges in a variety of configurations. PECVD technique has high probability to be a promising technique for new generation technologies, due to its feasibility and potentiality for large-area production with reasonable growth rates at relatively low temperatures. This method as compared with CVD has advantages such as low operating temperature, full step coverage and generally, high growth rate, high plasma density and reactive radical density. It also offers a better control of nanostructure ordering/patterning, due to the presence of energetic electrons, excited molecules and atoms, free radicals, photons and other active species in the plasma region, where occurs MLGNWs deposition [Droes SR, 1997]. The precursor gases used in these PECVD processes may vary. Many researcher groups used CH_4, C_2H_2, C_2H_4, C_2F_6 and CO_2 as precursor gas [Kondo S, 2009; Chatei H, 2006; Vizireanu S, 2009].

Moreover, etchant and diluent gases, such as H_2, O_2, N_2, NH_3, H_2O, as well as, noble gases He, Ne, Ar and Kr were used [Vizireanu S, 2009; Teii K, 2009; Zhu W, 1990]. For the MLGNWs growth, a broad number of substrates such as conductor, semiconductor, and insulator, was used [Wu YH, 2004; Malesevic A, 2008]. Vertical graphene was discovered in 2001, but there is still no specific description of the growth mechanism. Numerous researchers have proposed growth mechanisms for MLGNWs based on experiments performed in the early stages of deposition [Hiramatsu M, 2006; Kondo S, 2009; Teii K, 2009; Malesevic A, 2008; French BL, 2006]. In this thesis, the new proposed growth mechanisms will be presented.

Vertically oriented graphene nanowalls possess a number of unique mechanical, chemical, electronic, electrochemical and optoelectronic properties that could benefit their potential use in a wide range of applications. Many applications have already been described in the literature, such as field electron emitters, catalyst supports/templates, and hydrophobic coating (due to the H or F terminations) [Hiramatsu M, 2010] (Figure 1.17). MLGNWs due to the very low reflectance, high specific absorbance in thin transparent films have the possibility of being used as dark coating for a bolometer absorber [Krivchenko V, 2013]. The ability to tailor the band gap of GNWs opens new doors to their usage for the design and evolution in modern nano-electronic devices. On the other hand, the carrier concentration and mobility; the band gap inside the individual monolithic graphene nanowall sheets are also of great interest for realizing nanographene devices [Hiramatsu M, 2010]. This unique three-dimensional graphene structure possesses high hydrophobicity and outstanding electron conductivity. The in-situ one step growth method indicates the great potential of using VG in supercapacitors. Also MLGNWs can be used in flexible photovoltaic devices, field-effect transistors (FETs), sensors, charge trapping memory (CNT) [Liu XSJ, 2014]. In addition, MLGNWs is an eligible candidate for using in biocompatible scaffolds for osteoblast culture and tissue engineering [Ion R, 2016]. Electrophoretic deposition can be used to fabricate composite MLGNWs/graphite electrodes for electrochemical detection of DNA sequences with estimated zeptomole LODs [Akhavan O, 2012]. For each application, high-quality MLGNWs should be grown on suitable substrate. For example, MLGNWs grown on Cu foil becomes an excellent electrode for supercapacitors, meanwhile, MLGNWs on dielectric (SiO2) substrate could be used to fabricate gas or bio-sensors, also MLGNWs on semiconductor substrates could be used rather for potential application of solar cells [Li M, 2016].

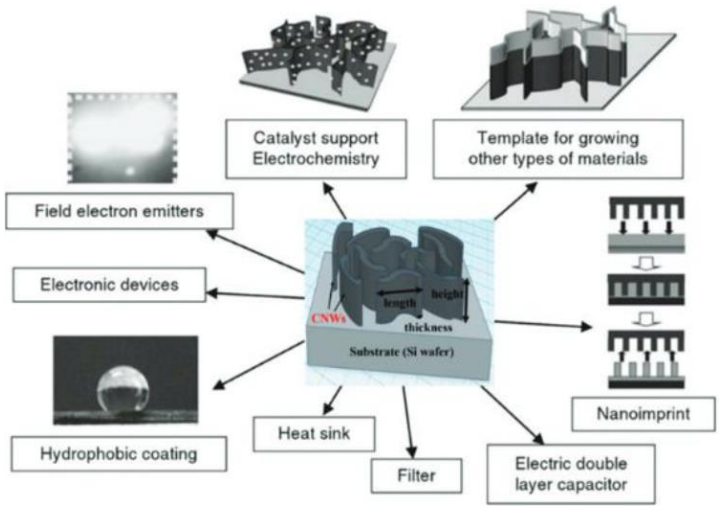

Figure 1.17 Schematic representations of the potential applications of MLGNWs [Hiramatsu M, 2010].

1.5 Objective

The main purpose of the thesis is to improve the synthesis parameters of carbon nanotubes and hybrid nanostructures on flexible and conductive substrates. For that, we will study three different technologies based on CVD, PVD, and plasma-liquid interaction. These studies are focused to the improvement of the electrodes of high specific capacitance.

These technologies also offer a diversity of production methods of nanomaterials, which open other future developments of flexible electrodes for supercapacitors and batteries, sensors, photo and electrocatalysis, and other developments like biosensors for smart wear.

Chapter 2

Characterization Techniques

In order to understand the material properties and functionality, we need to use different techniques to characterize and view the material and any change can happen to it from different aspects. In this work, it will be noticed that the most used techniques are the different electron microscopies such as scanning electron microscopy (SEM) for studying the morphology in general, transmission electron microscopy (TEM) to study the nanostructure of the material and its crystallinity. Some other techniques have been used to study more properties such as Raman Spectroscopy and X-Ray Photoelectron Spectroscopy (XPS) to study the chemical and structural properties. Both the substrate and the synthesized carbon materials must be studied in order to improve the surface modifications and carbon material growth conditions to reach the optimum possible conditions. Finally, we tested the materials as an electrode material for supercapacitors application using different electrochemistry techniques. Below we can find the different techniques that have been used.

2.1. Electron Microscopy

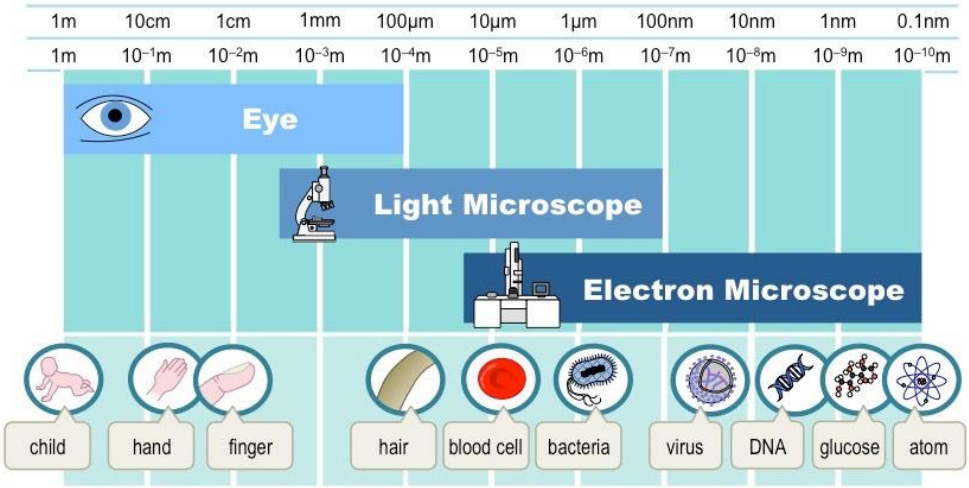

Figure 2.1: Resolution limitation of human eye versus different imaging techniques (Kaech 2018).

The unaided human eyes can resolve a distance of 0.2 mm apart while by adding a lens (aided eye), they are enabled to resolve until 0.1 mm distance. This limit is called the resolution power of human eye. To overcome these limitations, the microscope was developed and used as an efficient magnifying tool. Figure 2.1 shows a comparison of observing objects between the human eye and the optical and electron microscopies. According to Ernest Abbé law, the resolution limit of any optical system depends on two

factors, the wavelength of the light source (*λ*) and the numerical aperture of the lens (*NA*). This law applies for electrons as the electrons have the characteristic of both particles and wave where the higher speed of electrons, the smaller wavelength therefore higher resolution (Spence, 2017).

According to Abbe, the limits of resolution (*LR*) or the minimum resolvable distance d_o can be calculated by equation 2.1 as follows:

$$Limit\ of\ resolution = \ d_o = \frac{1.22\lambda}{2\ (n \sin \alpha)} = \frac{0.61\lambda}{(n \sin \alpha)} = \frac{0.61\lambda}{NA} \quad (2.1)$$

Where *n* is the refractive index and *α* is the semi-angle of the specimen. The *NA* has a maximum value of 1.4. where the short blue light (*λ*=436 nm) can yield a resolution up to 190 nm only.

Electron microscopy (EM) has been a revolutionary imaging technology that uses a focused accelerated beam of electrons which causes the diffraction effects to exist at a very small physical dimension. The EM has a larger resolving power than the optical spectroscopy because the electrons have a wavelength 100,000 times shorter than the photons of the visible light. In the electron microscope the electrons are directed using magnetic lenses much as the light is directed by optical lens in the light microscope.
The determination of the incident electron wavelength can be calculated using De Broglie's expression depending on the kinetic energy of the electrons, *k*, as follows:

$$\lambda = \frac{h}{p} = \frac{h}{\sqrt{2m_e\kappa}} \quad (2.2)$$

Where *h* is the Planck's constant, *p* is the electron momentum, and *m* is the electron mass (Rosenberg & Weis, 1983).

By considering the relativistic effects accompanying with the high energies, De Broglie's expression becomes as follows:

$$\lambda = \frac{h}{\sqrt{2m_e eV_e\ (1+\frac{eV_e}{2m_e c^2})}} \quad (2.3)$$

Where c is the speed of light, V_e is the acceleration potential of the microscope and e is the charge.

2.1.1. Scanning Electron Microscopy (SEM)

SEM is an advanced multifunctional instrument, mainly used to observe the surface phenomena of materials. When the specimen is shot by high energy electrons, the emitted X-ray/electrons are analyzed which allows it to provide multiple qualitative information about the sample such as the surface features and texture, arrangement of particles on the sample surface, size and shape. In general, it provides a composition, morphological, topographical, and crystallographic information.

SEM is considered as a leading instrument for obtaining a detailed visual image of a particle with a spatial resolution of 1 nm and high-quality (Brabazon & Raffer, 2000). Magnifications of up to 300,000 times are possible with this microscopy. Although SEM is only used to visualize the surface images of a material and does not provide any interior information, it is nevertheless a valuable tool (Mcmahon, 2007).

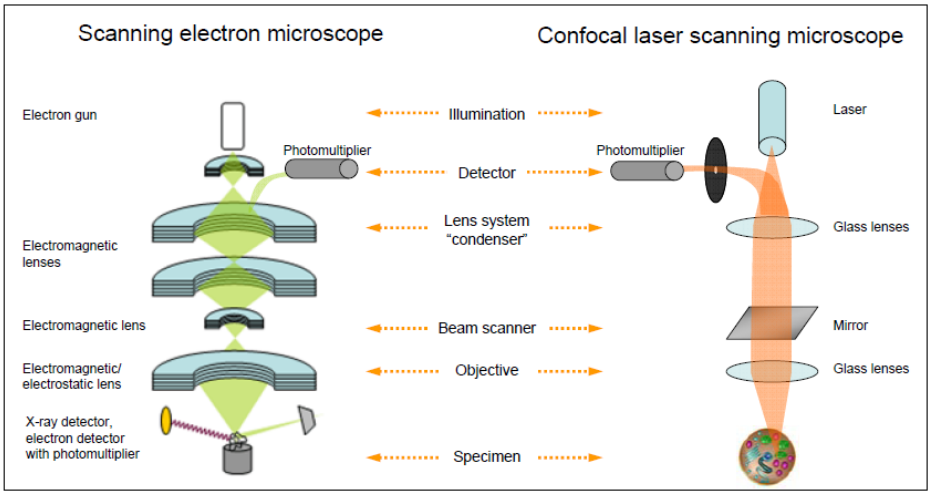

Figure 2.2: Similarity of scanning electron microscope with a confocal laser scanning microscope (Kaech, 2013).

The principle of SEM is based on releasing the primary electrons providing an energy to the atomic electrons of the sample which then can be released as the secondary electrons (SEs) which can be collected from each point of the specimen in order to form the image. Operating under vacuum is one of the basic requirements for SEM to obtain high resolution by avoiding the electrons interactions with any gas molecules inside the chamber. The primary electrons that are shot from the electron gun are accelerated either by heating or applying high energy between 1-40 keV (J. Goldstein et al., 2003).

SEM construction is similar in some sides with the confocal laser scanning microscope (Figure 2.2).

In general, there are two kind of interactions inside SEM elastic and inelastic interactions. Inelastic interactions are the ones in which the beam electron interacts with the electric field of the specimen atom electron, resulting in energy transfer from the beam electron to the specimen atom and potential ejection of an electron from that atom as SEs have energy less than 50 eV.

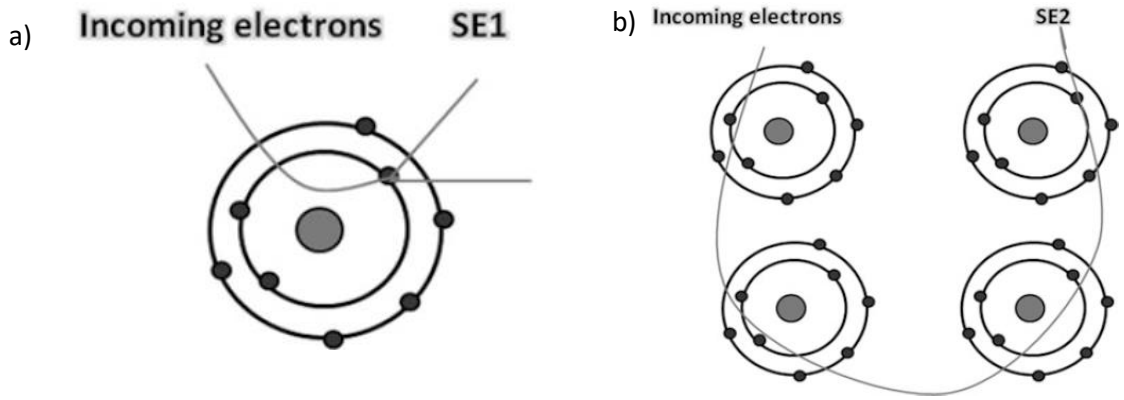

Figure 2.3: The electron beam interaction with the specimen and the emitted signals from the sample (Akhtar et al., 2018).

Secondary electron emission leaves a vacancy, which is then filled by an electron from a higher level orbital which results in the emission of high energy transition X-rays (Bondeson, 2007).

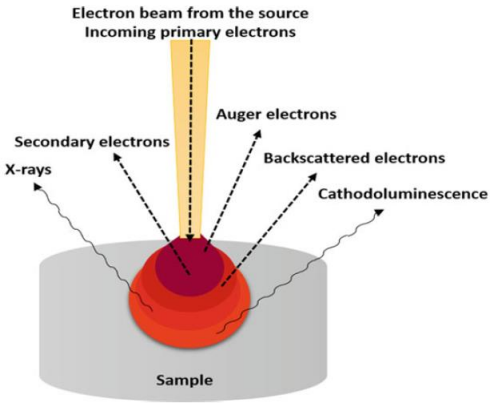

Figure 2.4: Secondary electrons a) SE1 and b) SE2 that are emitted from the sample in SEM (Akhtar et al., 2018).

Elastic interactions are those that occur between the electric field of the nucleus of a specimen atom and the primary electrons, and as a result of these interactions, the primary electrons' direction changes without a considerable change in their energy (1 eV) (Zhou et al., 2007).

Back scattered electrons (BSEs) are elastically scattered electrons that deflect back out of the specimen and their energies ranges between 50 eV to almost equal to the incident beam electrons. BSEs, in general, retain a minimum of 50% of the incident beam energy. Because secondary and backscattered electrons leave the sample at different depths, their energies are varied. SEs normally escape from a depth of around 5-50 nm, BSEs from a larger depth than SEs, while X-rays at far deeper levels (Figure 2.3)(Zhou et al., 2007).

SEs and BSEs are mainly used for the material imaging. SEs is usually important for studying the morphology and topography of the materials (McMahon, 2007). As the SEs produced because of the collision between the primary electrons and the weakly bonded outer electrons, their number is higher than the incoming electrons. This leads us to the concept of SE coefficient (δ):

$$\delta = \frac{Number\ of\ SEs}{Number\ of\ primary\ electrons} \tag{2.4}$$

SE coefficient is relatively not dependent to the atomic number of the sample atoms. The relation between the SE coefficient and the beam energy is inverse. As when we decrease the beam energy (Accelerating voltage), SE coefficient increases because of the interaction volume decrease.

There are two mechanisms where the SEs are produced, which can be differentiated as SE1 and SE2. SE1 are those that are extracted by the primary electron beam. When the primary electrons reach the material surface, some energy will be transferred to the outer sample electrons resulting in a high-resolution signal. When the electrons undergo many inelastic scatterings inside the specimen until they reach the surface, then they are called SE2 (Figure 2.4). The surface area of the generated SE2 is bigger than the electron beam spot. In general, the resolution of SE2 is weaker than for SE1. There are many factors that can affect of disturb the emission of SE such as atomic number, electron beam current and energy, work function of the surface and the sample surface curvature (Zhou et al., 2007).

SEM has three main components regardless the model or its specific functions, which are (table 2.1): (i) vacuum, (ii) electron gun, and (iii) the column which consists of

condenser and objective lenses, scanning coil, stigmator, detector and sample holder (Figure 2.2).

In principle, the gun initially emits an electron beam, which is maintained in a vacuum and travels vertically through electromagnetic fields and lenses. With the help of an objective lens, the electron beam is focused on the specimen. Using a deflector coil, the incident beam scans a specific spot of the surface of the.

The rastering pattern's size is controlled by the magnification. When the magnification is changed, the rastered area on the sample is resized. When the electron beam strikes the material, a large variety of signals are emitted from the specimen, including electrons and X-rays. Depending on the detector type, these signals are detected and transformed to signals, from which images are created.

The depth of field in the image leads to conveying three-dimensional information. The electron divergence angle, which is specified by the diameter of the objective lens aperture and the distance between the specimen and the aperture, determines the depth of the field. It is possible to reduce the beam divergence angle by increasing the working distance or decreasing the aperture diameter to increase the depth of field. Linear magnification is calculated by the (equation 2.5).

$$M = \frac{L}{I} \tag{2.5}$$

Where *L* is the raster's length of the cathode ray tube (CRT) monitor and *I* the raster's length on the surface of the sample (Vernon-Parry, 2000; Voutou & Stefanaki, 2008).

Thus, the signal generated by the electron-sample interaction provides precise information on the material, such as its exterior morphology (texture), chemical composition, crystal structure, and the material orientation. As a result of its large depth-of-field, the scanning electron microscope allows numerous specimens focus at once.

The intensity of signals from secondary electrons or backscattered electrons is mapped to construct images in the SEM. Because the SEM scan generator simultaneously generates an electron beam across the surface of the specimen and an electron beam on the viewing cathode-ray tube (CRT) or recording device, there is a point-to-point transfer of this intensity information.

The SEM also offers significantly better resolution, allowing for much higher magnification of narrowly spaced specimens. Because lenses are replaced by electromagnets, the researcher has far more control over the degree of magnification while using SEM. The SEM is one of the most often utilized devices in research today

because to its combination of increased magnification, greater depth of focus, improved resolution, and simplicity of sample surveillance (Ram et al., 2006).

There are three main typical types of electron guns in SEM (1) Tungesten hairpin filament which produces thermal emission of electrons by heating up to 2500 ^{o}C. (2) Lanthanum hexaboride (LaB) which is very similar to the tungsten one with the advantage of having a longer life time and providing larger maximum beam current. Richardson formular describes the current density of a thermionic source. (equation 2.6):

$$J = A.T^2.e^{\frac{\phi}{kT}} \quad (2.6)$$

Where both *A* and the work function ϕ are material-constants, *T* is the temperature in Kelvin (K), and k is the Boltzmann's constant.

The field emission gun (FEG) generates electrons without heating them, avoiding the problem of overheating. As a result, FEG is often referred to as a cold cathode field emitter. A tungsten wire with a sharp point (tip, radius less than 100 nm) is employed as the filament in FEG, and electrons are emitted by immersing the filament in a large electrical potential gradient. The significance of the short tip radius (100 nm) is that an electric field can be focused to such a high degree that the material's work function is decreased and electrons can released from the cathode (Sant'Anna et al., 2005). As a result, the field emission electron microscope (FESEM) introduced a new electron gun design. Field emission cathode emits electrons by applying a high electric field at the filament tip in this method. The degree and proximity of the electric field to the electron reservoir in the filament organize the speed with which electrons are ejected from the reservoir.

By producing finer beams with 1000 times the emission of a typical tungsten wire, this technique can withstand high current and provide more stability (Brabazon & Raffer, 2000). This design needs much higher vacuum levels (Alyamani & Lemine, 2012). Therefore, spatial resolution is improved, and sample charging is reduced. As a result, FESEM provides great performance, i.e. high resolution, which is achieved by using large probe currents and tiny diameter electron probes over a high energy range (1-30 keV).

A field emission gun is used in FESEM to provide a clearer image with less electrostatic distortions and a spatial resolution of less than 2 nm (that means 3-6 times better than SEM). For electrostatic focusing, the FESEM features two anodes. The extraction

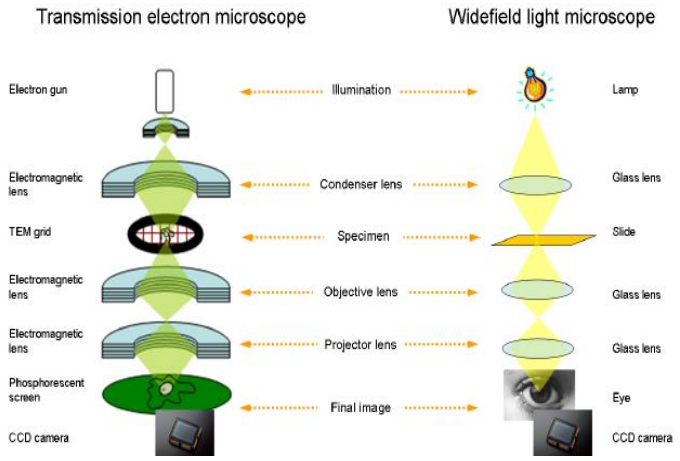

voltage (0.5 kV) between the field emission tip and the first anode (anode 1) controls the current emission (1-20 μA).

As a result of the applied potential difference V1 between anode 1 and the emission tip, an electric field is created, resulting in the emission of electrons (emission current). It is the beam's energy that determines the electrons' velocity in the column. When the accelerating voltage (Vo) (1–30 kV) applied between the cathode and the second anode (anode 2), it boosts the beam energy. In general, higher Vo means faster electrons travelling through the column and higher penetration power.

The resolution (ability to resolve two closely spaced points as two different entities) is determined by the voltage in combination with the beam diameter, which increases as the voltage increases (Sant'Anna et al., 2005).

	Tungsten	LaB_6	Thermal FEG	Cold FEG
Brightness (A/cm^{2}str)	10^5	10^6	10^8	10^8
Lifetimes (hrs)	40-100	200-1000	>1000	>1000
Source size	30-100 μm	5-50 μm	<5 nm	<5 nm
Energy spread (eV)	1-3	1-2	1.0	0.3
Current stability (%hr)	1	1	5	5
Vacuum (Torr)	10^{-8}	10^{-7}	10^{-11}	10^{-11}

Table 4.1 Comparison between different electron emitters (Akhtar et al., 2018)

Brightness, source size, and energy spread are three essential factors of electron emitters that may be compared for different types of electron emitters. The FEG has a higher brightness than the thermionic tungsten and LaB6 sources, although having a lower emission current (Table 4.1). Brightness is proportional to the accelerating voltage, which rises linearly (Zhou et al., 2007).

Figure 2.5: TEM similarity with a wide field light microscope (Kaech, 2013).

The majority of electron beam energy is lost in the form of heat creation at the irradiated site. Because of their low heat conductivity, polymer materials and biological specimens are easily destroyed by electron beams (Lloyd, 1987). There are some approaches that can be used , depending on the sample, to avoid the damage such as decreasing the electron beam intensity, shortening the exposure time and controlling the coating metal thickness on the specimen surface. To avoid the accumulation of electrons on the surface, which could diverge the incident beam, the sample is prepared on a conductive substrate.

SEM can measure and analyze the different parameters such as film thickness, surface morphology, size distribution (Barretoa et al., 2019), shape and dispersion of nanomaterials (Ramić et al., 2021), chemical compositions, and fracture and structural analysis.

In this work we have used mostly the secondary electrons to acquire the SEM images to study the morphology of the obtained structures. The morphology of the substrate modifications after treatments, catalyst nanoparticles, and the carbon materials were intensively studied during the experiments. This technique was used together with the EDX detector to have a general idea about the chemical composition of the microstructures of the material.

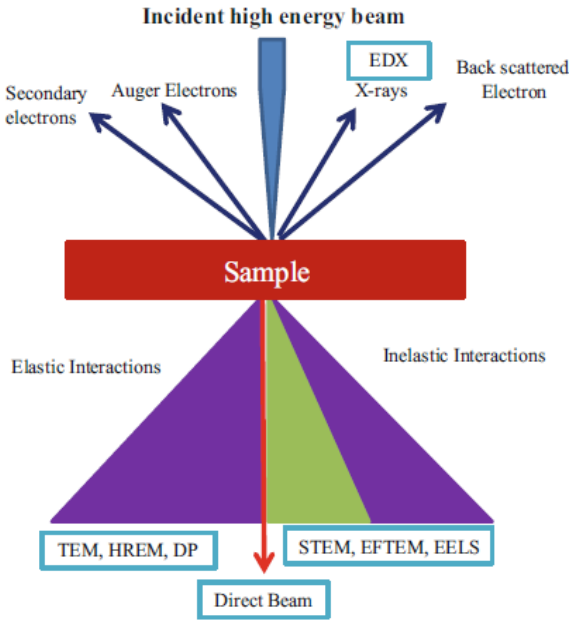

Figure 2.6: Schematic of electron interactions with matter and corresponding TEM techniques (Javed et al., 2018).

2.1.2. Transmission Electron Microscopy

Transmission electron microscopy (TEM) is a sophisticated scientific tool that uses electrons as an illumination source to produce detailed images of few nanometers object size. A focused electron beam is used to irradiate the sample, and the interaction between the electrons and atoms of the specimen provides a detailed and high-resolution image obtained by the transmitted electrons through the sample, allowing characteristics such as size, defects, crystal structure, and chemical composition to be observed. There are some similarities between TEM and light microscopy in that light is replaced by electrons and glass lenses are replaced with electromagnetic/electrostatic lenses (Figure 2.5).

The TEM resolution can be estimated using the previously mentioned relations of Abbe and de Broglie and by substituting the kinetic energy eV, we can obtain the following relation:

$$d = \frac{0.753}{\alpha V^{\frac{1}{2}}} \tag{2.7}$$

Where *d* is the resolution in nm, *α* half aperture angle, and *V* accelerating voltage. We can see clearly that higher acceleration voltage will improve the resolution, but it should be moderated in order to be able to collect information about the sample before/without destroying it.

In order to estimate a very precise limit of resolution, some other factors must be considered like the aberrations, and distortions caused by each lens and aperture (Sasaki et al., 2010). Moreover, this equation holds true as long as the electrons speed doesn't approach the speed of light. If so, we need consider the relativistic effects.

There are two types of electron guns used in TEMs for extracting and regulating electron beams, a thermionic emission which uses a heating source, and field emission where the electrons are generated by a needle-like tip by creating a large electric field around the sharp tip. Field emission sources are more monochromatic and provide higher coherency which makes it the preferable for high resolution images.

The electron beam is focused onto the sample by lenses once it is extracted from the source, and excess electrons are filtered out by apertures. The condenser lens is responsible for focusing the beam and illuminating the test subject. On the other side, the objective lens is employed to create images. To record and save the image, a CCD camera is placed directly beneath the screen.

According to the interactions between the electron beam and the specimen, we have three key imaging tools for studying the transmitted electrons: TEM, high resolution TEM

(HRTEM) and scanning transmitted electron microscopy (STEM). TEM and HRTEM are commonly used for studying the elastic collision signals while STEM is used for the inelastic signals (Figure 2.6) (Javed et al., 2018; Stankovich et al., 2006)

In conventional TEM, an electron beam of constant current density is directed towards a thin transparent specimen. With the help of the objective lens, a direct image will be recorded on an image plane by computing the scattered amplitudes in a particular direction. The image will be formed by combining these wave amplitudes (Joseph Goldstein, Joy, & LastNameRoming Jr., 1986). In other words, the diffracted beam that arose from the sample is combined to create the image. Conventional TEM operates at an accelerating voltage of 100-200 kV in most cases and can arise up to 500 kV for better resolutions depending on the microscope (Reimer & Kohl, 2008; Rosenauer, Krause, Müller, Schowalter, & Mehrtens, 2014). There are three modes the conventional TEM works with: low magnification, high magnification, and diffraction mode.
High-resolution TEM (HRTEM) provides atomic resolution micrographs of crystal surfaces and chemical composition at a spatial resolution of 1 nm. In some types of HRTEM nowadays it is possible to reach a resolving power of about 0.05 nm thanks to the improvements in aberration correctors, controlled sample environment, and digital detector sources (Garcia-Martinez, Li, & Davis, n.d.; Kirkland & Young, 2012).

In HRTEM, the image creation process takes place in two stages. The incident electrons interaction with specimen atoms results in elastic and inelastic scattering. The high resolution bright-field micrographs formation relies mainly on the elastically scattered electrons. On the other side, the inelastically scattered electrons are used in the energy electron-loss spectroscopy (EELS) and STEM to provide compositional and imaging information [221]. The incapability of HRTEM to distinguish between core and shell is one of its main limitations, e.g. it can't determine a precise structure of two different metals have a small lattice constant difference and similar crystal structure in the case of epitaxial growth of core on shell (Corain, Schmid, & Toshima, 2008).

Besides the aforementioned techniques, there is the STEM where the beam is focused and works as an optical probe to scan over the material. STEM works usually in dark-field imaging mode.

In TEM, all of the possible contrast arising phenomena must be recognized. There are three different forms of contrast mechanisms, i.e., mass thickness, diffraction, and phase-contrast. One mechanism or more can contribute significantly to form the image. Mass thickness contrast occurs when the objective aperture is positioned at the optical

center which can observed in any material such as amorphous, crystalline, biological, organic and inorganic. Thicker sections of the specimen will look darker compared to the thin parts (JS et al., 2008). Diffraction contrast (amplitude contrast) depends on the atomic number of the material atoms where the high atomic number materials will look darker compared with the low atomic number elements (PJ, MC, MJ, & M, 2011). It can be obtained in the case of low magnification which depends on the material nature, thickness, and orientation with the electron beam (Herzing, Richter, & Anderson, 2010). To image both transmitted and diffracted beams, the intermediate lens is focused on the objective lens specifically in the back focal plane. We can obtain a diffraction pattern on a specified area of the sample by introducing an aperture in the image plane of the objective lens, which leads to the selected area electron diffraction (SAED)

The third contrast is the phase contrast (interference contrast) which occurs when different phase electrons that pass through the objective aperture interfere (constructively or destructively) with each other (Bai, Zhong, Jiang, Huang, & Duan, 2010).

TEM has been used widely in many applications to study different parameters and properties of materials. In addition to the size, size distribution, defects and crystallinity, it went further more to study in situ the stress distribution of nanoparticles (Miyata et al., 2021) and liquid dynamics (Pu, Gong, & Robertson, 2020). As it is of our interest, there are some studies about the dynamic of CNTs and hybrid CNTs growth inside a TEM (Costa & Ferreira, 2016; Lin et al., 2006).

In this work, HRTEM was used for different samples of CNTs obtained by different approaches and metal oxide nanoparticles. The CNTs that were grown on a substrate were first scratched while the ones that were obtained without substrate where directly emerged in absolute ethanol and dispersed using super-sonicator for few minutes. To prepare the samples for HRTEM, few drops of the suspended particles and nanotubes were added to copper TEM grid. The HRTEM we used was a JEOL 2100 model.

2.2. Energy dispersive X-ray spectroscopy (EDX)

For the past 50 years, electron probe microanalysis (EPMA) has been widely used as one of the analytical techniques most commonly used for the characterization of solid state materials at micrometer scale with respect to their elemental composition (Fitzgerald, Keil, & Heinrich, 1968). The technique depends on analyzing the X-rays that are emitted by exciting the sample with an electron beam.

Energy-dispersive X-ray spectrometer (EDS) is one of the most important EPMA techniques as it is considered as an accurate quantitative method for the homogeneous chemical compositions samples that have a planar and smooth surface. Moreover, it is considered a quick and virtually nondestructive technique.

EDS can identify almost every element in the periodic table; only hydrogen and helium do not emit X-rays; beryllium (Be K at 108.8 eV) and even lithium (Li Ka at 54.4 eV) may be identified with a modern EDS system, although the lithium requires special analysis settings (Burgess, Li, & Holland, 2013).

One cubic micrometer is a round average for EDS, corresponding to the analyzable mass in picogram range. EDS analysis is commonly carried out with SEM or TEM. SEM typically operates at accelerating voltage up to 30 kV, resulting in a micrometer spatial resolution for EDS. When using STEM, a much higher beam accelerating voltage is used which makes EDS able to reach atomic resolution.

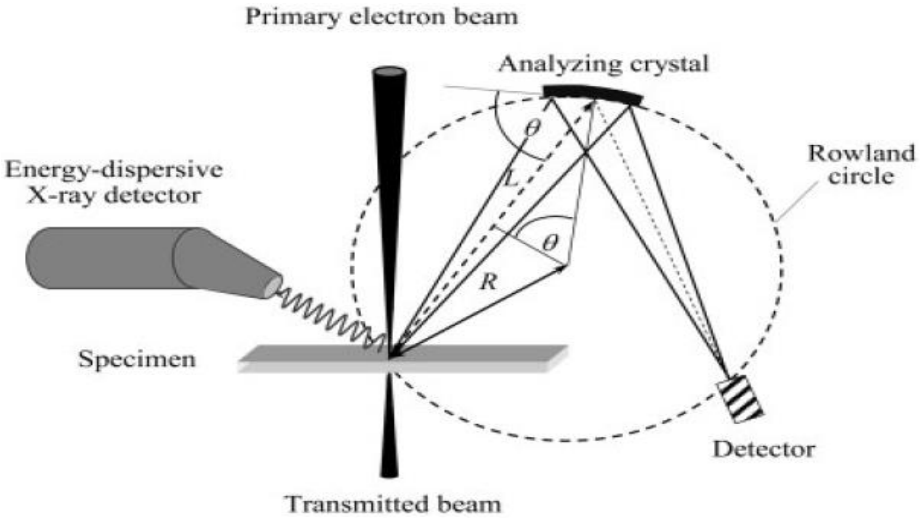

Figure 2.7: Typical arrangement of the EDS detector at SEM under a take-off angle (ToA) of 35 degrees (Hodoroaba, 2019).

X-ray is produced due to the inelastic collision between the incident electrons and the atoms of the specimen. The size of the interaction volume is determined by both, the incident beam accelerating voltage, and the average atomic number of the sample material. In other words, the greater the interaction volume is when the beam accelerating voltage is higher, and the smaller the interaction volume is when heavier or

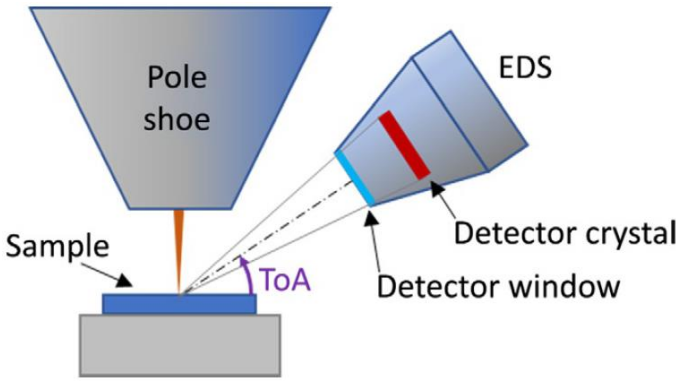

Figure 2.8: Schematic diagram of EDX spectrometry arrangement (Schneider, 2011).

denser samples are used (Hodoroaba, 2019).

By inelastic collisions, the primary electrons hitting the sample at energies up to 30 keV in a SEM (up to 300 keV in TEM) knocking out the secondary electrons from the inner shells of the atoms creating vacancies. At primary electron energies two to three times greater than the binding energy of the corresponding shell, the ionization probability is at its maximum. The energetic state of the ionized atom will be unstable after the secondary electron emission until a weaker bound electron from the outer shell fills the vacancy. The characteristic X-rays doesn't have a preferable emission direction which makes it emitted isotropically which means that the EDS will be able to detect a tiny proportion of the X-rays released into the 4π steradian sphere if it is situated at a certain angle. This angle is called take-off angle (ToA) (Figure 2.7) (Hodoroaba, 2019).

The detector slit, the surface of the analyzing crystal, and the tip of the electron probe on the specimen are all positioned on the perimeter of a focusing circle known as the Rowland circle. (Bertin, 1975)

The detector and the crystal are mechanically coupled where the detector moves in an angular amount 2θ forming an angle θ with the crystal (Figure 2.8). The X-ray wavelength, λ, measured is given by relationship:

$$\lambda = \frac{d}{R} L \tag{2.8}$$

Where R is Rowland circle radius and L is the variable distance between the specimen and the analyzing crystal (Schneider, 2011).

In EDS, X-ray line interferences are inevitable. This is because the EDS spectrometers has low energy resolution. The absorption of X-rays in the sample itself on their way to the EDS detector is one physical phenomenon relevant to the study of X-ray spectra. According to Beer–Lambert absorption law, the intensity of produced X-ray radiation is

reduced on its passage through the sample to the detector owing to photoionization and X-ray scattering. According to Beer–Lambert absorption law, the intensity of produced

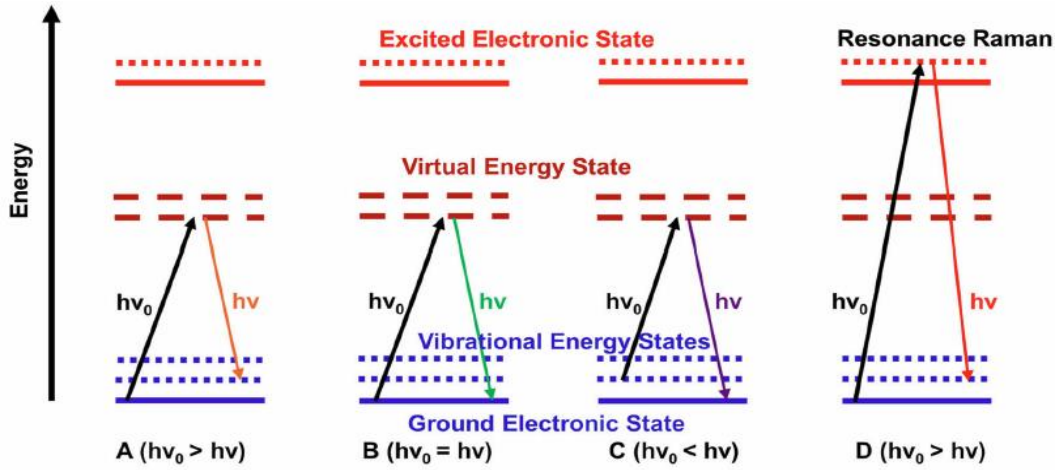

Figure 2.9: Types of light scattering where (A–D) represent Stokes, Rayleigh, anti-Stokes and resonance Raman scattering, respectively (Roy, Kanojia, Mukhopadhyay, & Eswara Prasad, 2021).

X-ray radiation is reduced on its passage through the sample to the detector owing to photoionization and X-ray scattering (self-absorption). There is some absorption occurs at the detector window of EDS as well. The contamination on the sample surface or even on the detector's window highly affect the analysis of nanostructures.

2.3. Raman Spectroscopy:

Raman spectroscopy is a strong non-destructive technique for nanomaterial characterization where it is used to analyze nanostructured materials' phases and phase transitions. The larger surface cross-section of nanomaterials allows Raman scattering to insight into nanoscale interactions (Gouadec et al., 2007). Raman scattering phenomenon has been used intensively to identify and study amorphous and crystalline materials, defects distribution, doping, shape and size of nanomaterials (Drescher & Kneipp, 2012). Different allotropes of carbon-based nanostructured materials were studied using Raman bands to determine their conductivity, structural, and compositional characteristics (Bokobza, Bruneel, & Couzi, 2015).

The main principle of Raman effect is the measurement of photons inelastic scattering from vibration-induced phonon modes of a material. Raman scattering is a two-photon phenomenon in which the photon emitted depends on the polarizability change that occurs during its mobility. The other photon is absorbed, resulting in an excited electronic state for the molecule. Rayleigh scattering is an elastic process, therefore there is no net energy transfer between matter and light (Hendra & Vear, 1970). Raman scattering, on the other hand, is an inelastic process in which the incident and emitted photons have different energies, causing the molecule to either be stimulated to a higher vibrational or rotational level or demoted to a lower level. Figure 2.9 shows the different types of light scattering (Roy et al., 2021).

Stokes lines (Figure 2.9 A) have a longer wavelength comparing with the exciting radiation and leads to a spontaneous Raman effect. The anti-Stokes lines appears only when the material is already excited e.g., at high temperature.

Moreover, Stokes lines are more intense than anti-Stokes lines where the molecule population in ground state is much higher than the vibrational excited state with $h\upsilon > k_B T$. Generally, Raman spectroscopy measures Stokes lines. Raman scattering is presented by arbitrary units of intensity as a function of wavenumber (cm^{-1}) (Rangan et al., 2020). Due to the tiny scattering cross-sections (usually 10^{-30} cm^2), Raman scattering is a weak process. Thus, to obtain more photons Raman scattered, then an intense radiation source is needed. One of the biggest obstacles for better signal-to-noise ratio in the pre-laser era was the experimental difficulty of detecting weak signals when strong background radiation exists. Therefore, the introduction of laser in addition to the improvements on the detectors have made a big difference. The use of a laser substantially improved the sensitivity of Raman spectroscopy, and it also cleared the way

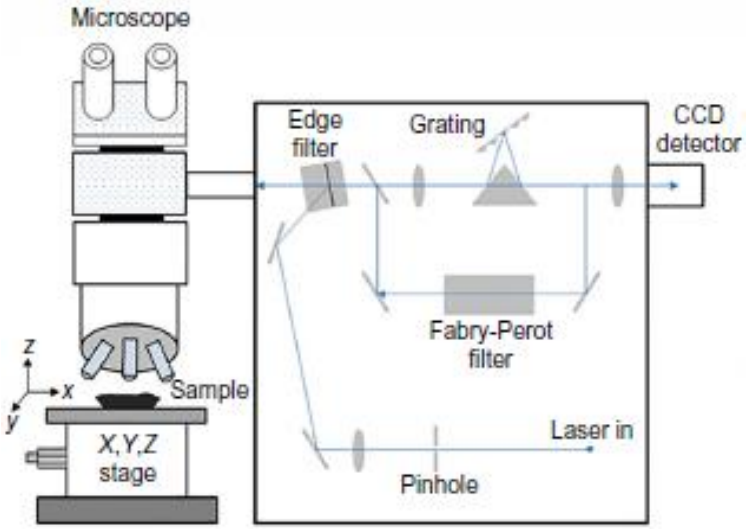

Figure 2.10: Scheme of Raman Spectroscopy (Szybowicz et al., 2018).

for novel spectroscopic techniques based on the stimulated Raman effect, such as coherent anti-Stokes Raman scattering (CARS) or hyperRaman spectroscopy (Camp Jr & Cicerone, 2015; Cheng & Xie, 2003).

Raman system typically consists of three major components, Excitation source (laser), wavelength selector (filter or spectrophotometer), and detector (photodiode array, CCD or PMT) (figure 2.10).

In Raman spectroscopy, it is possible to match the frequency of the pump photons to the energy of the electronic states, resulting in resonance effects (figure 2.9 D) which strongly depends on the density of electronic states (DOS) (Jorio et al., 2003). When the incident laser frequency is close to the absorption band, but not in the electrical excitation level, then it is known as pre-resonant Raman effect, and when the laser frequency is falls in the absorption band, it is known as rigorous resonant Raman effect (Asher, 2012). When compared to virtual-intermediate-state Raman scattering, the signal intensity of resonance Raman scattering is several times greater. In addition to the ability of investigating more dilute samples because of the stronger signals in resonance Raman

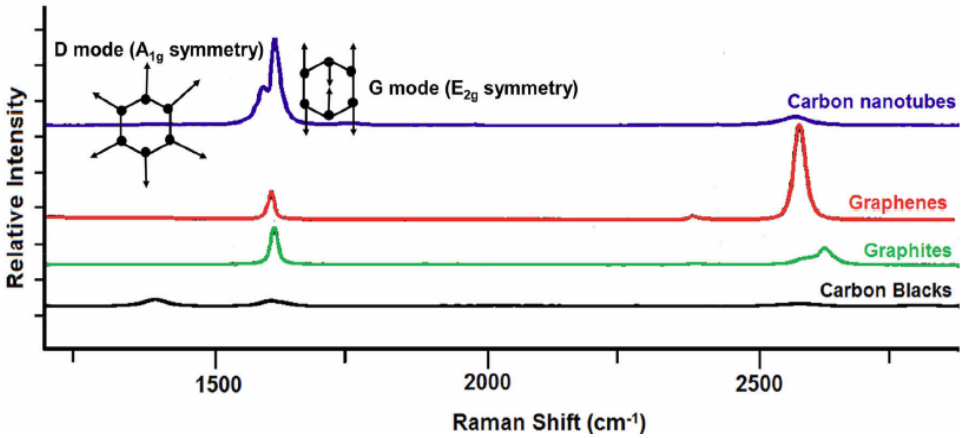

Figure 2.11: The representative Raman spectra of different allotropes of carbon where the D, G and 2D bands of carbon black, graphite, graphene and single walled carbon nanotube are demonstrated for comparative purpose (Roy et al., 2021).

scattering, it is also possible to obtain information about the interactions of vibrational and electronic motion by analyzing the excitation profile of different resonance Raman bands.

Another important characteristic of resonance Raman excitation is that a chromophore probe may be used to study a selective portion of the macromolecular aggregation; moreover, the molecular symmetry can be deduced from the polarization analysis of resonance Raman bands (Maultzsch, Telg, Reich, & Thomsen, 2005).

Raman spectroscopy has been intensively used as a quick and to characterize the different kinds of carbon materials such as graphene and carbon nanotubes (CNTs) showing the properties and characteristics of each one (Figure 2.11). Only a limited number of phonon modes for sp^2 carbons are Raman-active (namely those with A_{1g}, E_1 and E_2 symmetry for carbon nanotubes, and E_{2g} for graphite) (Saito, Hofmann et al., 2011). Raman spectroscopy allows studying the carbon nanotubes by characterizing the synthesis, purification, functionalization processes as well as the physical properties (Maultzsch et al., 2005) revealing the information of both vibrational and electronic properties. Figure 2.12 shows the different bands of Raman spectra for single-walled carbon nanotubes (SWCNTs) and multi-walled carbon nanotubes (MWCNTs).

The two spectra contain the G band at 1590 cm^{-1}, which is present in almost all carbon nanoforms spectra. D band is associated with some disorder in the graphene structure which is at around 1320 cm^{-1} and also related to the defects and shows a strong dispersion as a function of laser excitation energy. At Raman shift of 2700 cm^{-1}, 2D (G') band is observed which is an overtone of the G band that provides information about the electronic and geometrical structure using the double resonance process (Dresselhaus, Jorio, Hofmann, Dresselhaus, & Saito, 2010).

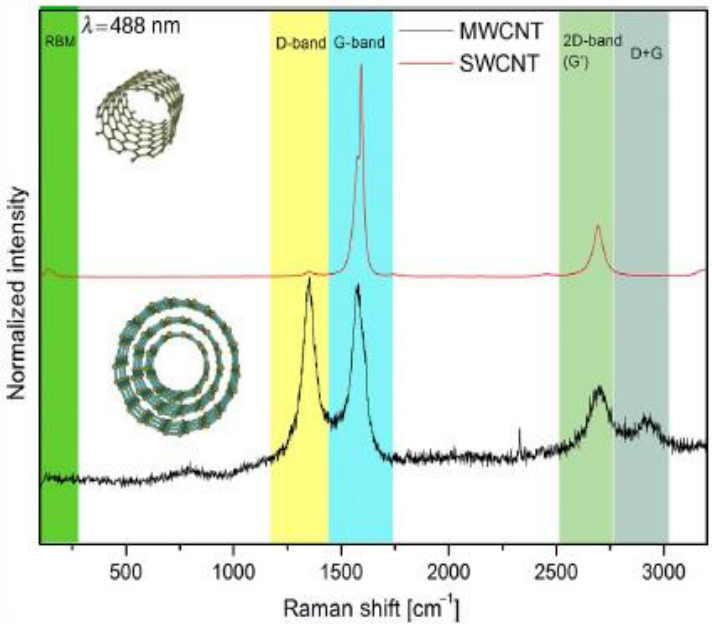

Figure 2.12: Raman spectra of SWCNT and MWCNT with their structures (Szybowicz et al., 2018).

There are some differences between the two spectra. The first is the bands that appears below 300 cm^{-1} in the spectrum of SWCNT. These bands are called the radial breathing mode (RBM). RBM provides information about the diameter of nanotubes in addition to the tube-tube interaction. We can't observe the RBM bands in the spectrum of MWCNTs because this signal come from the outer tube which has a large diameter, and it is too weak to be detected and the signal is broadened because of the inner tube diameters effect (Fantini et al., 2004). The other difference that can be observed between the two spectra is shape of G and D bands. In the SWCNT we can clearly observe the separated G bands (G^+ and G^-) and a prominent D band. In the MWCNTs we can observe the overtone (D+G)/(2G) band around 3000 cm^{-1} (Tan et al., 2002).

Carbon nanomaterials (or sp^2 system) have the G mode (tangential mode), which is connected to the C-C stretching mode (graphite tangential E2g Raman mode). This band is used to distinguish between different types of carbon. Similarly, for CNTs, this band distinguish the MWCNTs from SWCNTs, and the metallic from the semiconducting form. The G^+ doesn't depend on the tube diameter and it is related to the atomic vibration along the nanotube axis. In contrast, the G^- dependent of the tube diameter and curvature. It decreases with decreasing the tube diameter and it is related to the vibration along the nanotube circumference and it and increases with increasing the curvature of SWCNT (Jorio et al., 2004).

In the spectra of MWCNTs we can observe the D' band at around 1620 cm^{-1} which provides information about disturbances, defects, or impurities in the nanotubes structure. This band isn't active in the SWCNT spectra because the MWCNTs have a higher diversity of electronic states than a single wall (Antunes et al., 2006). It has been observed that the D band can shift by changing the laser wavelength. Pimenta et al. had found that the D band for MWCNTs was shifted from 1352 cm^{-1} when using blue laser (488 nm) to 1308 cm^{-1} for red laser (785 nm). According to literature, The D band position can change between 1250 cm^{-1} and 1450 cm^{-1} for carbon materials(Pimenta et al., 2000). It is also observed that the intensity of this band is related to the RBM intensity for small defect densities as the increase of its density provides information about the functionalization of SWCNTs (Vigolo et al., 2009).

The ratio of G and D bands intensities (I_D/I_G) can be used for material characterization especially for the quantification and purity analysis of CNTs.

Raman spectroscopy can be used to measure the crystalline size and distance between defects (L_a) which is calculated by the intensities of G and D bands (I_D/I_G) where they are

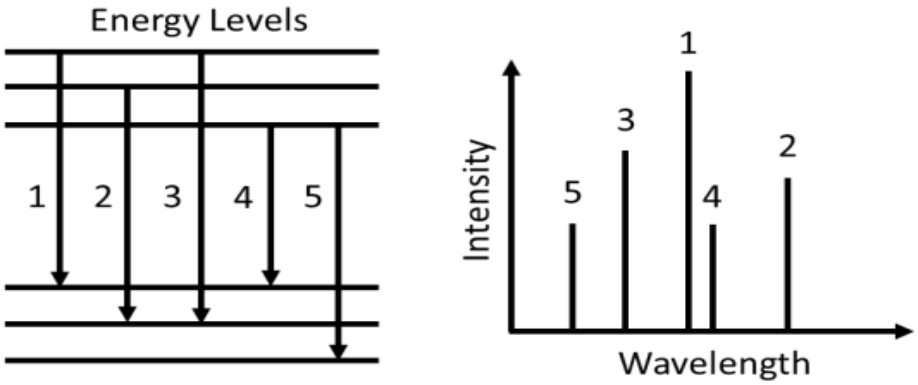

Figure 2.13: Energy levels involved in typical OES experiments (GAJENDRASING, 2020).

inversely proportional. The relation was found by Mallet-Ladeira after studying many graphitic structures as follows (Mallet-Ladeira et al., 2014):

$$L_\alpha(nm) = \frac{4.4}{\frac{I_D}{I_G}} \times \left(\frac{2.41}{E_L\,(eV)}\right)^4 \quad (2.9)$$

Where $E_L\,(eV) = \frac{1240}{\lambda(nm)}$

Thus, using this equation it is possible to obtain crystalline size information of carbon materials.

2.4. Optical emission spectroscopy (OES)

OES is a quick and non-intrusive in-situ plasma diagnosis technique, which provides information about the chemical composition, relative concentrations of plasma species, and the gas temperature. In principle, this technique examines the photons that are emitted from the atoms and/or molecules during their transition from an excited state of energy to a lower one (Figure 2.13).

Because the energy corresponding to these transitions is unique to each element or chemical, the species present in the plasma may be identified. The OES approach can even be used to determine the electronic temperature and density under thermal equilibrium conditions.

When we talk about emission lines, we're talking about both monatomic transitions and bands connected with molecules. These bands are formed by the transitions between rotational and vibrational states, as well as atomic transitions. These peaks can't be resolved individually as the resolution of a spectrometer, the minimum width of peak can be detected, is much bigger than the wavelength difference between two of these states. So, to assess its resolution, it is possible through measuring the full width at half maximum (FWHM) of a monatomic emission peak.

There are several primary mechanisms that contribute to the wavelength dispersion in terms of peak width (García Cespedez, 2008):

- The Heisenberg uncertainty principle

$$\Delta E.\Delta t \geq \hbar/2 \quad (2.10)$$

There is a fundamental broadening as the excited state half-life is limited, therefore an uncertainty in the associated energy is determined.

- The Doppler effect: The peak broadens around the maximum wavelength due to dispersion in the species' velocity (modulus and direction) with respect to the detector.
- The medium pressure: The closeness between colliding atoms or molecules causes a shift in the related energy levels, and therefore the emission lines.
- The Stark effect: Due to the electric field associated with charged particles (ions or electrons), the electronic levels of these atoms or molecules are unfolded when they collide with a neutral particle, contributing to the broadening of lines (Toncu, 2016; Touati, Chenini, & Meftah, 2020).

However, the fundamental broadening of the emission lines is usually determined by the apparatus resolution. The peaks intensity highly depends on the density of the generated plasma species. When we want to deconvolve a band or two very close peaks, it's necessary to know which mathematical function correlates or is closest to the shape of the observed peaks. When the Doppler effect is the major broadening mechanism, the peaks are Gaussian which is usually obtained at low pressure conditions, whereas the broadening caused by collisions generates a Lorentzian shape and this is usually the case at high pressure. When the peak is in intermediate, we can use a combination between Gaussian and Lorentzian function and this is called Voigt profile (Payling & Larkins, 2000). For spectrophotometers with nanoscale resolution, statistical error is the main cause of broadening, hence the peak shapes will be adjusted to the Gaussian.

Neglecting the contribution of other emissions and by analyzing solely the case where an electron collision excites a plasma particle from its ground state i to a state j then drops back to state i. The intensity of the electromagnetic emission will be:

$$I(\lambda_{ij}) = NP_{ij}A_{ij}(\lambda_{ij}) \quad (2.11)$$

Where λ_{ij} is the transition wavelength between state i and state , N is the excited state density and A_{ij} is the Einstein emission probability, and P is the electron impact excitation function which reflects the probability of exciting the state j by electron impact, starting from the ground state. P is a complex function of electron temperature T_e can be written as:

$$P = \int_0^\infty 4\pi v_e^2 \, dv_e \sigma_\lambda(v_e) v_e f_e(v_e, T_e, n_e) \quad (2.12)$$

Where v_e is the electron velocity, σ_λ is the cross section for emission of a photon of wavelength λ because of the electron impact excitement, and f_e is the electron distribution function which depends on the electron temperature and density (Hussein, 2010).

A further key consideration when working with a spectrum which is the baseline or bottom line. There are many factors contribute to forming the baseline:

- The inelastic scattering radiation of free electrons or their capture by ions.
- Black body radiation when a radiating element is present in the discharge volume at such a temperature that its maximum black body radiation spectrum falls in the region of the electromagnetic spectrum analyzed or is near to it.
- Parasitic radiation, such as ambient light either natural or artificial (García Cespedez, 2008).

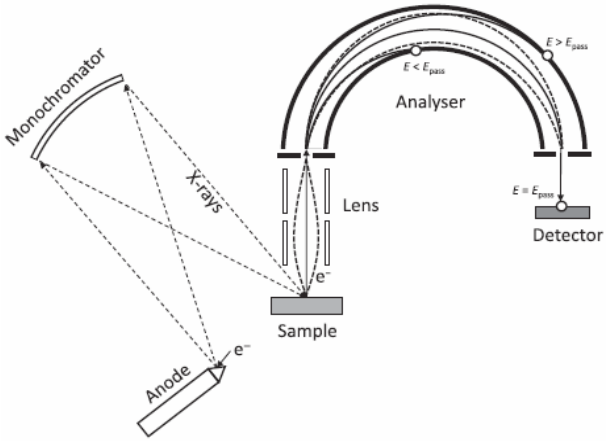

Figure 2.14: Schematic of a typical X-ray photoelectron spectrometer (Shard, 2020).

In order to obtain as precise result as possible, a spectrum of a monochromatic substance light source belong to a known element can be examined. Then the spectrometer can be calibrated according to the database of this element (Devia, Rodriguez-Restrepo, & Restrepo-Parra, 2015).

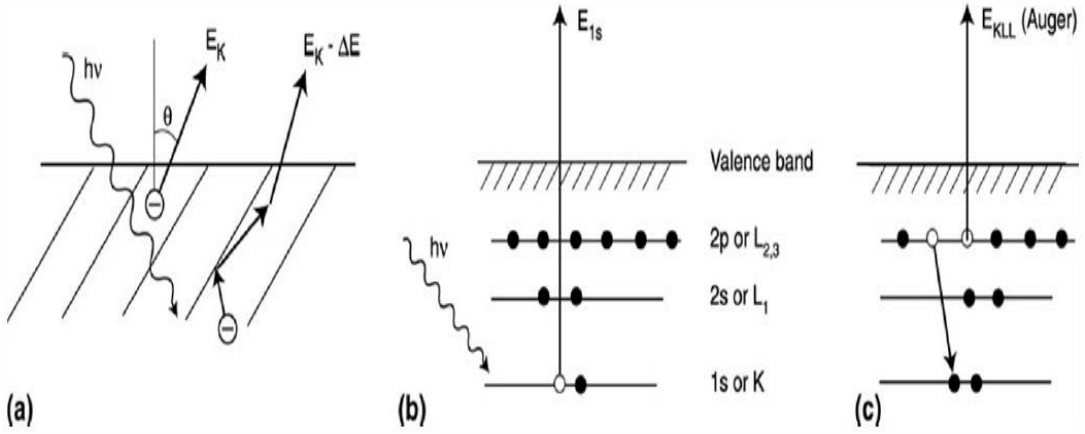

Figure 2.15: (a) Schematic of the XPS excitation process. (b) Schematic representation of the electron energy levels of a F atom and the photoionization of a F 1s electron. (c) Auger emission relaxation process for the F 1s empty-state produced in (b) (Tougaard, 2019).

2.5. X-ray photoelectron spectroscopy (XPS)

X-ray photoelectron spectroscopy (XPS), also known as electron spectroscopy for chemical analysis (ESCA), is a powerful technique to analyze and characterize the surface chemistry of materials providing valuable quantitative and chemical state information. XPS is regularly used to characterize a broad range of materials such as metal alloys (Li et al., 2018), catalysts (Voiry, Shin, Loh, & Chhowalla, 2018), semiconductors (Rahmayeni, Alfina, Stiadi, Lee, & Zulhadjri, 2019), coatings (Vashishtha & Sapate, 2018) and ion-modified materials (Rawat, Srivastava, Dixit, & Asokan, 2020). It also can be used to analyze materials after being treated e.g. fracturing, scrapping, or cutting.

For an XPS measurement, the typical depth of analysis is about 5 nm. By scanning the sample surface with a micro-focused X-ray beam, spatial distribution information may be obtained. In addition, Combining XPS measurements with ion milling (sputtering) to describe thin film structures can yield depth distribution information (Kalha et al., 2021). A typical XPS instrument schematic is illustrated in figure 2.14. Electrons expelled from the sample travel via a lens, which alters their kinetic energy and concentrates them on the entrance of the analyzer. The analyzer is made up of two concentric hemispheres, the inner of which has a positive charge compared to the outer. Electrons arriving the analyzer with the correct kinetic energy, pass energy (E_{pass}), will pass through the entrance aperture to the exit slit and strike the detector. The different kinetic energy

electrons will hit the metal hemispheres or the aperture, so they won't be detected (Shard, 2020).

The physics of XPS process is quite simple. An initial beam of soft X-rays interacts with surface of the specimen. This beam is typically Al K_α with photon energies of 1486.6 eV or Mg K_α with energies of 1253.6 eV. This interaction leads to the photoionization of the specimen's atoms, molecules, or ions resulting in the excitation and ejection of low-energy electrons (Figure 2.15 a &b). In the case that is illustrated in figure 2.15, a 1s electron of binding energy E_B is photo-excited by a photon of energy hv where the sample work function Φsample is required to remove the sample from the solid (Tougaard, 2019). This energy is obtained as the electron enters the spectrometer, where it must overcome the spectrometer's work function. The binding energy of the atom's photoelectron can be calculated as follows:

$$E_B = hv - E_K - \Phi \quad (2.13)$$

Where h is Planck's constant, v is the frequency of the incident photon, Φ is the sample work function. X-ray photoelectron spectrum can be obtained as a function of kinetic energy or the bending energy of the measured photo-excited electrons where they are equivalent and linked according to eq 2.13. (Suga & Sekiyama, 2021).

Apart from the characteristics of the detected peaks, other phenomena such as Auger electron emission and satellite peaks are also visible in XPS spectra. Auger peaks are among the most conspicuous non-characteristic peaks in the spectrum due to the Auger effect. In Auger effect, when a low energy electron is ejected because of the X-ray, it creates a vacant orbital. A higher orbital electron will fill this vacancy emitting a characteristic radiation equal to the energy of the transition orbitals difference which is considered as a secondary X-ray (Figure 2.15 c). This new X-ray ejects other electron from the atomic shell which is called Auger electron with binding energy as follows:

$$E_B = hv - E_K \quad (2.14)$$

Precisely, the work function of the spectrometer Φ_{spec} must be included so eq 2.14 becomes:

$$E_B = hv - E_K - \Phi_{spec} \quad (2.15)$$

Accordingly, Auger's electrons binding energy does not correspond to that of the predicted energy levels for the atomic species that are produced by the X-ray of XPS source. Also, Satellite peaks can be observed when using a non-monochromatic X-ray source (Kumar, 2018).

The binding energy of the photoelectron peak exhibits minor fluctuations for nearly all elements, which reflect the chemical environment of the element in question. We obtain the information on chemical bonding from the valence and Auger peaks because chemical bonds generally affect the density of states in the valence band The energy

position of the photoelectron core level peaks is the most essential source of chemical state information in XPS. Despite the fact that the core levels aren't directly engaged in chemical bonding, their binding energy is affected by the chemical environment. Simply the "chemical shift" is caused by a change in electrostatic potential within the valence electrons' orbitals (the location of the core electrons). Therefore, as the charge of the effective valence electron around the atom changes by Δq, the core electrons potential of this atom will change by $\Delta q/(4\pi\varepsilon_0 r)$, and correspondingly the core level binding energies will change (Tougaard, 2019).

The distance electrons travel is defined by two terms, the electron inelastic mean free path (IMFP) and the electron effective attenuation length (EAL). IMFP is the average distance travelled be electrons prior to an inelastic event. If elastic scattering is negligible, then the electrons move in straight lines through the material with the initial energy diminishing exponentially as distance increases. This will permit simple calculations of Lambert's law related to the material thickness. But when the elastic scattering is considered, the electrons deviation will cause inaccuracy in the calculations when using IMFP. This will allow using EAL for more accuracy. There are predictive formulae were developed by Seah for calculating λfor IMFP with 16% error (Seah, 2012a), or L for EAL with 18% error (Seah, 2012b) as follows:

$$\lambda = \frac{(0.73+0.0095E^{0.872})}{Z^{0.3}} \tag{2.16}$$

$$L = \frac{(0.65+0.007E^{0.93})}{Z^{0.38}} \tag{2.17}$$

Where E is the kinetic energy of electrons in eV and Z is the average atomic number of the material.

Despite the fact that eqs (2.16) and (2.17) aren't precise, they are important because they show that the energy dependency of the IMFP and EAL is the same for all materials, which is useful for quantitative composition analysis (Shard, 2020).

For data understanding and differentiation, there are three main components in XPS spectrum:

1- Peaks' position on the energy axis (usually in term of binding energy).
2- Peaks intensity at specific binding energy of the ejected electron from a specific orbital in the element.
3- Width of the peak (FWHM).

After hitting the neutral sample by X-ray, the ejected electrons will leave the sample nonneutral. As a result, if the neutrality is not maintained, an excess of positive charge

will be left on the sample providing higher pull to the expelled electrons adding extra binding energy. This increase in binding energy will shift the XPS peaks from their real positions. This means that in order for the sample to remain at the actual state, the emitted electrons must be balanced by supplying additional electrons. In the case of conducting samples, this can be solved by connecting the sample electrically with the instrument. In the case when the sample in an insulator, it can be solved either by providing low-energy electron beam to the surface of the sample where it should be adjusted to have the same current of the ejected photoelectrons (Kumar, 2018), or by calibrating the energy scale by setting a well-defined peak to the value of its binding energy, e.g. carbon 1s to 285.0 eV (Tougaard, 2019).

It is possible in XPS to investigate the internal inhomogeneities of the sample. As XPS is surface-sensitive technique, it can obtain the electronic structure information of a material up to few nanometers below the surface of the sample. But with using ion beam bombardment to etch the surface of the sample, it is feasible to obtain information of the

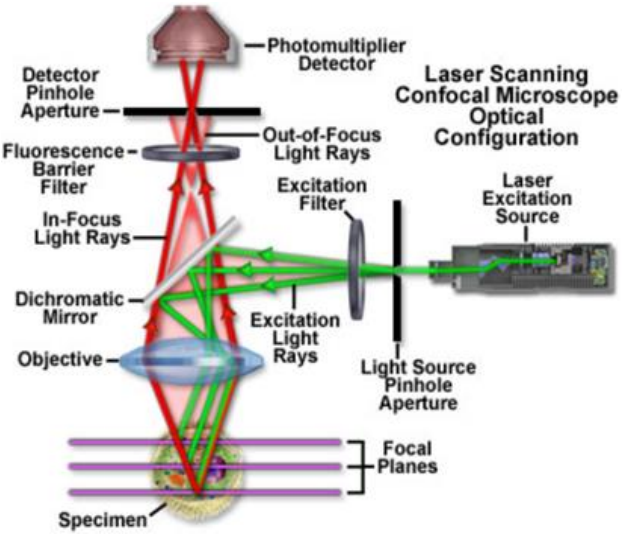

Figure 2.16: Confocal microscope configuration (Olympus, 2020).

sample's interior after each cycle of etching which is called depth profiling (Vempati, Hess, & Cocke, 1996).

2.6. Confocal Microscope:

Confocal microscopy is one of the non-destructive techniques that allows studying the topography of the material's surface. In general, the key to the confocal approach is to use the spatial filtering techniques to remove out-of-focus light from specimens whose thickness surpasses the immediate plane of focus.

One of the main differences between the conventional widefield optical microscope and the confocal beside the resolution is the fluorescence emission in the thick samples. In conventional microscope, the secondary florescence emitted by the specimen obscures

the resolution of features that are located at the objective focal plane. When the specimen thickness (roughness) is higher than 2 micrometers, higher degree of emission will be obtained which leads to losing most of the fine details. Confocal microscopy is able to exclude the secondary fluorescence in locations away from the focus plane (background information). The confocal microscopy principle is illustrated in figure 2.16. (Olympus, 2020).

The laser system (excitation source) emits a coherent light that passes via a pinhole aperture located at a conjugate plane (confocal) and second pinhole aperture situated in front of the detector (photomultiplier tube). The laser will be reflected using a dichromatic mirror and scanned over the sample in a specific focal plane. Secondary fluorescence that is emitted from different points of sample at the same focal plane refracts back by the dichromatic mirror and are focused at the pinhole aperture of the detector as confocal point. The secondary fluorescence that is emitted from the planes' points below and above the objective focal plane is not confocal with the pinhole. Most of this extraneous fluorescence isn't caught by the photomultiplier since only a tiny portion of the emitted out-of-focus florescence arrives the pinhole aperture so it doesn't contribute to the final image. The fluorescence barrier and excitation filters, and the dichromatic mirror fulfill the same function as in the conventional widefield microscope (Vorburger, Song, Petraco, & Lilien, 2019). In confocal microscope, refocusing the objective moves the emission points to a new plane on the specimen which becomes confocal with the pinhole apertures of the detector and light source (Olympus, 2020).

The illumination source and acquiring images are also different between the confocal microscope and the conventional optical microscope. In the conventional widefield microscope, the sample is illuminated entirely using incoherent mercury or xenon arc-discharge lamp and the produced image of the fluorescence emission can be seen directly or projected to the detector or the film plane. In the confocal microscope the image formation is different as there are multiple laser excitation sources and a scan head with optical components. Acquiring images using the confocal needs a compromise between resolution, scan time, and the specimen photo-destruction as a better resolution needs longer scan time (St Croix, Shand, & Watkins, 2005). For acquiring the images, photomultipliers are used in addition to the processing and analysis of images using a computer. The scan head is considered as the heart of the confocal microscope. Its rule is the rasterizing the excitation scans and gathering signals from the sample that are needed to form the final images. Typically, it consists of the laser sources, dichromatic mirrors, fluorescence filter, and the photomultiplier tube (Reilly & Obara, 2021).

The confocal microscope we use in our group is SENSOFAR microscope and we use SensoMap software for collecting and processing data. The Abbott-Firestone curve,

commonly known as the bearing area curve (BAC) analysis, is a significant tool included in this program. This statistical approach allows the determination of an object's surface texture (Jurečka, Imamura, Matsumoto, & Kobayashi, 2018) and the material distribution (keyence, 2019).

2.7. Electrochemical characterization

The electrochemical characterization allows us to evaluate the electrochemical properties of our materials that will be used later for devices such as capacitors, batteries, and sensors. This can be done by understanding the reaction mechanism at different interfaces. In our study, we synthesized the carbon materials to be used as electrodes for supercapacitors. Thus, the electrochemical analysis will allow us to know the reaction mechanism at the electrode/electrolyte interface.

The study of chemical changes produced by the passage of an electric current and the generation of electrical energy by chemical reactions represent the main part of this area. Electrochemistry, in reality, includes a wide range of phenomena (such as electrophoresis and corrosion), devices, and technologies.

Electrical measurements on chemical systems are carried out in many different ways by scientists for a wide range of purposes such as obtaining thermodynamic data about a reaction, generating an unstable intermediate such as a radical ion and study its rate of decay or its spectroscopic properties, or analyze a solution for trace amounts of metal ions or organic species. There have been several electrochemical techniques developed (Brad & Faulkner, 2001).

Understanding the underlying principles of electrode reactions and the electrical characteristics of electrode-solution interfaces is required for developing applications. A major focus of research is on the processes and variables that influence the transfer of charge across the interface of chemical phases, such as between an electronic conductor (electrode) and an ionic conducting medium (electrolyte).

Charge is transferred through the electrode by electrons (and holes) movement. The charge is carried by the ions' movement in the electrolyte phase. The most often used electrolytes are those that contain ionic species, such as, H^+, Na^+, Cl^-, in either a nonaqueous solvent or water. The electrolyte must be electrically conductive to be useful in the electrochemical experiment. Experimentally, a collection of interfaces are studied together in the electrochemical cells which generally defined as two electrodes separated by at least one electrolyte phase (Brad & Faulkner, 2001).

Regardless of equipment, all electrochemical methods have common features. There are five concepts must be kept in mind to understand the electrochemistry (Harvey, 2001):

1- The analyte's form is determined by the electrode's potential at its surface.

For example, if an electrode is emerged in a solution of Fe^{3+} and Sn^{4+} and its potential is adjusted to 0.5V, the Fe^{3+} will reduce to Fe^{2+}, but he Sn^{4+} will not. Figure 2.17 shows the ladder diagram for the Fe^{3+}/Fe^{2+} and the Sn^{4+}/Sn^{2+} equilibria.

2- The analyte concentration on the electrode's surface may differ from its bulk concentration.

3- The analyte might participate in other reactions than the oxidation-reduction.

4- The rate of oxidation or reduction of an analyte is measured by the current.

5- Current and potential can't be controlled simultaneously.

Electrochemical cells consist of two, which is the simplest, or more electrodes in addition to electronic circuits to control and measure the current and voltage for the

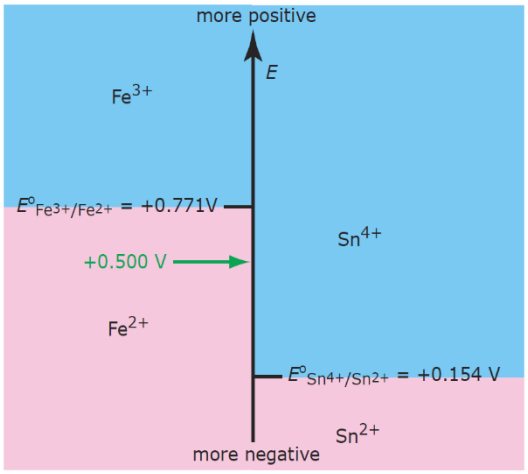

Figure 2.17. Redox ladder diagram for Fe^{3+}/Fe^{2+} and for Sn^{4+}/ Sn^{2+} redox couples (Harvey, 2001).

electrochemical measurements. The electrode's potential is sensitive to the analyte's concentration, and it is called the working electrode. The second electrode is the counter electrode which completes the circuit and provides a reference potential, ideally constant, against the measured working electrode's potential (Figure 2.18). If the potential of the counter electrode is not constant, we replace it with two electrodes; a reference electrode which has a constant potential and an auxiliary electrode to complete the circuit. As mentioned before, it is not possible to control current and potential simultaneously. Therefore, we have only three possibilities for doing the experiments: (1) measuring the potential when the current is zero, (2) controlling the potential when the

current is constant, or (3) controlling the current when the potential is constant. All the above-mentioned designs rely on ohm's law which states that the current i, passing through an electrical circuit of a resistance R, generates a potential E:

$$E = iR \tag{2.18}$$

Potentiometer is the technique we use when measuring the potential of an electrochemical cell when the current is zero. Figure 2.19 shows a schematic diagram of a manual potentiometer. According to ohm's law the currents in the upper and lower halves are:

$$i_{up} = \frac{E_{PS}}{R_{ab}} \tag{2.18a}$$

$$i_{low} = \frac{E_{cell}}{R_{cb}} \tag{2.18b}$$

where E_{PS} is the potential of the power supply, R_{ab} is the resistance between points a and b of the slide-wire resistor, E_{cell} is the potential difference between the working electrode and the counter electrode, and R_{cb} is the resistance between the points c and b of the slide-wire resistor. When $i_{up} = i_{low} = 0$, no current flows through the ammeter and the potential of the electrochemical cell is

$$E_{cell} = \frac{R_{cb}}{R_{ab}} \times E_{PS} \tag{2.19}$$

Modern potentiometers employ an operational amplifier to obtain high impedance voltmeter that can measure a potential with a drawing current of less than 10^{-9}A.

Galvanostats is used when we need to control the flowing current through an electrochemical cell. Figure 2.20 shows a schematic diagram of a constant-current galvanostat. The current flowing through the working electrode is:

$$i = \frac{E_{PS}}{R + R_{cell}} \tag{2.20}$$

where E_{PS} is the potential of the power supply, R is the resistance of the resistor, and R_{cell} is the resistance of the electrochemical cell. If R >> R_{cell}, then the current between the working and auxiliary electrodes isÑ

$$i = \frac{E_{PS}}{R} \approx constant \tag{2.21}$$

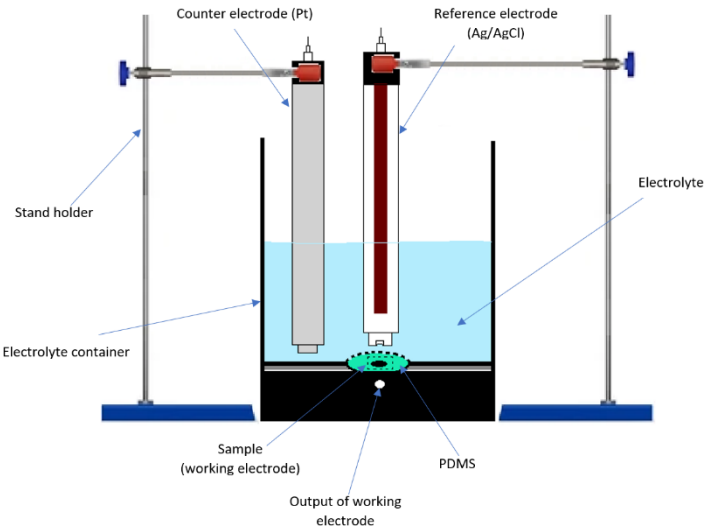

Figure 2.18: Scheme of three-electrode electrochemical cell.

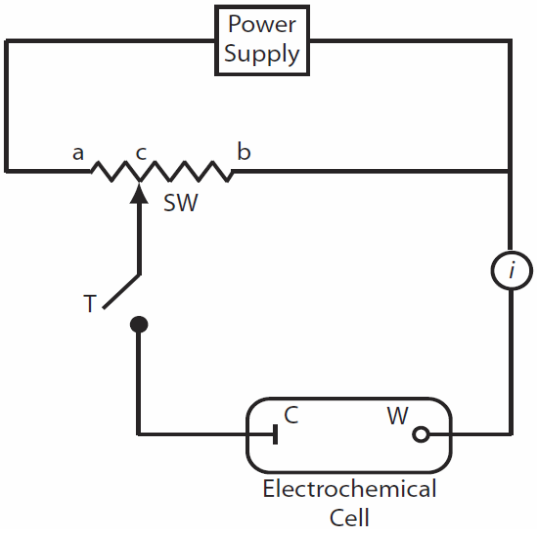

Figure 2.19: Schematic diagram of a manual potentiometer: C is the counter electrode; W is the working electrode; SW is a slide-wire resistor; T is a tap key and i is an ammeter for measuring current (Harvey, 2001).

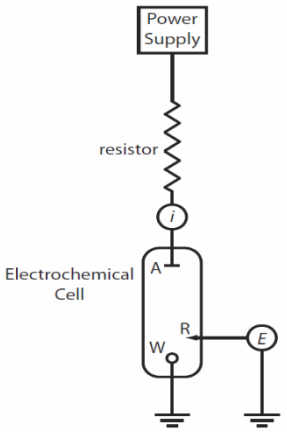

Figure 2.20: Schematic diagram of a galvanostat: A is the auxiliary electrode; W is the working electrode; R is a reference electrode, E is a high-impedance potentiometer, and i is an ammeter. The working and reference electrodes are connected to a ground (Harvey, 2001).

Potentiostat is used to control the working electrode's potential. Figure 2.21 shows a schematic diagram for manual potentiostat. The working electrode's potential is measured relative to a constant-potential reference electrode which is connected with the working electrode through a high-impedance potentiometer. The drifting of the working electrode's potential can be adjusted by adjusting the slide wire resistor. In the modern potentiostats, a waveform generator is connected which allows applying a time-dependent potential profile (Harvey, 2001).

2.7.1. Double layers supercapacitors (DLSCs)

Conventional capacitor is a passive electronic component consists of two conducting electrodes of identical area A separated a distance d in vacuum. When applying a potential on a capacitor, the charges will accumulate on the electrodes where there is a dielectric separates the charges of two electrodes which produce an electric field allows the capacitor storing energy. In supercapacitor, also called electrochemical capacitors, the charges accumulate in the electric double layer (EDL) at the interface between the electrode and electrolyte when the electrodes are polarized by an applied voltage and the separation between charges is in order of few angstroms (0.3-0.8 nm). The negative ions will accumulate on the positively polarized electrode and the opposite for the positive ions (Kiamahalleh, Zein, Najafpour, Sata, & Buniran, 2012).

The double layer capacitor electrochemical process can be represented as:

Positive electrode:

$$E_s + A^- \leftrightarrow E_s^+ // A^{-1} + e^{-1} \quad (2.22)$$

Negative electrode:

$$E_s + C^+ + e^- \leftrightarrow E_s^+ // C^+ \quad (2.23)$$

Overall reaction:

$$E_s + E_s + C^+A^- \leftrightarrow E_s^+ // A^{-1} + E_s^+ // C^+ \quad (2.24)$$

Where E is the carbon electrode surface, // represents the double layer as the charges are accumulated on the two sides of the double layer, and C and A are the cations and the anions of the electrolyte, respectively.

Electrons are transported from the positive electrode to the negative electrode by external power sources during the charge, as indicated in (equations 2.22 and 2.23); while positive and negative ions are removed from the bulk electrolyte and transferred to the electrode surfaces. During the discharge, electrons leave from the negative to the positive electrode via the load, while ions are discharged from the electrode surface and returned to the electrolyte's bulk (Conder, Fic, & Matei Ghimbeu, 2019). The electrolyte is also an active material because, as shown in the overalll reaction (equation 2.25), salt (C^+A^-) in the electrolyte is consumed during charging (Zheng, Huang, & Jow, 1997). Therefore, the anions and cations move between the solution and the charged surfaces while the electrons move to and from the electrode surfaces through the external circuit (Figure 2.22).

In theory, no chemical or phase changes occur at the electrode/electrolyte contact (Wang, 2012). The charging of EDL capacitors (EDLCs) is extremely fast due to the EDL's purely physical formation without the need to electrochemical reactions. In

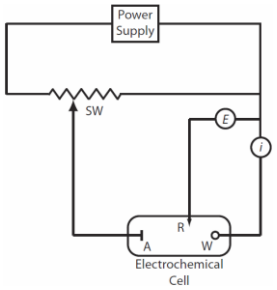

Figure 2.21: Schematic diagram for a manual potentiostat: W is the working electrode; A is the auxiliary electrode; R is the reference electrode; SW is a slide-wire resistor, E is a high-impendance potentiometer; and i is an ammeter (Harvey, 2001).

contrary, batteries store energy through redox processes.

In (figure 2.23), a double-layer is formed by a compact layer (Helmholtz-layer) with a thickness of 0.3-0.8 nanometers, equivalent to the diameter of solvent molecules and ions that reside on it, as well as an extensive diffuse layer with dimensions of (1-100 nm) depending on the electrolyte concentration (Béguin, Presser, Balducci, & Frackowiak, 2014; Hussain, Amade, Moreno, & Bertran, 2014).

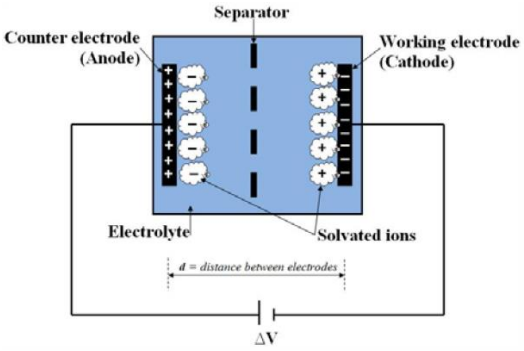

Figure. 2.22: Schematic diagram of an electrochemical double-layer capacitor (Kiamahalleh et al., 2012).

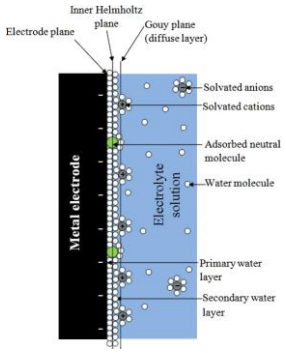

Figure. 2.23: A double layer model formed at electrode_electrolyte interface (Kiamahalleh et al., 2012).

The specific capacitance (C_{sp}) for one electrode (using three-electrodes cell) of supercapacitor can be calculated as following:

$$C_{sp}(Fg^{-1}) = \frac{4C}{M} \tag{2.25}$$

Where C is the capacitance that can be obtained from two-electrodes cell and M is the active material mass. To calculate the energy density (E) and power density (P) of supercapacitor, the following equations are used:

$$E = \frac{(CV^2)}{2} \tag{2.26}$$

$$P = \frac{V^2}{(4R_S)} \tag{2.27}$$

Where C is the specific capacitance, V is the cell voltage, and R_s is the equivalent series resistance (Chen & Dai, 2013).

In electrochemistry, the study of the loss (oxidation) or gain (reduction) of electrons in a substance as a result of electrical stimulation provides information about the concentration, kinetics, reactions mechanism, chemical status and other characteristics of a species in solution in addition to the information related to the electrode surface.

As can be concluded, in the electrochemical experiment we can measure one or more of four parameters: potential (E), charge (Q), current (I), and time (t). the system response depends on the parameters we use as an excitation signals.

2.7.2. Electrochemical measurements

A- Cyclic voltammetry (CV)

It is a common potential-dynamic electrochemical technique, used for obtaining qualitative and quantitative information about the electrochemical reaction on the electrode surface and the solution such as electrochemical kinetics, reaction reversibility, reaction mechanisms, electrocatalytical processes, and electrode structures effects on these parameters. The current flowing between the working electrode and the counter electrode can be recorded while scanning the electrode potential (difference between working electrode and reference electrode). After that, the current flowing through the working electrode is plotted as a function of electrode potential to produce a CV, as illustrated in Figure 2.24 (Yu, Chabot, & Zhang, 2013).

The cyclic voltammetry peak current can be calculated by Randles-Sevcik equation:

$$i_P = (2.69 \times 10^5) n^{3/2} A D^{1/2} \nu^{1/2} C = KC \tag{2.28}$$

Where n is the electrons number in the redox reaction, A is the working electrode area, D is the diffusion coefficient for the electroactive species, ν is the scan rate, and C is the electroactive species concentration at the electrode.

B- Charge-discharge curve (CDC)

The charging–discharging curve (CDC) is one of the most accurate methods for determining a supercapacitor's capacitance energy density, power density, equivalent series resistance, and cycle life. CDCs are normally done by applying a constant cell current and recording the cell voltage as a function of charging or discharging time (Figure 2.25). When utilizing a constant current (I_{cell}), the supercapacitor charging voltage (V_{cell}) can be represented as a function of time (t) as following

$$V_{cell} = I_{cell}R_{esr} + I_{cell}\frac{t}{C_T} \quad \text{(Charging process)} \qquad (2.29)$$

Where R_{esr} is the equivalent series resistance. This equation suggests that the cell voltage and charging time are linearly proportional. After the supercapacitor has been charged to the maximum cell voltage (V_{cell}^{o}), the discharge process at constant current (I_{cell}) starts where the cell voltage (V_{cell}) can be expressed as following:

$$V_{cell} = -I_{cell}R_{esr} + (V_{cell})_{max} - I_{cell}\frac{t}{C_t} \quad \text{(Discharging process)} \qquad (2.30)$$

C- Electrochemical Impedance Spectroscopy (EIS)

EIS, also called AC impedance spectroscopy, is a valuable technique to study the electrode-electrolyte characteristics related to metal corrosion and electrodeposition. In supercapacitors, EIS can be used to find the capacitance and equivalent series resistance (ESR) (Yuan, Song, Wang, & Zhang, 2010).

The ESR is a real series resistance in electrochemical supercapacitors that forms by different reasons such as the resistance of the electrolyte and the external lead contact, the electrode resistance and the resistance of the contact between the current collector and the electrode layer.

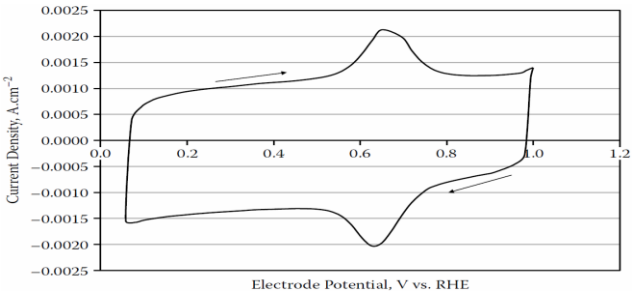

FIGURE 2.24: Cyclic voltammograms of 5 wt% Fe-Nx/C coated on glassy carbon electrode surface, recorded in N2-purged 0.5 M H_2SO_4 solution. Fe-N_x/C loading = 150 μg·cm^{-2}. Potential scan rate = 50 mV/s (Yu et al., 2013).

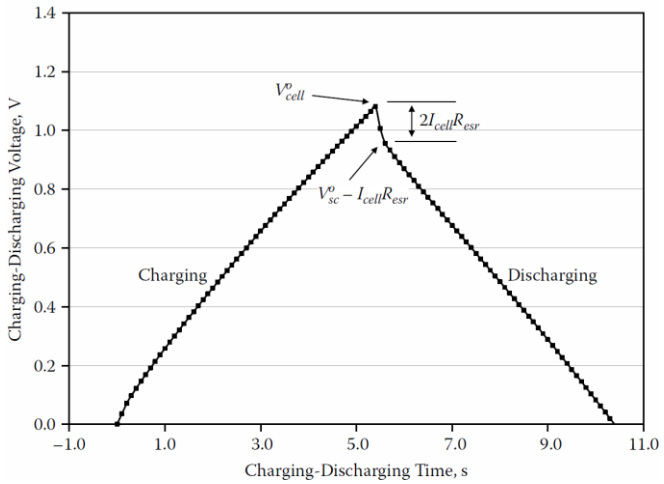

Figure 2.25: Charging–discharging using a two-electrode test cell in which both electrodes are identical (symmetric cells) (Ban et al., 2013).

Because the ESR limits the rates at which the capacitance can be charged or discharged when a given current or voltage is applied, it is an essential parameter in evaluating a supercapacitor's performance, particularly its power density.

Using a very small AC signal to analyze electrical characteristics is an important advantage as it doesn't disturb the properties of the system. During the experiment, a small AC amplitude signal is applied to the supercapacitor covering a frequency range from 0.001 to 1,000,000 Hz. It is possible to utilize either voltage control (potentiostatic) or current control (galvanostatic) mode. The impedance responses are recorded as a relation between the imaginary and real resistances (or impedances). This plot is called Nyquist plot.

An equivalent circuit (EC) may be built for a symmetric supercapacitor with both double-layer and pseudocapacitances. Figure 2.26 shows different ECs models where R_{esr} is the equivalent series resistance, C_{dl} is the double-layer capacitance, R_{ct} is the charge transfer resistance of the electrochemical reaction producing pseudocapacitance, C_F is the pseudocapacitance, and R_p is the parallel resistance of the leakage reaction (Yu 2013).

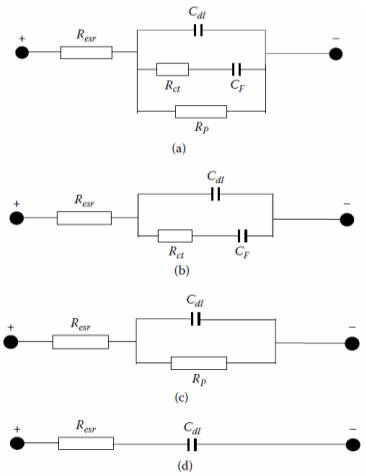

Figure 2.26: ECs for supercapacitor containing both double-layer and pseudocapacitances. (a) Complete model. (b) Model without parallel leaking reaction. (c) Model without pseudocapacitance generating reaction. (d) Model without both parallel leaking reaction and pseudocapacitance generating reaction (Yu et al., 2013).

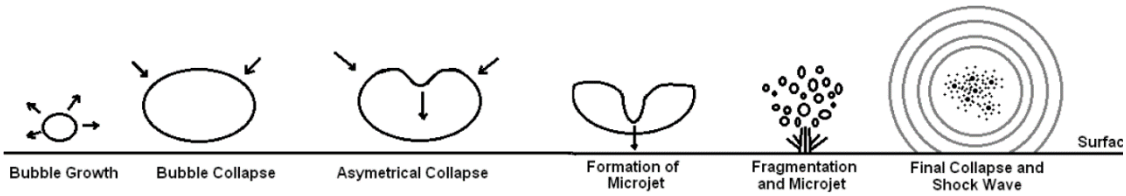

Figure 2.27: The formation and collapse of a typical cavitation bubble at a frequency of 25 kHz. The total time of this phenomena is $< 40\,\mu s$ (Kieser, Phillion, Smith, & Mccartney, 2011).

2.8 Ultrasonic equipment (Sonicators)

Ultrasonics is the sound waves science of frequencies higher than 20 kHz. The use of these frequencies leads to a process called ultrasonication or supersonicator. The ultrasonication is used in many applications e.g., water, food, coating, cleaning, paint and pharmaceutical applications. It can be used as well for providing energy for certain chemical reactions or speeding dissolution.

The principle of the supersonicator depends on the propagation of ultrasonic waves in a solvent. There is continuous transition in non-elastic medium like water and most liquids as long as the amplitude or "loudness" of the sound is relatively low. However, when amplitude increases, the magnitude of the negative pressure in the rarefaction zones is large enough to cause the liquid to fracture due to the negative pressure, resulting in cavitation. Cavitation "bubbles" form as the liquid fractures or rips at rarefaction areas due to the negative pressure of the sound wave in the liquid. The cavitation "bubbles" fluctuate under the influence of positive pressure as the wave fronts pass, ultimately

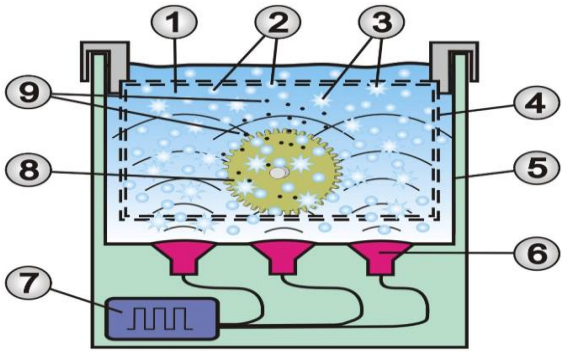

Figure 2.28: Schematic set-up of Ultrasonic bath and the process: 1. Cleaning solvent, 2. Cavitation bubbles, 3. Bubbles implosion, 4. Concave insert, 5. Stainless steel tank, 6. Oscillating systems, 7. Ultrasound generator, 8. Sample to be cleaned, and 9. Dissolved dirt particles (Conrad, 2020).

expanding to an unstable size. Thus, implosions arise from the rapid collapse of the cavitation "bubbles," which cause shock waves to be radiated from the collapse locations (Figure 2.27). This collapse and implosion of the huge number of bubbles through the liquid result in the effects of ultrasonication. A very high temperature (about 5000 K) and pressure (up to 2000 atm) are reached during the implosion with a velocity reaches up to 280m/s (Kieser et al., 2011). The supersonicator can be used in the lab as an ultrasonic bath or an ultrasonic probe.

2.8.1 Ultrasonic Bath

Ultrasonic bath consists of ultrasonic tank filled with a cleaning agent, oscillating systems and an ultrasound generator (Figure 2.28). When the ultrasound is activated, the generator supplies the oscillating systems with electrical energy. These transfer the oscillations to the cleaning fluid. The oscillation causes a rapid pressure tension change in the cleaning solution leading to the phenomena explained above (Conrad, 2020).

2.8.2 Ultrasonic Probe

Ultrasonic The probe sonicator has the same physical principle of the bath sonicator but the difference is in the inserting the probe directly into the sample (Figure 2.29). Because of the high-intensity energy transfer caused by direct contact, the sample can be processed faster. The diameter of the tip is a main factor to determine the intensity as the smaller tip diameters deliver high-intensity sonication, but the energy will be focused in a small area. The probe could contain a single, dual, four, or even more tips (Figure

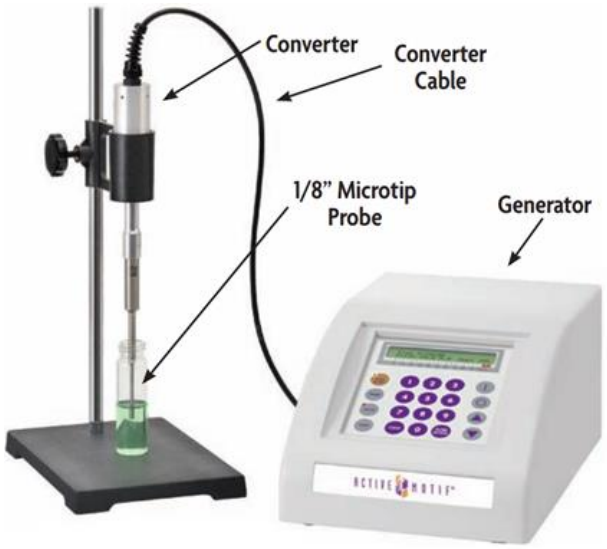

Figure 2.29: Probe sonicator with a digital controller to control the ultrasound waves amplitude and pulses time using a fixed frequency of 20kHz (Active Motive, 2020).

2.30). Usually, the probes are made of titanium, and they can be replaceable or solid (Pethe, 2021).

In this work, we used the supersonicator for three purposes:

1- Cleaning substrates with different solvents before using them.

2- dissolving different salts in water for high concentration electrolyte.

3- dispersing the CNTs to study the properties of a single tube.

Figure 2.30: Supersonicator probes of 1, 2, 4, and 24 tips (Pethe, 2021).

Chapter 3

Experimental concepts and setups

The caron material synthesis and functionalization were carried out in different reactors using different processes and methodologies in order to optimize the synthesis conditions in addition to the substrate treatment before the synthesis and the treatment of the obtained carbon materials. These reactors with their different setups depend mainly on using atmospheric pressure of ultimate dry ambient or using plasma of a very low pressure of the used gases which requires ultra-high vacuum before introducing any gases. In this chapter, the reactors configurations and technologies, and their related parameters such as vacuum, plasma, gases effect, catalysts and different processes can be used inside will be explained in detail.

3.1 Vacuum

Vacuum is defined as the state at which the pressure or the gas density contained in a space is less than that of its surrounding atmosphere. The lowest pressure on earth is 300 *mbar* exists on

Vacuum range	Pressure range (mbar)	Typical applications
Low	$33 < P < 1.0 \times 10^{3}$	Vacuum cleaner, mechanical handling, vacuum forming.
Medium	$1.0 \times 10^{-3} < P < 33$	Vacuum drying, vacuum freeze (food industry).
High (HV)	$1.0 \times 10^{-6} < P < 1.0 \times 10^{-3}$	Production of microwave, light bulbs, vapor deposition.
Very high (VHV)	$1.0 \times 10^{-9} < P < 1.0 \times 10^{-6}$	Electron microscopes, X-ray and gas discharge tubes, electron beam welding.
Ultra-high (UHV)	$1.0 \times 10^{-12} < P < 1.0 \times 10^{-9}$	Particle accelerators, space simulators, material research, semiconductors.
Extreme high (XHV)	$P \leq 1.0 \times 10^{-12}$	Particle accelerators, space simulators, advanced semiconductor devices.

Table 3.1. vacuum ranges and their typical applications (Chambers et al. 1998).

the Everest Mountain, accordingly, any pressure below this value is considered vacuum.
Vacuum can be classified to different ranges starting from the low vacuum at 33 *mbar* until the extreme high vacuum at 10^{-12} *mbar*. The classification of vacuum ranges and their applications according to the American Vacuum Society is shown in table 3.1 (Chambers et al. 1998).

The vacuum is needed for other general applications such as avoiding contamination or electrical charges in high voltage devices, decreasing the heat loss and providing thermal isolation (Kim 2014).

Ideal gas laws

A gas confined in a container can be characterized by three variables; volume (*V*), pressure (*P*), and temperature (*T*) while the gas amount can be described in different ways such as the mass (*m*), particle number (*N*), and the amount of substance (*v*) (Jousten 2016). When dealing with vacuum, the amount of substance [mol] is the best way to describe the gas amount because it scales it to a reference quantity, which is Avogadro's number N_A:

$$\nu = \frac{N}{N_A} \tag{3.1}$$

Avogadro's number is a constant defined as the number of gas particles in one mole (6.02×10^{23} *particles/mole*)

In addition, there are other ways to describe the gas amount such as the mass density (ρ) (*kg.m*$^{-3}$), number density (n) ($m-3$), and the molar mass (M) (kg.mol^{-1}).
The ideal gas law is the equation of the gas state, and it is dependent on some assumptions; where the molecules are in a constant state of motion in all directions, the volume where the gas exists contains a large number of particles, the gas molecules are assumed to be spheric with a distance between them very large compared to their diameters, and the molecules don't exerts forces to each other unless they collide and the collision is elastic (O'Hanlon 2003).
There are different gas laws explain the relation between some parameters when others are constant when handling a fixed amount of gas. For example, Boule-Mariotte law describes the volume-pressure relationship when the temperature is constant, Charles's law describes the volume-temperature relation when the pressure is constant, and Gay-Lussac's law describes the

pressure temperature relation when the volume is constant. Avogadro's law describes the relation between the container volume and the amount of gas at a fixed pressure and temperature.
The combined gas law gives the relation between the volume, temperature, pressure, and amount of gas to be (Jousten 2016):

$$\frac{p.V}{T} = constant \tag{3.2}$$

The constant is proportional to the amount of gas, which can be represented by mass (m), particles number (N), number density (n), or amount of substance (ν). The constant to be represented as a number density can be written as:

$$p = n.k.T \tag{3.3}$$

Where p is pressure, n is the number density, k is Boltzmann's constant ($1.38 \times 10^{-23}\ J.kg^{-1}.K^{-1}$), and T is the temperature in K.

According to Dalton's law, the total pressure of mixture of gases is the sum of the partial pressure of the individual gases:

$$P_{total} = P_1 + P_2 + \cdots + P_i \tag{3.4}$$

Therefore, the ideal gas law can be presented as:

$$P_{total} = (n_1 + n_2 + \cdots + n_i).k.T \tag{3.5}$$

The collision between two the molecules with each other or with the container walls changes their velocity and direction. The particle velocities distribution depends on the temperature and the particles' mass according to Maxwell-Boltzmann velocity distribution (O'Hanlon 2003):

$$\frac{dn}{d\nu} = \frac{2N}{\pi^{1/2}}.\left(\frac{m}{2kT}\right)^{3/2}.\nu^2.e^{-\left(\frac{m\nu^2}{2kT}\right)} \tag{3.6}$$

Where *N* is the total number of molecules, m is the mass of molecules (kg), K is Boltzmann constant, and T is the temperature in [K]. Figure (3.1) represents Maxwell-Boltzmann velocity distribution.

The parameters average velocity (v_{avg}), most probable velocity (v_P), and the root mean square velocity (v_{rms}), can be expressed from equation (3.6) respectively as following:

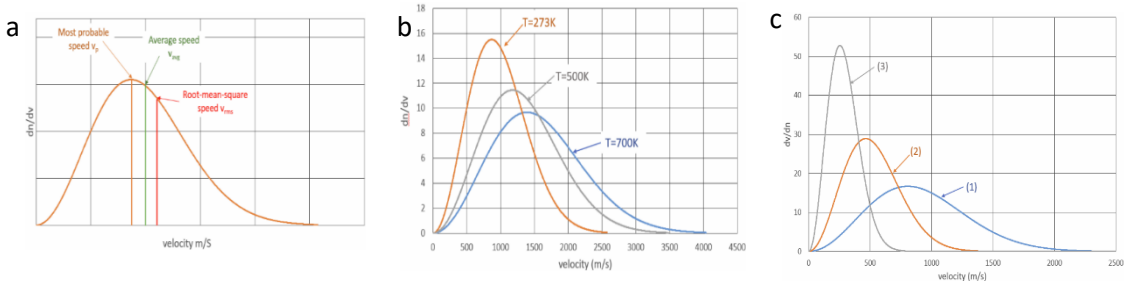

Figure 3.1. Maxwell-Boltzmann velocity distribution b) with different temperatures and c) with different masses where $m_1<m_2<m_3$ (Al-Dmour 2020).

$$v_{avg} = \sqrt{\frac{8kT}{\pi m}}\ , \quad v_P = \sqrt{\frac{2kT}{m}}\ , \quad v_{rms} = \sqrt{\frac{3kT}{m}} \tag{3.7}$$

As we can observe in figure (3.1), the velocities shifted towards higher values when increasing the temperature, but the peak has been reduced in order to keep the same amount of gas molecules (same area under the curve). The opposite happens when the mass increases where the velocities curve shifted to lower values and the peak has increased when increasing the mass (Al-Dmour 2020).

Mean free path

The average distance that the gas molecules travel before collision between each other or with the container walls is called the mean free path (*MFP*). *MFP* depends on the diameter of the gas molecules, temperature, and the pressure according to the following relation:

$$\lambda = \frac{k.T}{\sqrt{2}.\pi.d^2.P} \tag{3.8}$$

Where λ is the mean free path (*m*), d is the molecular parameter (*m*), p is the pressure (*Pa*), k is Boltzmann constant, and T temperature [*K*]. By substituting eq (3.3), and considering T is the room temperature and $d = 3.7 \times 10^{-10}\ m$ for N_2 molecules, λ (*cm*) will become (Chambers et al. 1998):

$$\lambda = \frac{6.6\times10^{-3}}{P\ (mbar)} \quad (3.9)$$

Vacuum range	Gas density (cm^{-3})	Mean free path (cm)	Impingement rate ($cm^{-2}.s^{-1}$)	Collision rate ($cm^{-3}.s^{-1}$)	Monolayer formation time (s)
	n	λ	Z_A	Z_V	τ
atm.	10^{19}	10^{-5}	10^{23}	10^{29}	1×10^{-9}
medium	10^{16}	10^{-2}	10^{20}	10^{23}	1×10^{-6}
high	10^{13}	10	10^{17}	10^{17}	1×10^{-3}
Very high	10^{10}	10^{4}	10^{14}	10^{11}	10
Ultra-high	10^{7}	10^{7}	10^{11}	10^{5}	180

Table 3.2. Approximate gas properties at varies vacuum levels (Marquardt 1999).

Table (3.2) shows the different vacuum levels in relation with pressure, gas density, mean free path, impingement time, collision rate, and monolayer formation. The impingement time is the number of particles incident upon a unit surface are per unit time (Al-Dmour 2020).

Gas flow

The removal of gas from a container to obtain vacuum depends on the gas flow. There are several flow regimes could exist during the pressure reduction. The flow of gas is determined by the gas viscosity when the pressure reduces from the atmospheric to a low vacuum. Then the flow will go to the molecular flow regime when the pressure reduces more where the pressure will be governed by the molecular behavior of the gas.

The different gas flow regimes are shown in figure (3.2). the viscous behaviour can be turbulent when the gas velocity is high or laminar when the velocity is low where the gas will flow in parallel layers with some friction with the walls of the container. When the gas flowing in the molecular regime, the molecules will be moving randomly. The intermediate regime exists when the flow has both; the viscous and the molecular behaviour

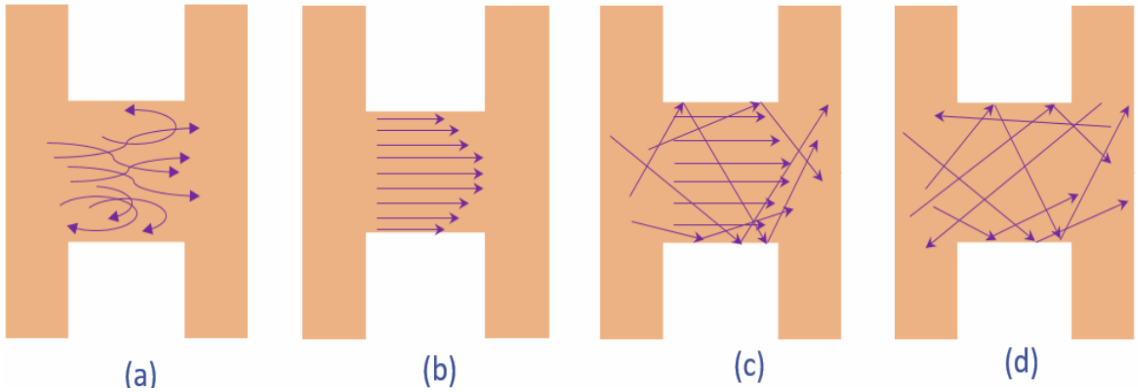

Figure 3.2. Illustration of the various gas flow regimes through a pipe in a vacuum chamber: viscous flow, which is of two types: (a) turbulent, (b) laminar, intermediate flow (c), and molecular flow (d) (Al-Dmour 2020).

The different flow regimes can be differentiated by the dimensionless Knudsen number (Kn), which is the ratio of the mean free bath (λ) and diameter of the pipe (D) as follows:
The dimensionless Knudsen number (K_n) is used to differentiate between the different flow regimes, and is defined as the ratio of the mean free path to the dimension of the chamber (e.g., dimeter of the pipe (*D*)):

$$K_n = \frac{\lambda}{D} \tag{3.10}$$

The viscous regime exists when $K_n < 0.01$, while the intermediate when $0.01 < K_n < 0.5$, and the molecular when $K_n > 0.5$. In addition, when the mean free bath is larger than the container dimensions (e.g. tube diameter), then the gas flow is molecular because the collision between the particles is less likely and the particles will collide with the walls of the chamber.
The gas transported per unit time is the flow rate. The flow rate can be defined in many ways, e.g., volumetric, mass, molar, and particle flow rate (Chambers et al. 1998). The volumetric flow rate ($\dot{V}$) can be expressed as following:

$$q_V = \frac{\Delta V}{\Delta t} = \dot{V} \tag{3.11}$$

Where ΔV is the transported volume of gas (m^3) and Δt is the transportation time (s) (Al-Dmour 2020).

Pumping speed and throughput

The pumping speed S [l.s^{-1}] is the rate at which the pump can remove the gas from the system where it can be defined as the gas volume removed from the system per unit time (volumetric flow rate):

$$S = \dot{V} \tag{3.12}$$

Throughput (Q) [mbar.l.s^{-1}] is the gas quantity expresses in pressure-volume units flowing across a specific cross-section per unit time. The relationship between the pumping speed and the throughput can be expressed as follows:

$$Q = p.\dot{V} = p.S \tag{3.13}$$

Figure (3.3) shows the difference between the throughput and the pumping speed, and the pressure of a vacuum system.

Conductance

When the gas flows through a pipe, the pipe will show a resistance to this flow, which will reduce the pressure along the pipe. This resistance is called the impedance (Z). The conductance is the inverse if the impedance, which is the constant in the proportionality between the throughput and the pressure drop through the pipe (Weston 1985):

$$Q = C(p_1 - p_2) \tag{3.14}$$

The conductance depends on many factors such as the temperature, gas species, geometry, and the pressure in case of the viscous regime.

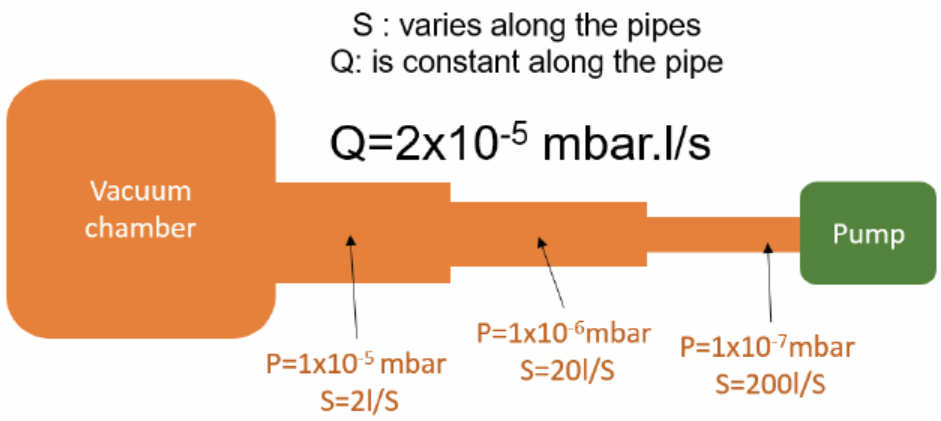

Figure 3.3. An example of the relation between the pumping speed, throughput, and the pressure of a vacuum system (Al-Dmour 2020).

The conductance depends on many factors such as the temperature, gas species, geometry, and the pressure in case of the viscous regime.

The vacuum system usually consists of many pipes in which they are connected in parallel or series. When the pipes are connected in series, each one will have a different conductance but all of them will have the same throughput. While when the pipes are connected in parallel, each one will have its own conductance and throughput (Figure 3.4). To be able to estimate the pressure profile through the system, the total conductance should be estimated by equation (3.14), which will result:

For parallel connection, $C_{total} = C_1 + C_2 + \cdots = \sum_i^N C_i$ (3.15)

For Series connection, $\frac{1}{C_{total}} = \frac{1}{C_1} + \frac{1}{C_2} + \cdots = \sum_i^N \frac{1}{C_i}$ (3.16)

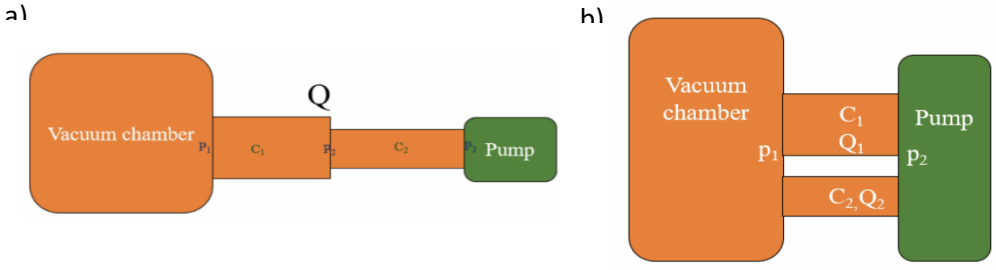

Figure 3.4. A vacuum system with two tubes connected in a) series and b) parallel (Al-Dmour 2020).

Gas sources in vacuum systems

The residual gas can find its way to the vacuum system through several processes mainly (Rinolfi 2016):

I. Outgassing: is the spontaneous release of the gas from a solid or liquid.
II. Degassing: deliberate removal of the gas from a solid or liquid.
III. Desorption: release of the adsorbed species from the surface of a solid or liquid.

There are different ways can allow the gas getting into the vacuum system such as back-streaming of gas from the pump, virtual leaks, permeation, Bulk diffusion, and evaporation (Figure 3.5) (Weston 1985) .

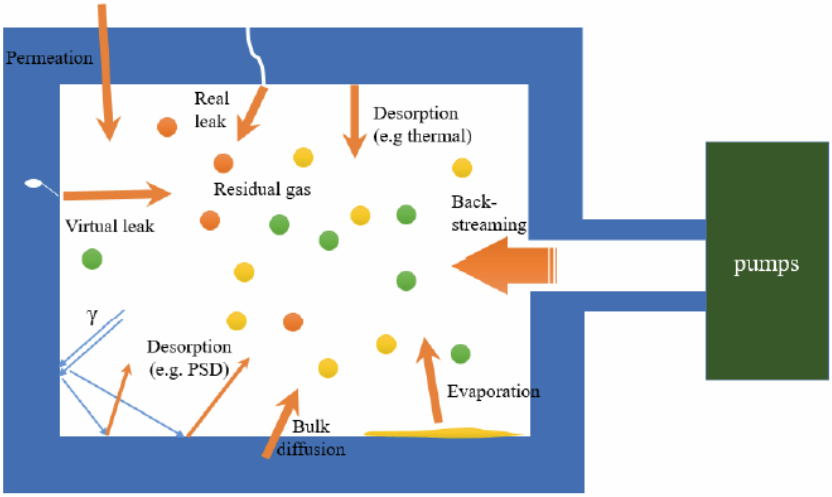

Figure 3.5. Possible sources of gas inside a vacuum chamber (Al-Dmour 2020).

Safety aspects of vacuum technology

There are many safety hazards must be taken into account when handling vacuum systems such as (Mattox 2010):

- The accumulation of the hazardous gases in the pump oil and the cryo-sorption pumps, which needs more attention during the maintenance and disposal.
- An explosion can happen when pumping pure oxygen using a hydrocarbon pump.

- Avoiding putting a floating material in the plasma as it can cause a high electrical potential with other parts of the system. It is recommended to have all the external touchable parts by human grounded.
- Quartz vacuum windows allow the UV radiation to be transmitted from the plasma causing damage to the exposed eyes.

Weston (Weston 1985) explained in details the effect of vacuum on different materials such as glass, metals, and ceramics.

Although the vacuum systems are required in many industry fields, but the real need of such systems created some drawbacks such as the equipment complexity and its high cost.

3.2 Plasma

When temperature increases, molecules become more energetic and the matter will be transformed in a sequence; solid, liquid, gas and finally plasma which is considered the fourth state of matter. Plasma is an ionized gas, which means that there is at least one electron is attached to the atom or molecule leading to converting the atom or molecule into positively charged ions. These electric charges (electrons and ions) make the plasma electrically conductive, internally interactive, and strongly responsive to electromagnetic fields. The term 'plasma' is used when the ionized gas is electrically neutral, which means the balance between the electron density and the positive ions, and contains sufficient number of electrically charged particles that can affect its electrical properties and behaviour (Fridman 2008). The physical state when the physical state of the an ionized gas in which the densities of positive and negative particles are approximately equal is called quasi-neutrality (KEIDAR and BEILIS 2018).
Plasma constitutes more than 99% of the universe and the term was first introduced by Irving Langmuir (1928) because it is multicomponent and strongly interacting ionized gas, so it reminded him of the blood plasma. Plasma exists neutrally but also can be made in laboratory and industry which provide opportunities to many applications, including electronics, thermonuclear synthesis, and lasers.

Two main characteristics of plasma's behaviour can indicate the considered kind of plasma, which are the plasma's oscillations and Debye length. The two parameters can quantitively describe the plasma and they depend on its density and temperature. Any shift between the electrons with

respect to the ions will lead to a charge separation, which will produce an electric field in order to restore the unperturbed plasma. Debye length can be defined as a characteristic scale at which the charge separation exists when the electric field produced by this separation is small enough that can't restore (violate) the quasi-neutrality.

The potential energy of a charged particle when there is a full charge separation L_D is of the order of the thermal energy of the particle particle $k_B T_e$. The maximum potential energy can be obtained by the full separation can be considered as a planar capacitor to be as following:

$$e\varphi \sim \frac{e^2 L_D^2 N_0}{\varepsilon_0} \sim k_B T_e \tag{3.17}$$

Where k_B is Boltzmann constant and N_0 is charge particles density. From this relation we can estimate the characteristic distance of charge separation which is:

$$L_D = \sqrt{\frac{\varepsilon_0 K_B T_e}{e^2 N_0}} \tag{3.18}$$

L_D is what we call *Debye length.*

The same expression can be obtained by considering the potential shielding in plasmas. First, we will consider an initially neutral plasma with density N_0 is disturbed by, for example, immersing a 1D transparent sheet (plane geometry) having a negative potential Φ_0 with respect to the plasma (Figure 3.6). The ions and electrons distribution will be rearranged to a new state corresponding to the disturbed electric field. The ions will be assumed as not moving on time scale because they are heavier than electrons and therefore their response time is much larger. This will allow us assuming that the ions density N_i will remain the same as before, which is N_0. On the other side, the electrons will respond to the repulsive electric field and their density will decrease. The electrons density can be calculated by Boltzmann relation as:

$$N_e = N_0 \, e^{\frac{e\varphi}{K_B T_e}} \tag{3.19}$$

Where T_e is the electrons temperature, φ is the potential, and e is the electron charge.

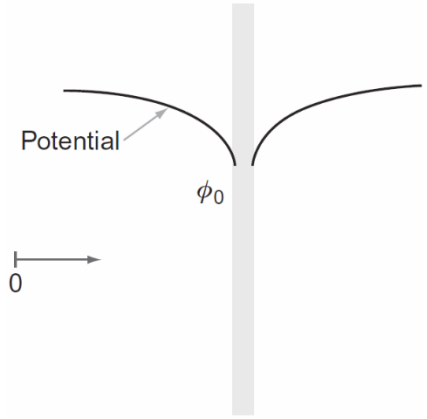

Figure 3.6. Debye length definition from the electric field shielding argument (KEIDAR and BEILIS 2018).

Using Poisson equation we can calculate the potential distribution in the perturbed region as follows:

$$\frac{d^2\varphi}{dx^2} = \frac{e}{\varepsilon_0}(N_e - N_i) \tag{3.20}$$

φ can be solved to be:

$$\varphi = \Phi_0 e^{\left(\frac{-x}{L_D}\right)} \tag{3.21}$$

Equation (3.21) shows that at distance L_D, disturbed φ will be significantly decreased and shows the screening length over which the plasma neutrality will be preserved. Thus, the electric field will be shielded at the Debye length scale and plasma will remain quasi-neutral away from the perturbed region. This means that the electric field will not affect the particles that are far from the Debye length (Fridman 2008).

Plasma Equilibrium

The plasma equilibrium is a term used to describe the plasma chemical composition. To understand it, we neeed to identify the degree of ionization. Consider a plasma consists of electrons, ions and atoms. When the plasma is low ionized plasma, i.e., $n_e \ll n_a$, the ionization degree is defined as:

$$\alpha = \frac{n_e}{n_a + n_e} \approx \frac{n_e}{n_a} \tag{3.22}$$

where n_e is the electrons density and n_a is the density of particles.

We have two reactions in the thermodynamic equilibrium: a direct reaction leads to ionization that is considered as the electron impact ionization, and a back reaction leads to recombination. In other words, the stoichiometric equation will be:

$$a + e \leftrightarrow i + 2e \tag{3.23}$$

With a rate of ionization being $k_i.n_a.n_e$ and rate of recombination $k_r.n_a.n_e$ where k_i and k_r are, respectively, the ionization and recombination coefficients. The ionization equilibrium is when the ionization and recombination rates are equal. The equilibrium constant $K(T)$ can be expressed as following:

$$K(T) = \frac{k_r}{k_i} = n_i.n_e/n_a \approx \frac{n_e^2}{n_a} \tag{3.24}$$

The equation can be solved for the electron density. The equilibrium constant dependent on the temperature is called a function of pressure in the system. If it is possible to specify the equation of state for plasma, then this equation can be used to calculate the electron density as a function of temperature (KEIDAR and BEILIS 2018).

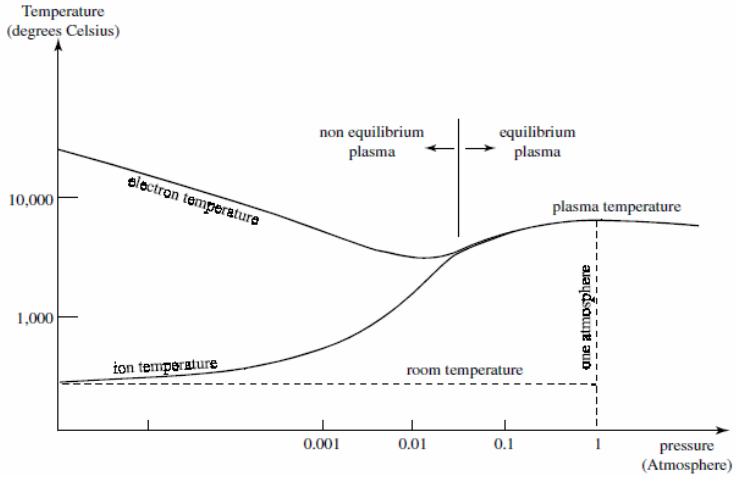

Figure 3.7. Temperature and pressure domain for equilibrium and non-equilibrium plasma for DC discharges (Eliezer and Eliezer 2001).

In industrial plasma, the equilibrium plasma or thermal plasma has the same temperature for both electrons and ions while the non-equilibrium plasma has the electrons hotter than ions but the gas pressure is lower (Eliezer and Eliezer 2001; National Academies of Sciences 2021).

This leads us to classify the plasma into thermal (hot) and non-thermal (cold) plasma. The hot plasma exists in the case of thermal equilibrium where the temperature of electrons and heavy ions are equal. Thermal plasma is widely can be found in the universe (Mouawad et al. 2012). Non-thermal Plasmas (Cold Plasma) manifests a behavior outside the thermodynamical equilibrium, which is the case when the electrons have much higher temperature than ions (Hnatiuc et al. 2012).

Electrons magnetic confinement

The ionized gas ability to maintain an electric current is emphasized in the presence of a magnetic field. According to the electrostatics laws, a particle with charge *q* and mass *m* in the existence of an electric field *E* moves in the direction of the field in an accelerated movement associated with force F_E ($F_E = qE$). Under these conditions, the presence of a magnetic induction B disturbs the movement of the particle due to Lorentz force. In the case that this magnetic field perpendicular to velocity ν, this force is given by $F_B = q \times \nu \times B$, and forces the particle into a circular motion around the magnetic field. The joint action of both fields gives rise to a complex movement, which depends on the speed and initial direction of the particle. In the most general case, in which the E and B fields are stationary with a constant value with time (Figure 3.8), the particle describes a trajectory described by a helical curve around the magnetic field, with a constant radius, whose value is given by the so-called Larmor radius, R_L:

$$R_L = \frac{m\nu_\perp}{qB} \tag{3.25}$$

where $\nu_\perp$ is the velocity perpendicular to the magnetic field. The corresponding angular frequency, r_L, called cyclotronic frequency is given by:

$$r_L = \frac{qB}{m} \tag{3.26}$$

The magnetic confinement is used in general for industrial application. We use it for magnetron sputtering which requires lower gas pressure in order to obtain the plasma (Pantoja-Suárez 2019).

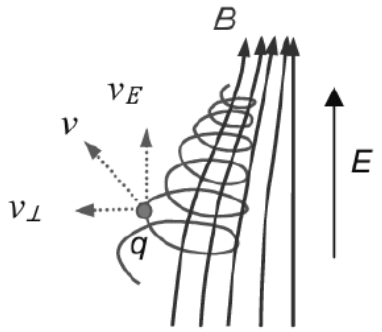

Figure 3.8. Cyclotronic movement of a charged particle, q, in presence of an electric field E, and a magnetic field, B, of variable intensity (Albella 2018).

Radio Frequency Plasma

The radio frequency power supplies produce the plasma either inductively (ICP) or capacitively (CCP) coupling energy at a frequency in the range of radio spectrum (1KHz to 103MHz). in the case of CCP, the AC voltage is provided to power electrodes through a capacitor while the other one is grounded. The capacitor rapidly charges at the positive AC half, which causes the voltage drop over the plasma. The inductive coupled discharge uses the configuration of a cylindrical helical coil where the electromagnetic induction provides the corresponding electric current. The passing of RF current through the coil develops the time-varying magnetic flux that largely induces the RF sinusoidal electrical field that sustains the plasma discharge and accelerate the free electrons (Mehmood et al. 2018) .

Plasma chemistry

Plasma is broadly used in practice, as it offers three attractive features for chemistry applications: (1) some plasma components temperatures and energy density can exceed those of the conventional chemical technologies, (2) the plasma ability to produce high concentrations of energetic and chemically active species (e.g., electrons, ions, atoms and radicals, excited states, and different wavelength photons), and (3) plasma systems can go far from the thermodynamic equilibrium by having a high chemically active species concentration and preserving the bulk temperature as low as room temperature. These features allow the focusing on the traditional chemical processes, increase of their efficiency, and leads to successful simulation of chemical reactions that are impossible in conventional chemistry. Plasma chemistry is a rapidly growing

field of science and engineering, with applications ranging from microfabrication in electronics to aircraft protective coatings, from treatment of polymer fibers and films to medical cauterization for wound treatment, and from ozone production to plasma televisions.

Large concentrations of charged particles (electrons, negative and positive ions), excited atoms and molecules (electronic and vibrational excitation play a prominent role), active atoms and radicals, and UV photons make chemically active plasma a multi-component system that is extremely reactive. In plasma-chemical kinetics, each component of the chemically active plasma performs a unique function. Electrons, for example, take energy from an electric field initially and subsequently transfer it across other plasma components and particular degrees of freedom within the system.

Plasma-chemical processes may typically be controlled and optimized by changing properties of the electron gas (density, temperature, and electron energy distribution function). Ions are charged heavy particles that can contribute significantly to plasma-chemical kinetics either because of their high energy (as in sputtering and reactive ion etching) or because of their capability to decrease chemical reaction activation barriers. This second property of plasma ions results in the plasma or ion catalysis, which is important in plasma-assisted ignition and flame stabilization, fuel conversion, hydrogen generation, and exhaust gas cleaning, and even direct plasma treatment of live tissues. The vibrational excitation of molecules makes an important contribution to plasma chemical kinetics as the plasma electrons with energies around 1 eV primarily can transfer most of the energy in such gases as N_2, CO, CO_2, H_2 into vibrational excitation.

Plasma technologies have a wide range of applications in today's world, spanning a wide range of sectors. Plasmas can be used to achieve high energy efficiency, high specific productivity (productivity per unit volume of reactor), and high selectivity for a variety of chemical processes. For example, when dissociating the CO_2 in a non-equilibrium plasma supersonic flow condition, the selectivity can reach up to 90% of the total discharge power in order to produce CO when the vibrational temperature is about 4000 *K* and the translational temperature is only about 100 *K*. The main point for practical application of any chemical process in a specific plasma system is to identify the appropriate regime and optimal plasma parameters among the large number of possibilities substantial to the systems far from thermodynamic equilibrium.

Specially, providing a high operating power to the plasma chemical reactor as well as high energy input selectivity while preserving non equilibrium plasma conditions. The current thermal plasma generators provide a wide range of operating power starting from less than 1 *kW* to over 50 *MW*.

Despite delivering adequate power levels, these generators are not well suited to the needs of plasma chemistry, which necessitates selective reactant treatment and great efficiency.
The major drawback of thermal plasmas for plasma-chemical applications is that the reaction media overheats when energy is uniformly consumed by the reagents into all degrees of freedom, therefore, the high energy consumption is needed to quench the reagents. This will reduce the energy efficiency and selectivity of such systems (Fridman 2008).

3.3. Physical Vapor Deposition (PVD)

Physical vapor deposition (also known as thin film deposition) is an atomistic deposition process in which material is vaporized as atoms or molecules from a solid or liquid source and transported as a vapor through a vacuum or low pressure gaseous (or plasma) environment to the substrate, where it condenses. PVD methods are often used to deposit films with thicknesses ranging from a few nanometers to thousands of nanometers; however, they may also be utilized to obtain multilayer coatings, graded composition deposits, very thick deposits, and freestanding structures. The substrates might be extremely tiny or large and its shape ranges from the flat surfaces to complex geometries.

Physical vapor deposition can be used to obtain thin films of pure elements, alloys, or compounds using reactive deposition processes. The compounds can be deposited using the reaction between the deposited material with the ambient gas such as using N_2 gas while depositing titanium (Ti) to obtain titanium nitride (TiN). Quasi-reactive deposition is the deposition of a compound material from a compound source contains a volatile reactive species that can be lost during the condensation and transport, which will require the existence of partial pressure of a compensating reactive gas; for example, the quasi-reactive deposition of ITO (indium–tin oxide) needs to be sputtered in an O_2 ambient to substitute its loss during the deposition.

The main PVD processes are arc vapor deposition, ion plating, vacuum deposition (evaporation), and sputter deposition (Figure 3.9).

Vacuum deposition

It can be called vacuum evaporation as well. It is a PVD process where the material reaches the substrate from the source with a little or without any collisions between the gas molecules using a thermal vaporization source with a trajectory of “line to sight”. The gaseous contamination is

very low because of the vacuum environment of deposition. Depending on the level of contaminations that is allowed in the system, the working gas pressure of such process ranges between 10^{-5} *Torr* to 10^{-9} *Torr*. The rat of thermal vaporization is high comparing to other vaporization techniques. The composition of the material evaporated from the source is proportional to the relative vapor pressures of the materials in the molten source.

Arc vapor deposition

It is a technique that vaporizes a cathodic electrode (cathodic arc) or anodic electrode (anodic arc) and deposits the evaporated material on a substrate using a high current, low voltage arc. The vaporized material is strongly ionized, and the substrate is typically biased to speed up the ions (film ions) as they approach the substrate surface. This technique is used to deposit hard and decorative coatings. The film ions of this technique is useful for the ion plating process.

Ion plating

IT is a technique uses a synchronized or periodic bombardment of film deposition by atomic-sized energetic particles allowing the modification and properties control of the thin film. This process is called ion-assisted deposition (IAD) or ion vapor deposition (IVD). there are many important variables in this process such as: the energy, mass, flux of the bombarding species, and the ratio of the bombarding particles to the depositing particles. The vaporization of the depositing material can be achieved by evaporation, arc corrosion, sputtering, or by decomposing a chemical vapor precursor. The bombardment energic particles are typically inert or reactive gas ions, or film ions as mentioned in the previous paragraph (Mattox 2010).

Sputtering

Sputtering (Physical sputtering) is a technique comprises the physical *not thermal) vaporization of atoms from a surface by momentum transfer using a bombarding energetic atomic-sized particles which are usually a gaseous material ions accelerated in an electric field. Chemical sputtering (Roth 1983) is a concept associated with the sputtering when there is a volatile species resulted from the bombardment of the reactive species with the target surface. Chemical sputtering is known as reactive plasma etching (RPE) or reactive ion etching, and it is commonly used for patterning the thin films (Manos and Flamm 1989).

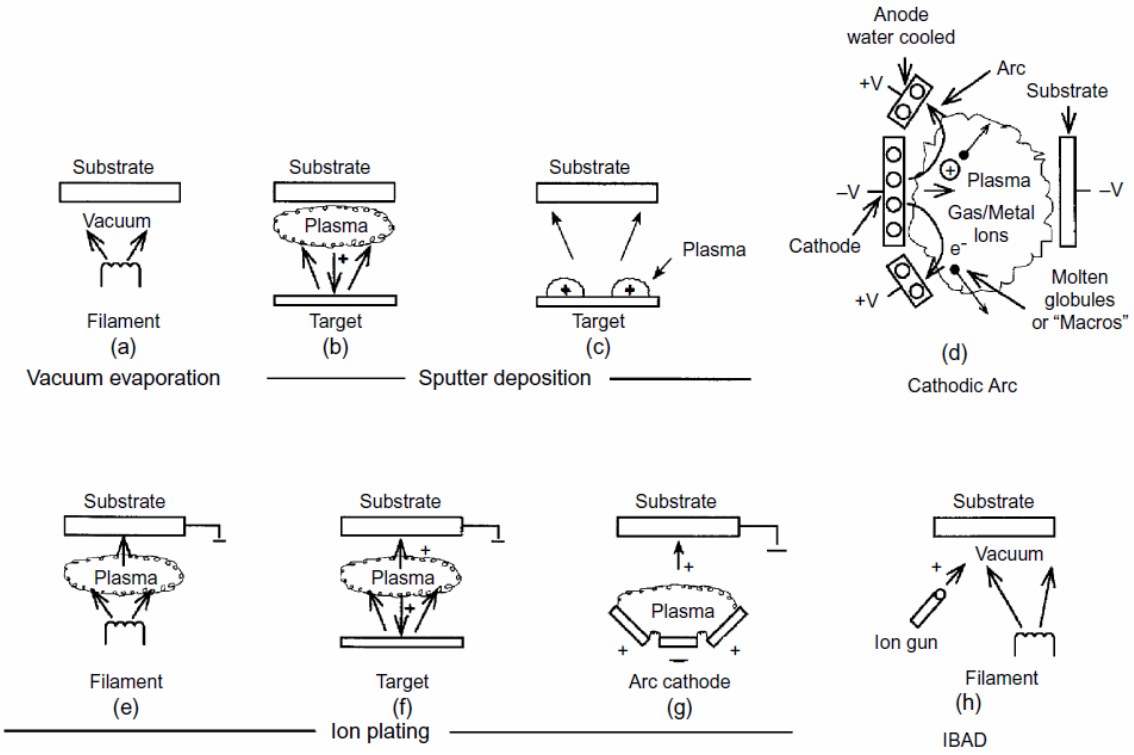

Figure 3.9. Physical vaporization techniques: a) vacuum evaporation, b) and c) sputter deposition in plasma, d) cathodic arc, and ion plating using e) thermal evaporation, f) sputtering, and g) arc vaporization, and h) Ion-beam assisted deposition (Mattox 2010).

The term “sputtering’ means that the bombarded surface is the only source of the deposited material is the only source of the deposited material in addition to the reactive gas elements that are used during the process, which will be called reactive sputter deposition (Westwood 2018). The process usually indicated as ion beam sputtering, magnetron sputtering, RF sputtering, or unbalanced magnetron sputtering depending on its the configuration. The process can also be called bias sputtering when a bias is placed on the substrate leading to synchronized ion bombardment (Berg and Katardjiev 1994).

Usually, Ar^+ ions are used for sputtering because it is an inert gas, so it tends not to react with the target material or combine with any process gases. It also produces high deposition rate because of its high molecular weight, and it is considered relatively cheap (Msi-pse 2021).

Sputtering can be achieved in:

1- A good vacuum (<10^{-5} *torr*) using ion beams.
2- A low-pressure gas environment in which sputtered particles are transferred from the target to the substrate without gas phase collisions (i.e. pressure less than 5 *mtorr*), using plasma as an ion source.
3- Higher-pressure gas (i.e. pressure between 5 *mTorr* and 50 *mTorr*) in which gas phase collisions and thermalization of the ejected particles exist but the gas phase nucleation is not important as the gas pressure is low enough (Mattox 2010).

RF Sputtering

The frequencies of RF sputtering are typically more than 1 *MHz* with a configuration in which its RF power is capacitively coupled to a target through a matching network with a return current path to ground through the chamber walls and ground electrodes. Because the ions in the plasma are unable to follow the electric fields at these frequencies, while the electrons can, the space between the plasma and the target acts as a rectifier. This rectifying action creates a negative DC bias on the cathode's surface creating an ion current to flow constantly to the target, resulting in continuous sputtering. This allows for the sputtering of an insulating target. Conductive targets can be sputtered by RF when it contains a thin insulating layer.

There are to main disadvantages of RF sputtering. First, the deposition rate is about 50% of the DC rate under similar conditions where the loss is due to the power dissipation in plasma heating. Second, the RF configuration and its need to a matching network doubles the cost per watt comparing with the DC or AC. The universality of the RF sputtering is the main advantage. In principle, any target material can be sputtered by RF without arcing and this lowers the particulate counts in the film. However, particles being released from fixturing because of differential thermal expansion or mechanical vibration can easily violate this advantage.

We need to clarify the difference between RF sputtering and AC sputtering. Alternative current (AC) sputtering is a technique in which an AC is applied between two separated targets. This technique is simply DC sputtering at frequencies of a few tens of kilohertz, with the anode and cathode switching roles every half cycle. As a result, each target sputters for about half of the AC cycle. The absence of DC current flow through the target and no current flow through the chamber walls to ground distinguish the AC sputtering. This allows for the sputtering of conducting targets that are coated by a thin insulating layer, but not targets that are themselves insulators (table 3.3) (Glocker et al. 2018).

	AC	RF	DC	Pulsed DC
Net DC current flow	No	No	Yes	Yes
Current to ground	No	Yes	Yes	Yes
Anode required	No	No	Yes	Yes
Targets	dual	single/dual	single	single/dual
Target type	conducting	insulating/conducting	conducting	conducting
Poisoned target mode	stable	stable	arcing	arcing

Table 3.3. comparison of current flows and target characteristics for relative sputtering system (Glocker et al. 2018).

Magnetron sputtering

The usual sputtering tool's poor deposition rate, high discharge voltage, and high working gas pressure necessitated a new technique. The deposition rate had to be increased, the discharge voltage had to be reduced, and the operating pressure range had to be extended. This was accomplished by using a static magnetic field to increase the lifetime of electrons in the vicinity of the cathode target (Wasa and Hayakawa 2003; Gill and Kay 2004).

This can be achieved by magnetron sputtering discharge, which is based on the magnetic confinement of electrons. The configuration of magnetron sputtering is the same as the usual sputtering arrangement in addition to two cylindrical magnets placed directly behind the target (Figure 3.10). The term “planar” refers to the flat cathode target, which can be circular or rectangular. In the planar configuration, the magnetic field lines are generated from the central magnet and go toward the annular one (Waits 1998).

The application of an external magnetic field to confine the electrons is a distinguishing feature of the magnetron sputtering discharge. Crossed electric and magnetic fields, E and B, respectively, confine electrons in closed $E \times B$ drift loops near the negatively biased cathode target. As a result of the presence of both a magnetic field B and an electric field E, the path of electrons in magnetron sputtering discharges is complicated. Permanent magnets or current-carrying coils provide the magnetic field B, while the electric field E is within the plasma sheath and pre-sheath. The sputtering effectiveness can be described by the sputter yield. Sputter yield γ is the number of removed atoms from the target for each ion. It depends on many factors, i.e., energy and mass of bombarding ions, incidence angle, and the surface binding energy. The maximum transferable energy in a collision must be larger than the surface binding energy.

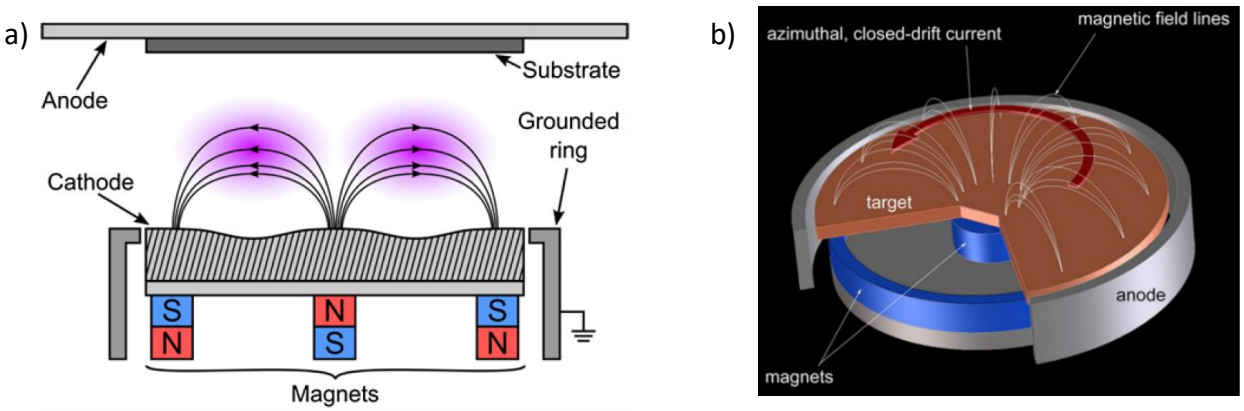

Figure 3.10. a schematic of the planar magnetron sputtering configuration: a) side view and b) a 3D representation (Anders 2011; Gudmundsson 2020).

Balanced and unbalanced magnetrons

If the magnetic flux through the outer magnetic pole (annular) is equal to the flux of the inner pole (central), then the magnetron sputtering discharge is considered to be balanced (Figure 3.11a). In this case, the magnetic trap confines the plasma just in front of the target leading to lower impingement by ions. *Window and Savvides* (Savvides and Window 1998; Window and Savvides 1998), have developed an unbalanced magnetron in order to increase the ion flux which depends on strengthening or weakening the magnetic flux through one of the two magnetic poles. There are two types of unbalancing. In type I, the filed lines are originated from the central magnet while some don't pass to the annular one, which goes toward the chamber walls causing a low plasma density (Figure 3.11b). In type II, the field lines are originated from the annular magnet and some don't pass to the central (Figure 3.11c).

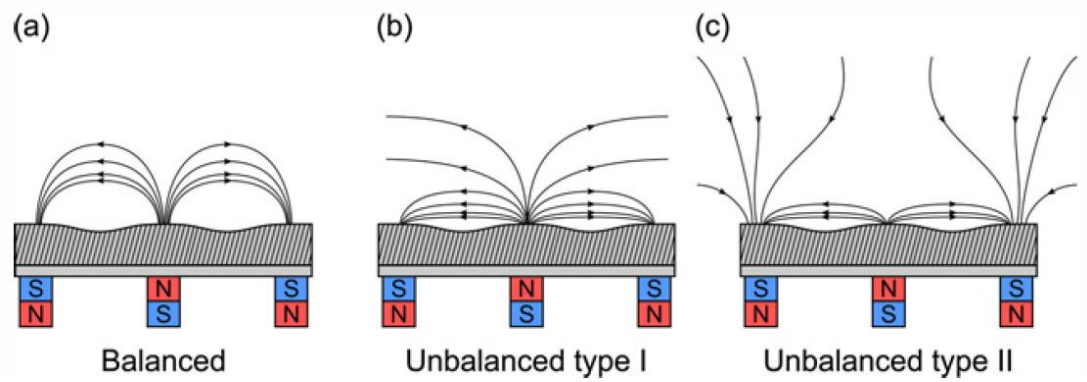

Figure 3.11. A schematic of the magnet configuration in planar magnetron sputtering discharges. The three cases, (a) all the field lines that originate from the central magnet enter the annular magnet (balanced), (b) all the field lines originate from the central magnet, while some do not enter the annular magnet (unbalanced type I), and (c) all the field lines originate from the annular magnet, and some do not enter the cylindrical central magnet (unbalanced type II) (Gudmundsson 2020).

Some secondary electrons can go away from the target and toward the substrate along these magnetic field lines. As a result, the plasma is not strongly confined to the cathode target zone but might flow out toward the substrate. As a result, the ion current density in the region of the substrate increases dramatically. As a result, a substrate bias can control the energy of the ions attacking the substrate during film formation. Subsequently, the energy of the bombarding ions can be tuned by a substrate bias (Gudmundsson 2020).

The contamination during sputtering is expected which can be related to the target, processing gases, or the deposited film. The contamination of target can be partially solved by cleaning It frequently, but it will be difficult when it is porous as it will allow the outgassing. For the same reason we can obtain contaminations from the deposited material when it is deposited for a long time which will increase its surface area and porosity.

Advantages and Disadvantages of Sputter Deposition

The sputtering process has many advantages can be summarized as following (Mattox 2010):

1- The process is easy reproducible, and any material can be sputtered, i.e., element, alloy, or compound
2- The sputtering target provides a stable and long-life vaporization source.

3- In some configurations, the target can provide a large area vaporization source and a specific vaporization geometry.
4- The sputtering target can be adapted to the substrate such as cone or sphere
5- The radiant heating is low compared to the vacuum evaporation.
6- The molecules can be dissociated fully or partially when using chemical vapor precursors.

There are also many drawbacks in some cases such as:

1- The sputtering energy goes mainly into heat in the target which requires a cooling system, so it isn't energy-efficient.
2- Sputtering targets are often expensive.
3- The ejection sputter pattern is non-uniform in many sputtering systems, requiring additional fixturing, equipment, or source design to deposit films with uniform characteristics.
4- Sputter vaporization rates are low when compared to thermal vaporization rates.
5- Sputter targets, especially the insulators, can be delicate and easily shattered during handling or by a non-uniform heating.
6- Short-wavelength radiation and high-energy particles may bombard substrates and films, impairing their performance.
7- Contaminants on deposition chamber surfaces are easily desorbed in plasma-sputtering because of heating and ion scrubbing.

3.4. Chemical vapor deposition (CVD)

Chemical vapor deposition (CVD) is a process of a volatile compound chemical reaction of a material to be deposited with other gases atomisticaly on a suitable substrate to form a nonvolatile solid (Ohring 2002). CVD technique is used to obtain high quality of solid materials involving chemical reactions between organometallic or halide compounds under vacuum.

CVD differs from PVD in that it uses a multidirectional deposition method to deposit material onto the substrate, whereas PVD uses a line-of-site impingement method. CVD is frequently used in microfabrication techniques to deposit materials in a variety of morphologies, such as monocrystalline, polycrystalline, amorphous, and epitaxial. In contrast to PVD, in CVD, a mixture of gases interacts chemically with the bulk surface of the material, causing chemical decomposition of some of the particular gas elements leading to the formation of a solid coating on the base material's surface. CVD is used in a variety of industries, including the deposition of

refractory materials (nonmetallic materials that can endure extremely high temperatures) on turbine blades to considerably improve their wear and thermal shock resistance. There are many CVD techniques depending on the environment or the reaction assistants, i.g., atmospheric-pressure CVD (APCVD), low-pressure CVD (LPCVD), ultrahigh vacuum CVD, plasma-enhanced CVD (PECVD), floating catalyst CVD (FC-PECVD), Inductively coupled plasma CVD (ICP-CVD), microwave plasma-assisted hot filament CVD, metaleorganic CVD, photo-initiated CVD, atomic layer deposition, spray pyrolysis, liquid-phase, epitoxy, etc (Shishkovsky and Lebedev 2011). There are other hybrid processes involves the features of both CVD and PVD (Ohring 2002; Behera et al. 2020).

Figure (3.12) shows the fundamental sequential steps that occur in each CVD process, which are the following (Ohring 2002):

1- Reactant delivery from the gas inlets to the reaction zone by convection and diffusive transport.
2- Gas-phase chemical processes to develop novel reactive species and by-products.
3- The initial reactants and their products are transferred to the substrate surface.
4- adsorption and diffusion of the chemical species on the substrate surface.
5- Surface-catalyzed heterogeneous reactions that result in film formation.
6- desorption of the volatile by-products of the surface reactions.
7- Transport of reaction by-products out from the reaction zone by convective and diffusive transport

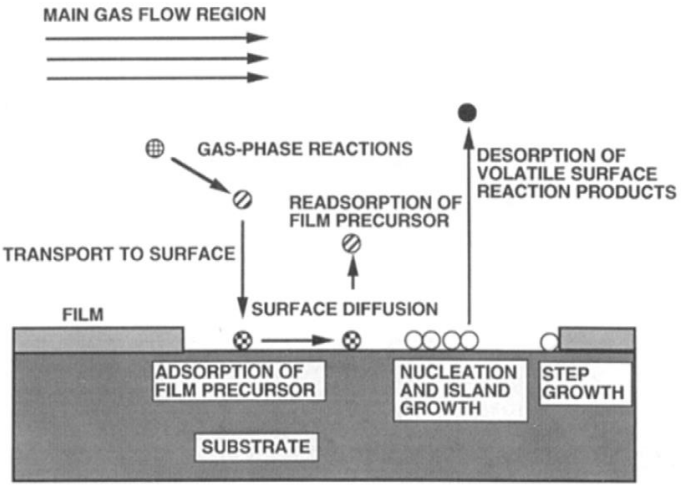

Figure 3.12. Sequence of gas transport and reaction processes contribution to CVD film growth (Ohring 2002).

Plasma Enhanced Chemical vapor deposition (PECVD)

An RF field is used to excite glow-discharge plasmas in the bulk of PECVD operations. The reason for this is that the majority of films produced using this process are dielectrics, making DC discharges impossible. The RF frequencies used are typically between 100 *kHz* and 40 *MHz*. Electron and positive ion densities vary between 10^9 and $10^{11} cm^{-3}$ in a low gas pressure environment, which is normally maintained between 50 *mtorr* and 5 *torr*, and average electron energies range from 1 to 10 *eV*.

This intense discharge is enough to dissociate gas molecules into a variety of component species, including ions, atoms, and molecules in ground and excited states, free radicals, molecular fragments, etc. As a result of the interactions among the reactive species in PECVD, the process can be acheived at considerably lower temperatures than thermal CVD reactors that do not use plasma activation. Therefore, some impossible high-temperature reactions may now be achieved on temperature-sensitive substrates.

Sheath Voltage

Ions and electrons oscillate inside a narrow, constrained space in RF plasma. The density of electrons and ions in such region then rises to the point where both electrons and ions spread toward outside the plasma, which means they collide with the electrodes at first. The number of collisions is proportional to electron or ion density and velocity. Electrons, on the other hand, have a velocity that is around three orders of magnitude greater than that of ions. As a result, the flow of electrons from plasma to electrodes exceeds the flow of ions, and electron fluxes toward the electrodes are induced. If the electrodes are floating or electrically isolated, they become negatively charged, and the electric potential of the plasma becomes positive with respect to the electrodes. The induced potential is called the sheath voltage (V_{sheath}). This potential assumes a value that balances the electron and ion fluxes. V_{sheath} is can be expressed as following:

$$V_{sheath} = \frac{kT_e}{2e} \ln\left(\frac{8M}{\pi m_e}\right) \tag{3.27}$$

where T_e is the electron temperature, e is the charge of an electron, M is the mass of an ion, and m_e is the mass of an electron. This equation only applies to electrodes that are electrically isolated. Even if the electrodes are not totally separated or floating in the real PECVD system, eq. (3.27) may be employed roughly since the currents provided to the electrodes from the outside during deposition are not as big as the interior currents induced by electron collisions at the electrodes.

Furthermore, in most situations, the two electrodes of RF signals are not identical. When the regions of two electrodes differ slightly, one electrode is inadvertently biased to the positive versus the other electrode. Because one electrode is frequently grounded, it has a bigger size than the other due to the addition of the chamber wall's area. As in DC-PECVD, anode and cathode electrodes are used in RF-PECVD. Of course, applying an external voltage can be used to regulate the bias voltage (Matsumura et al. 2019).

PECVD process can be used to modify the surface properties such as the material hardness, fatigue, adhesion, friction, corrosion, resistivity, oxidation, and the dielectric properties (Fridman 2008).

Advantages and disadvantages of PECVD

As a summery and conclusion of the advantages of PECVD process (Pantoja-Suárez 2019):

1- It is able to achieve low temperature reactions that can't be achieved with the thermal CVD process.
2- Reducing the mismatch between the substrate and the thin film compared to thermal CVD
3- The rate controlling factor is surface kinetics, which leads to greater uniformity.
4- The possibility of forming amorphous or polycrystalline deposits that has superior characteristics.
5- The possibility to use organic and inorganic precursors.
6- It doesn't depend strongly on the substrate geometry and composition.

There are also some drawbacks such as:

1- Getting a pure material deposit is not easy. Desorption of byproducts and other gases, notably hydrogen, is almost retained as part of the deposit.
2- PECVD produces unfavorable compressive stresses in the deposit, especially at lower frequencies. This problem can be obvious in the thick films like metallurgical applications, as they carry peeling and breaking.
3- Depending on the precursor gases, toxic, explosive, and/or extremely corrosive gases may be created.

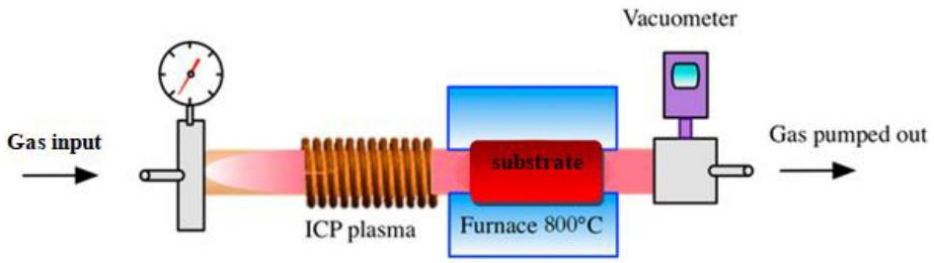

Figure 3.13. Schematic image of ICP-CVD system (Wu et al. 2017).

Inductively coupled plasma CVD (ICP-CVD)

The Inductively coupled plasma (ICP), is a high density plasma operates at a relatively low pressure (10 *Pa*). Plasma can be obtained inside a chamber, which is surrounded by an inductive coil antenna (Figure 3.13). The system can work in two geometries, planar and geometrical. The plasna one uses a coil antenna of a flat metal wound in spiral, which works as electrode. In the cylindrical one, the antenna is shaped like a helical spring. It is different from the capacitely coupled (CCP) plasma mode as the CCP is produced by two parallel plane electrodes seperated by a distance (Avetisyan 2019).

CCP has a higher operating pressure, higher electron density, and lower electron energy as compared to the ICP. Langmuir probe measurements showed that the electron density ranges between 10^9 to 10^{10} m^{-3} for the CCP and 10^{10} to 10^{12} cm^{-3} for microwave and ICP plasmas (Hopwood et al. 1998; Lieberman and Lichtenberg 2005). The plasma obtained from this technique can be combined with high temperature for ICP-CVD process in order to form crystalline materials as we will see in the following chapters.

3.5. Reactors and set-ups of material synthesis

During the work that has been achieved in this thesis, three reactors were used. Carbon nanotubes (CNTs) were prepared in two reactors; one for the synthesis of the vertically aligned CNTs (VACNTs) on a substrate using the plasma enhanced chemical vapor deposition (PECVD) process and the other is a tubular reactor for the synthesis of CNTs without substrate using the floating catalyst chemical vapor deposition (FC-CVD) process. The third one is also a tubular reactor was used for the synthesis of graphene nanowalls (GNWs) to obtain the hybrid structure of CNTs-GNWs using the inductively coupled plasma chemical vapor deposition (ICP-CVD) and

was used as well for plasma functionalization. In addition to these reactors, a plasma-liquid set-up was used to produce metal oxide nanoparticles out of metal foils.

3.5.1 Carbon nanotubes reactor of VACNTs

This reactor is a 304 stainless steel cylindrical chamber which is able to reach a high vacuum ($5x10^{-5}$ *Pa*). The main purpose of this reactor is to synthesize VACNTs in two processes (steps) without breaking the vacuum which leads to avoiding any oxidation could happen to the samples during preparation. These two steps are the sputtering and the PECVD. The reactor as shown in figure (3.14.) consists of four heads; three are used for sputtering where it allows to fix one target on each in addition to the fourth head which is used for the PECVD process. The system is automated and controlled by a computer using a LabVIEW interface allows controlling the process conditions.

The system consists of a three-pumps vacuum system, different vacuum gauges (pressure sensors), mass flow controllers, manual and automatic gates, sample-loading system, pyrometer, heating system, and RF-power supply.

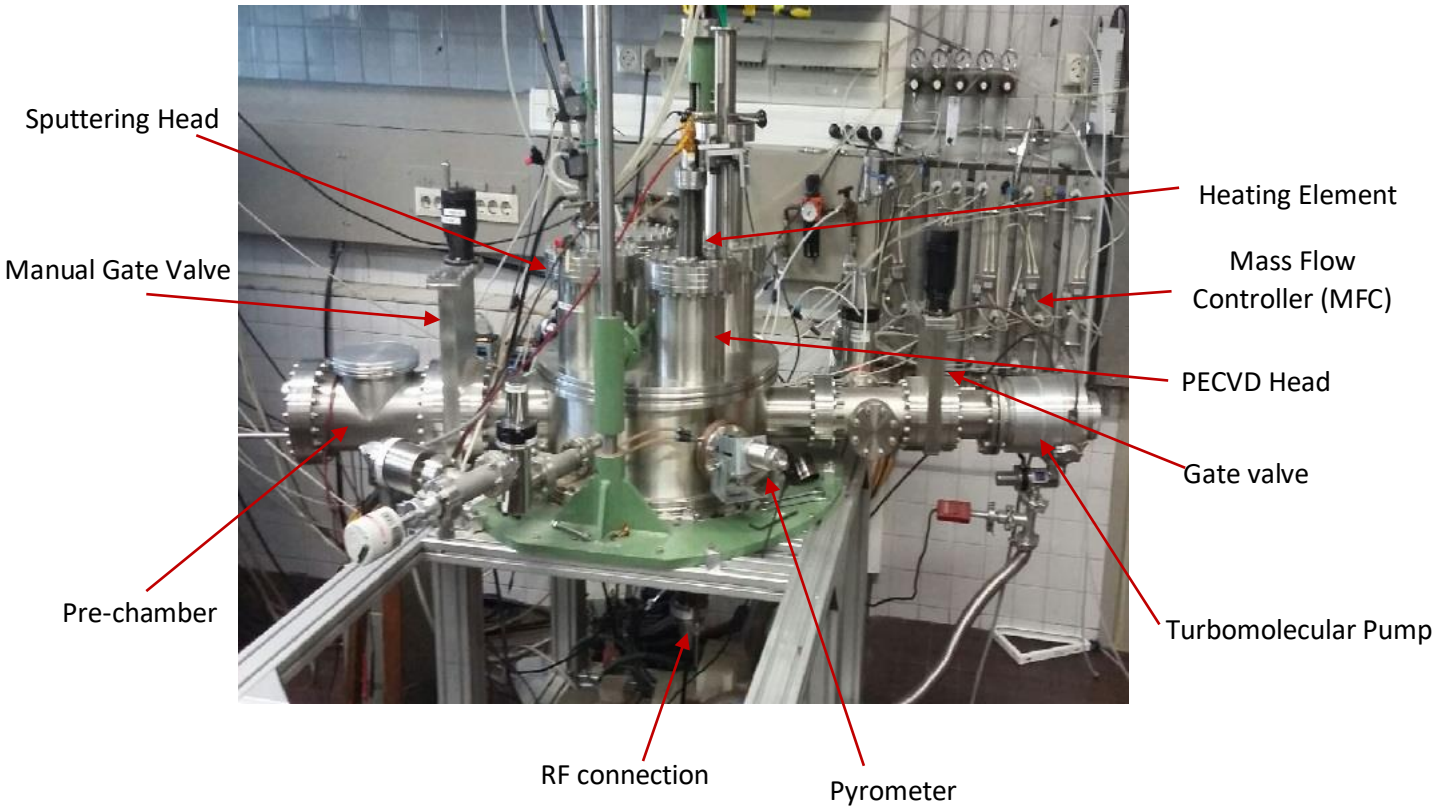

Figure 3.14. Vertically aligned carbon nanotubes (VACNTs) reactor set-up.

The vacuum system consists of three different models of pumps. Each one is used to maintain a specific level of vacuum depending on our need. In general, to obtain a vacuum in the reactor when the vacuum is broken can be done using the three models in three steps:

1- LEYBOLD TRIVAC rotary pump is a mechanical pump used to reach a pressure up to 10 *Pa* when starting from the atmospheric pressure. The pressure value that the rotary pump can reach depends on the size of the pump and the volume of the chamber (Figure 3.15).

2- Rotary pump which is used to reduce the pressure from 10 *Pa* to 0.5 *Pa*. It consists of two counter-rotating interconnected rotors spinning in opposite directions in a high momentum. This pump can't be used for high pressures, e.g. atmospheric pressure, to avoid heating the internal parts which will lead to break it (Figure 3.16-a).

3- LEYBOLD TMP360C turbomolecular pump which is used to obtain a very high vacuum which can reach in our case a pressure $5x10^{-5}$ Pa. its working principle depends on the high momentum of many rotors as shown in figure (3.16-b). We could use the turbomolecular pump to maintain a specific pressure inside the chamber. The pressure value depends on both; the size of the pump and the chamber volume. We have studied the relation between the *Ar* gas flow with the corresponding pressure when only using the turbomolecular pump (Figure 3.17).

a)

b)

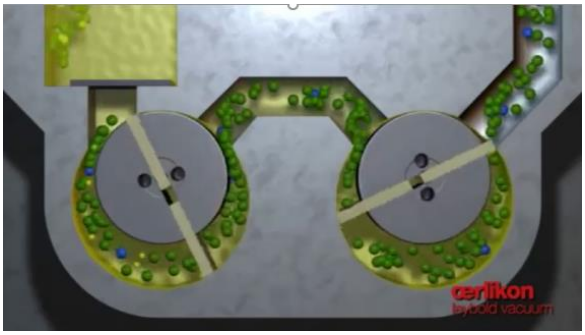

Figure 3.15. a) Outer shape of the rotary pump and b) a scheme of its working principle (Gaines 2019).

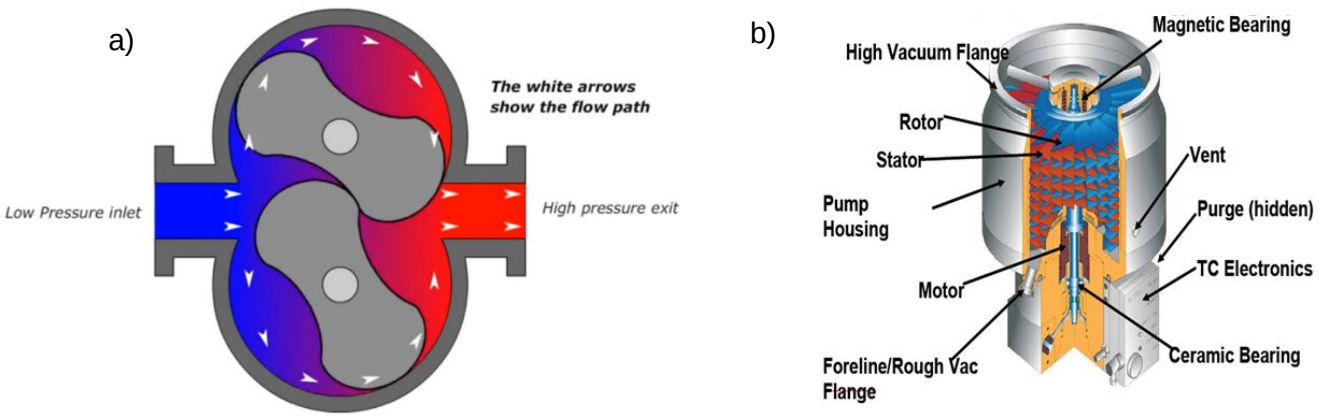

Figure 3.16. a) Scheme of the working principle of the roots pump (mekanizmalar 2012) and b) Scheme of the internal parts of the turbomolecular pump (Gaines 2019).

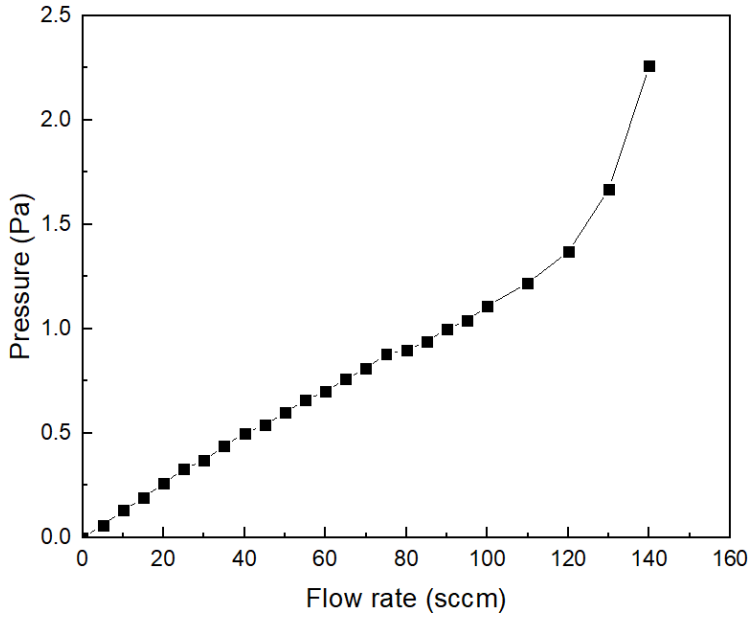

Figure 3.17. Relationship between the flow rate of Ar gas with the pressure inside the reactor when using the turbomolecular pump for evacuation.

To measure the pressure inside the reactor we use three main sensors (Gauges):

1- Thermal conductivity gauge (Pirani):

The working principle of Pirani gauge depends on the thermal conductivity of the gas. Normally it is calibrated for N_2 but we use it for air in general and for a range starting from the atmospheric pressure to 1 *Pa.* The filament represents an arm in Wheatstone bridge. The heating voltage which is applied to the bridge controlled in a way to keep the filament resistance and therefore its temperature constant. The heat transfer will increase by increasing the pressure which means increase in the voltage reading across the bridge. Therefore, this change of voltage reading is translated to a change of pressure (Figure 3.18).

a)

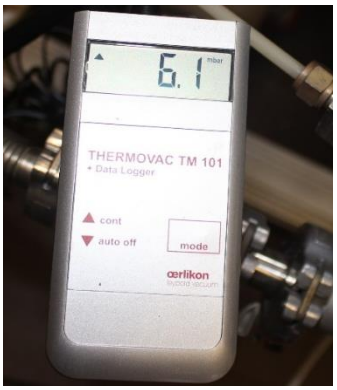

b)

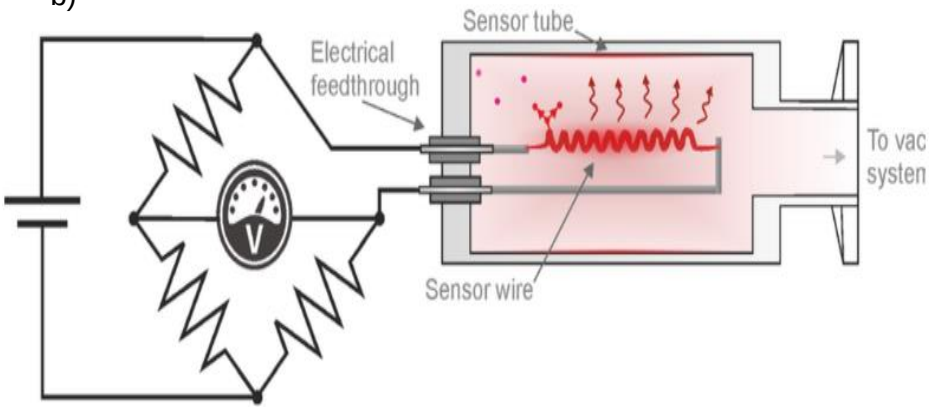

Figure 3.18. a) Picture of the thermal conductivity gauge in our lab and b) a scheme of its working principle (Sens 2021).

2- Cold Cathode Ionization Vacuum Gauge (Penning)

The penning gauge measures the pressure through a gas discharge within a gauge head where the ignition of gas discharge is done by applying a high tension. The resulting ion current is output signal that is proportional to the pressure. The gas discharge is maintained at low pressures with the help of a magnet. We use this sensor for measuring pressure in high vacuum.

3- Capacitance Vacuum Gauge

The pressure sensitive diaphragm of the capacitive gauge is made of Al_2O_3. The “capacitive” term corresponds to the plates of a capacitor. The distance between these two plates changes

according to the pressure which means change in the capacitance. The resultant electrical measurement signal is converted to a proportional value of pressure (Collon 2008).

Mass flow controller

Mass flow controller is a device combines both mass flow sensing and control of gas flow. The MFCs are designed and calibrated to control a specific gas in a limited range of flow rates. MFC consists of a mass flow meter (MFM), feedback controller, and control valve.

MFMs and MFCs depend on the thermodynamic principles. The MFC may consist either two or three wires. In the three-wire sensor, the MFM uses a resistance wire of high temperature coefficient to measure the temperature difference across a heater ($\Delta T = T_2 - T_1$) (Figure 3.19). The temperature difference is proportional to the mass flow rate according the relationship:

$$\Delta T = (\alpha . P_w) \,/\, (\frac{\Delta m}{\Delta t} . C_p) \tag{3.28}$$

where P_w is the heater power setting, C_p is the heat capacity of the gas, α is a proportionality constant and $\frac{\Delta m}{\Delta t}$ is the mass flow rate. The two-wire sensor is the common one where it depends on a resistance wire with a high temperature coefficient to be used as a sensor and heater (Figure 3.19).

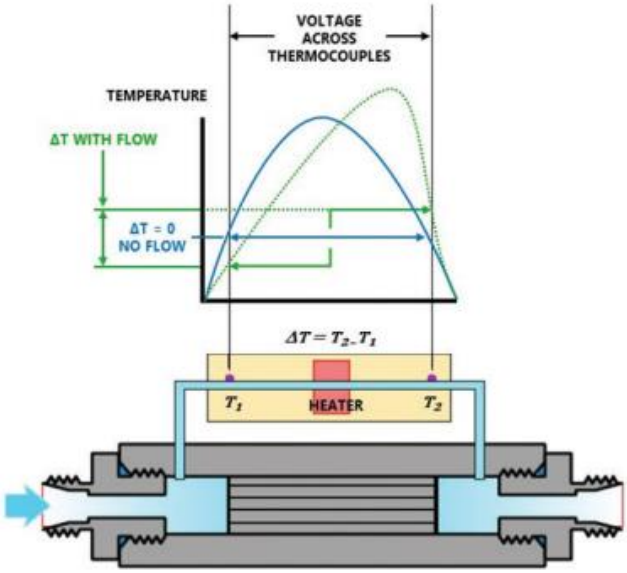

Figure 3.19. Basic Principles of thermal MFM measurements (MKS 2021).

Pre-chamber

The prechamber is one of the main parts of our reactor. It is shown on the left side of figure 3.15. It contains the lock-system which we use to introduce the sample inside the chamber or taking it out which can be done with connecting an arm with the sample holder as seen in figure (3.20). On the other side, we use the pre-chamber to obtain a good vacuum inside before introducing the sample inside the main chamber to reduce the waiting time for obtaining high vacuum before starting any process.

a)

b)

Figure 3.20. a) Front view of the sample holder showing the locking position and b) the arm that we use to lock the sample holder.

Pyrometer and heating system

The heating element in our reactor is a graphite resistance of 1.79Ω which is lowered to be on top of the sample with a distance of ≈15 cm (Figure 3.21 a). in order to measure the temperature on our sample, we use a pyrometer (CALEX TL-TG-13) which can measure the temperatures between 300C and 1300 C. It measures the surface temperature of an object by sensing the heating/infrared radiation emitted from the object. the temperature is controlled using a feedback circuit which allows to maintain the required temperature of the even the temperature increasing rate.

a) 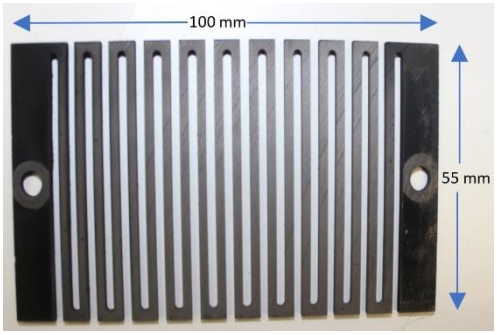

b) 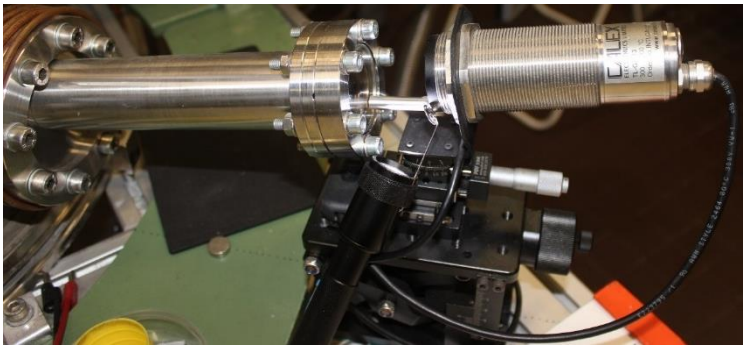

Figure 3.21. a) The graphite resistance we use for heating purpose and b) the pyrometer we use to measure the temperature on the sample surface.

RF power supply (matching box)

The power supply we used during our experiments is a radio frequency (RF) connected with a matching network. The purpose of the matching box connected with the RF-power supply is to maximize the transferred power and minimize the back reflected power. The matching network usually as shown in the figure (3.22a). It consists of a coil and two variable capacitors (Figure 3.22b). To transfer the power from the RF generator to the reactor, it will pass through a first coaxial cable, matching box and the second coaxial cable. The cables have a characteristic impedance of 50 ohms, while the plasma reactors are far from the 50 ohms. The idea is to moderate the impedance (the total impedance of the circuit with the cable and the plasma reactor) to be 50 ohms with 0 phase corresponding to the incoming signal from the RF generator. This can be done by changing the capacitance of the two capacitors as shown in figure (3.22b). This can be adjusted manually or automatically depending on the device.

When an RF electric field is applied to the vacuum chamber, the electrons will be driven back and forth and hit the powered electrode at each RF half cycle. A blocking capacitor available in the tuning network acts as a conductor for the RF field and as an insulator for a self-induced field. The hitting of electrons on the powered electrode allows building up in addition to the AC field a negative DC field which is called DC self-bias (Figure 3.23). The value of the bias DC depends on many factors such as ratio between the cathode and anode surface area and the pressure and type of the gas (Palomar 2021).

a)

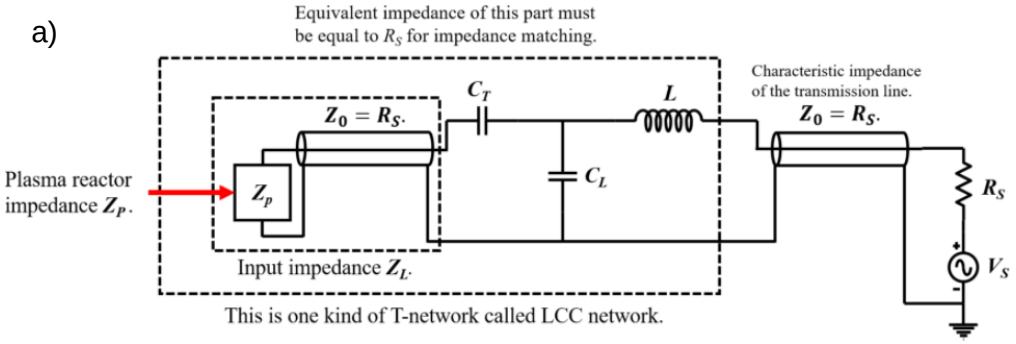

b)

Figure 3.22. a) Matching network to moderate the RF impedance and b) top view of a matching box showing its internal parts (iTecTec 2021).

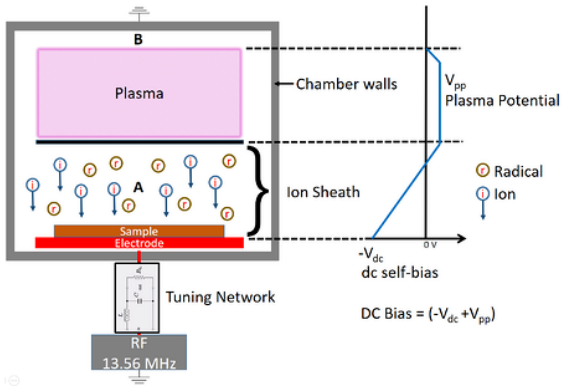

Figure 3.23. a scheme showing the principle of the DC self-bias (Palomar 2021).

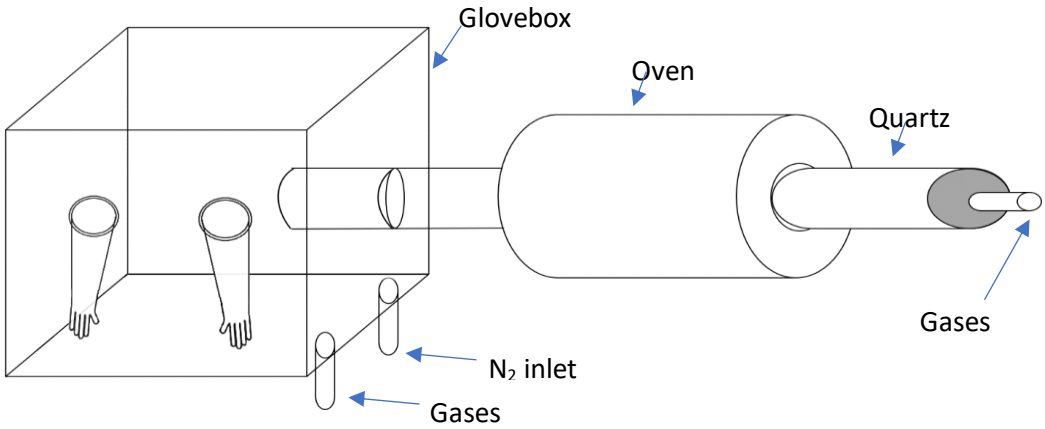

Figure 3.24. Scheme shows the main parts of the FC-CVD reactor connected with a glovebox.

3.5.2. Reactor of free-substrate CNTs

This reactor is a tubular reactor connected from one side with the gas lines and the other side is inserted in a glovebox (Figure 3.24). This reactor is used to achieve floating catalyst CVD (FC-CVD) process. The glovebox contains an inlet hole connected with N_2 gas line to keep the pressure value close to the atmospheric pressure to allow using the gloves to be able to extract the synthesized material from the quartz tube. There is another hole in the glovebox which is connected to a rotary pump to be used as an outlet to remove the residual gases from the glovebox. The flow of all gases is controlled by mass flow controller (MFC).

3.5.3. Graphene Nanowalls reactor

It is a tubular furnace reactor works as well at low pressure using the inductively coupled plasma CVD (ICP-CVD). The reactor consists mainly of a quartz tube, a double shell tubular oven with the ability to heat up to 1100 ^{0}C, a coil, RF power supply, and two vacuum pumps; rotary and turbomolecular (Figure 3.25).

When the RF power (13.56 *MHz*) is applied to the coil, the plasma will be generated in the chamber. The coil inductance obeys the following relationship:

$$L_{coil} \approx N^2 \mu_0 \mu_r (\frac{D}{2}) \left[\ln\left(\frac{8D}{d}\right) - 2\right] \quad (3.29)$$

Where L_{coil} is the conductance of the coili in Henry (*H*), N is the turns number, μ_0 is the permeability of free space ($4\pi \times 10^{-7}\ H/m$), μ_r is the relative permeability, D is the loops diameter, and d is the wire diameter.

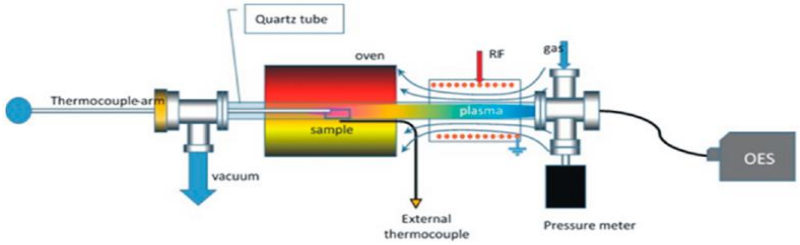

Figure 3.25. Scheme shows the main parts of the ICP-CVD reactor (Amade et al. 2019).

3.5.4. Metal Oxide nanoparticles set-up

Hybrid plasma-liquid methods represent an emerging class of synthesis techniques that have attracted great interest due to their simplicity and ability to produce, rapidly and relatively cheap,

a wide variety of materials, such as metallic, semiconductor, bimetallic and colloidal metal oxide nanoparticles from simple

and environmentally friendly precursors. The set-up is very simple as it contains high-voltage power supply, flow mass controller, and a thin tube of Ni (Figure 3.26).

Figure 3.26. scheme shows the main parts of the plasma-liquid interaction process.

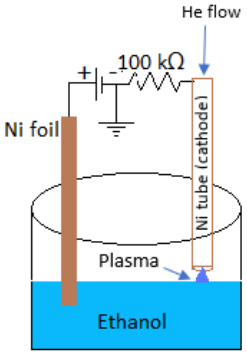

Chapter 4

CNTs growth on highly flexible Papyex® substrate

4.1. Introduction

Carbon nanostructures form a large set of varied morphologies related with the also a wide range of possibilities provided by chemical vapour deposition activated by low pressure plasma. Descriptions of novel carbon structures and morphologies have appeared for more than three decades, during which several experiments for the synthesis of carbon nanostructures have been suggested. The main structures that have been investigated are such as micro and nanostructured diamond, diamond like carbon (DLC), amorphous carbon (a-C) and hydrogenated amorphous carbon (a-C:H), carbon nanotubes (CNT) and carbon nanowires, carbon nanoparticles, graphene nanostructures e.g. single layer (SLG) or few layers graphene (FLG) (Sullivan et al. 2000; Robertson 2002; Paillet et al. 2018).

This broad family of carbon allotropes can be distinguished by the extreme hardness, ultra-low friction, anti-wear, chemical protection, biocompatibility, low surface energy, extremely high specific surface, emission via field effect, luminescence, and extreme electronic characteristics such as high and low gap energy, extreme electronic mobility and very high current density (Falcao and Wudl 2007).

Carbon nanostructures are used in a variety of sectors, including energy, chemistry and electrochemistry for catalysts, protective materials for metal tools and polymers, electrodes for super capacitors and batteries, sensors, and high power electric and electronic devices. The carbon structures are also used in the field of light emitting and other optoelectronic devices, where doped carbon-based amorphous films, such as a-C:H and a-C:N:H films, which exhibit remarkable performance as good light emitting sources (Robertson 2006).

There are different techniques are used to obtain the carbon materials. The technique we will consider during this chapter and the following chapters is the CVD and its related techniques. MWCNT growth through CVD is a promising (Kumar and Ando 2010) method that provides for fine control over length, diameter, and placement. Plasma enhanced chemical vapor deposition

(PECVD) (Hofmann et al. 2003) in particular is an effective approach for growing vertically aligned carbon nanotubes (VACNTs), which are suitable for a wide range of applications.

The inertness of CNT surfaces and their limited solubility in solvents are significant barriers in real-world applications (Han et al. 2009b; Gil Min et al. 2020). As a result, it is valuable to be able to functionalize the surface of CNTs by including diverse chemical groups. CNTs may be functionalized using a variety of methods, including air oxidation, light oxidation (Kalbacova et al. 2021), ozone oxidation (Lebrón-Colón et al. 2011), and electrowetting (Han et al. 2009a).

Furthermore, it has been demonstrated that treating CNTs with certain acids (e. g., refluxing in HNO3 or H2SO4) opens nanotube tips and introduces oxygen-containing groups (Datsyuk et al. 2008). The primary goal of the oxidative treatment is to remove metallic catalyst particles utilized in the production of nanotubes as well as amorphous carbon formed as a byproduct of the synthesis.

The majority of treatment approaches include long-time processes with a relatively low yield of pure nanotubes (Sun et al. 2002). It is preferable if the treatment is surface-exclusive in order to retain the bulk qualities. The plasma approach is an efficient, quick, and adaptable technology with minimal impacts on the surface and neighboring regions of CNTs that can be easily modified through intensity (Abbas et al. 2007). The plasma's excited species, radicals, electrons, ions, and UV radiation interact intensely with the surface of CNTs, breaking the C=C bond and forming active sites where chemical groups are linked. A broad range of functional groups may be injected into the plasma depending on plasma parameters such as power, pressure, gas mixture, and treatment duration.

4.2. Growth mechanism of VACNTs

CNTs production was carried out on a flexible and conductive Papyex® graphite paper by PECVD process (Figure 4.1.). The base pressure of the chamber was reduced to a value of $2x10^{-4}$ Pa in order to prevent any contamination during the process. The first step was the deposition of the catalyst thin film which is considered as the guidance for the nanotubes growth. The Fe deposition was calibrated using 2 Pa of Ar using a flow of 136 sccm by RF-magnetron sputtering using a power of 60 W. For the calibration, we deposited the Fe thin film for 30 minutes on a patterned glass. The thickness of the obtained thin film was later checked used the confocal

microscope as shown in figure 4.2. As the resolution of the confocal is too low, we double checked the thickness of the obtained film using a profilometer as we obtained the same result. The deposition rate using the parameters mentioned above is 0.032 nm/s. The methodology we followed to grow the CNTs after the deposition of the thin film is illustrated in figure 4.3. The thin film is heated gradually in order to obtain nano islands of Fe, which will represent the seed of the CNTs under pressure 2 mbar and flow rate 100 sccm of H_2 to avoid the oxidation of any residual oxygen inside the chamber. Once we reach to a specific temperature, we fix the temperature for 2 minutes before we start the plasma for the CNTs growth. Then, the CNTs can grow using the plasma of NH_3 (50sccm) and C_2H_2 (100 sccm) under a total pressure of 1 mbar and an RF power of 50 W. in order to optimize the growth process, we optimized three parameters: Fe thickness, temperature, and the PECVD time. Firstly, we used a range of Fe thickness between 0.5 nm and 3 nm by fixing the temperature at 680°C and the PECVD time to 900 s.

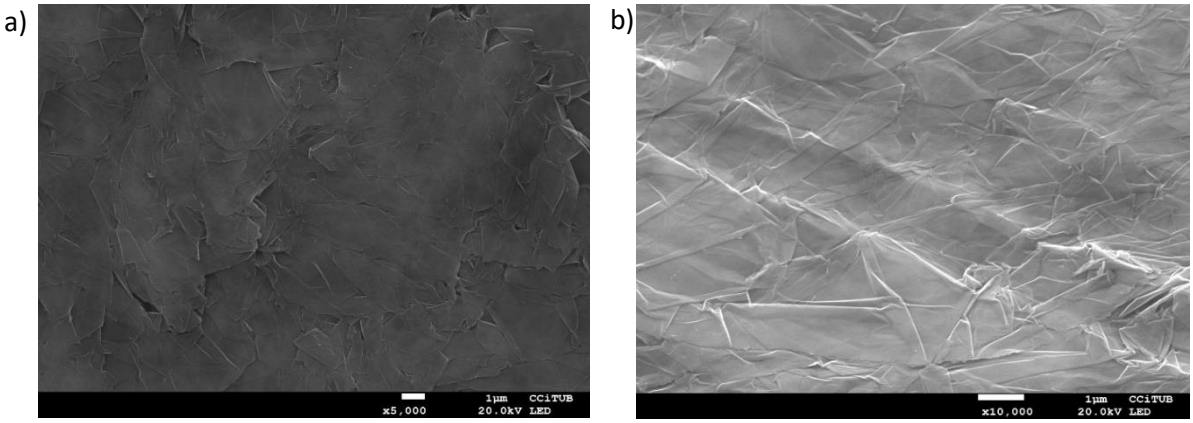

Figure 4.1. SEM images of Papyex® graphite paper as received.

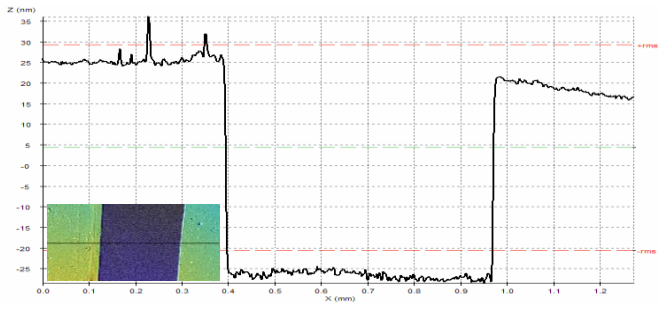

Figure 4.2. A topography image obtained by the confocal microscope to measure the thickness of Fe thin film.

The optimum result was using Fe thickness of 2.5 nm as it resulted the higher density and longer CNTs (Figure 4.4). Then we fixed the Fe thickness at 2.5 nm and the growth time at 900 s and applied different temperatures range from 600°C to 750°C (Figure 4.5).

The optimum temperature we obtained was by using 700°C. The final parameter we changed is the PECVD time where we used a time range between 300 s and 1200 s (Figure 4.6). As a result, we obtained the optimum parameters using 900 s of PECVD time, 700°C, and using 2.5 nm of Fe thin film thickness (Figure 4.7).

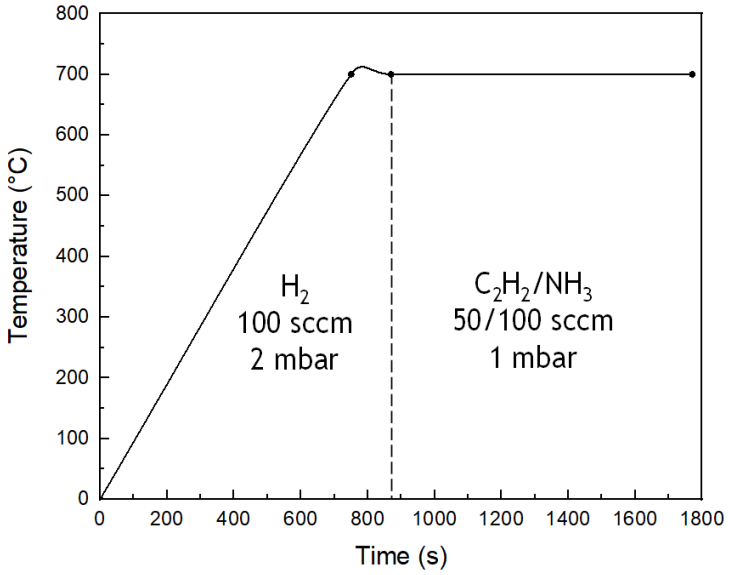

Figure 4.3. A chart illustrating the parameters used for the growth of CNTs on a graphite paper.

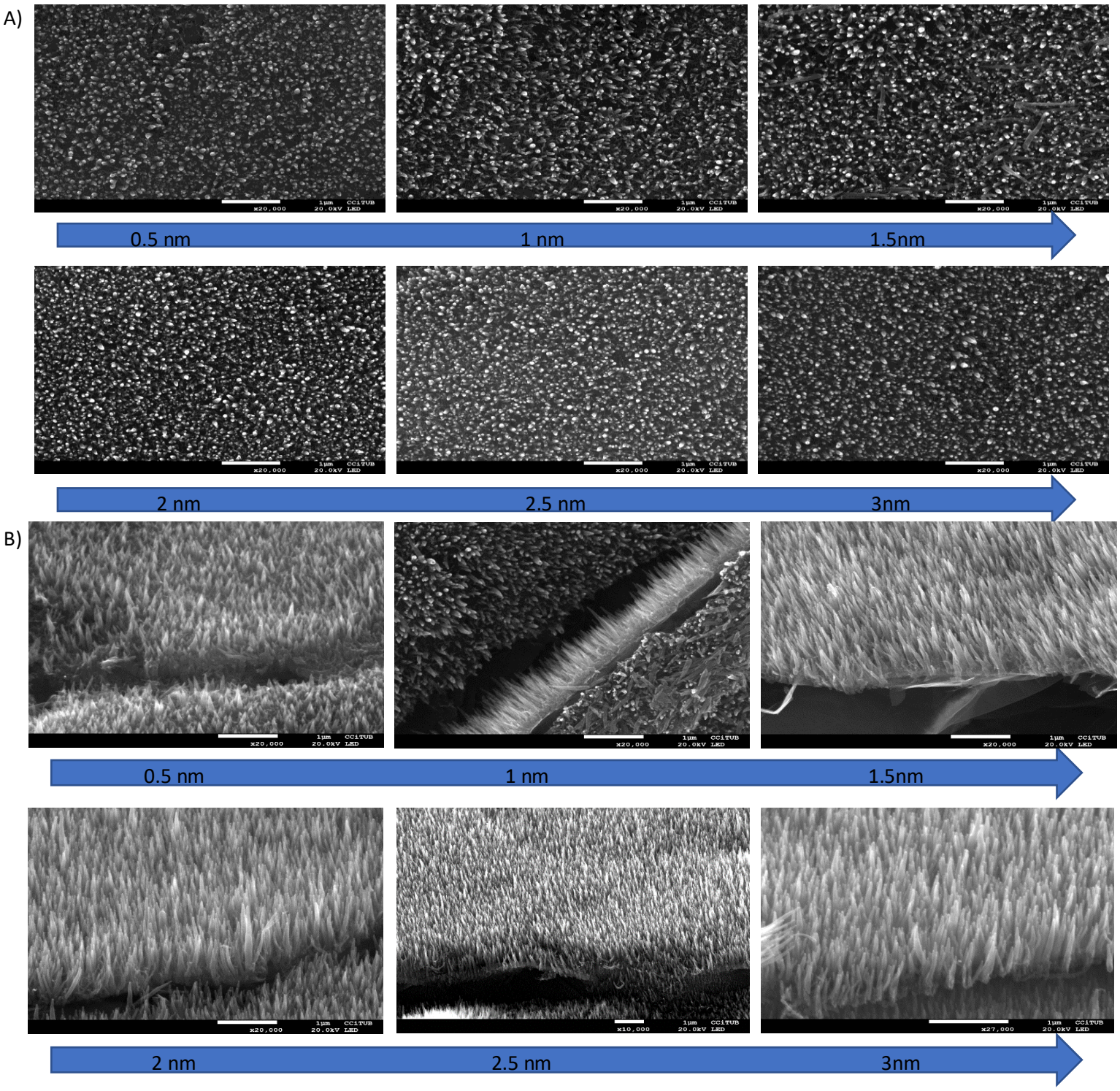

Figure 4.4. SEM images of VACNTs using different Fe thin film thicknesses. A) Top view and B) side view.

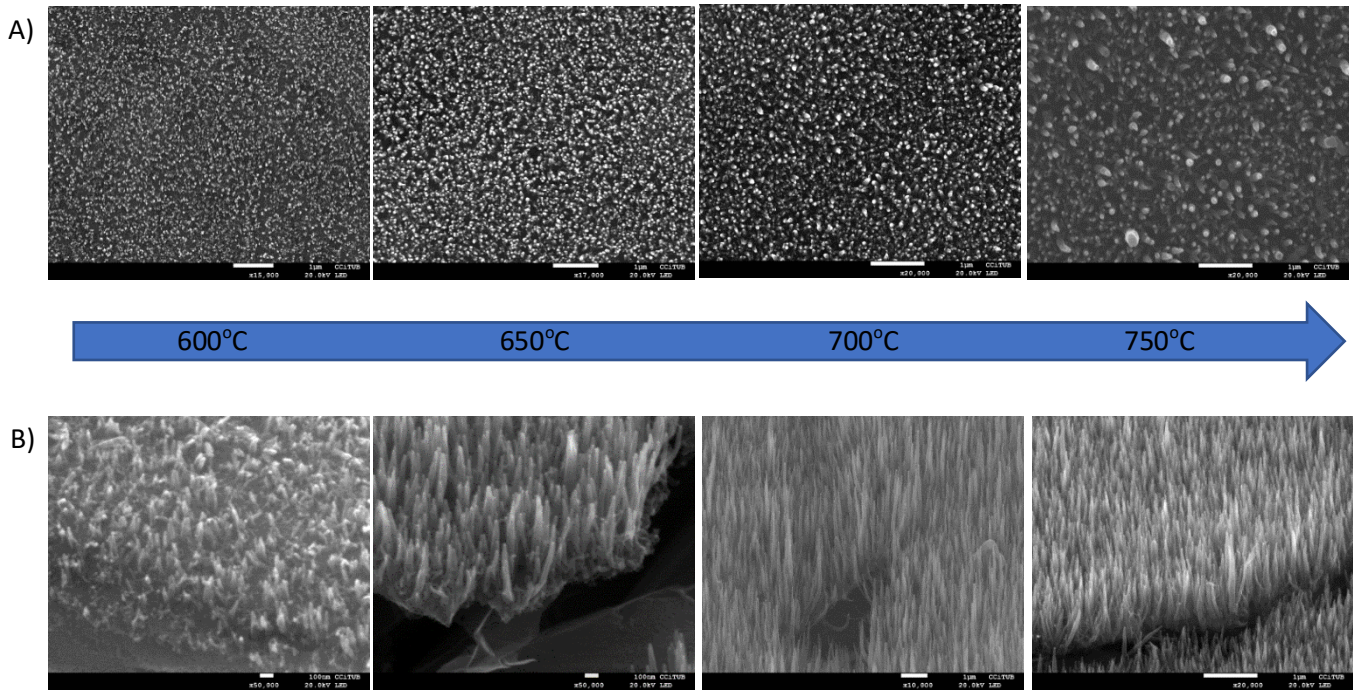

Figure 4.5. SEM images of VACNTs using different PECVD temperatures. A) Top view and B) side view.

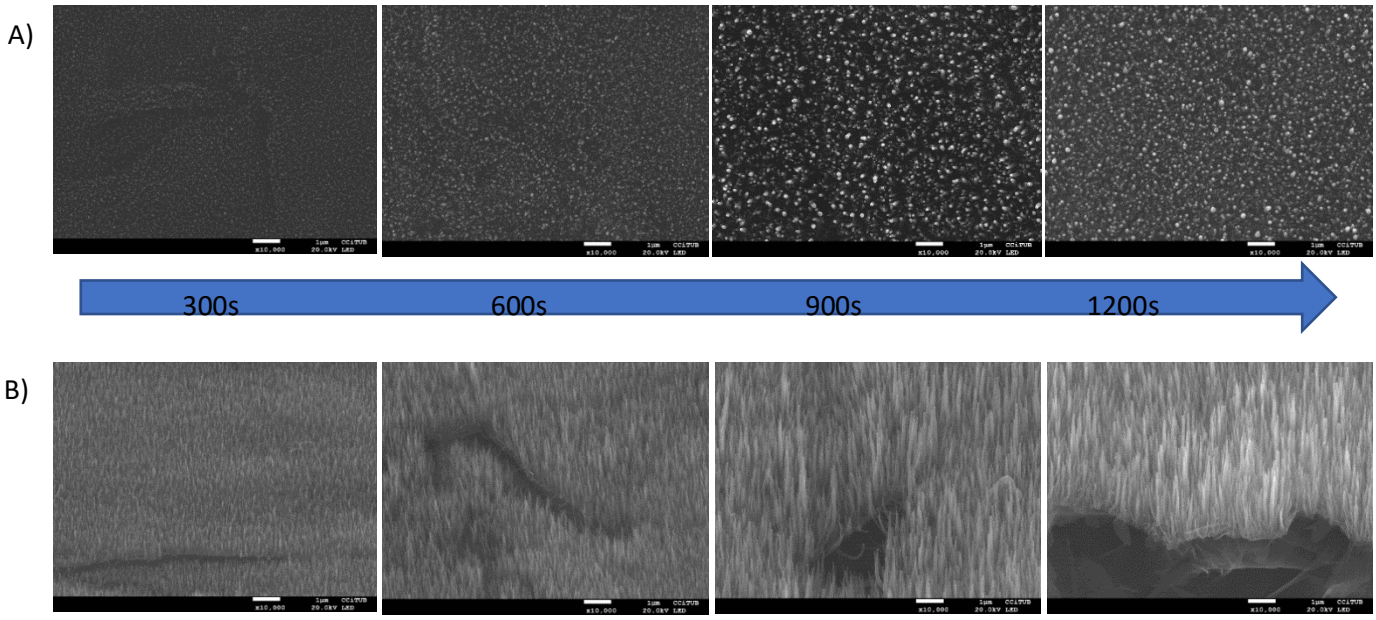

Figure 4.6. SEM images of VACNTs using different PECVD times. A) Top view and B) side view.

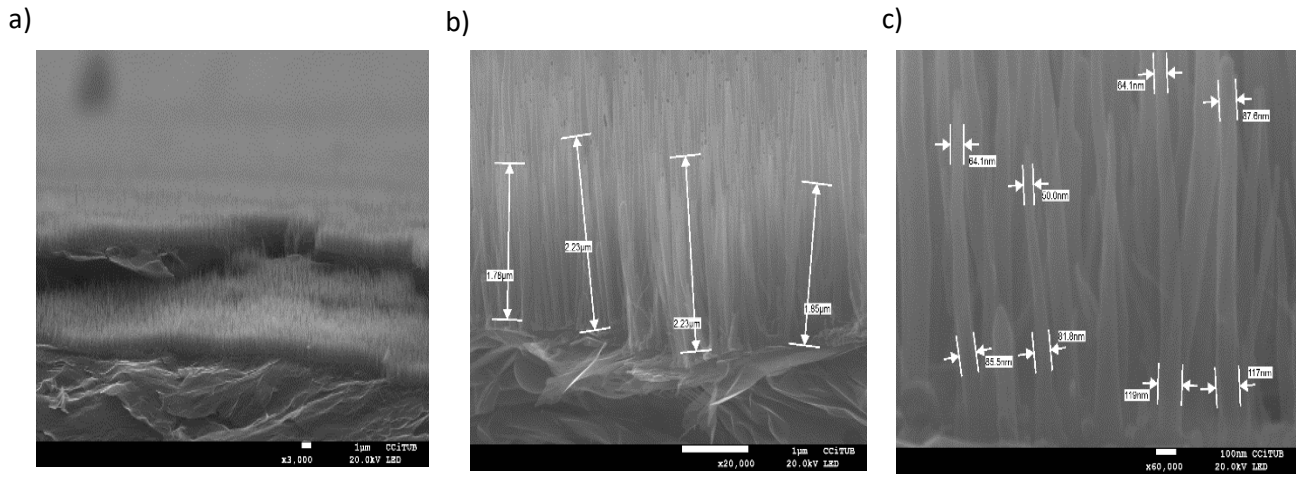

Figure 4.7. SEM images show the morphology of CNTS. a) side view of the sample, b) showing the length of CNTs, and c) showing the diameter.

The importance of the NH_3, or any rich hydrogen gas, is to obstruct the formation of amorphous carbon that results during the dissociation of C_2H_2 molecules, which will start to accumulate on the grown nanotubes causing the poisoning of the catalyst particles resulting in short nanotubes combined with a non-crystalline carbon (Figure 4.8.). Because of the relative weakness of its molecular bonds, NH_3 decomposes preferentially before C_2H_2 at high NH_3 ratios. This slows the decomposition of the C_2H_2, resulting in the regulated quantities of carbon required for nanotube synthesis and the development of clean, well-aligned carbon nanotubes. At high C_2H_2 ratios, there is insufficient NH_3 to adequately inhibit C_2H_2 breakdown, resulting in increased carbon production and amorphous carbon deposition on the substrate. Through the formation of reactive atomic hydrogen, NH_3 plays an important function in eliminating any excess of carbon (Bell et al. 2007).

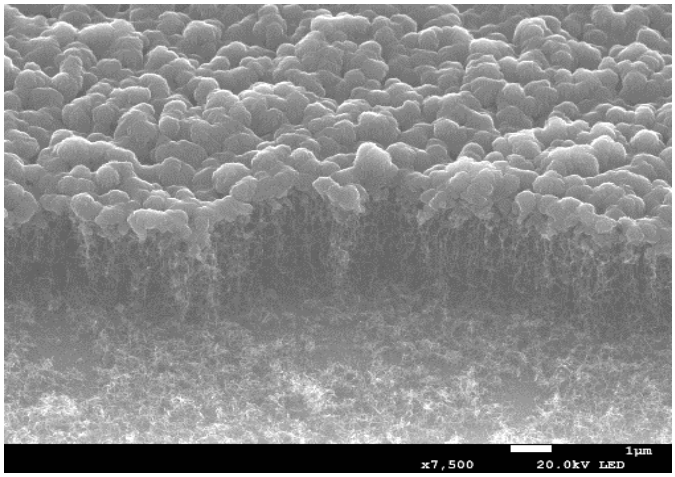

Figure 4.8. CNTs combined with amorphous carbon obtained after not using NH_3.

It is very important to keep the substrate surface very clean where the dust or any contamination can easily act as a barrier, which prevents the deposition of the catalyst particles on the substrate on some spots. Figure 4.9. shows a SEM image of CNTs obtained by (water assisted) WACVD where it is very clear the hole of 100 µm of diameter inside the forest of nanotubes, owing to a surface contamination of the substrate (probably a dry drop of some contaminant).

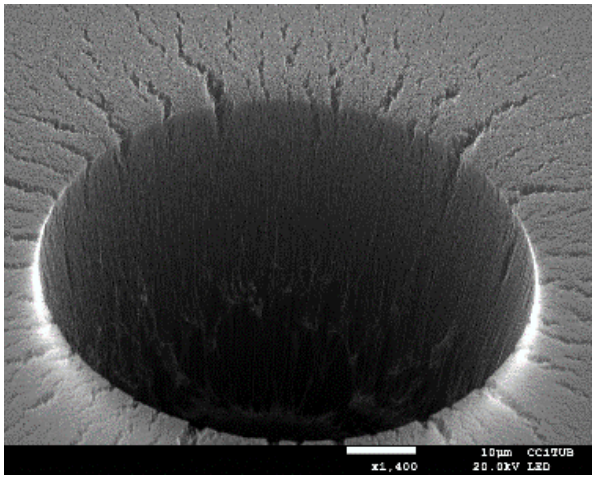

Figure 4.9. SEM image of CNTs obtained by WACVD process shows the effect of contaminant of the substrate surface.

The VLS description published by Baker et al. (Baker et al. 1982) for carbon filament growth is widely believed to be relevant to carbon nanotube growth, at least when metal catalyst particles are used. HRTEM was used to confirm the tubular structure of the CNTs. The nanotubes with

catalyst on their top surface are shown in Figure 4.10-a. The side walls of CNTs include amorphous carbon, which is often a byproduct of the PECVD development process. The elongated catalyst particle at the tip of the CNT (Figure 4.10-b) clearly demonstrates the tip growth process. The arrows inside the nanotube show the graphene layers at various distances inside the nanotube. This structure is defined by the bamboo-like form of the CNTs as opposed to the hollow cylindrical shape in which the nanotube inside is void.

A bamboo-shaped nanotube is made up of regular cone shaped compartment. The periodic precipitation of graphite sheets on the top of the catalyst particle causes compartment creation in the bamboo-like structure. Because its bonds are weaker than those of H_2, NH_3 is easily dissociated. The discovery of bamboo-structures in nitrogen-containing plasma and hollow tubes

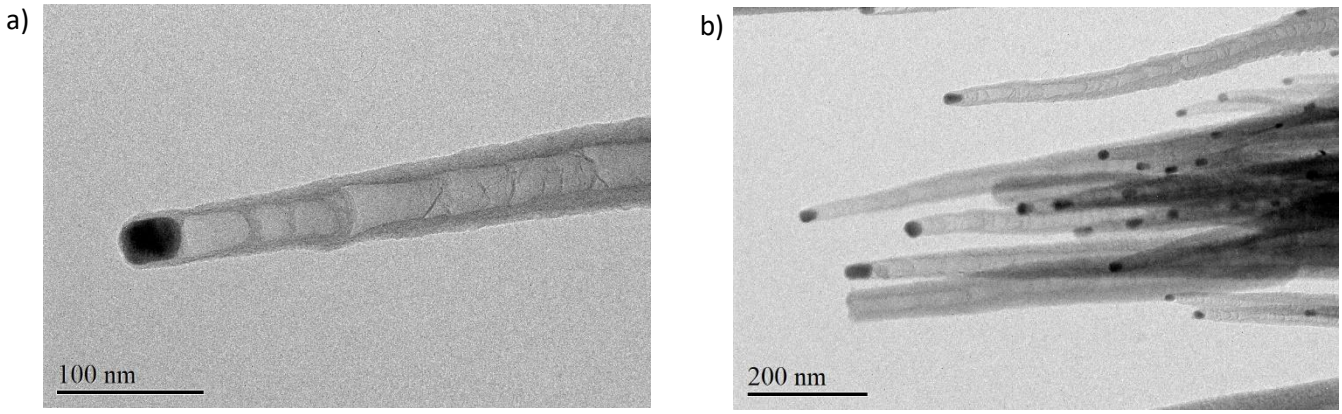

Figure 4.10. HRTEM images of CNTs grown on Papyex® graphite paper.

in nitrogen-free plasma by Martin S. Bell et al. (Bell et al. 2007) shows that nitrogen or CN (carbon-to-nitrogen ratio) played a crucial role in the compartment formation. They discovered that CN is essential in the creation of bamboo-like structures. Furthermore, CNTs are thought to develop by surface (SD) and/or bulk diffusion (BD) of carbon species through catalyst particles. High CN concentrations facilitated BD of carbon via Fe particles while suppressing SD by maintaining the catalyst surface clean (Bell et al. 2007).

There's also the potential of CN diffusion through the Fe particles (Bell et al. 2006). However, because CN or N have extremely limited solubility in Fe, the concentration of N or CN in Fe is expected to be much lower than that of carbon. The size of the catalyst particle limits the growth tube's outer diameter. The local geometry of the catalyst particle stimulating the tube's

development controls the shape of the tip (Srivastava et al. 2006). Nanotube fabrication necessitates the controlled deposition of carbon, which may then self-assemble into an energetically favorable nanotube shape. This regulated deposition rate is achieved by combining two reactions: dissociation of a carbon-rich gas (in our example, C_2H_2) and elimination of excess carbon, which would otherwise result in amorphous carbon deposits.

Functionalization of CNTs

CNTs have two distinct reactive zones: the fullerene-like tube ends and the less reactive hexagonal cylindrical tube walls. Because of their significant curvature, the carbon bonds at the tips are under more strain and provide a region of elevated reactivity and lower activation energy for oxidation processes; hence, oxidation is predicted to begin at the tips rather than the cylindrical walls (Hussain et al. 2015).

The O_2 plasma process was utilized to remove amorphous carbon and Fe particles, as well as to functionalize the surface of CNTs by adding different oxygen functional groups such as carboxyl and hydroxyl groups, which increase the hydrophilicity of the nanotubes. These functional groups on the side walls of CNTs are advantageous for contributing faradaic capacitance to the overall capacitance of the supercapacitor in aqueous solution. Nonaqueous solutions, on the other hand, are unsuitable because they quickly breakdown at 1.2 V and emit some gases (Yu et al. 2013).

Other researchers have employed H_2O gas or Ar/H_2O gas mixture in earlier studies (Chen et al. 2009, 2010). The oxygen plasma interacts chemically and physically with the nanotubes through a strong protonic bombardment, whereas an argon mixture includes physical effects (sputtering) while reducing the chemical effects. Furthermore, rather than microwave power, we employed radio frequency (RF) power to ignite the plasma, as described in the majority of Ar/O_2 plasma studies (Chen et al. 2009, 2010). At relatively low power densities (0.5 $W \cdot cm^{-2}$) RF plasma (Abbas et al. 2007) looks remarkably steady and uniform across a broad region.

In this work, the O_2 plasma was applied using a flow rate 100 sccm of O_2 gas at 0.5 mbar, and an RF power of 70 W. we functionalized the nanotubes using two different period of time 30 s and 60 s (Figure 4.11). We have observed that the CNTs were shortened after 60 s of O_2 plasma as the plasma started to etch them (Hussain et al. 2013).

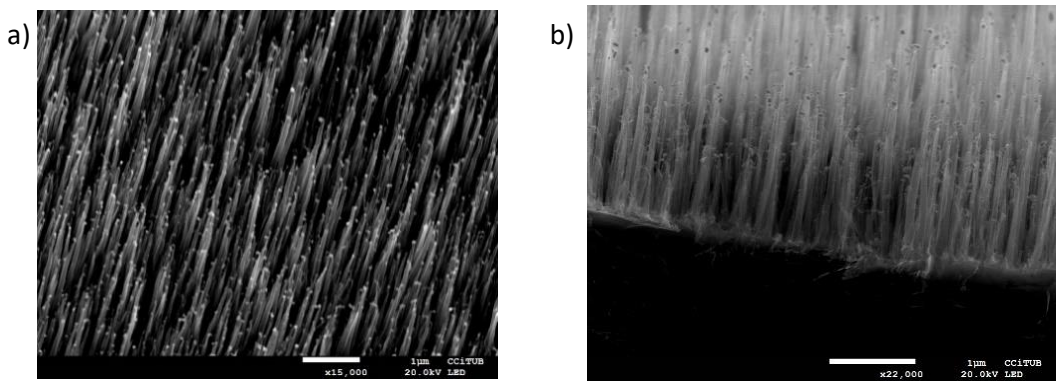

Figure 4.11. SEM images of CNTs functionalized by O_2 plasma for: a) 30 s and b) 60 s.

4.3. Growth mechanism of GNWs

Plasma enhanced chemical vapour deposition is a common method for the production of MLGNWs. The growth mechanism of graphene nanowalls (MLGNWs) strictly depends on the plasma type. In case of vertical nanostructure fabrication, it is important to elucidate the specific species, such as carbon and hydrogen contained radicals, which are responsible for the successful growth of nanowalls. The growth mechanism of vertical free-standing nanostructures has not been discussed much compared to various techniques for thin film deposition, which have been developed earlier. There are various hypotheses about the GNW growth process. However, there is no unified theory to unveil the growth mechanism. In this chapter, we propose a mechanism for the growth of vertical graphene by plasma-enhanced vapor deposition (Avetisyan 2019).

The surface reactions in vapor deposition processes are controlled by nucleation and growth stages, and high performance can be achieved by:

(1) the selective production of specific reactive species crucial for the film growth and nucleation.

(2) the efficient transport of essential species onto the growing surface.

(3) the control of surface reaction for both, nucleation, and subsequent growth.

Plasma is an essential factor for the vertical growth of carbon and graphene. The reactions under plasma activated by remote ICP, used to minimize the orientational effect of the plasma electrical fields during the catalyst-free growth of graphene nano-sheets (Cuxart et al. 2017):

(a) warrant for a low graphene defect density via low plasma kinetics (low energy species during our ICP-CVD processes).
(b) decouple the dissociation process of the gas from the growth process of graphene on the substrate (because the remote plasma, in our process).
(c) tune the precursor gas chemistry (high presence of C-C dimers in our processes) in view of improving the graphene growth.
(d) reduce the growth temperature as compared to conventional chemical vapor deposition (CVD).

In particular ICP is a relatively economical processes and simply way for producing a significant variety of carbon micro and nanostructures, like graphene and graphene nanowalls. The ICP configuration has a number of advantages, such as high energy density, larger plasma volume and, consequently, high growth rate (Hiramatsu et al. 2013). The growth process of vertical

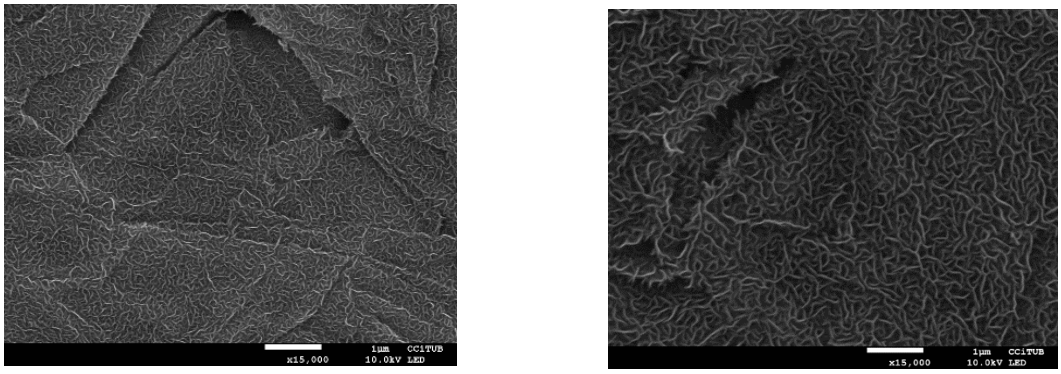

Figure 4.12. Two images of GNWs grown on Papyex® paper using ICP-CVD process.

graphene is affected by diverse parameters, such as the type of precursor gas, temperature, pressure, deposition time, substrate materials and plasma power. Also, catalysis-free direct synthesis of MLGNWs in suitable substrate is an additional characteristic of the random oriented nanostructures. Therefore, vertical structures need to be characterized and analyzed at various stages of growth, including the nucleation, vertical growth, and completion of the free-standing vertical nanostructures. We could successfully grow the GNWs directly on the Papyex® paper using an RF power of 400 W to obtain a plasma of CH_4 with a flow of 10 sccm under pressure of 400 mtorr and temperature 750°C for 30 min. (Figure 4.12)

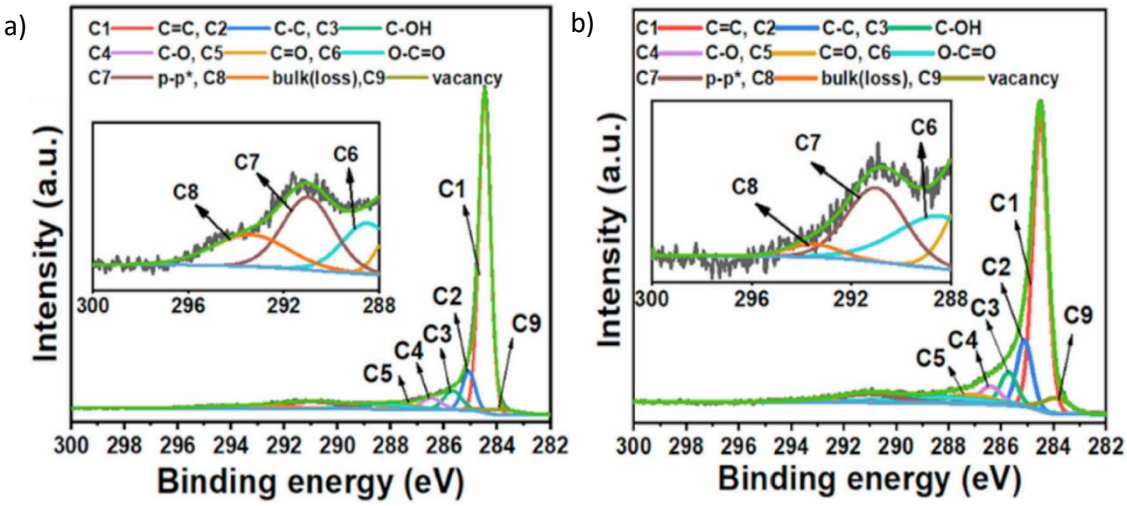

Figure 4.13. High resolution deconvoluted spectra C 1s for a) graphite paper and b) GNWs (Hussain et al. 2021).

The XPS analysis was carried out for the graphite paper and for the GNWs grown over it. The elemental composition analysis reveals that the as received Papyex® sample consists of C1s (98.68 at.%) and O1s (1.32 at.%) while the GNWs sample consists of C1s (96.89 at.%) and O1s (3.11 at.%). The higher ratio of oxygen in GNWs in comparison to the graphite paper is probably due to the existence of defect sites and grain boundaries in the graphene, which readily react with atmospheric oxygen when the sample is removed from the reactor. The asymmetric shape of high resolution C1s spectra indicates the presence of other chemical moieties at the surface of the both samples. The deconvolution of C1s spectra for graphite paper and GNWs shows 9 peaks. The main C1s peak at 284.5 ± 0.2 eV was characterized as C1 (C=C)/sp2 hybridized graphite like carbon. The C2 peak at 285.1 ± 0.2 eV was a feature of C–C/sp3 hybridized carbon atoms. The C3 peak at 285.8 ± 0.1 eV corresponds to the C–OH chemical group. The C4 (C–O) peak at 286.4 ± 0.1 eV, C5 (C=O) at 287.3 ± 0.2 eV, and C6 (O–C=O) at 288.4 ± 0.1eV indicate the presence of alcohol/ ether, carbonyl and carboxylic groups, respectively (Bertóti et al. 2015; Hussain et al. 2018). The C7 peak located at 291.0 ± 0.1 eV and C8 at 293.5 ± 0.2 eV were designated as shake up satellite (p-p*) and bulk-loss, respectively (Girard-Lauriault et al. 2012). Due to the high number of defects in GNWs, the percentage of adsorbed impurities as oxygen functional groups is higher in comparison to FGS. In addition, a peak at 283.9 ± 0.1 eV was assigned to vacancy-like defects

(Ganesan et al. 2016). In the case of Si/VG/FGS, C1, C2, and C3 peaks appear at the same binding energies as those for FGS and VG/FGS (Hussain et al. 2021).

We finally applied the same conditions for the growth of GNWs on the CNTs to be able to obtain a hybrid structure with greater surface are (Figure 4.14) in order to use it as electrode for supercapacitor.

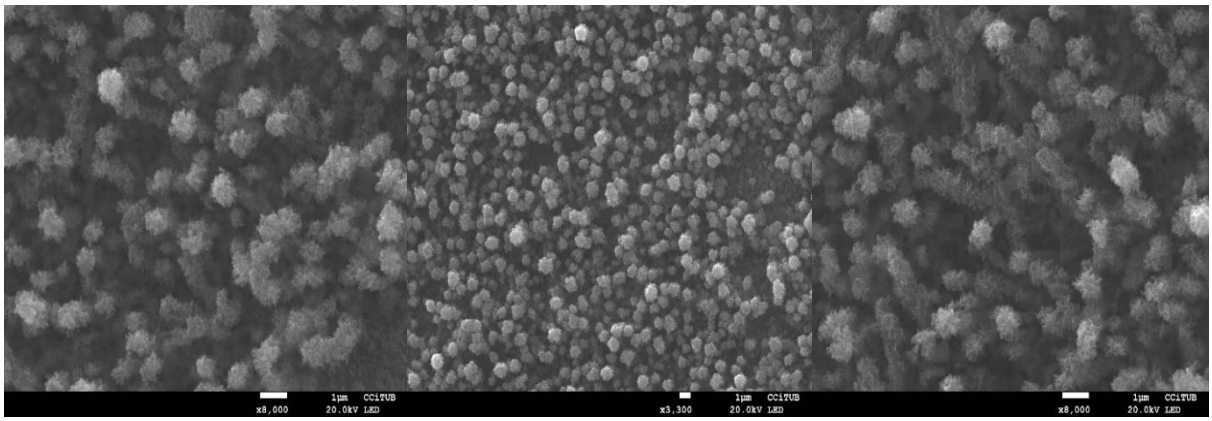

Figure 4.14. SEM images of CNTs covered by the GNWs over Papyex® paper.

4.4. Results and discussion

4.4.1. Raman spectroscopy

Raman Spectroscopy was used to evaluate the quality of CNTs and hybrid structure of CNTs and GNWs. This kind of carbon-based material displays two characteristic bands, the tangential stretching G mode (1500-1600cm^{-1}) and the D mode (1330-1360 cm^{-1}) (Korneva 2008) (see Figure 4.15). In addition, multi wall carbon nanotubes (MWCNTs) present a band in the range 1617 to 1625 cm^{-1} called D'-band that corresponds to defects on the side walls of CNTs (Lehman et al. 2011). D'-band is related with disordered graphitic lattice. These bands are activated by defects due to the breaking of the crystal symmetry that relax the Raman selection rules (Merlen et al. 2017). The D band, like the D'-band, is a double resonance Raman mode which can be attributed to the presence of disordered graphitic lattice (Düngen et al. 2017), double resonance effects in sp^2 carbon and other defects (Osswald et al. 2007; Lehman et al. 2011). Following the deconvolution process presented by (Sadezky et al. 2005) in Raman spectra were possible identified two additional bands (Figure 4.15). One denoted as A Band (1500 cm^{-1}), related with

amorphous carbon (Düngen et al. 2017), and the other one denoted as D'' band (1200 cm^{-1}). I band according with (Venezuela et al. 2011), it is mainly due to phonons associated to the $K\Gamma$ direction in the Brillouin zone. As this band is related with very defective samples, (Bokobza et al. 2015) determined the behavior of the I band, by means the identification of two new bands (D* and D**) lying close to the D'' band on defective aromatic carbons (graphite nanoplatelets, heat treated glassy carbons, pyrograph nanofilaments, and multiwall nanotubes) (Bokobza et al. 2015). In our case, for carbon nanotubes, the line shape of the D'' mode is significantly broadened due to contributions from different tubes in or close to resonance with the excitation laser (Herziger et al. 2014). It is necessary to take into account that the Raman intensity of the defect-induced lines (e.g., D, D', and D'' bands) is proportional to the average number of defects in the material (Venezuela et al. 2011). In that sense, the number of defects in the CNTs can be estimated by using the intensity ratio between D band and G band (I_D/I_G). As the I_D/I_G ratio decreases, so does the number of structural defects present in the CNTs (Hussain et al. 2014). For sample obtained by PECVD the value of the ratio I_D/I_G is reducing from 1.24 to 0.83 with the plasma functionalization (Figures 4.16-4.19). The Raman features are given in Table 4.1. The difference is considerable and is most likely due to the different amount of amorphous carbon present in the first one. For "pure" amorphous carbons, the Raman spectra can be seen as simpler, because only a broad asymmetric band is seen close to 1500 cm^{-1}. However, this is incorrect, and for several reasons. First, many different kinds of amorphous carbon exist: sp^2 dominated ones (a-C), sp^3 dominated ones (ta-C, referring to tetrahedral amorphous carbon), one containing hetero atoms such as H (a-C:H, ta-C:H, an others) or N. Their structure and properties are related but widely varying. Second, as there is some aromatic carbon embedded in their structure, some resonance occurs (Merlen et al. 2017). There is another approach that identifies the type of amorphous carbon. It is possible to discriminate between types of amorphous carbon with the G-band data. (Pardanaud et al. 2014) related the shift and width (FWHM) of the G band with the type of amorphous carbon.

If one uses $FWHM_G$ (Γ_G) (Figure 4.15) as an indicator of local disorder close to sp^2 bonds in the material (which can be related to the size of the clusters and/or to the sp3 content close to sp^2 bonds), one can use this parameter in order to have an idea of where is the sample situated in Ferrari's three stage model''. With this in mind, nanocrystalline graphene (nc-G) is more ordered than a-C:H/D which are themselves more ordered than ta-C:H and ta-C. The presence of hydrogen systematically diminishes the shift of the G band (for ta-C/ta-C:H and a-C/ta-C:H) (Merlen et al. 2017). The value of crystallite size (L_a) for the sample obtained by PECVD is less

than that of the sample obtained by the hybrid structure of GNWs and CNTs. L_a was found lower for the hybrid structure. This makes sense, the sample of CNTs alone, which has less amorphous carbon and therefore more defects, has a higher crystal size than that obtained for the hybrid structure, which has less amorphous carbon. Besides, this is in accordance with the established by the I_D/I_G ratio, the CNTs sample has a greater degree of disorder than the sample of hybrid structure.

For graphene, as it has different electronic structures close to the *K* point, and because the double resonance mechanism connects phonons to the electronic structure, the shift, shape (composed of several overlapped bands), and intensity of the 2-band(s) can be used to distinguish from monolayer up to 5-10 stacked layers. The relative intensity ratio between the 2D and G bands was also found to be dependent on the number of layers: I_{2D}/I_G is close to 3 for monolayer graphene, and falls down to 0.3 for highly oriented pyrolytic graphite (HOPG) (Merlen et al. 2017). In figure 4.15 it is also possible to distinguish three weak bands that are close to 2D band. In the literature these 2D sub-bands are denominated D+D'', D+D' and 2D' and are found at 2460, 2940 and 3230 cm^{-1}, respectively (Merlen et al. 2017). The number and origin of the 2D sub-bands have been understood for multilayer graphene (Ferrari et al. 2006) in the framework of the double resonance mechanism and more complex things can occur such as folding (Podila et al. 2012), misorientation (Poncharal et al. 2008), and stacking faults that can modify the intensities and shape (Merlen et al. 2017). In our case these bands can be attributed to the existence of graphene in the hybrid nanostructure. G, 2D and 2D sub-bands are sensitive to defect density in the MWCNTs, including the ones related to tube diameter and number of walls (Antunes et al. 2007).

In summary, this technique provided enough information to ensure that the CNTs samples have different characteristics. Not only morphological, as could be seen in the SEM images, MWCNTs with different structural quality were obtained. In accordance with the development of the D''-band, the PECVD process produced forest of MWCNTs with a large percentage of amorphous carbon. On the other hand, the hybrid structure had less amorphous carbon.

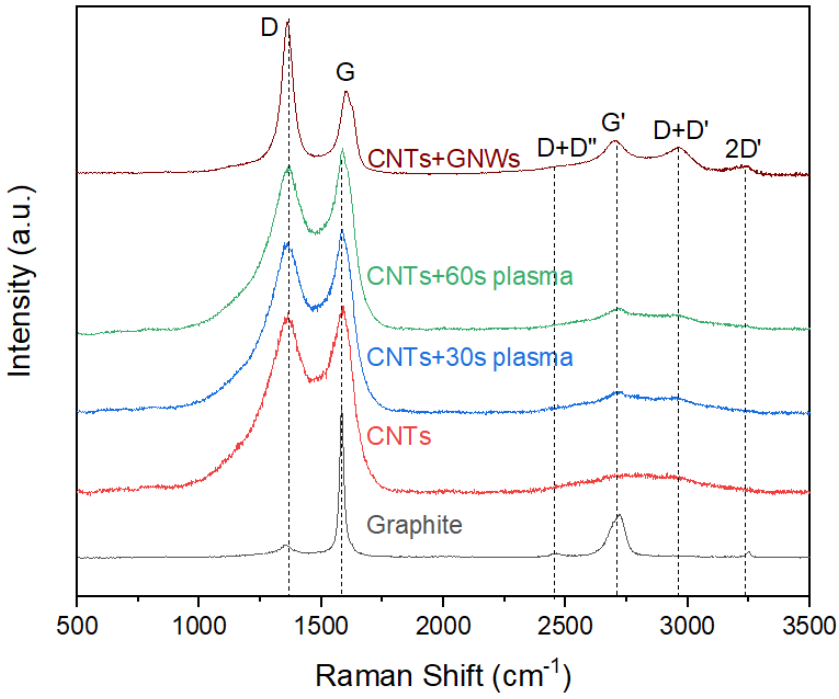

Figure 4.15. Raman spectra for CNTs grown over Papyex® paper before and after plasma functionalization, and the hybrid structure of CNTs and GNWs

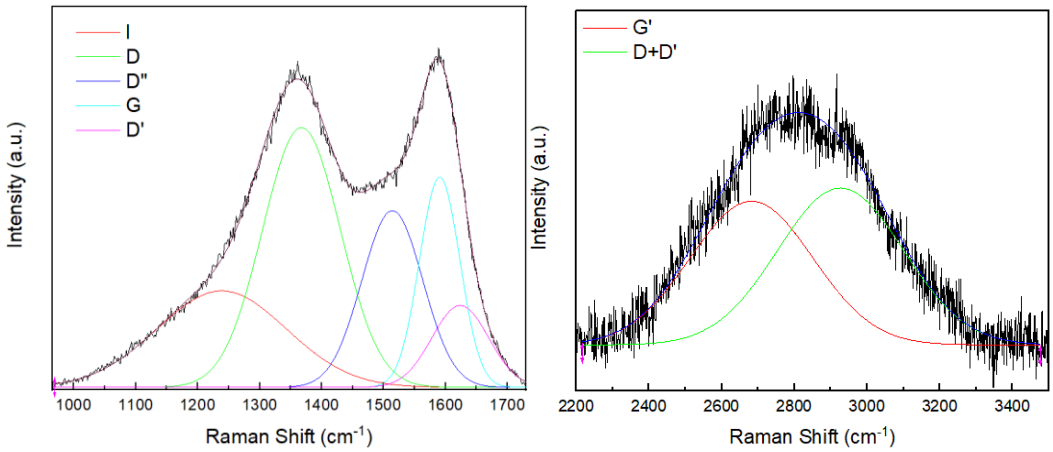

Figure 4.16. D, G, and 2D bands deconvolution for MWCNTs.

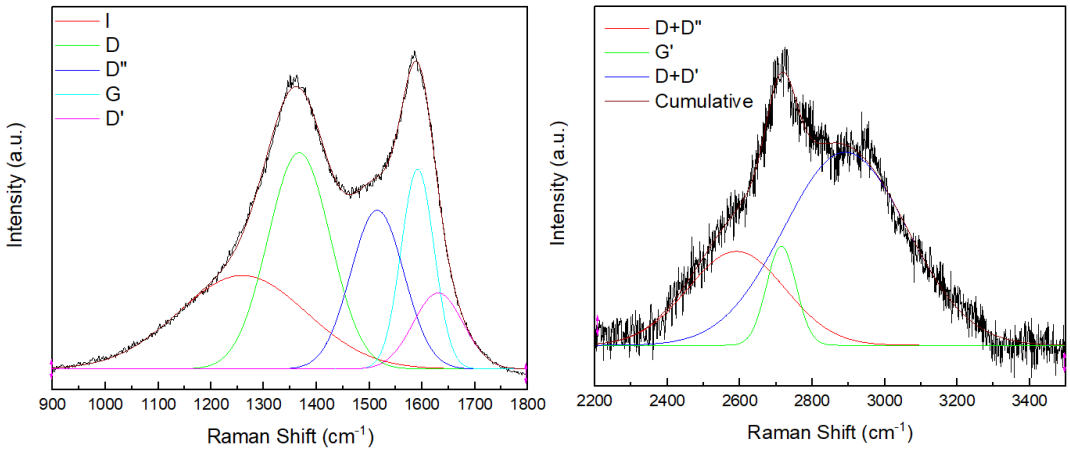

Figure 4.17. D, G, and 2D bands deconvolution for MWCNTs after applying O_2 plasma for 30 s.

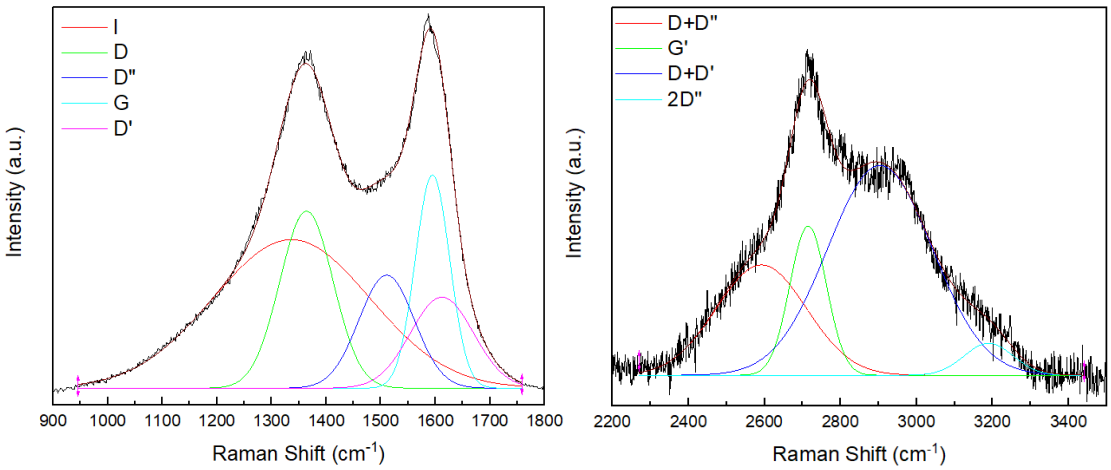

Figure 4.18. D, G and 2D bands deconvolution for MWCNTs after applying O2 plasma for 60 s.

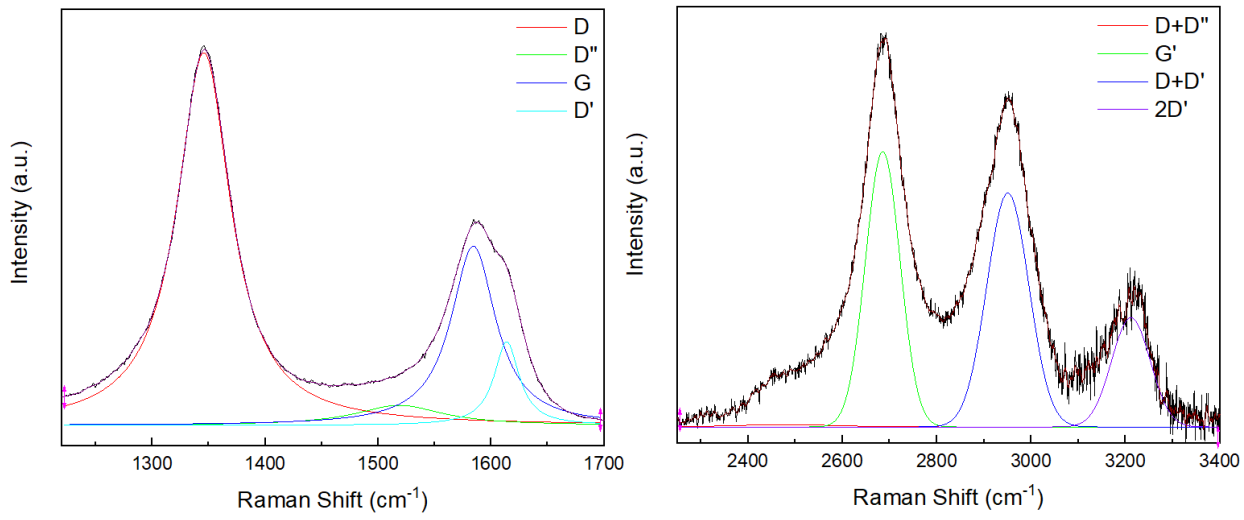

Figure 4.19. D, G, and 2D bands deconvolution for hybrid structure of MWCNTs and GNWs.

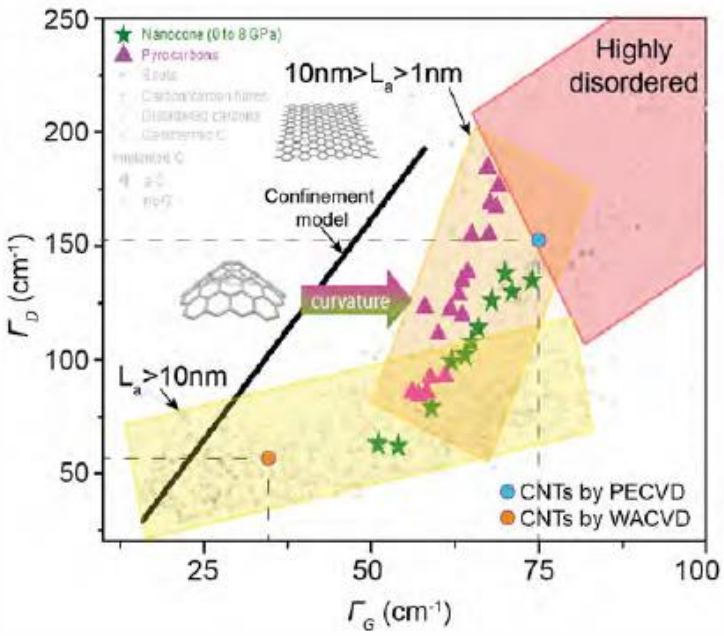

Figure 4.20. Γ_D vs. Γ_G plot for a large variety of disordered aromatic carbons (Merlen et al. 2017).

		I	D	D''	G	D'	D+D''	G'	D+D'	2D'	I_D/I_G	L_a (nm)
CNTs	Position (cm^{-1})	1238.66 ± 9.77	1367.43 ± 1.17	1514.12 ± 8.98	1590.55 ± 1.82	1623.71 ± 93.33		2682.04 ± 16.72	2926.76 ± 56.17		1.24	4.05
	FWHM (cm^{-1})	245.83 ± 13.19	148.24 ± 3.1	115.9 ± 10.54	76.75 ± 11.57	107.96 ± 32.96		397.46 ± 28.75	405.9 ± 21.31			
	Intensity (a.u.)	14.61 ± 0.79	39.34 ± 4.07	26.75 ± 6.39	31.83 ± 5.58	12.4 ± 4.13		3.02 ± 1.52	3.3 ± 0.81			
CNTs +30'' plasma	Position (cm^{-1})	1259.22 ± 3.06	1367.13 ± 0.91	1515.09 ± 3.49	1591.59 ± 0.92	1630.38 ± 30.46	2590.65 ± 18.11	2714.44 ± 1.35	2891.19 ± 10.24		1.08	4.66
	FWHM (cm^{-1})	285.51 ± 8.51	139.54 ± 3.6	118.7 ± 6.48	73.4 ± 4.36	111.17 ± 16.75	314.98 ± 21.47	96.24 ± 4.87	400.33 ± 12.77			
	Intensity (a.u.)	15.17 ± 0.46	35.09 ± 2.92	25.76 ± 2.87	32.41 ± 6.31	12.33 ± 2.87	1.98 ± 0.36	2.09 ± 0.22	4.07 ± 0.28			
CNTs +60'' plasma	Position (cm^{-1})	1336.46 ± 12.73	1364.07 ± 2.13	1510.87 ± 32.58	1594.85 ± 0.69	1612.18 ± 71.4	2591.47 ± 14.02	2714.51 ± 1.22	2903.59 ± 5.4	3189.58 ± 6.45	0.83	6.06
	FWHM (cm^{-1})	338.54 ± 22.14	114.79 ± 5.04	119.27 ± 25.51	74.21 ± 4.76	136.14 ± 24.13	279.69 ± 18.99	113.53 ± 4.31	324.16 ± 14.68	152.29 ± 16.46		
	Intensity (a.u.)	20.56 ± 4.77	24.51 ± 4.23	15.64 ± 7.17	29.51 ± 8.41	12.6 ± 5.53	2.08 ± 0.3	2.81 ± 0.28	3.95 ± 0.27	0.6 ± 0.14		
CNTs+GNWs	Position (cm^{-1})		1345.78 ± 0.11	1518.72 ± 6.2	1584.31 ± 0.59	1613.8 ± 0.59	2685.43 ± 0.34	2777.25 ± 20.89	2950.56 ± 0.48	3211.4 ± 0.89	2.08	2.41
	FWHM (cm^{-1})		3882.37 ± 28.62	342.42 ± 83.4	1558.18 ± 113.44	407.75 ± 58.97	86.31 ± 1.1	537.31 ± 18.43	104.93 ± 1.43	96.45 ± 2.52		
	Intensity (a.u.)		42.65 ± 0.45	2.31 ± 0.63	20.53 ± 1.8	9.57 ± 1.61	5.04 ± 0.12	2.11 ± 0.18	4.28 ± 0.1	2 ± 0.08		

Table 4.1. Data of Raman fitting for CNTs before and after plasma functionalization, and for the hybrid structure of CNTs and GNWs.

4.4.2. Optical Emission spectroscopy (Avetisyan 2019)

Fig. 4.21-a shows the OES spectra for the evolution of the CH_4 precursor gas radicals from 5 to 25 min. of deposition. In thermal CVD, only ~0.0002% of incoming methane dissociates forming active species in the gas phase at a temperature of 900°C. However, due to plasma activity, more than 80% of the methane dissociates to give rise to other species such as H, H_2, CH and C_2H_2

(Cruden and Meyyappan 2005). We observed that recombination lines of the atomic (656 nm, H_α) and molecular (550-650 nm, H_2) hydrogen dominate in the emission spectrum. This high H content depends on the CH_4 gas precursor (1:4). H atoms are formed as a result of CH_4 dissociation in a high plasma density and provide effective removal of amorphous carbon (etching), which contributes to the ulterior growth of MLGNWs, where pure hydrocarbon radicals can simultaneously serve as a carbon source or as a by-product after hydrogen etching. Emission lines of CH radicals at 387 nm and 430 nm, C_2 Swan band system in the range 465-590 nm and Balmer lines at 410 nm, 434 nm, 486 nm, and 656 nm were also analyzed. During plasma deposition CH_4 precursor was able to easily convert to CH_X (x = 1-3) radicals, to produce carbon dimers (C_2) through radical recombination and subsequent dissociation (Hofmann et al. 2003). The C_2 Swan band system has a large influence on the nucleation process (Mantzaris et al. 1998). OES spectra within 5 minutes of deposition show a Swan band system with high intensity, which decreases after 10 minutes due to the nucleation in the first stage of growth. The radical density of C_2 ranging from 10^{17}-10^{19} m^{-3}, in ICP system, is favorable for the initial growth of vertical nanostructures. Furthermore, the hydrogen plasma has proven to be effective in promoting the crystallinity of the carbon materials by the following factors: (1) atomic hydrogen can preferentially etch amorphous phase and (2) atomic hydrogen can induce crystallization (Vizireanu et al. 2010). Cheng et al. reported that, hydrogen radical etched away loosely bonded carbons and promoted the graphitization in diamond like carbon (DLC) films. In our case the hydrogen radical would etch away disordered components (carbon atoms) such as amorphous carbon rather than ordered, because the bond strength of disordered carbons is weaker than that of ordered ones. Therefore, hydrogen radical would etch away disordered phase selectively and by this way decrease of the disordered carbon formation, which would affect positively to the growth of MLGNWs (Avetisyan 2019).

We have also checked the OES for the oxygen plasma functionalization of the hybrid structure (Figure 4.21-b).

Electron impact excitation of ground-state molecular and atomic oxygen leads to emission at 844.6 and 777.4 nm, which is predicted by the following mechanisms:

dissociative excitation $e + O_2 \rightarrow e + O^* + O$

and direct impact excitation $e + O \rightarrow e + O^*$

where O* refers to the O(3p5P) state which emits at 777.4 nm and to the O(3p3P) state which emits at 844.6 nm (Krstulović et al. 2006). Walkup *et al* showed that in oxygen plasma the 844.6 nm oxygen emission line is more reliable than the 777.4 nm (Walkup et al. 1998), hence, in these figures the intensity of the 844.6 nm O emission line is shown. As is clear, increasing oxygen gas flowrate leads to a slight decrease in the density of atomic oxygen and oxygen molecular ions. This is attributed to the recombination of active species: e +O_2 → 2e + O_2^+ (Lieberman and Lichtenberg 2005).

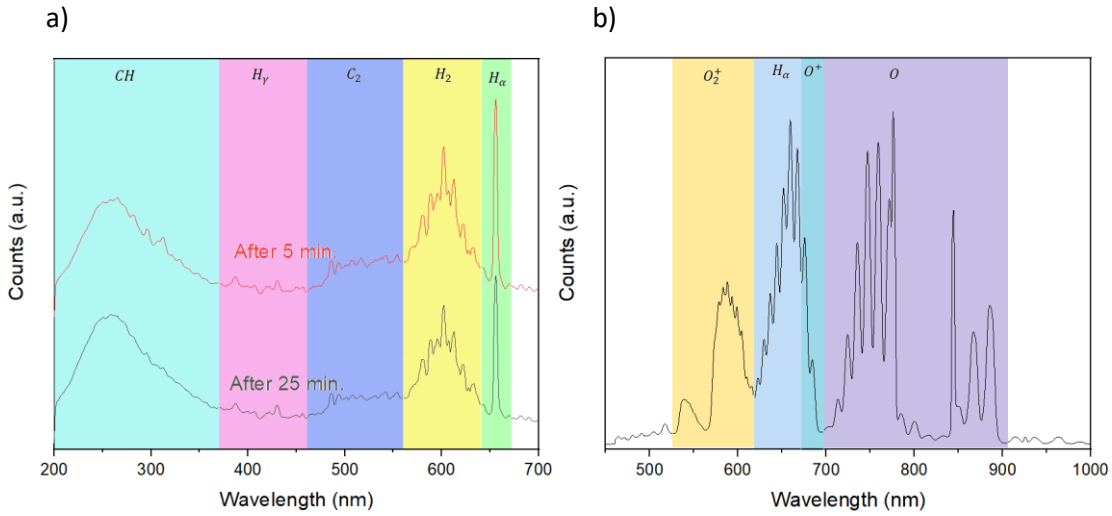

Figure 4.21. a) Optical emission spectra from the CH_4 methane plasma taken at different deposition times; and b) Optical emission spectra from the O_2 plasma.

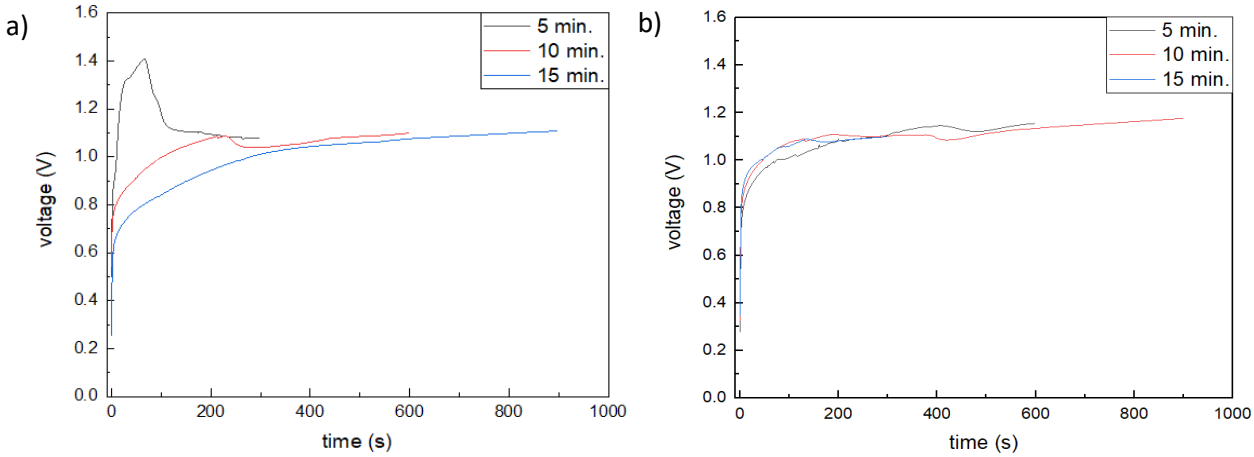

Figure 4.22. Voltage vs. time during the deposition of the MnO_2 for a)CNTs and b) CNTs+GNWs.

4.4.3. Electrodeposition of MnO_2

The prepared samples of CNTs and carbon hybrid structure over Papyex® paper were used as electrodes for supercapacitors. As know, the MnO_2 has high specific capacitance which leads us to use the large surface area of our carbon materials as a base of the MnO_2. The MnO_2 was deposoited electrochemically using 0.2 M of Mn_2SO_4 in a solution of Na_2SO_4 of 0.1 M concentration. We deposited the MnO_2 for different periods of time (5, 10, and 15 min.) and we studdied the morphology of the obtained samples using SEM, EDS, Raman, and the electrochemical characterization for super capacitors. The chart in figure 4.22. shows the voltage change during the deposition of the MnO_2 for different times. In the three experiments for both structures, we used the same amount of MnO_2 which is 0.5 ml but the dropping was faster or slower depending on how fast we need to deposit the material (Figure 4.23).

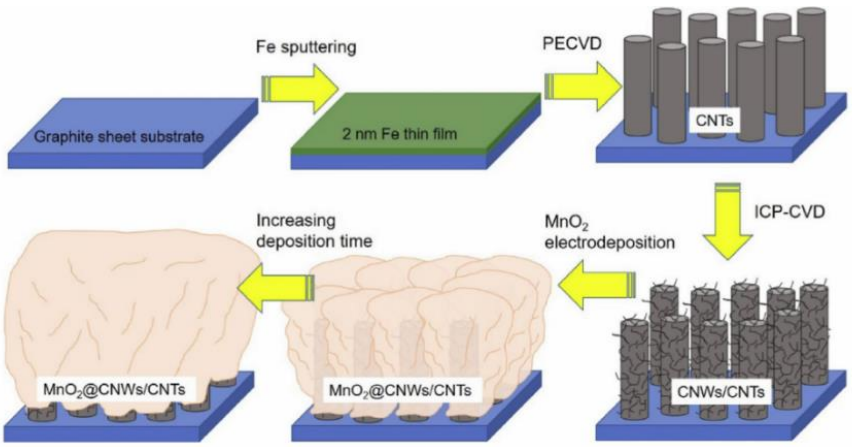

Figure 4.23. Scheme of the overall synthesis process of manganese oxide/carbon-carbon nanocomposite. Graphite sheet is used as the substrate and different steps/techniques are required for the production of the supercapacior electrodes: magnetron sputtering of Fe, RF-PECVD, ICP-CVD, and MnO_2 electrodeposition (Amade et al. 2021).

4.4.4. Scanning Electron Microscope and Energy-dispersive X-ray spectroscopy

By showing directly the SEM images of CNTs+MnO_2 and the CNTs+GNWs+MnO_2 after MnO_2 for different times, we can observe that the manganese oxide was decreasing until 15 min. (Figure

4.24). The atomic concentration of C, Mn and O_2 obtained from the EDS are shown in table 4.2 (Figure 4.25).

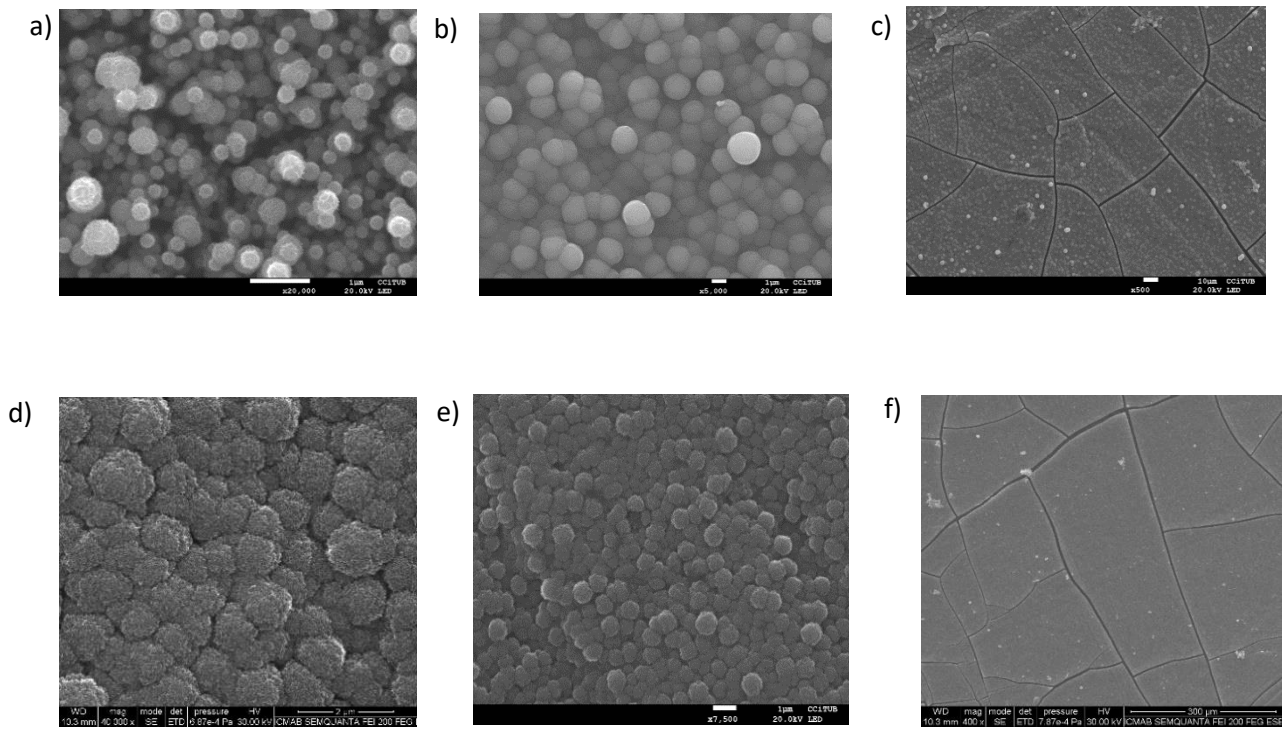

Figure 4.24. SEM images of (a-c) CNTs with the deposited MnO_2 for 5, 10, and 15 min. respectively, and (d-f) CNTs+GNWs with deposited MnO_2 for 5, 10, 15 min. respectively.

Sample	Mn (At%)	O (At%)	C (At%)
CNTs+GNWs+5 min. MnO_2	32.45	41.81	11.73
CNTs+GNWs+10 min. MnO_2	31.98	49.47	2.58
CNTs+GNWs+15 min. MnO_2	53.80	49.06	2.58
CNTs+5 min. MnO_2	25.85	38.00	23.06
CNTs+10 min. MnO_2	39.36	41.89	7.06
CNTs+15 min. MnO_2	43.10	41.32	5.19

Table 4.2. At% of Mn, O, and C after the electrodeposition of MnO_2 on different samples.

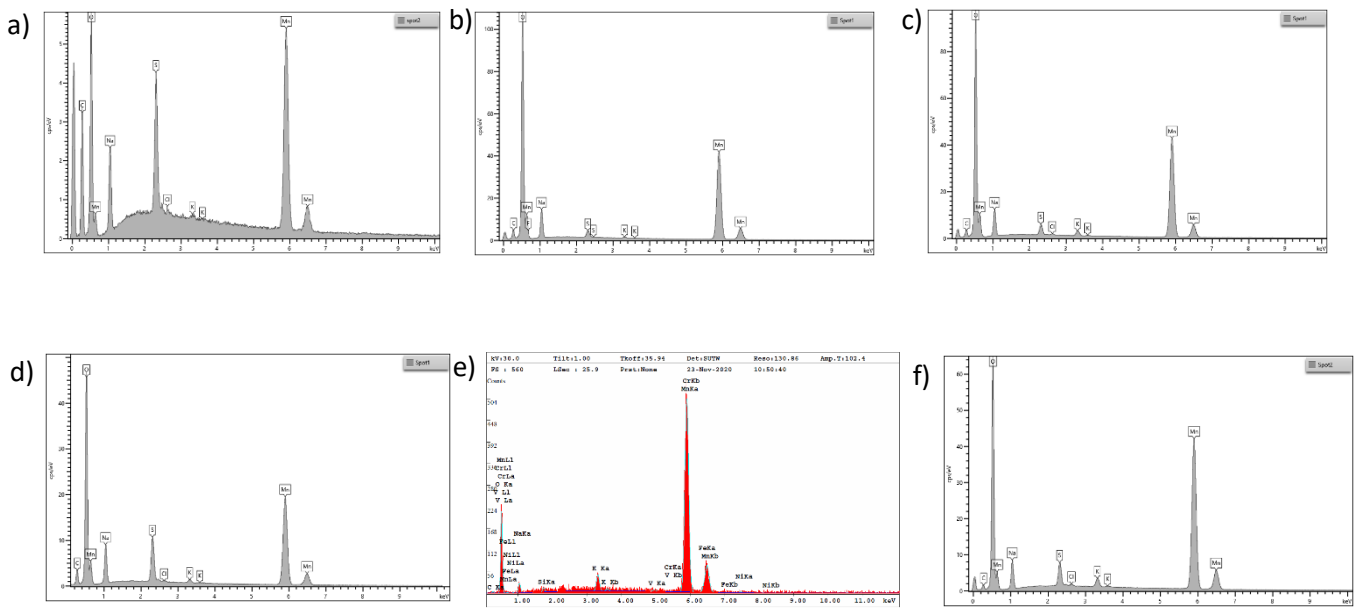

Figure 4.25. EDS spectra of (a-c) CNTs with the deposited MnO_2 for 5, 10, and 15 min. respectively, and (d-f) CNTs+GNWs with deposited MnO_2 for 5, 10, 15 min. respectively.

4.4.5. Raman Spectroscopy of MnO_2

The samples were characterized after the electrochemical of MnO_2 deposition where the carbon bands start to disappear as we increase the MnO_2 deposition time as it covers the carbon material (Figure 4.26).

The MnO_x where obtained in the range of 175 cm^{-1} and 633 cm^{-1}. The strongest peak we obtained at 633 cm^{-1} which is due to the symmetrical stretching vibrations (Julien et al. 2003; Gao et al. 2009). At low wave number region, two peaks were observed at 175 cm^{-1} and 283 cm^{-1}. The one at 175 cm^{-1} can be ascribed to the external vibration because of the MnO_6 octahedral translational motion (Wang 2012; Cheng et al. 2014) while the 283 cm^{-1} band is assigned to the δ-MnO_2 layered structure (Julien and Massot 2002). The two bands indicate as well the existence of the tunnel like structures of α-MnO_2 phase (Roychaudhuri et al. 2018). The peak at 576 cm^{-1} is also coming from the basal plane of the MnO_6 (Hsu et al. 2011).

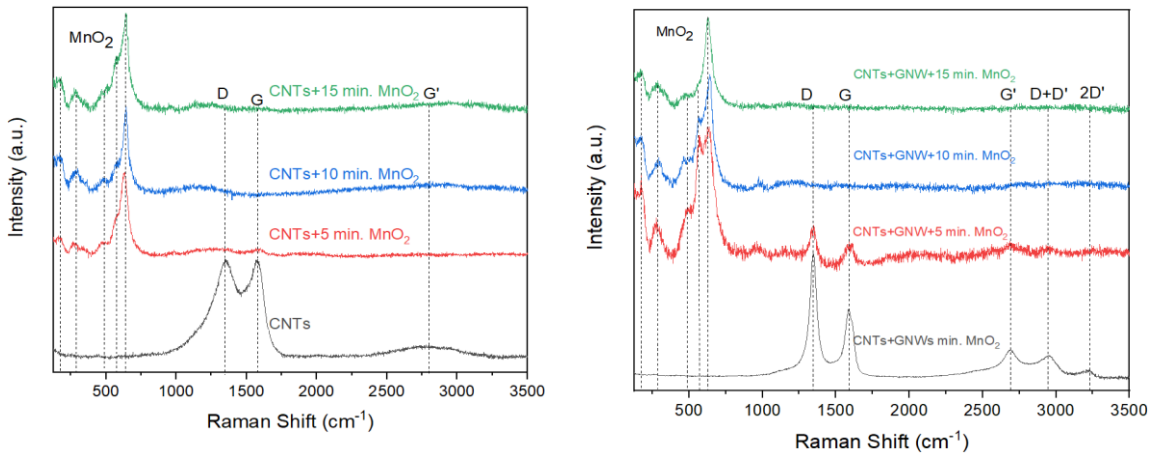

Figure 4.26. Raman spectra of the CNTs and hybrid structure carbon material before and after the deposition of MnO_2 for 5, 10, and 15 min.

4.4.6. Cyclic Voltammetry

After the deposition of the MnO_2, the average specific capacitance of the samples in 1 M Na_2SO_4 solution was determined from the cyclic voltammograms. In general, the specific capacitance of the samples (both structures: CNTs and hybrid) increased until the deposition of MnO_2 for 10 min. then it started to decrease when the deposition time increased, which can happen because the MnO_2 is fully blocking the carbon structure and therefore lower specific area.

Figure 4.27 shows the cyclic voltammograms at a scan rate of 5 mVs^{-1} of MWCNTs Untreated CNTs present almost a rectangular-shape voltammograms associated with double layer capacitance. The Cyclic voltammetry was achieved using a three-electrodes cell which is explained in the previous chapter.

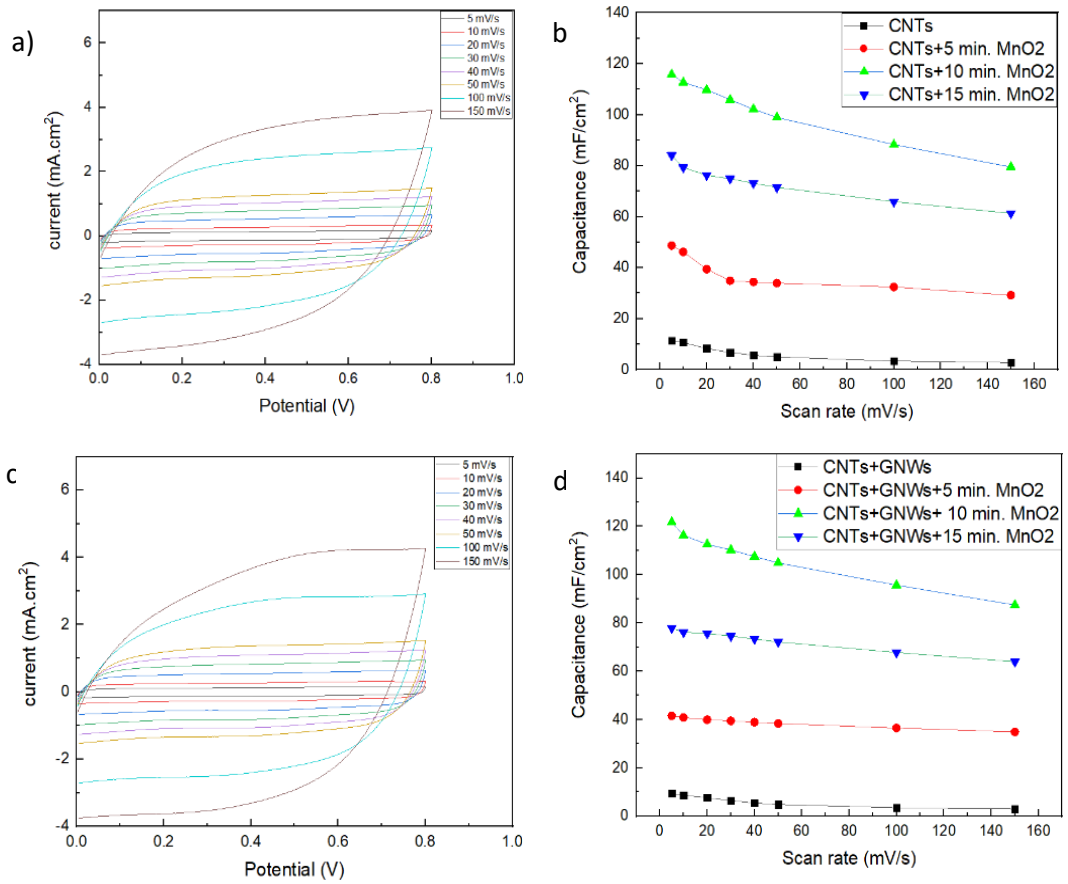

Figure 4.27. a,c) Cyclic Voltammetry at different scan rates for CNTs and hybrid carbon structure (CNTs+GNWs) after 10 min of MnO_2 deposition, respectively, and b,d) Specific capacitance vs. scan rate of CNTs and hybrid structure grown on Papyex® paper before and after the deposition of MnO_2. Still the increase was not as high as the specific capacitance of CNTs and hybrid structure are 115.8 and 121.7 mF/cm^2.

We observed that the hybrid carbon structure before the deposition of MnO_2 had a lower specific capacitance than the CNTs, which can be explained by the existence of the amorphous carbon when depositing the GNWs on the surface of CNTs. When we deposited the MnO_2, the specific capacitance of the hybrid structure started to increase more than of the CNTs where its high specific area played an important role in increasing the specific area of the MnO_2.

4.4.7. Electrochemical impedance

Electrochemical impedance spectroscopy was performed by applying an alternating voltage of 10 mV between 0.1 Hz and 100 kHz. This technique provides more information on the

electrochemical processes that take place at the interfaces and the bulk of electrode materials. An equivalent circuit can be found describing the different processes such as load transfer resistance, diffusion or capacitance. However, this is beyond the scope of this work, and only interception with the x-axis, which is related to electrochemical series resistance (ESR), will be comment. The ESR is the result of all the contact resistances, electrolyte resistance and electrode resistances that are present in our system and is a crucial parameter for fast charge/discharge rates. In the case of CNTs this resistance increases once MnO_2 is deposited, due to the additional resistance of the oxide layer (Figure 4.28). In the case of GNWs the ESR increased and, with the increase of the MnO_2 deposition time, the oxide layer becomes thicker and therefore more resistive as expected. The ESR values range was between 1.1 and 10.5 Ω.

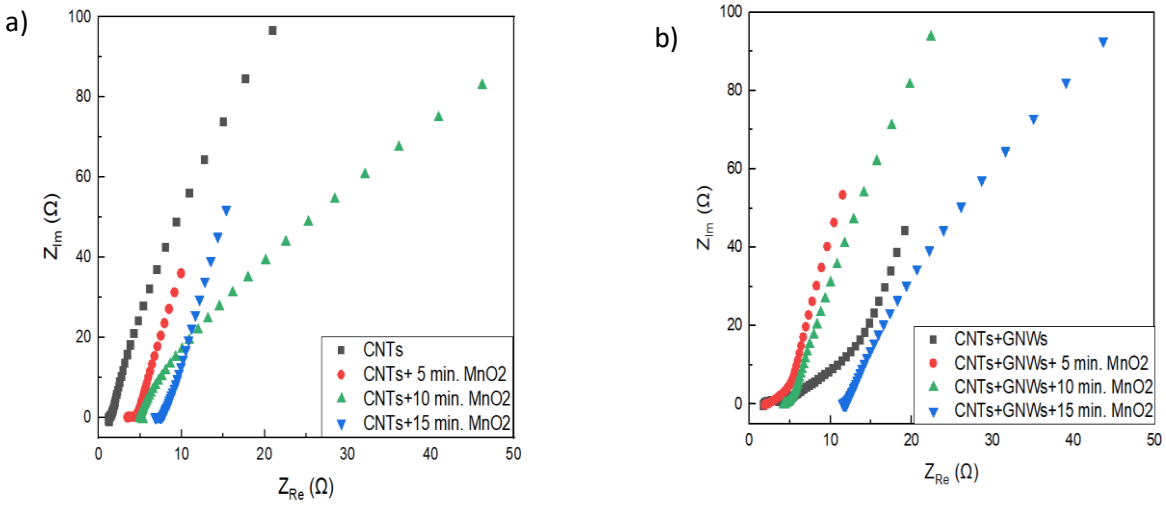

Figure 4.28. Impedance spectra of a) CNTs before and b) hybrid carbon structure before and after the deposition of MnO_2.

4.5. Conclusions

The carbon nanotubes growth parameters over a high flexible and conductive Papyex® graphite paper was optimized in order to obtain a high-density and long CNTs using PECVD process. The optimized parameters were the thickness of the catalyst thin film, PECVD temperature, and the growth time. Different oxygen plasma times were applied on the CNTs to increase its morphology to allow the diffusion of ions through the porous nanotubes when using them as electrode for supercapacitors, which was proved by Raman spectra. The CNTs were used as a support for the growth of GNWs using ICP-CVD process leading to a hybrid structure allowing the increase of the surface area. The CNTs and hybrid carbon nanostructure were used to deposit MnO_2 electrochemically in order to increase the specific capacitance. The capacitance increased until a deposition time 10 min of MnO_2 and started to decrease again when the deposition time increased more as the MnO_2 layer blocked the pores, such as it was observed by SEM. After 10 min of the deposition of MnO_2, the specific capacitance increased from 11.4 mF/cm^2 to 115.8 mF/cm^2 for CNTs and from 9.42 to 121.7 mF/cm^2 for the hybrid structure at scan rate 5 mV/s. This result is relatively high with other complex techniques(Yang and Ionescu 2017; Deghiedy et al. 2022; Hou et al. 2022) .The EDS result showed the increase of the at% for Mn and O_2. The ESR of all samples was determined. It was found that it increases with increasing MnO_2 deposition time. ESR values are generally in the range of 1.1 Ω to 10.5 Ω for all samples.

Chapter 5

Direct Growth of CNTs on SS310S.

5.1. Introduction

Carbon nanotubes (CNTs) have garnered a well-deserved reputation throughout time. Research and industry organizations all over the globe are continually enhancing their manufacturing due to their physical, chemical, electronic, thermal, mechanical, and optoelectrical qualities, which now can be used for testing the covid (Ji et al. 2017; MIT 2021). It is a versatile substance that may be acquired in the form of a coating, a powder, or even fibers (An et al. 2017). Industrial techniques, for example, have been devised to create long fibers and subsequently to construct high-performance mechanical conductive meshes (Lepró et al. 2010). It is also available in powder form, which serves as a reinforcing material (Kowalczyk et al. 2015). This material may also be used to make flexible screens, sensors, and energy storage devices. One of the applications where CNTs and other carbon-based materials shine is in the creation of energy storage systems (Kang et al. 2017). The industry of next-generation batteries and supercapacitors is continually encouraging the development of novel materials that fulfill existing requirements (Ke and Wang 2016).

CNTs are chemically and thermally stable, and they may be functionalized (Adamska and Narkiewicz 2017). CNTs may also be grown on a variety of rigid and flexible substrates. Silicon is one of the most often utilized rigid substrates. A thin coating of catalyst material is applied on silicon wafers with a native silicon oxide layer (Hussain et al. 2012). When heated, the thickness of these layers must be sufficient to produce nanoislands. The sort of CNTs formed is determined by the shape, distribution, and, of course, the type of catalyst material present in the nanoislands (Loiseau and Gavillet). Iron, nickel, and cobalt are among the most frequent elements employed as catalysts (Harutyunyan et al. 2005).

Rigid substrates, on the other hand, are not appropriate in many practical circumstances. Because they are incompatible with industrial production methods, they can only be used in labs. As a result, research organizations' emphasis is increasingly concentrated on flexible substrates. CNTs may be acquired on flexible substrates in two ways: they can be transferred from rigid substrates, or they can be grown directly on flexible substrates (Moreno et al. 2014). The first option is inconvenient due to a lack of control. The second strategy, which has been employed

by several researchers, provides better control over the characteristics of CNTs. Sheets of copper, nickel, aluminum, various kinds of steel, or graphite paper are utilized as flexible substrates. Diffusion barrier systems, often composed of oxides or nitrides, are used to prevent the diffusion of catalyst nanoparticles. Furthermore, multilayer structures that function as buffer layers are often put between the diffusion barrier and the substrate. The buffer layers compensate for the thermal expansion coefficient discrepancy. Diffusion barrier and buffer layer technologies, on the other hand, minimize the electrical contact between the substrate and carbon nanotubes (Yang et al. 2014).

Another method for obtaining CNTs on flexible substrates has been used. These nanostructures have been reported to develop on stainless steel without the need of diffusion barriers, buffer layers, or external catalytic material. The biggest impediment is removing the stable layer of chromium oxide from the surface. Mechanical (grinding and polishing) or chemical techniques can be used to remove the natural oxide coating. The alloying elements (Fe, Ni, Mn, Cr) then function as catalysts and accelerate the development of CNTs directly on the metallic substrate when heated in a reducing environment. The given results suggest that a high level of control over the growing process was attained. CNTs with a homogeneous distribution and vertical alignment have been discovered. There is also an ohmic contact between the substrate and the CNTs. Until date, every research has concentrated on enhancing the growing process of carbon nanotubes. However, little or nothing is mentioned concerning the substrate's integrity. There is sufficient scientific data to suggest that prolonged exposure of stainless steel to high temperatures in the presence of hydrogen can significantly impair its characteristics (Han et al. 1998; Marchi et al. 2020).

In this chapter, the process of CNTs growth will be carried out directly on SS310S. This kind of stainless steel is considered as a good candidate if we compare it with other SS alloys as it contains a higher level of Cr (25%) and Ni (20%) which can contribute to the synthesis of CNTs in one continuous step for reduction (removing the native oxide layer from the surface) and synthesis, which, till this moment, hasn’t been reported.

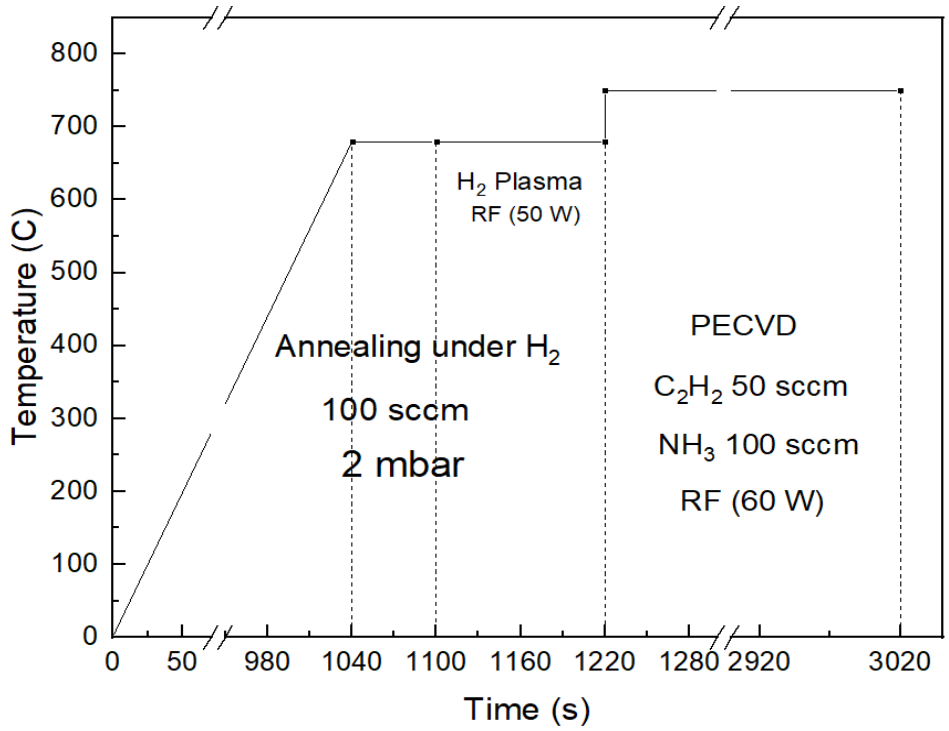

Figure 5.1. Chart illustrating the parameters and methodology for the direct growth of CNTs on SS310S.

5.2. Growth mechanism of CNTs

CNTs production was carried out on a flexible SS310S substrate by PECVD process. The base pressure of the chamber was reduced to a value of $2x10^{-4}$ Pa in order to prevent any contamination during the process. Different from the usual process that we used in the previous chapter, we started the annealing process directly as the purpose is to use the catalyst particles of the SS310S itself to grow the CNTs. Figure 5.1. shows the mechanism we followed to grow the CNTs. The substrate was heated gradually in order to reach a high temperature (680 °C) to start the reduction process. The reduction process was achieved using H_2 gas under a pressure 2 mbar and flow rate 100 sccm. We originally use the H_2 to avoid any oxidation on the substrate as we aim to remove the native oxide layer. Once we reach to a specific temperature, we fix the temperature for 1 minutes to stabilize before we start the plasma of H_2 for 2 min. in order to start the reduction using RF power of 70 W. Previous reports showed that this is enough time to get rid of the native oxide(Pantoja-Suárez 2019). Once we finish the reduction process, the catalyst nano-islands will be already formed, which in our case they could be Fe, Cr, or Ni because the

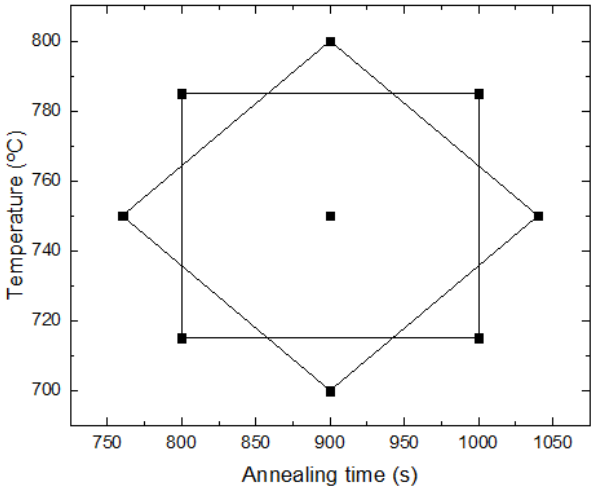

Figure 5.2. Box-Wilson experimental design of optimizing CNTs growth on SS310S. The chosen parameters are the annealing time and the PECVD temperature.

alloy is rich of these elements and all the three elements are good candidates for the growth of the CNTs. For CNTs synthesis we also use the PECVD process but this time the PECVD temperature can be different from the annealing and reduction. CNTs grew using the plasma of

NH_3 (50sccm) and C_2H_2 (100 sccm) under a total pressure of 1 mbar and an RF power of 50 W. In order to optimize the growth process, we used Box-Wilson experimental design to optimized two parameters: annealing time, and the PECVD temperature, where the other parameters kept fixed including the PECVD time which was 30 min. for all the experiments (Figure 5.2). Box-Wilson experimental design as shown in figure 5.2, depends on choosing 9 points on a plane of two variables, then using Statgraphic software we can predict the optimum parameters we can choose. The optimum parameters we chose is to obtain long nanotubes, with smaller diameter and high density.

After preparing all the experiments, we checked the samples by SEM to study the characteristics of each one. Table 5.1. shows a summary of the results of each experiment in Box-Wilson experimental design. The same values are represented in Figure 5.4

After entering all the details in Statgraphic software and doing some kind of simulation, we could obtain the desirability in 3D. The desirable parameters provided by the software were setting the annealing ramp time to 1010 s and the PECVD temperature to be 700 °C (Figure 5.5). As this temperature is the minimum we have used in our experimental design, we tried to fix all the

parameters and reduce it but the result wasn't as good as the one obtained from the experimental design desirable parameters.

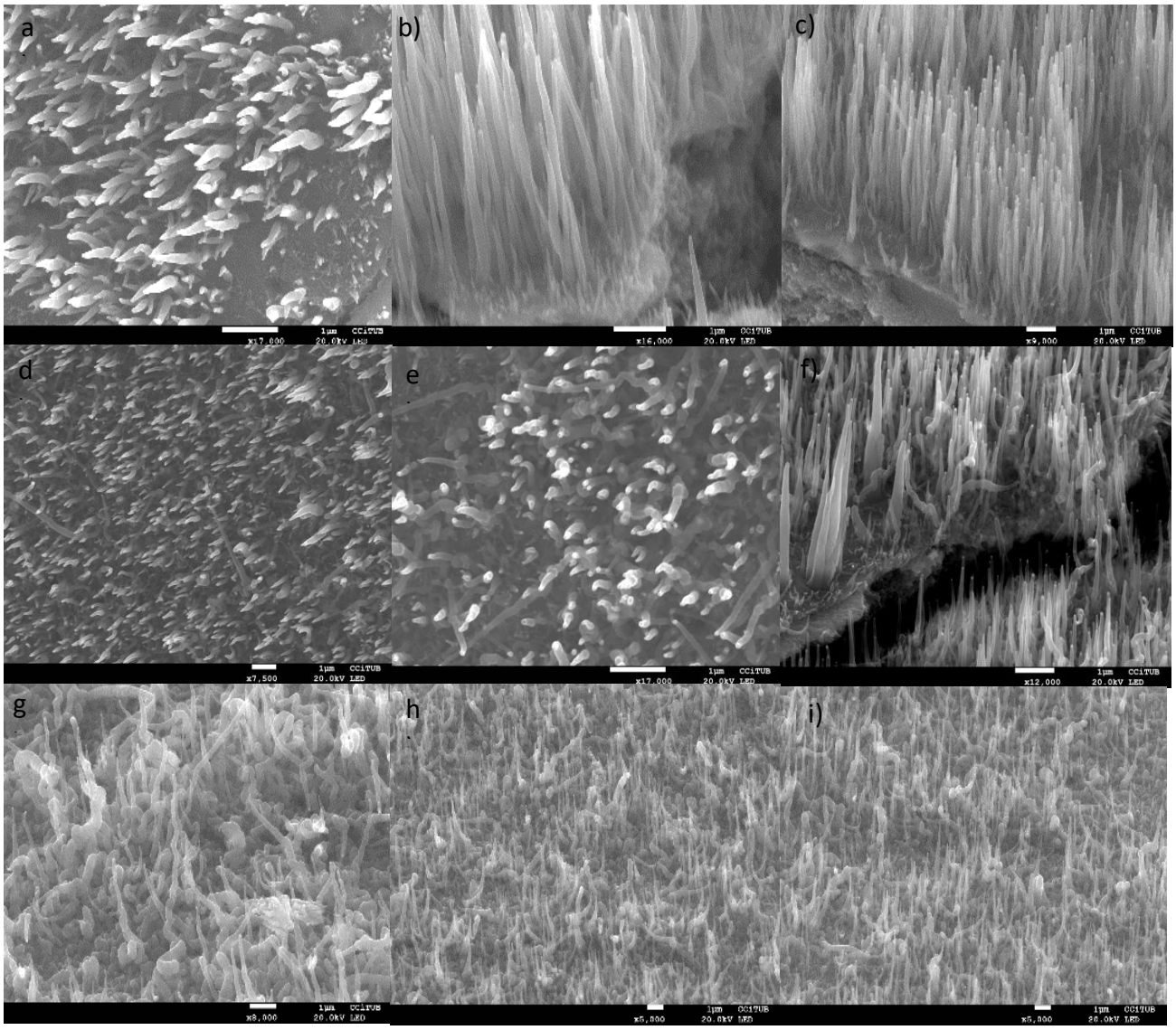

Figure 5.3. SEM images of the 9 experiments of Box-Wilson experimental design. Samples (1-9) in table 5.1. corresponds to the images (a-i) respectively.

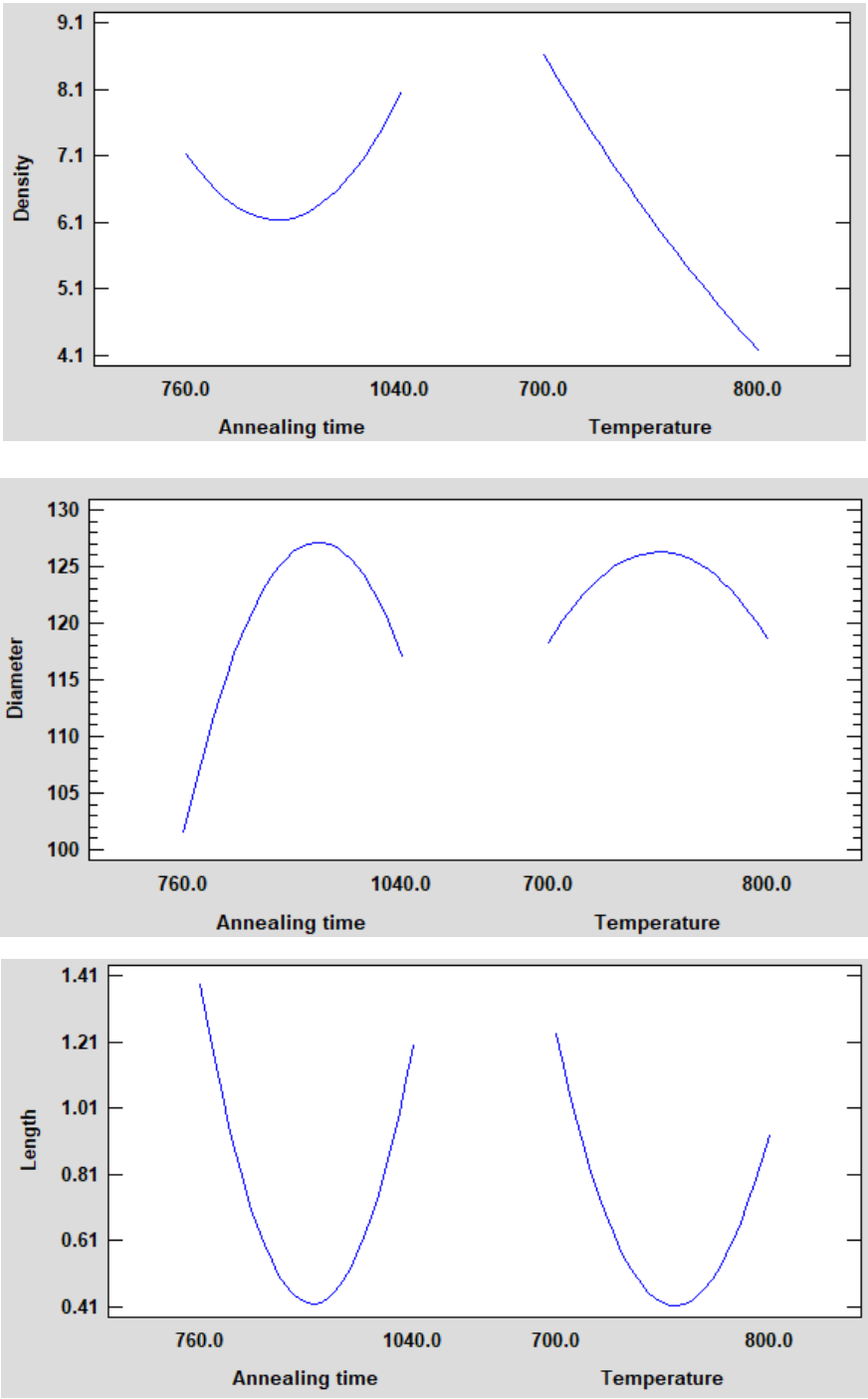

Figure 5.4. Illustration of the temperature and annealing time effect on the CNTs grown directly on SS310S.

Sample	Time (s)	Temperature (°C)	Density (μm^{-1})	Length (μm)	Diameter (nm)
1	900	700	5.221365	0.849766	108.7746
2	800	715	9.731785	1.365004	124.8769
3	1000	715	12.04325	1.867277	123.6125
4	760	750	8.230812	1.313392	79.88462
5	900	750	6.171119	0.421301	126.2959
6	1040	750	7.671007	0.957027	112.9392
7	800	785	1.90645	1.332064	129.1961
8	1000	785	2.940629	0.809076	128.2517
9	900	800	8.296635	1.006697	103.4179

Table 5.1. Box-Wilson experimental design for optimizing the CNTs growth directly on SS310S

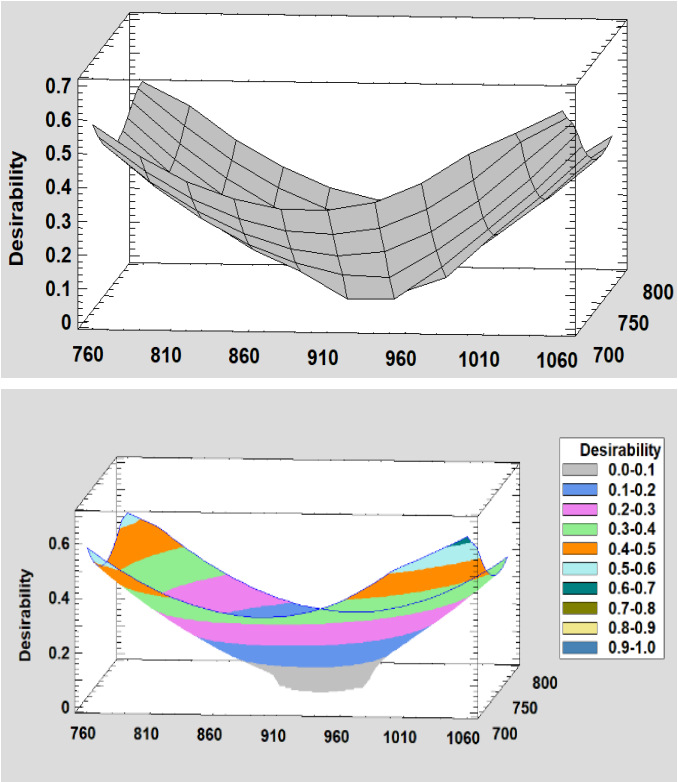

Figure 5.5. 3D representation of the desirability of parameters. The z-axis represents the annealing time (760-1060 s) while the z-axis represents the PECVD temperature (700-800 °C).

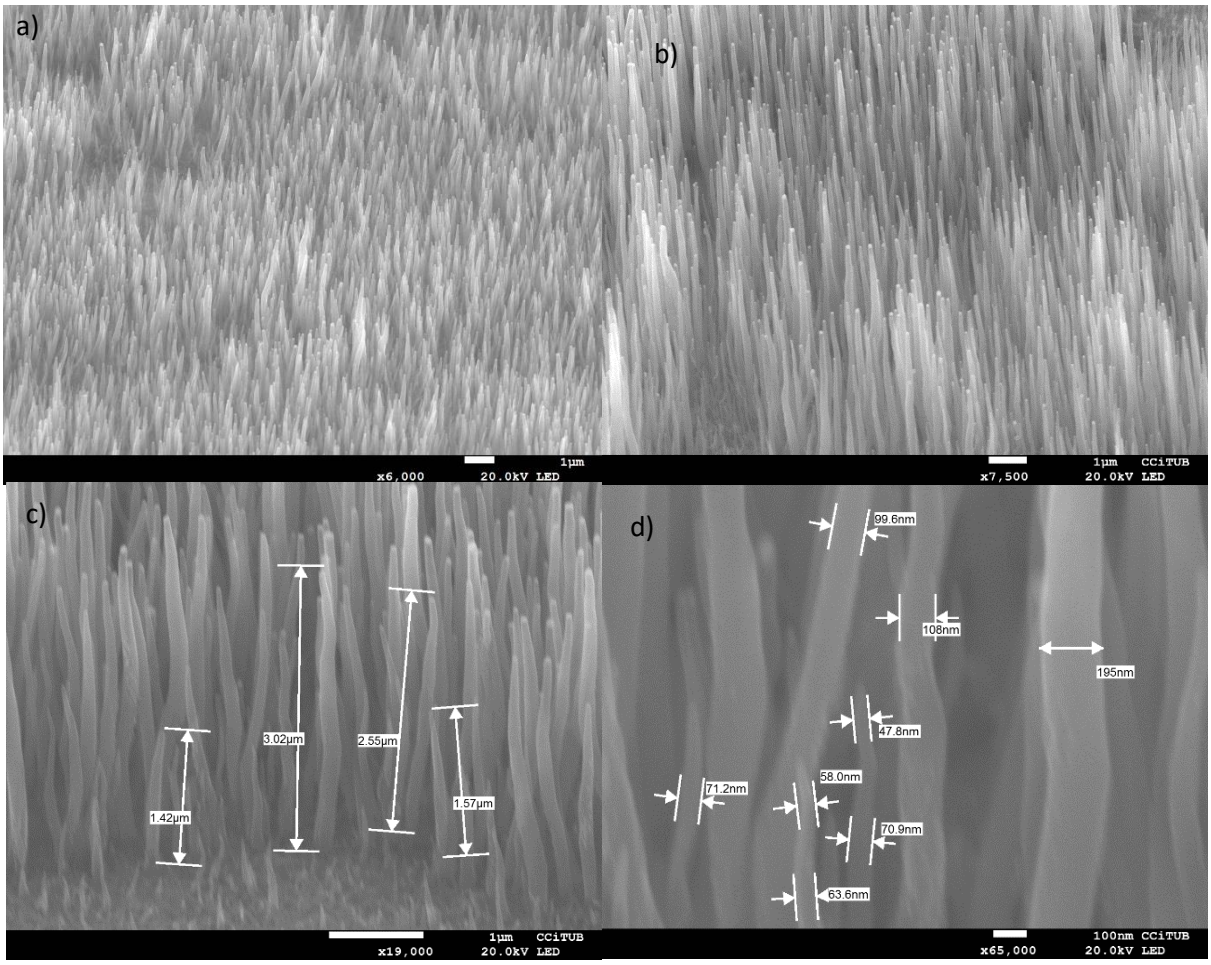

Figure 5.6. SEM images of the directly grown CNTs obtained by PECVD after applying the desired parameters of Box-Wilson experimental design.

HRTEM was used to confirm the tubular structure of the CNTs. The nanotubes with catalyst on their top surface are shown in Figure 5.7. The side walls of CNTs include amorphous carbon, which is often a byproduct of the PECVD development process. The elongated catalyst particle at the tip of the CNT (Figure 5.7-a) clearly demonstrates the tip growth process. The arrows inside the nanotube show the graphene layers at various distances inside the nanotube. This structure is defined by the bamboo-like form of the CNTs as opposed to the hollow cylindrical shape in which the nanotube inside is void.

A bamboo-shaped nanotube is made up of regular cone shaped compartment. The periodic precipitation of graphite sheets on the top of the catalyst particle causes compartment creation in the bamboo-like structure. Because its bonds are weaker than those of H_2, NH_3 is easily dissociated. The discovery of bamboo-structures in nitrogen-containing plasma and hollow tubes in nitrogen-free plasma by Martin S. Bell et al. (Bell et al. 2007) shows that nitrogen or CN (carbon-to-nitrogen ratio) played a crucial role in the compartment formation. They discovered that CN is essential in the creation of bamboo-like structures. Furthermore, CNTs are thought to develop by surface (SD) and/or bulk diffusion (BD) of carbon species through catalyst particles. High CN concentrations facilitated BD of carbon via Fe particles while suppressing SD by maintaining the catalyst surface clean (Bell et al. 2007).

There's also the potential of CN diffusion through the catalyst particles particles (Bell et al. 2006). However, because CN or N have extremely limited solubility in Fe, the concentration of N or CN in Fe is expected to be much lower than that of carbon. The size of the catalyst particle limits the growth tube's outer diameter. The local geometry of the catalyst particle stimulating the tube's development controls the shape of the tip (Srivastava et al. 2006). Nanotube fabrication necessitates the controlled deposition of carbon, which may then self-assemble into an energetically favorable nanotube shape. This regulated deposition rate is achieved by combining two reactions: dissociation of a carbon-rich gas, which is in C_2H_2 in our case, and elimination of excess carbon, which would otherwise result in amorphous carbon deposits. Figure 5.7-b shows a nanotube without the catalyst particle, which might be removed during the dispersion of CNTs using the ultrasonic bath to prepare it for TEM. TEM was used also to do mapping for a tube to have an idea about the metallic elements that contributed in the growth of the tube. The mapping was done for C, Fe, Ni, Mn, Mo, O, and cupper (Figure 5.8.). The main elements that contributed

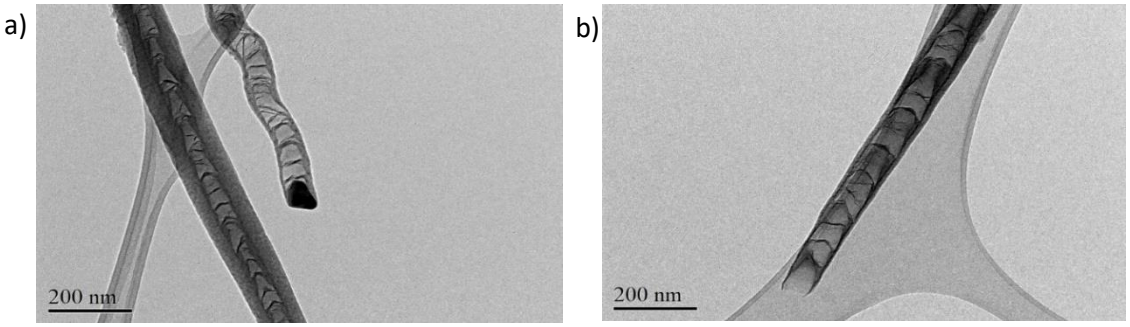

Figure 5.7. TEM images of CNTs grown directly on SS310S with a) the catalyst particle at the tip and b) with a removed catalyst particle.

in the growth of the nanotube were Fe and Ni, and Cu. We found that the only the Ni was also distributed along the walls of nanotubes.

5.3. Growth mechanism of GNWs

Carbon nanostructures were grown in an inductively coupled plasma chemical vapour deposition (ICP-CVD) reactor, which was modified and improved from another described elsewhere (Avetisyan 2019). The new system was configured to work at 13.56 MHz at an RF power of 400 W using a thermostatic tubular oven and a pressure control system. It consists of a long quartz tube (150 cm long, and 60 mm of diameter) having an RF anti-resonator coil manufactured by winding a copper tube with a diameter of 6 mm and a length of a quarter of the wavelength (552.7 cm) on a cylinder with a diameter of 10 cm and a length of 23 cm. The purpose of this work is to obtain a hybrid structure of CNTs-GNWs on SS310 substrate. Before we grew the nanowalls on the CNTs we obtained synthesized them directly on the SS310 alloy. Carbon nanostructures were deposited on SAE 310 stainless steel (SS310) substrates. SS310 stainless steel is chemically more stable against oxygen and chemicals than others such as Cu for use as an electrode. We chose SS310 stainless steel for its characteristics, such as, metallic conductivity, chemical stability, resistance to high temperatures, high Cr content that reduces nucleation of carbon from the formation of Fe nanoparticles (Pantoja-Suárez 2019), carbon compatibility, inertness, and possibility of achieving it as thin elastic sheets. These characteristics makes SS310 suitable for the present study. For the determination of the mass growth rate, SS310 substrates of equal dimensions (50 mm long, 38 mm width, and 100 μm thick) were used in order to obtain the deposited mass of carbon. The values obtained in a multitude of samples varied between 2 and 5 mg for deposition times of 30 minutes.

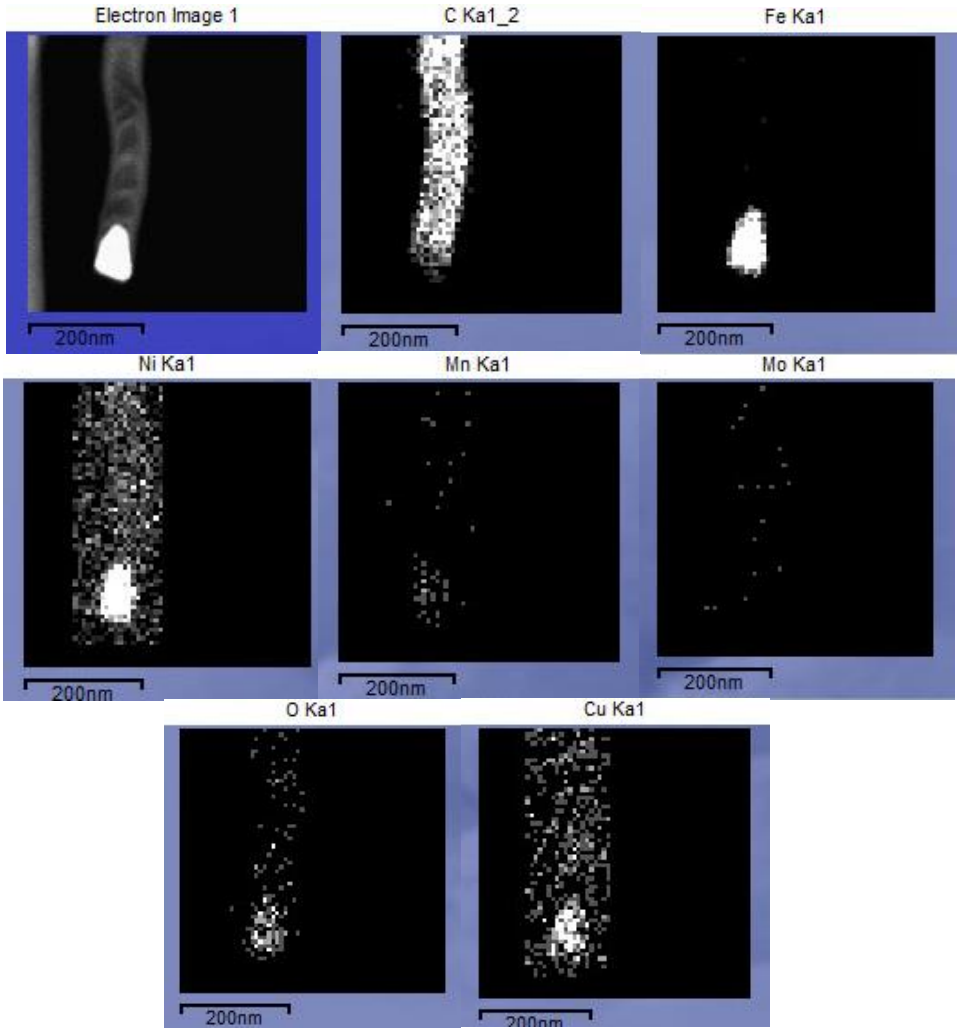

Figure 5.8. HRTEM-EDS mapping of a carbon nanotube grown on SS310 substrate.

Prior to the growth of carbon nanostructures, it is necessary to clean the quartz tube of possible carbon contamination from a previous process. Normally, a small gaseous flow of oxygen (99.99%) is introduced at a pressure of 50 Pa, which when excited by a 400 W RF plasma for about 30 min at room temperature, completely oxidizes the deposited carbon species on the inner surface of the quartz tube. Once the tube is totally transparent, the sample can be introduced into the reactor mounted on its graphite holder. SS310 substrates are routinely cleaned with isopropanol in a 20 min ultrasonic bath. Then, the substrates are weighed using a precision 100 µg balance and introduced mounted on the graphite substrate holder inside the quartz tube. The flat SS310 substrate on the substrate holder is positioned parallel to the quartz tube and 15 mm

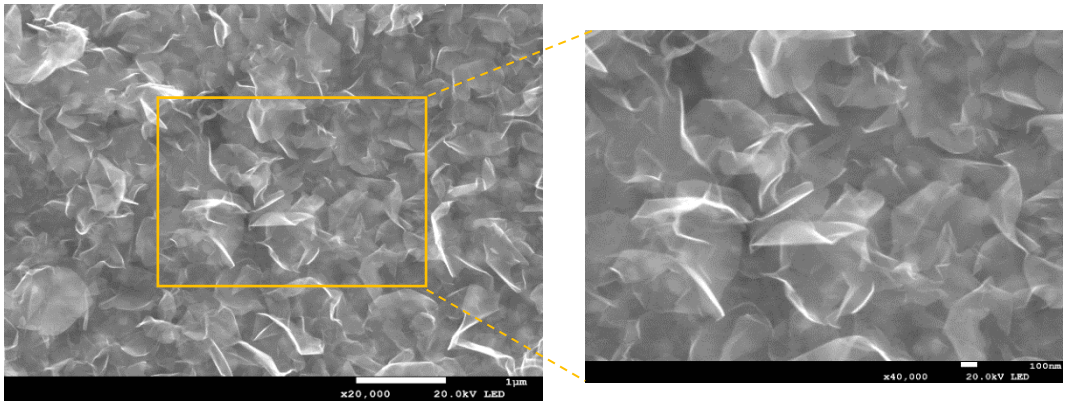

Figure 5.9. FE-SEM images of GNWs grown on SS310 stainless steel using ICP-CVD process.

from its central axis. The substrate remains oriented at a small angle of 5° with respect to the horizontal axis of the tube and against the incident gas flow. The position of the substrate corresponds to the centre of the tubular oven, 40 cm from the radio frequency antenna. The quartz tube is evacuated by means of a 65 l/s turbo-molecular pump to an ultimate pressure, usually between 10^{-3} and 10^{-4} Pa. A small flow of H_2 (10 sccm) is introduced at a pressure of 1 Pa and the oven heated by a ramp temperature of 1ºC/s to the desired temperature to 750 °C. Once the temperature of the sample has stabilized, the hydrogen pressure in the quartz tube is increased to 50 Pa by throttling the conductance valve closing the turbo-molecular pump, and a 400W RF plasma is turned on for 10 s. This operation enables the surface of the SS310 substrate to be activated by reducing the surface oxide. Subsequently, and without delay, a flow of 10 sccm of high purity methane (99.995%) is introduced and the hydrogen flow is cut off. At that moment, the growth of carbon nanostructures begins. The growth conditions (temperature, gas flow, pressure and RF-power) are maintained for 30 min and then the plasma is turned off. The gas flow is cut off and the temperature is reduced to values close to room temperature within a 15 min interval while the reactor is evacuated to the ultimate pressure. Once the sample has cooled, it can be extracted from the quartz tube.

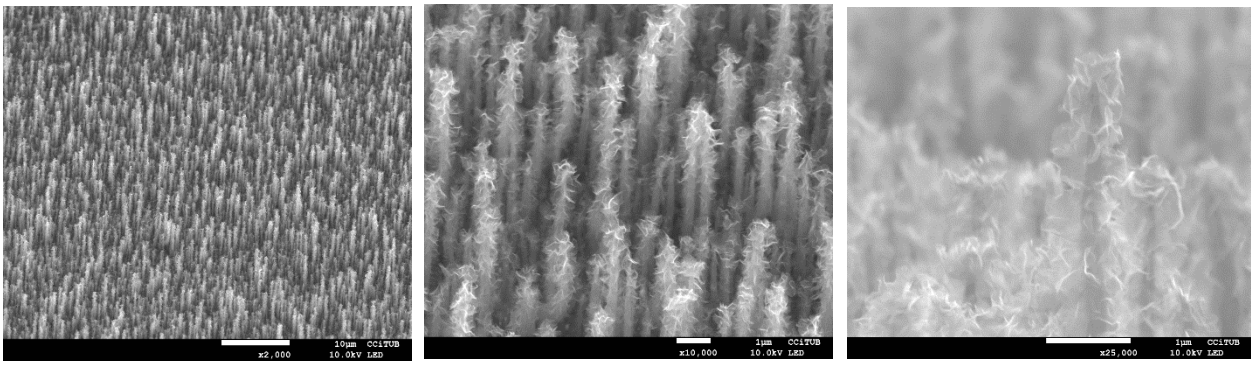

Figure 5.10. SEM image of CNTs covered by GNWs on SS310 substrate

We applied the same previous conditions of GNWs growth but without the plasma of H_2 at the beginning of the process to avoid the etching of CNTs. We obtained a fully decorated CNTs as shown in figure 5.10)

5.4. Results and discussion

5.4.1. Raman spectroscopy

Raman Spectroscopy was used to evaluate the quality of CNTs and hybrid structure of CNTs and GNWs. This kind of carbon-based material displays two characteristic bands, the tangential stretching G mode (1500-1600cm^{-1}) and the D mode (1330-1360 cm^{-1}) (Korneva 2008) (see Figure 5.11). In addition, multi wall carbon nanotubes (MWCNTs) present a band in the range 1617 to 1625 cm^{-1} called D'-band that corresponds to defects on the side walls of CNTs (Lehman et al. 2011). D'-band is related with disordered graphitic lattice. These bands are activated by defects due to the breaking of the crystal symmetry that relax the Raman selection rules (Merlen et al. 2017). The D band, like the D'-band, is a double resonance Raman mode which can be attributed to the presence of disordered graphitic lattice (Düngen et al. 2017), double resonance effects in sp^2 carbon and other defects (Osswald et al. 2007; Lehman et al. 2011). Following the deconvolution process presented by (Sadezky et al. 2005) in Raman spectra were possible identified two additional bands (Figure 5.11). One denoted as A band (1500 cm^{-1}), related with amorphous carbon (Düngen et al. 2017), and the other one denoted as D" band (1200 cm^{-1}). I band according with (Venezuela et al. 2011), it is mainly due to phonons associated to the $K\Gamma$ direction in the Brillouin zone. As this band is related with very defective samples, (Bokobza et al.

2015) determined the behavior of the I band, by means the identification of two new bands (D* and D**) lying close to the D'' band on defective aromatic carbons (graphite nanoplatelets, heat treated glassy carbons, and multiwall nanotubes) (Bokobza et al. 2015). In our case, for carbon nanotubes, the line shape of the D'' mode is significantly broadened due to contributions from different tubes in or close to resonance with the excitation laser (Herziger et al. 2014). It is necessary to take into account that the Raman intensity of the defect-induced lines (e.g., D, D', and D'' bands) is proportional to the average number of defects in the material (Venezuela et al. 2011). In that sense, the number of defects in the CNTs can be estimated by using the intensity

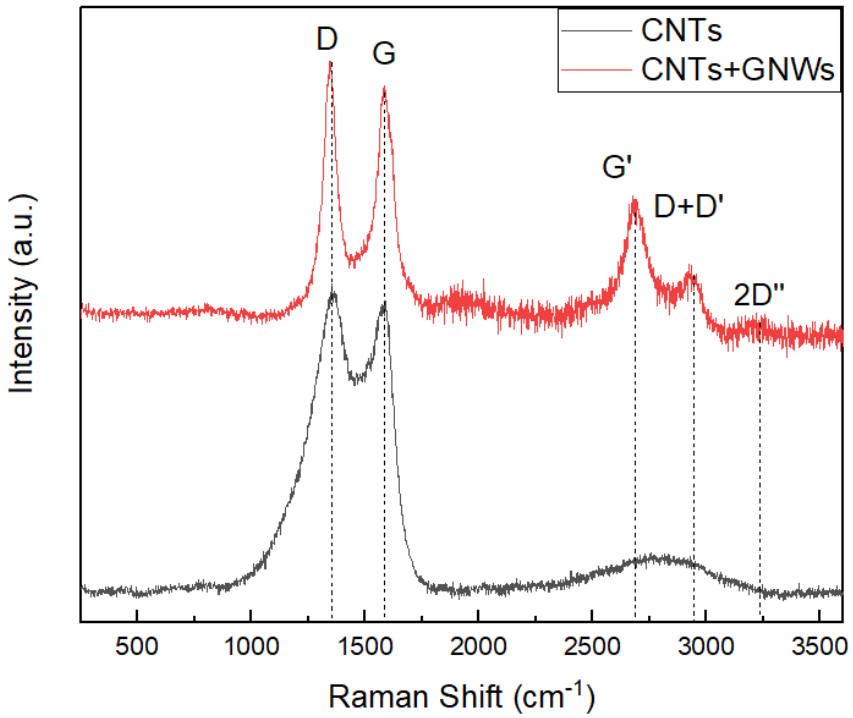

Figure 5.11. Raman Spectra for CNTs grown over SS310 substrate and the hybrid structure of CNTs-GNWs

ratio between D band and G band (I_D/I_G). As the I_D/I_G ratio decreases, so does the number of structural defects present in the CNTs (Hussain et al. 2014). The I_D/I_G ration was 1.24 for the CNTs obtained by PECVD and decreased to 1.08 after the deposition of GNW (Figure 5.12). The Raman features are given in Table 5.2. The difference is considerable and is most likely due to the different amount of amorphous carbon present in the first one. For "pure" amorphous carbons, the Raman spectra can be seen as simpler, because only a broad asymmetric band is seen close to 1500 cm^{-1}. However, this is incorrect, and for several reasons. First, many different kinds of

amorphous carbon exist: sp^2 dominated ones (a-C), sp^3 dominated ones (ta-C, referring to tetrahedral amorphous carbon), one containing hetero atoms such as H (a-C:H, ta-C:H, an others) or N. Their structure and properties are related but widely varying. Second, as there is some aromatic carbon embedded in their structure, some resonance occurs (Merlen et al. 2017). There is another approach that identifies the type of amorphous carbon. It is possible to discriminate between types of amorphous carbon with the G-band data. (Pardanaud et al. 2014) related the shift and width (FWHM) of the G band with the type of amorphous carbon.

In Figure 5.12 it is also possible to distinguish three weak bands that are close to 2D band. In the literature these 2D sub-bands are denominated D+D'', D+D' and 2D' and are found at 2460, 2940 and 3230 cm^{-1}, respectively (Merlen et al. 2017). The number and origin of the 2D sub-bands have been understood for multilayer graphene (Ferrari et al. 2006) in the framework of the double resonance mechanism and more complex things can occur such as folding (Podila et al. 2012), misorientation (Poncharal et al. 2008), and stacking faults that can modify the intensities and shape (Merlen et al. 2017).

In our case these bands can be attributed to the existence of graphene in the hybrid nanostructure. G, 2D and 2D sub-bands are sensitive to defect density in the MWCNTs, including the ones related to tube diameter and number of walls (Antunes et al. 2007). This explains the distinguished D+D’ and 2D’ in Figure 5.12-d.

In general, this technique provided enough information to ensure that the CNTs samples have different characteristics. Not only morphological, as could be saw in the SEM images, MWCNTs with different structural quality were obtained. In accordance with the development of the D''-band, the PECVD process produced forest of MWCNTs with a large percentage of amorphous carbon. On the other hand, the hybrid structure had less amorphous carbon.

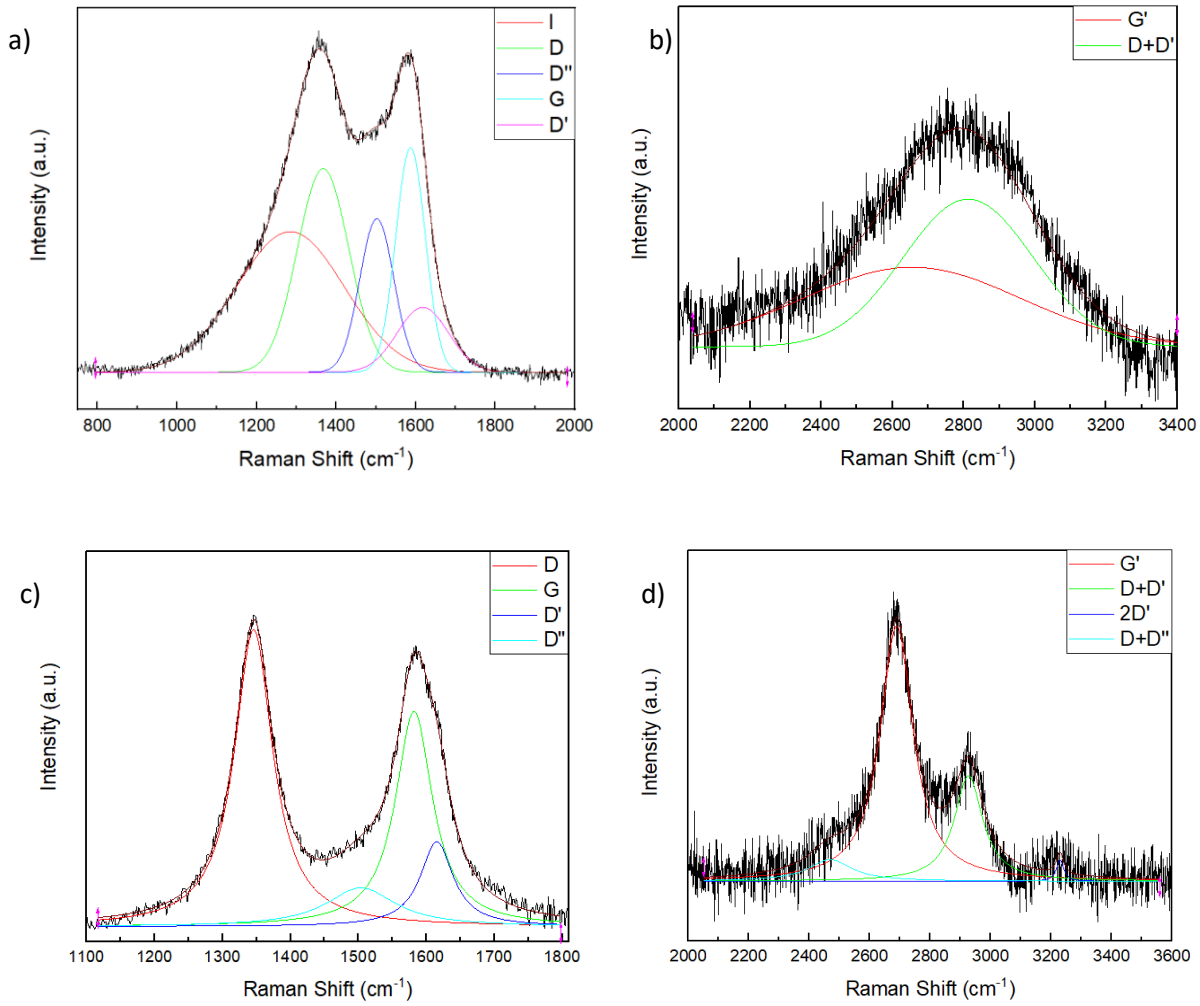

Figure 5.12. Raman Spectra showing the main D, G, and 2D bands for: a,b) CNTs and c,d) CNTs+GNWs both grown on SS310 substrate.

		I	D	D''	G	D'	D+D''	G'	D+D'	2D'	I_D/I_G	L_a (nm)
CNTs	Position (cm^{-1})	1284.71 ± 19.25	1367.28 ± 1.93	1502.31 ± 4.61	1587.05 ± 1.68	1617.98 ± 69.7		2654.37 ± 11.67	2812.79 ± 10.11		1.24	4.05
	FWHM (cm^{-1})	320.41 ± 17.51	152.61 ± 6.4	101.29 ± 5.37	87.73 ± 6.21	152.31 ± 8.9		723.2 ± 66.13	429.77 ± 22.61			
	Intensity (a.u.)	12.25 ± 0.73	17.73 ± 1.12	13.38 ± 1.04	19.58 ± 8.11	5.65 ±1.83		1.19 ±0.13	2.2 ±0.2			
CNTs + GNWs	Position (cm^{-1})		1345.76 ± 0.19	1581.77 ± 1.65	1503.59 ± 6.74	1615.21 ± 3.14	2468.52 ± 10.81	2689.04 ± 0.75	2926.89 ± 1.54	3230 ± 3.6	1.08	4.65
	FWHM (cm^{-1})		68.63 ± 0.7	66.71 ± 5.05	124.8 ± 16.8	58.88 ± 6.16	183.85 ± 37.98	1615.06 ± 31.74	579.91 ± 23.11	29.12 ± 8.4		
	Intensity (a.u.)		15.98 ± 0.23	2.09 ± 0.2	11.59 ± 3.04	4.57 ± 0.69	0.65 ± 0.31	0.67 ± 0.18	7.85 ± 0.23	3.24 ± 0.2		

Table 5.2. Data of Raman fitting for CNTs of both CNTs and the hybrid carbon structure grown on SS310 substrate.

5.4.2. Optical Emission spectroscopy

Fig. 4.21-a shows the OES spectra for the evolution of the CH_4 precursor gas radicals from 5 to 25 min. of deposition. In thermal CVD, only ~0.0002% of incoming methane dissociates forming active species in the gas phase at a temperature of 900°C. However, due to plasma activity, more than 80% of the methane dissociates to give rise to other species such as H, H_2, CH and C_2H_2 (Cruden and Meyyappan 2005). We observed that recombination lines of the atomic (656 nm, H_α) and molecular (550-650 nm, H_2) hydrogen dominate in the emission spectrum. This high H content depends on the CH_4 gas precursor (1:4). H atoms are formed as a result of CH_4 dissociation in a high plasma density and provide effective removal of amorphous carbon (etching), which contributes to the ulterior growth of MLGNWs, where pure hydrocarbon radicals can simultaneously serve as a carbon source or as a by-product after hydrogen etching. Emission lines of CH radicals at 387 nm and 430 nm, C_2 Swan band system in the range 465-590 nm and Balmer lines at 410 nm, 434 nm, 486 nm, and 656 nm were also analyzed. During plasma

deposition CH_4 precursor was able to easily convert to CH_X (x = 1-3) radicals, to produce carbon dimers (C_2) through radical recombination and subsequent dissociation (Hofmann et al. 2003). The C_2 Swan band system has a large influence on the nucleation process (Mantzaris et al. 1998). OES spectra within 5 minutes of deposition show a Swan band system with high intensity, which decreases after 10 minutes due to the nucleation in the first stage of growth. The radical density of C_2 ranging from 10^{17}-10^{19} m^{-3}, in ICP system, is favorable for the initial growth of vertical nanostructures. Furthermore, the hydrogen plasma has proven to be effective in promoting the crystallinity of the carbon materials by the following factors: (1) atomic hydrogen can preferentially etch amorphous phase and (2) atomic hydrogen can induce crystallization (Vizireanu et al. 2010). Cheng et al. reported that, hydrogen radical etched away loosely bonded carbons and promoted the graphitization in diamond like carbon (DLC) films. In our case the hydrogen radical would etch away disordered components (carbon atoms) such as amorphous carbon rather than ordered, because the bond strength of disordered carbons is weaker than that of ordered ones. Therefore, hydrogen radical would etch away disordered phase selectively and by this way decrease of the disordered carbon formation, which would affect positively to the growth of MLGNWs (Avetisyan 2019).

We have also checked the OES for the oxygen plasma functionalization of the hybrid structure (Figure 4.21-b).

Electron impact excitation of ground-state molecular and atomic oxygen leads to emission at 844.6 and 777.4 nm, which is predicted by the following mechanisms:

Dissociative excitation $e + O_2 \rightarrow e + O^* + O$

Direct impact excitation $e + O \rightarrow e + O^*$

where O^* refers to the O(3p5P) state which emits at 777.4 nm and to the O(3p3P) state which emits at 844.6 nm (Krstulović et al. 2006). Walkup *et al* showed that in oxygen plasma the 844.6 nm oxygen emission line is more reliable than the 777.4 nm (Walkup et al. 1998), hence, in these figures the intensity of the 844.6 nm O emission line is shown. As is clear, increasing oxygen gas flowrate leads to a slight decrease in the density of atomic oxygen and oxygen molecular ions. This is attributed to the recombination of active species: $e + O_2 \rightarrow 2e + O_2^+$ (Lieberman and Lichtenberg 2005).

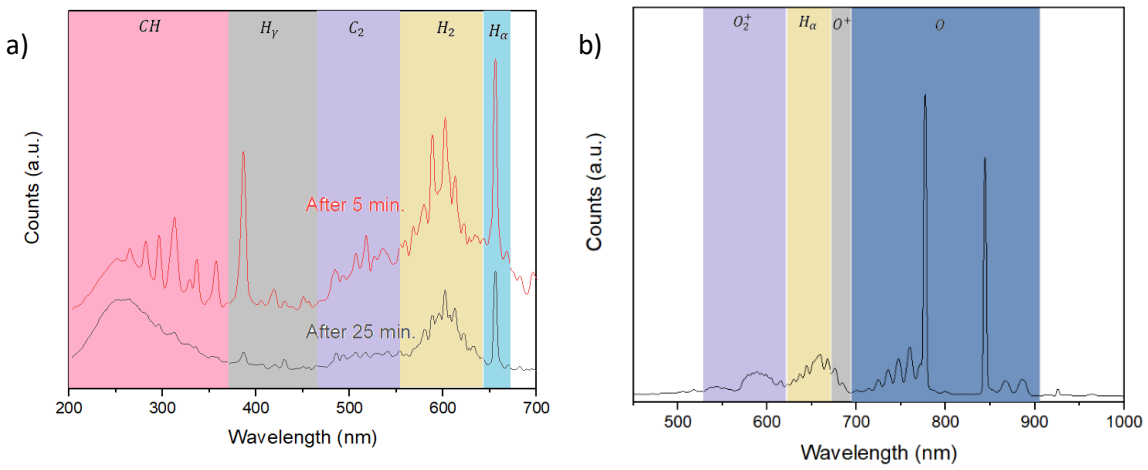

Figure 5.13. a) Optical emission spectra from CH_4 methane plasma taken at different deposition times; and b) Optical emission spectra from the O_2 plasma.

5.4.3. Electrodeposition of MnO_2

The prepared samples of CNTs and carbon hybrid structure over Papyex® paper were used as electrodes for supercapacitors. As know, the MnO_2 has high specific capacitance which leads us to use the large surface area of our carbon materials as a base of the MnO_2. The MnO_2 was deposoited electrochemically using 0.2 M of Mn_2SO_4 in a solution of Na_2SO_4 of 0.1 M concentration. We deposited the MnO_2 for different periods of time (5, 10, and 15 min.) and we studdied the morphology of the obtained samples using SEM, EDS, Raman, and the electrochemical characterization for super capacitors. The chart in figure 5.14. shows the voltage change during the deposition of the MnO_2 for different times. In the three experiments for both structures, we used the same amount of MnO_2 which is 0.5 ml but the dropping was faster or slower depending on how fast we need to deposit the material.

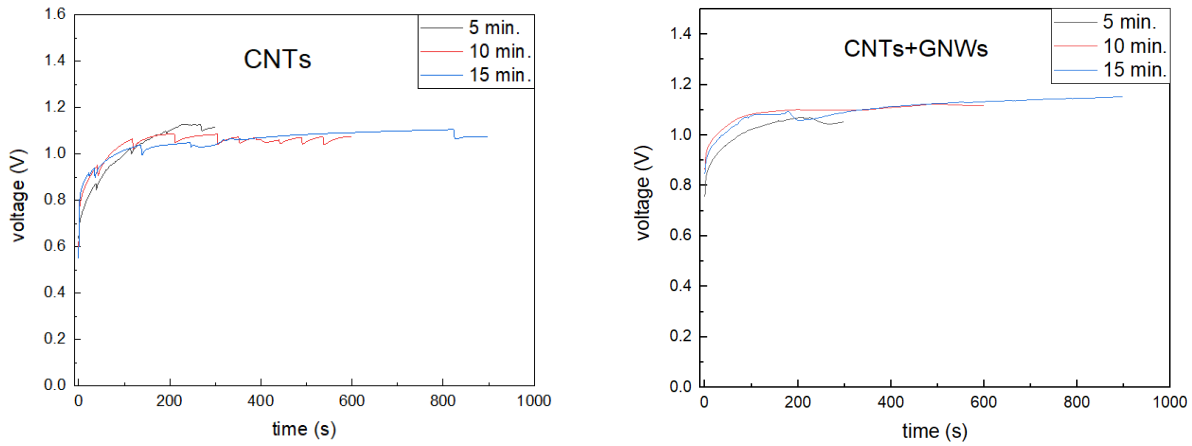

Figure 5.14. Voltage vs. time during the deposition of the MnO_2 for a) CNTs and b) CNTs+GNWs on SS310 substarte.

5.4.4. Scanning Electron Microscope and Energy-dispersive X-ray spectroscopy

By looking at the SEM images of CNTs+MnO_2 and the CNTs+GNWs+MnO_2 after MnO_2 for different times, we can observe that the manganese oxide was increasing until 15 min. (Figure 5.15). The atomic concentration of C, Mn and O_2 obtained from the EDS are shown in table 5.3 (Figure 5.16).

Sample	Mn (At%)	O (At%)
CNTs+GNWs+5 min. MnO_2	38.37	17.28
CNTs+GNWs+10 min. MnO_2	48.53	22.47
CNTs+GNWs+15 min. MnO_2	60.48	25.31
CNTs+5 min. MnO_2	13.62	7.34
CNTs+10 min. MnO_2	24.39	9.65
CNTs+15 min. MnO_2	31.33	14.01

Table 5.3. At% of Mn and O after the electrodeposition of MnO_2 on CNTs and hybrid carbon structure on SS310

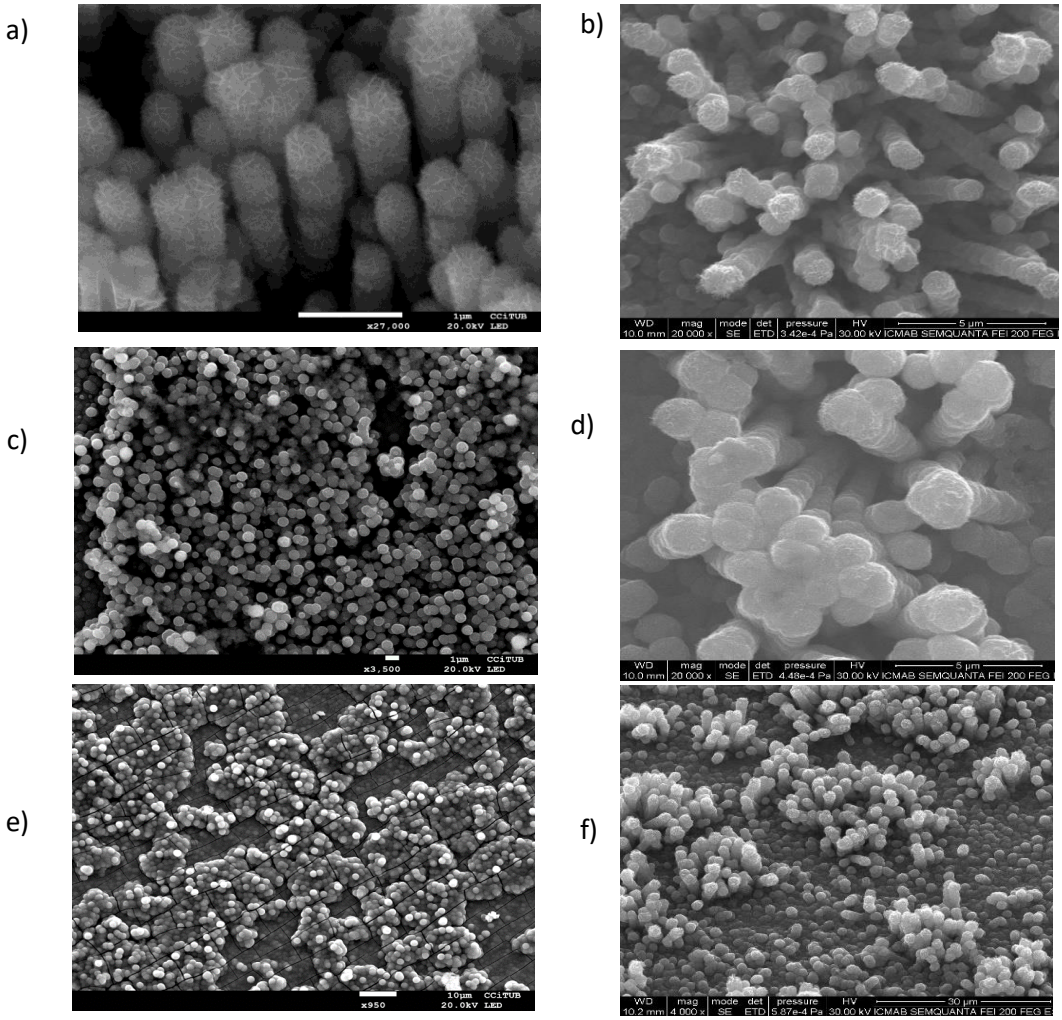

Figure 5.15. SEM images of (a, c and e) CNTs with the deposited MnO_2 for 5, 10, and 15 min. respectively, and (b, d, and f) CNTs+GNWs with deposited MnO_2 for 5, 10, 15 min. respectively.

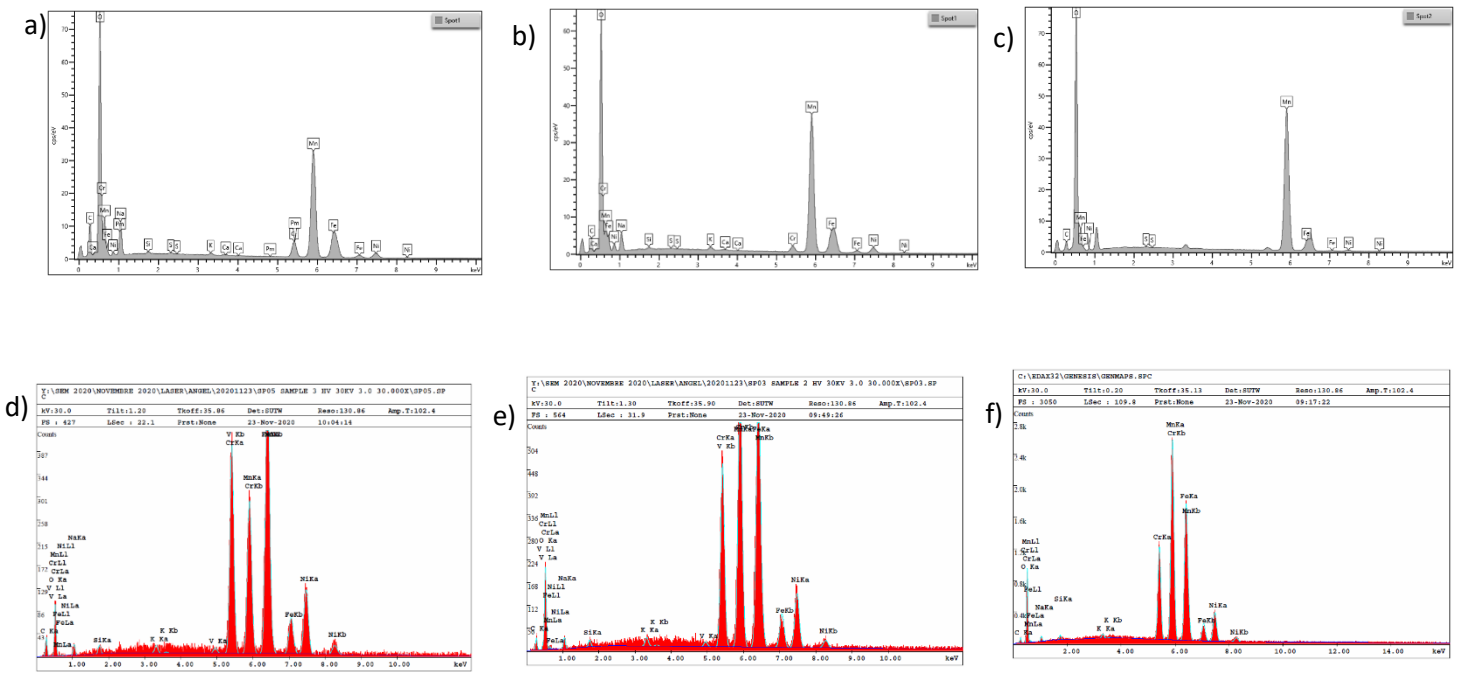

Figure 5.16. EDS spectra of (a-c) CNTs with the deposited MnO_2 for 5, 10, and 15 min. respectively, and (d-f) CNTs+GNWs with deposited MnO_2 for 5, 10, 15 min. respectively.

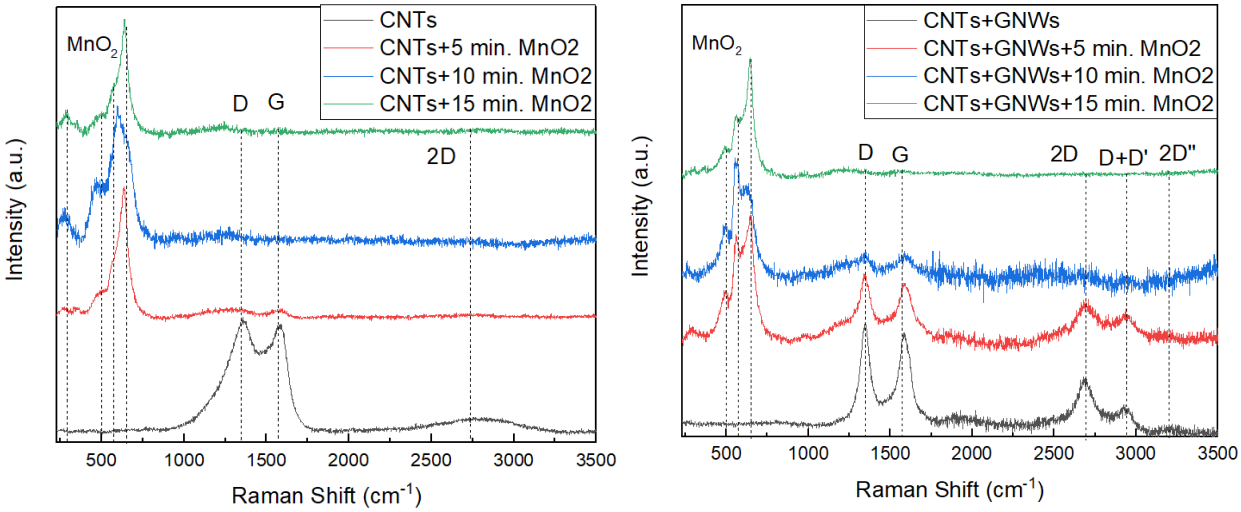

Figure 5.17. Raman spectra of the CNTs and hybrid structure carbon material before and after the deposition of MnO_2 for 5, 10, and 15 min.

5.4.5. Raman Spectroscopy of MnO_2

The samples were characterized after the electrochemical of MnO_2 deposition where the carbon bands start to disappear as we increase the MnO2 deposition time as it covers the carbon material (Figure 5.17). The MnOx where obtained in the range of 175 cm^{-1} and 633 cm^{-1}. The strongest peak we obtained at 633 cm^{-1} which is due to the symmetrical stretching vibrations (Julien et al. 2003; Gao et al. 2009). At low wave number region, two peaks were observed at 175 cm^{-1} and 283 cm^{-1}. The one at 175 cm^{-1} can be ascribed to the external vibration because of the MnO_6 octahedral translational motion (Wang 2012; Cheng et al. 2014) while the 283 cm^{-1} band is assigned to the δ-MnO_2 layered structure (Julien and Massot 2002). The two bands indicate as well the existence of the tunnel like structures of α-MnO_2 phase (Roychaudhuri et al. 2018). The peak at 576 cm^{-1} is also coming from the basal plane of the MnO_6 (Hsu et al. 2011).

5.4.6. Cyclic Voltammetry

After the deposition of the MnO_2, the average specific capacitance of the samples in 1 M Na_2SO_4 solution was determined from the cyclic voltammograms. In general, the specific capacitance of the samples (both structures: CNTs and hybrid) increased until the deposition of MnO_2 for 10 min. then it started to decrease when the deposition time increased, which can happen because the MnO_2 is fully blocking the carbon structure and therefore lower specific area.

Figure 5.18 shows the cyclic voltammograms at a scan rate of 5 mVs^{-1} of MWCNTs Untreated CNTs present almost a rectangular-shape voltammograms associated with double layer capacitance. The Cyclic voltammetry was achieved using a three-electrodes cell which is explained in Chapter 3. The specific capacitance increased from 3.1 mF/cm^2 for CNTs to 128.21 mF/cm^2 for hybrid carbon structure at scan rate 5 mv/s after 10 min. of MnO_2 deposition.

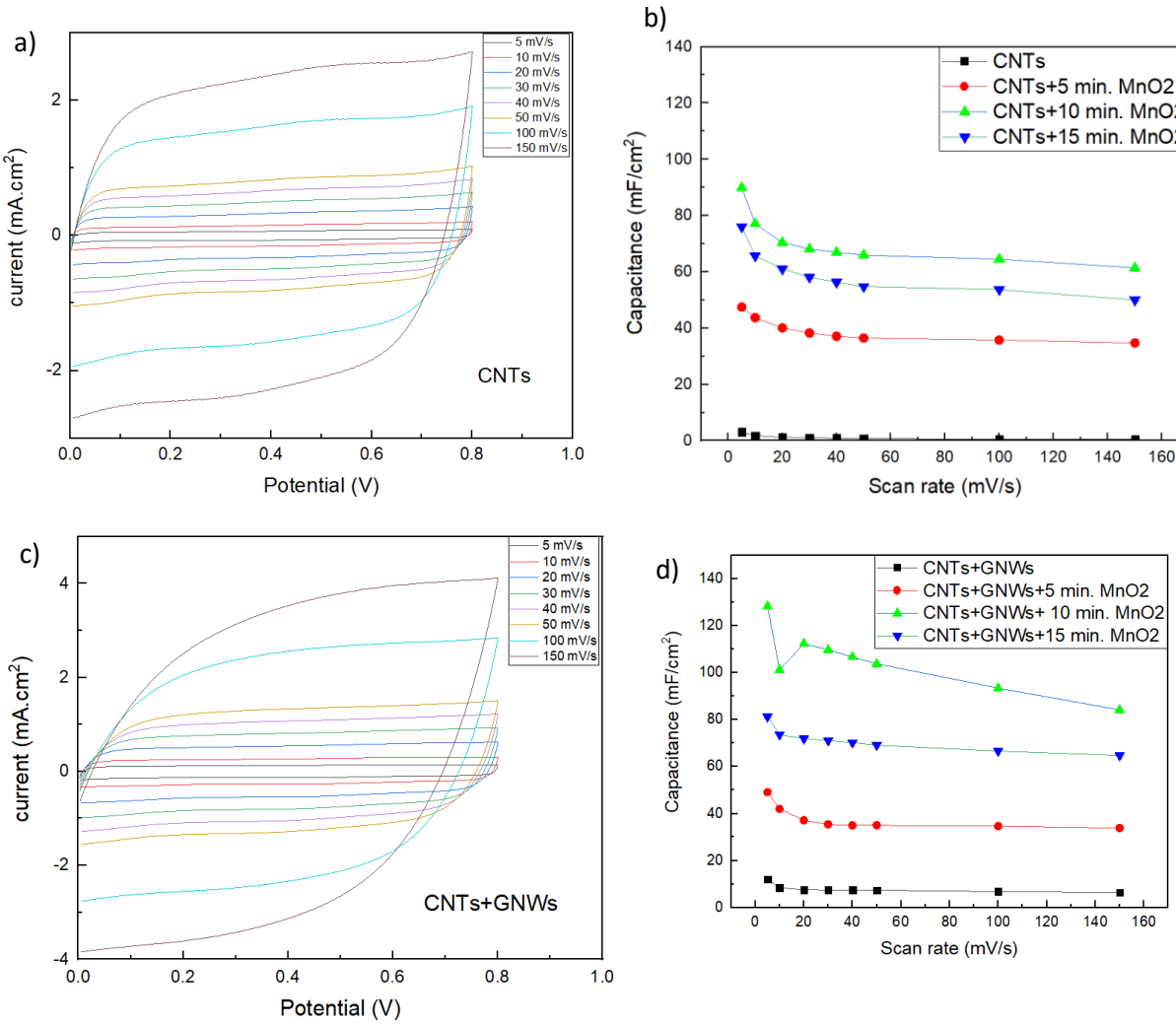

Figure 5.18. a,c) Cyclic Voltammetry at different scan rates for CNTs and hybrid carbon structure (CNTs+GNWs) after 10 min of MnO_2 deposition, respectively, and b,d) Specific capacitance vs. scan rate of CNTs and hybrid structure grown on SS310 substrate and after the deposition of MnO_2. Still the increase was not as high as the specific capacitance of CNTs and hybrid structure are 89.9 and 128.21 mF/cm^2.

We observed that the hybrid carbon structure before the deposition of MnO_2 had a higher specific capacitance than the CNTs which increased from 3.1 mF/cm^2 to 12.0 mF/ cm^2 as expected and proved from Raman spectra where the hybrid structure was in general more crystalline. When we deposited the MnO_2, the specific capacitance of the hybrid structure started

to increase more than of the CNTs where its high specific area played an important role in increasing the specific area of the MnO_2.

5.4.7. Electrochemical impedance

Electrochemical impedance spectroscopy was performed by applying an alternating voltage of 10 mV between 0.1 Hz and 100 kHz. This technique provides more information on the electrochemical processes that take place at the interfaces and the bulk of electrode materials. An equivalent circuit can be found describing the different processes such as load transfer resistance, diffusion or capacitance. However, this is beyond the scope of this work, and only interception with the x-axis, which is related to electrochemical series resistance (ESR), will be comment. The ESR is the result of all the contact resistances, electrolyte resistance and electrode resistances that are present in our system and is a crucial parameter for fast charge/discharge rates. In the case of CNTs this resistance increases once MnO_2 is deposited, due to the additional resistance of the oxide layer (Figure 5.19). In the case of GNWs the ESR increased when depositing MnO_2 for 5 min. but then decreased with longer time deposition, while in the CNTs samples the ESR increased from 0.5 to about 2.5 Ω, which is expected as with the increase of the MnO_2 deposition time, the oxide layer becomes thicker and therefore more resistive as expected. In general the ESR values range was between 0.5 and 3.75 Ω.

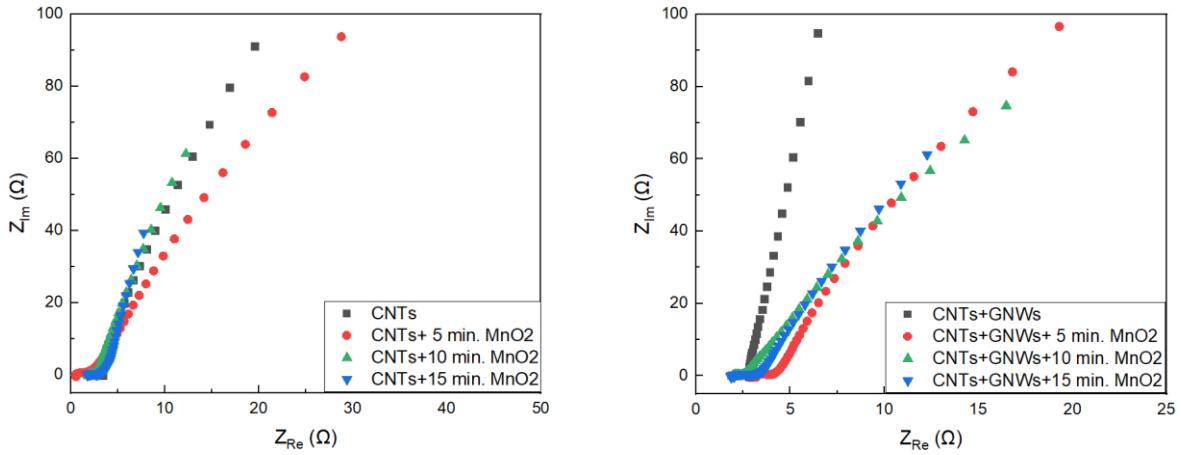

Figure 5.19. Impedance spectra of a) CNTs before and b) hybrid carbon structure before and after the deposition of MnO_2.

5.5. Conclusions

The carbon nanotubes were successfully grown over a flexible SS310 alloy after optimizing the parameters using Box-Wilson experimental design. The experimental design could optimize the annealing time and the PECVD temperature. Prior to starting the growth of nanotubes, H_2 plasma was applied on the substrate at 680 °C for the reduction process to remove the native oxide layer from the surface of the substrate. No previous preparation or polishing was done to the substrate. The parameters that were provided by the experimental design were annealing time 1010 s and PECVD temperature 700 °C. The obtained CNTs were about 3.02 µm long with a diameter about 71.2 nm. Using EDS-HRTEM mapping, we could find that two catalyst elements contributed in the growth of the nanotubes, which are Fe and Ni. The CNTs were used as a support for the growth of GNWs using ICP-CVD process leading to a hybrid structure allowing the increase of the surface area. The CNTs and hybrid carbon nanostructure were used to deposit MnO_2 electrochemically in order to increase the specific capacitance. The capacitance increased until a deposition time 10 min of MnO_2 and started to decrease again when the deposition time increased more as the MnO_2 layer blocked the pores as it was observed by SEM. After 10 min of the deposition of MnO_2, the specific capacitance increased from 3.1 mF/cm^2 to 89.9 mF/cm^2 for CNTs and from 12.0 to 1218.2 mF/cm^2 for the hybrid structure at scan rate 5 mV/s. This result is relatively high comparing with other complex techniques as there is no publications on growing the nanotubes on SS310 and the process was done in one continuous step for both processes, reduction and CNTs growth. The EDS result showed the increase of the at% for Mn and O_2. The ESR of all samples was determined. It was found that it increases with increasing MnO_2 deposition time. ESR values are generally in the range of 0.5 Ω to 3.75 Ω for all samples.

Chapter 6

Synthesis of CNTs and metal oxide nanoparticles at atmospheric pressure

6.1 Introduction

Carbon nanotube (CNT) is one of the widely studied nanomaterials from the carbon family (Paradise and Goswami 2007; Ferreira et al. 2019; Yadav et al. 2019a). CNTs possess extraordinary mechanical, thermal, chemical, optical and electronic properties, which can be exploited for potential use in various fields (Thostenson et al. 2001). After extensive efforts by various scientists and engineers across the globe, CNTs and CNT based products have been commercialized, majorly consisting of multiwalled CNTs (MWCNTs) (Dasgupta et al. 2014; Pirard et al. 2017). Whereas commercial products based on single-walled carbon nanotubes (SWCNTs) are still in the development phase. Depending upon the chirality, single-walled carbon nanotubes (SWCNTs) can be either metallic or semiconducting (Baughman et al. 2002). Metallic SWCNTs (m-SWCNTs) are widely used in the conductive coatings, specifically for solar cells, organic light emitting diodes, electrochromic devices, etc. (Maeda et al. 2008) while, semiconducting SWCNTs (s-SWCNTs) are widely used as a channel material for field effect transistors, low-cost printable devices, etc. (Fujii et al. 2009). Various methods, such as, arc discharge, laser ablation and catalytic chemical vapour deposition (C-CVD) have been studied for the synthesis of SWCNTs. Out of these three methods, C-CVD is widely studied due to inherent potential for large scale production (Yadav et al. 2017). Most of the synthesis routes end up with producing mixture of m-SWCNTs and s-SWCNTs which impede the process of commercialization of SWCNT based products. In the past two decades enormous efforts have been devoted in order to synthesize SWCNTs with single chirality or either metallic or semi-conducting. The approaches utilized by various researchers can be classified into two, i.e. post synthesis separation and direct controlled growth (Liu et al. 2017). In post synthesis separation, the mixture of SWCNTs is separated by exploiting the differences in physical and chemical properties. Density gradient ultracentrifugation (Arnold et al. 2006), gel chromatography , dielectrophoresis (Lee et al. 2005), polymer wrapping (Zheng and Diner 2004), aromatic extraction (Li et al. 2004a), selective oxidation (Miyata et al. 2005), DNA recognition (Zheng et al. 2003), etc. are few examples of post synthesis separation techniques. These techniques are quite effective in term of separation of metallic and semiconducting SWCNTs, but not cost effective. In addition, usage of complex physical and chemical treatments results in contamination of SWCNTs and incorporation of defects in the

structure. In order to circumvent the separation problem, it is always desirable to have SWCNTs with uniform type having majorly metallic or semiconducting i.e. by direct controlled growth. Direct synthesis of SWCNTs with specific type (m or s) has been studied by various groups in last two decades (Xu et al. 2017; Cheng et al. 2018). Detailed analysis of the reported literature suggests that the type of SWCNTs i.e. either m-type or s-type gets fixed during nucleation stage itself, since along the length of SWCNTs no change in type is observed (Arenal et al. 2012). Exception to this Zhao et al. (Zhao et al. 2016) recently reported variable chirality along elongation of SWCNTs using tandem plate CVD where the synthesis temperature varied periodically. Hence, in order to have SWCNTs with specific type (m or s), control over the nucleation step during synthesis of nanotubes is of utmost importance while maintaining the synthesis temperature constant throughout the experiment. In C-CVD, various parameters such as type of carbon source [32,33], synthesis temperature (Lolli et al. 2006), catalyst type (Bachilo et al. 2003; Sanchez-Valencia et al. 2014), system pressure (Bachilo et al. 2003), growth time (Yang et al. 2015), carrier gas composition (Harutyunyan et al. 2009; He et al. 2010), etc. affect the nucleation and subsequently the type of the grown CNTs. It is quite interesting to observe that more than two decades after discovery of CNTs (Iijima 1991) in 1991 and paramount synthesis of SWCNTs (Bethune et al. 1993; Iijima and Ichihashi 1993) in 1993. Various strategies utilized by different groups for selective growth of SWCNTs (either m-type of s-type) are listed in Table 1. Bachilo et al. (Bachilo et al. 2003) reported selective synthesis of s-SWCNTs (~57%) mainly consisting of SWCNTs with chiral index (6, 5) and (7, 5). CoMoCAT method was utilized for the synthesis with CO as carbon source at 5 atm. In order to have fine control over the active catalyst cluster, lower ratio of Co:Mo (1:3) was used which aids in the formation of smaller diameter s-SWCNTs. Zhang et al. [46] reported highly selective synthesis of s-SWCNTs (~99%) by utilizing selective etching of m-SWCNTs. Ethanol was used as carbon source with cobalt deposited on SiO2/Si as catalyst at 800 °C and 1 atm. Post synthesis of SWCNTs, exposure to methane plasma followed by vacuum annealing leads to selective etching of m-SWCNTs. Harutyunyan et al. (Harutyunyan et al. 2009) reported selective synthesis of m-SWCNTs (~91%). They found that the catalyst morphology and the chirality of SWCNTs are interdependent. In situ TEM studies were also reported in support of the hypothesis. Catalyst morphology was modulated by varying the ambient conditions during thermal annealing of the catalyst. In addition, oxidative species such as water were utilized in order to increase the fraction of m-SWCNTs. Loebick et al. (Zoican Loebick et al. 2010) have reported the usage of bimetallic catalyst i.e. CoMn on MCM-41 silica templates with CO as carbon source and hydrogen as carrier gas at 1 atm. Shape and size of catalyst i.e. Co in presence of Mn played a major role in selective synthesis of s-SWCNTs (~93%). In addition, they also reported

that the size and shape of catalyst is dependent on the synthesis temperature, while lower synthesis temperature favoured synthesis of s-SWCNTs. Che et al. (Che et al. 2012) reported selective synthesis of s-SWCNTs (~97.6%) using isopropanol as carbon source and iron deposited on quartz as catalyst (Yadav et al. 2019b).

6.2. FC-CVD and properties of obtained CNTs

Floating catalyst chemical vapour deposition (FC-CVD) is one-step process driven synthesis of "direct-spun" CNT aerogels (Li et al. 2004b), drawing on earlier papers pointing to CNT aerogel synthesis in closed reactor tubes (Cheng et al. 1998; Pimenta et al. 2000; Chen et al. 2009). The decomposition of simple iron, sulfur and carbon precursors in a high temperature tubular furnace results in catalyst nanoparticles suspended in a continuously flowing buffer gas (principally H2) from which a high concentration of individual CNTs (typically of up to 15 nm diameter (Moisala et al. 2003; Li et al. 2004b) grow. The individual CNTs are attracted to one another via van der Waals dispersion forces, creating bundles (typically of 30-50 nm diameter) which at the same time become entangled with one another, forming a continuous, me-chanically cohesive CNT network, commonly referred to as an "aerogel".

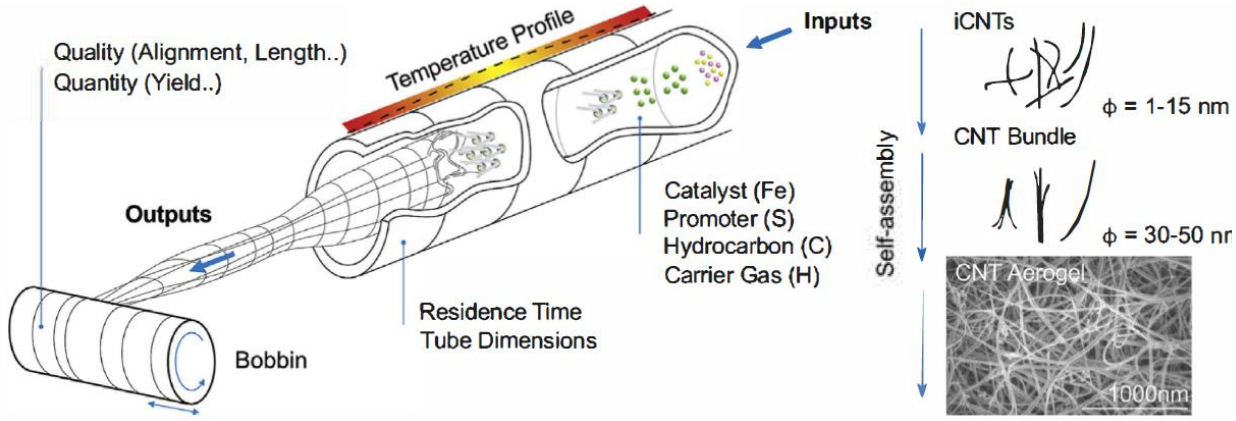

Figure 6.1. Schematic of direct-spinning CNTs process listing the parameters required for quantitative mapping and showing the self assembly of the macroscopic material from individual CNTs (typically 1-15 nm diameter) through bundles (typically 30-50 nm diameter) to a contibuous aerogel. Input parameters required are catalyst, promoter, hydrocarbon and carrier gas and corresponding flow rates. Output parameters required are product quantity (mass, density) and quality (CNT alignment, hexagonal lattice uniformity, diameter, wall number, length of individual CNTs and purity(Weller et al. 2019).

While early reports estimated nanotube lengths to be of the order of hundreds of microns up to 1 mm (Conroy et al. 2010), in most cases the CNT lengths have not been measured. Recent work by Tran et al. (Tran et al. 2017) assessed CNT minimum lengths to be of the order of a few microns by oxidising direct-spun CNT samples, followed by sol-ubilisation in chlorosulfonic acid. Bulmer et al. (Gspann et al. 2017) determined a length of about 10 µm between CNT defects in direct-spun samples and proposed that these defects could be interpreted as ends of tubes in very pure samples. These minimum values are still significantly longer than the lengths of individual CNTs found in high-purity commercial samples such as HiPco 188.3 (0.29 µm), HiPco 183.6 (1.51 µm), SWeNT CG300 (0.71 µm), and UniDym OE (1.92 µm) (Tran et al. 2017).

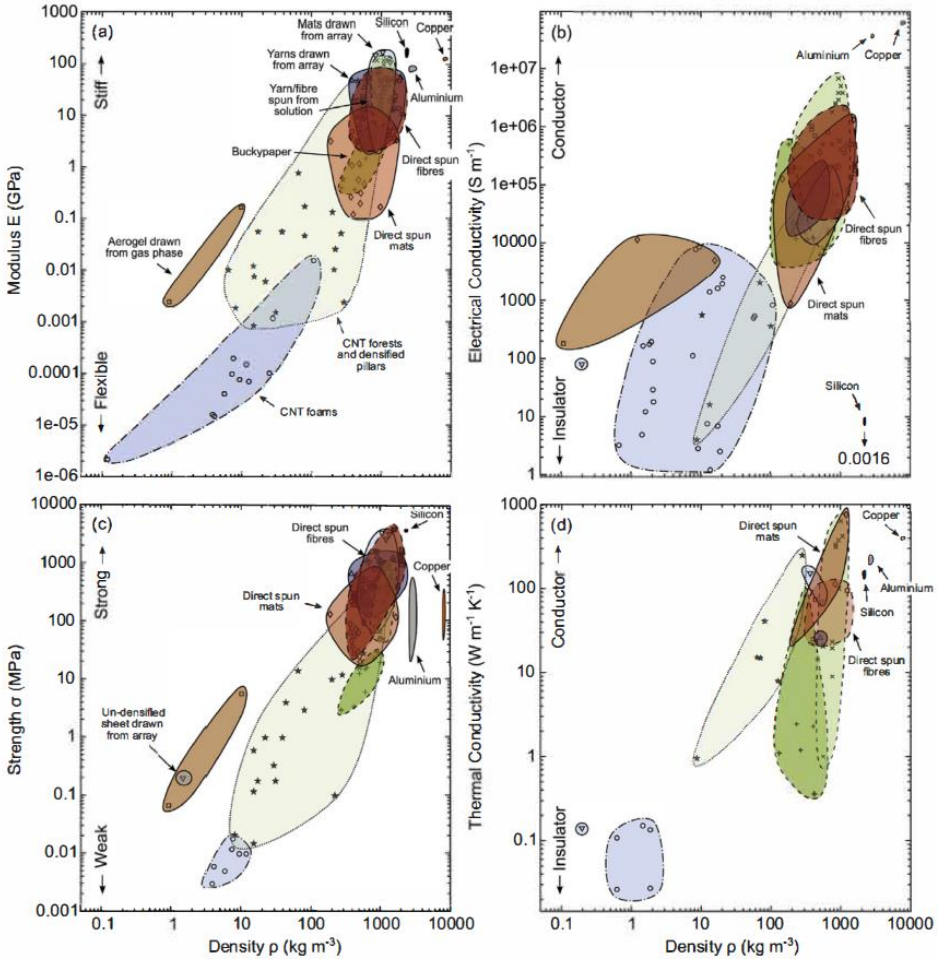

Figure 6.2. Macroscopic properties of various CNT materials compared with those of silicon, copper and aluminium plotted as a function of density. The properties highlighted are (a) Young's modulus, (b) electrical conductivity, (c) tensile strength and (d) thermal conductivity(Weller et al. 2019).

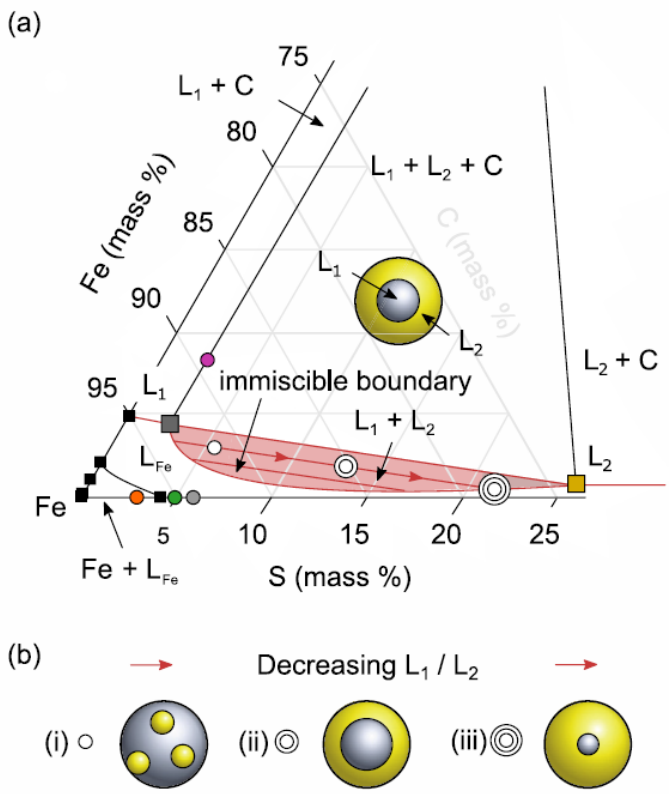

Figure 6.3. (a) Bulk equilibrium section (mass percentages) of the Fe-C-S ternary phase diagram at 1400 °C. Black squares on the Fe(S) axis mark phase changes on the related Fe-C(Fe-S) binary phase diagrams. The schematic within (a) shows the two immiscible carbon and sulfur-rich liquids L_1 and L_2 that comprise an active catalyst nanoparticle. The orange, green and grey (purple) circles indicate an active (inactive) catalyst mass composition in the absence of carbon. Single, double and triple-circled points indicate catalyst nanoparticles of decreasing L_1/L_2 ratios of 3, 1 and 0.25, respectively with (b) illustrating the impact of this on the catalyst composition (Weller et al. 2019).

The aerogel can be extracted from the furnace system and collected on a bobbin. The aerogel can be treated in-line with a solvent, where capilla1y action causes condensation to form a thin microfibre ("direct-spun fibre"). Alternatively multiple layers of the uncondensed aerogel can be collected on a bobbin to create a sheet of CNT material ("direct-spun mat"), which can be treated with solvent to allow some condensation if required. The FC-CVD pro-cess is illustrated in Fig. 1, which shows the input flows required for the synthesis, the types of output flows which can be recorded, and a schematic of the bundling mechanism which creates the aerogel, further

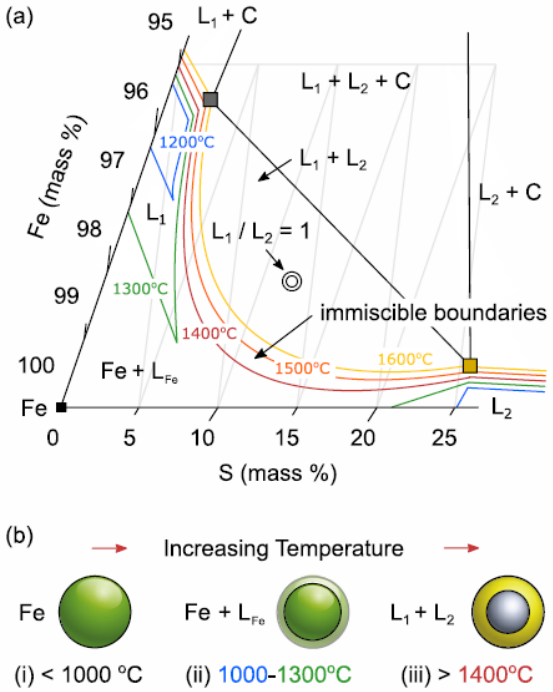

Figure 6.4. (a) Bulk equilibrium section (mass percentages) of the Fe-C-S ternary phase diagram at various temperatures between 1200 °C and 1600 °C. The carbon and sulfurrich liquids phases L_1 and L_2 exist above 1200 °C with the immiscible boundaries occurring for a range of Fe:C:S compositions at temperatures above 1300 °C. The double-circled point is located in (a) where the Fe:C:S composition corresponds to $L_1/ L_2=1$ with (b) showing the impact of increasing temperature on the phases of this catalyst nanoparticle (Weller et al. 2019).

illustrated by an example scanning electron microscope (SEM) image of a typical aerogel material.

The methods for producing macroscopic CNT materials have been refined since their initial inceptions, producing microfibres, mats and films with increasingly superior properties. Data in Fig. 2 hows the mechanical, electrical and thermal properties of direct-spun materials up to early 2016 for thermal properties and early 2017 for the remainder, compared to other carbon materials and conventional high strength or high conductivity materials (aluminium, copper, silicon) (Weller et al. 2019).

The properties of direct-spun materials compare very favourably to, and in some cases outperform, the established materials, particularly when their low densities are considered. As shown in Fig. 2, direct spun fibres can reach Young's modulus values of 100 GPa (Vilatela and Windle 2012), tensile strengths of 3.75 GPa (Wang et al. 2014), electrical conduc-tivities of 2 x

10^6 sm^{-1} (Wang et al. 2014) and thermal conductivities of 95 W m^{-1} K^{-1} [40]. More recent thermal conductivity data shows values up to 900Wm-1 K^{-1} for macroscopic direct-spun fibre samples (Gspann et al. 2017)

The portfolio of the current direct-spun product properties, combined with the relative simplicity of the direct-spun production method and the potential to improve properties further towards those of individual CNTs has, therefore, attracted significant in-dustrial interest due to the wide range of fields where application of these materials might induce step changes in tech-nologies. Various reviews and publications provide excellent summaries of applications of macroscopic CNT materials, including those from direct-spun production methods, covering areas such as electrical applications (Yu et al. 2016), composites (Yadav et al. 2017), synthesis (Janas and Koziol 2016), smart textiles (Foroughi et al. 2016) and improvement in strength (Jung et al. 2018).

6.3. Process mechanism

The trends observed from mapping the experimental data and the associated conclusions regarding the roles of the key elements (Fe, S, C, H) in the direct-spinning process facilitate a much richer description of their roles.

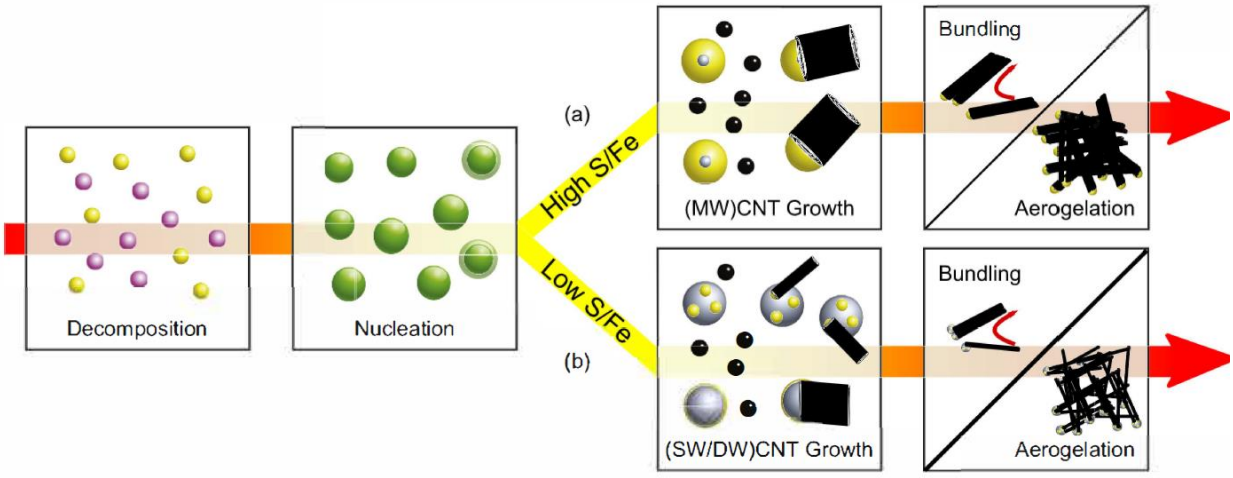

Figure 6.5. Schematic showing the impact of high (a) and low (b) sulfur to iron ratios on direct-spun CNT product synthesis. High S/Fe ratios favour MWCNT synthesis while low S/Fe ratios favour SW- or DWCNT synthesis due to the different catalyst nanoparticles formed. The pink, yellow and black circles represent decomposition of precursor sources releasing iron, sulfur and carbon, respectively (Weller et al. 2019).

(Tafwidli and Kang 2017) work on the Fe-S-C ternary phase diagrams has allowed a more accurate determination of the phase boundaries from 1600 to 1200 °C as shown in figure 6.4-a. This new information highlights that the coexistence of the carbon-rich liquid (L_1) and sulfur-rich liquid (L_2) phases, for a given Fe:C:S ratio, only occurs above 1400 °C in Figure 6.4-a. Between 1200 °C and 1300 °C, both phases can exist, but only at high C (mass%) and high S (mass%), respectively, represented by the areas bounded by the blue and green isothermal phase boundaries, respectively. The first step in the reaction pathway in figure 6.5. represents the decomposition of iron and sulfur precursors, releasing the corre-sponding Fe (pink) and 5 (yellow) atoms for catalyst nanoparticle nucleation. Carbon precursor molecules have not undergone pyrolysis at this stage, so are not illustrated in this step. The second step represents catalyst nano-particle nucleation, promoted by s with catalyst nanoparticle structures starting off as Fe and Fe + L_{Fe} as shown in figure 6.4. Catalyst nanoparticles increasing in temperature will be evolving towards L_1 + L_2 structures capable of rapid CNT growth but diffusion losses of small catalyst nanoparticles and evaporation of the remaining particles will be competing with this process.

At the renucleation and CNT growth stage, the pathways differ depending on whether high (Figure 6.4-a) or low (Figure 6.4-b) S/Fe ratios are present, however for both routes the CNT growth is driven by acetylene-like pyrolytic carbon compounds. Sufficient dilution of the entire reaction system by carrier gas is required such that carbon molar concentration does not exceed 3%. The presence of H also chemically suppresses soot formation.

Figure 6.5-a illustrates how a high S/Fe ratio leads to catalyst nanoparticles of predominantly L_2 composition (see Fig. 8(b)(iii)), therefore the whole diameter of the catalyst nanoparticle is used for CNT growth, generally favoring MWCNT synthesis. Where the S/ Fe ratio is high, results point towards H being utilized in the reac-tion to remove excess S from the catalyst into the gas phase, ig. figure 6.5-b illustrates how a low S/Fe ratio leads to catalyst nanoparticles of predominantly L_1 composition with only a little L_2 (figure 3-b (i)). This restricts the sizes of the sites from which CNTs grow, favoring rapid growth of nanotubes of small diameter, therefore predominantly SWCNTs or DWCNTs, with the possibility of growing more than one CNT from each catalyst nanoparticle.

The final steps on both pathways represent the self-assembly of CNTs into bundles driven by van der Waals dispersive forces and the further assembly of bundles to create the continuous aerogel which allows continuous, direct spinning of the macroscopic CNT material (Weller et al. 2019).

6.4. Classification of bulk material

Methods for producing CNT materials may be divided into three families, together resulting in eight different types of CNT material.

Figure 6.6. illustrates the three families, the methods which comprise them, and their morphologies. The first family involves processing vertically aligned CNTs grown from substrates by chemical vapor deposition; these CNT 'forests' may be (i) densified into pillars, (ii) spun into 1-dimensional fibers, or (iii) drawn into aligned 2- dimensional mats. The second family utilizes liquids to create suspensions or solutions of short, mass-produced CNTs. CNT-solvent solutions can be filtered to create (iv) random planar 'buckypaper' mats, or spun into coagulating fluids to produce (v) single fibers. Porous CNT foams (vi) are often produced from aqueous gel precursors by critical point drying, or freeze drying. The final family uses direct-spun carbon nanotube aerogels, produced via the 'Windle process'. Direct-spun fibers (vii) are produced by on-line solvent condensation of the aerogels; alternatively, the spinning of aerogel layers onto a rotating mandrel, with or without solvent condensation, produces direct-spun mats, labelled (viii). Charts that summarize the elastic moduli, strength, and electrical and thermal conductivity as a function of density for these CNT-based materials are presented in figure 6.2. Note that the bulk density of CNT materials ranges from a few kg/m3 for CNT foams to over 1000 kg/m3 for CNT fibers, whilst their moduli range from tens of kPa to hundreds of GPa. Large differences in strength and conductivity are also observed. Wide property variations occur between classes and also within individual material classes. For example, direct-spun materials exhibit a large variation in mechanical properties due to their range of material alignment and density (Alemán et al. 2015). The macroscopic modulus of CNT materials is much below the Voigt upper bound, based on the in-plane modulus of a CNT wall (i.e. graphene). A similar observation can be made for strength as follows. If the ultimate tensile strength of CNT walls is assumed to be 100 GPa, all CNT morphologies lie more than an order of magnitude below the Voigt bound for ultimate tensile strength, as illustrated in Fig. 6.2-b. In broad terms, the moduli and compressive yield strength of CNT foams and CNT forest based materials appear to scale with density ρ according to $E \sim \rho^3$ and $\sigma \sim \rho^2$ respectively. This scaling law is representative of cellular solids of low nodal Connectivity (Treacy et al. 1996).

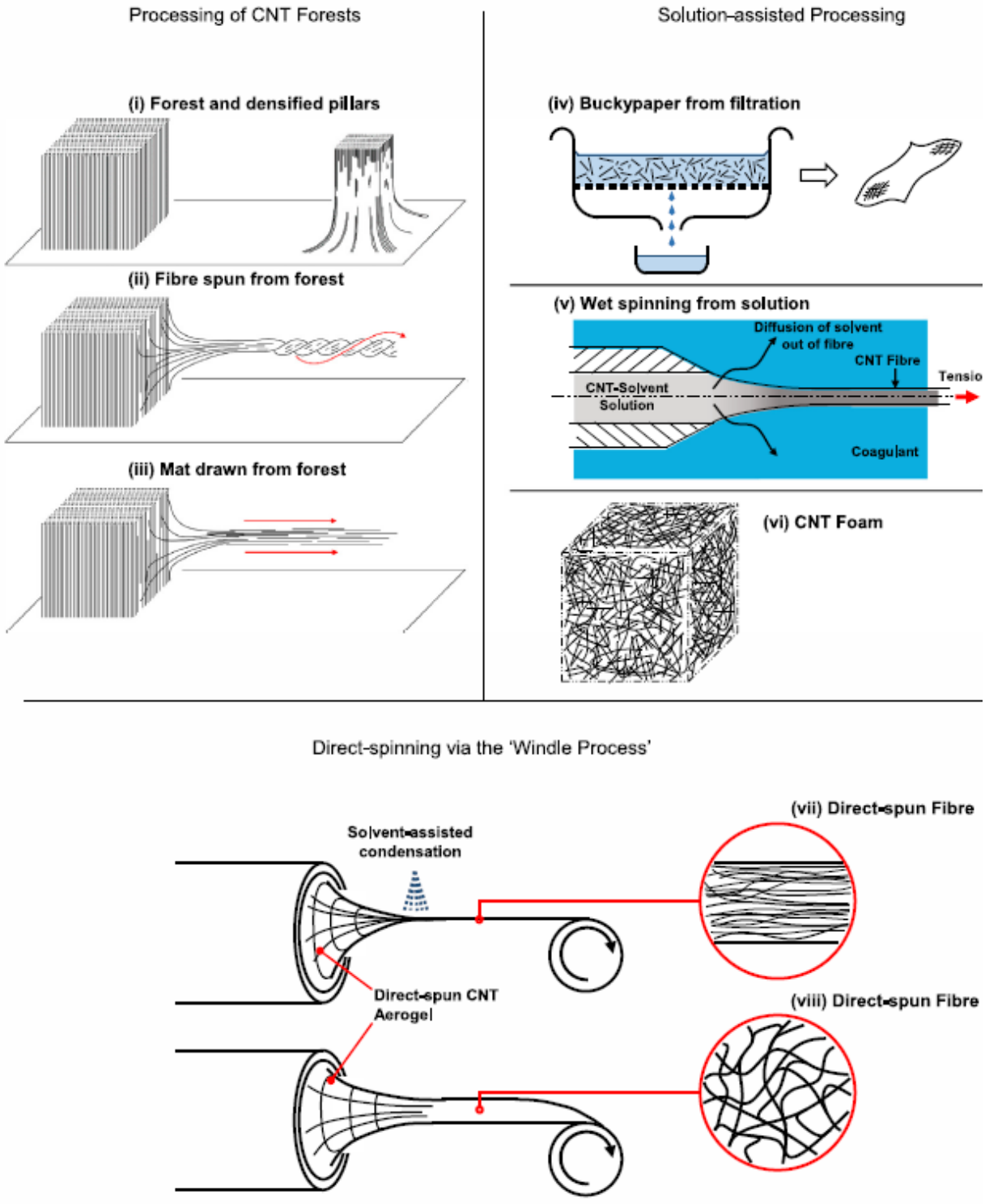

Figure 6.6. Classes of bulk materials and production methods (Bruggeman et al. 2016).

6.5. Plasma-Liquid interaction process

Plasma–liquid interactions are becoming an increasingly important topic in the field of plasma science and technology. The interaction of non-equilibrium plasmas with a liquid state is important in many applications ranging from environmental remediation to material science and health care. Cavendish's famous work 'experiments on air' from 1785 might be the first report involving plasma–liquid interaction and dealt with the production of nitric acid by an electric spark in air (Cavendifli and Read June 1785). Experiments dealing with the interaction of plasmas and liquids in the context of electrochemistry date back more than 100 years ago (Gubkin 1887). Up to about 30 years ago, the main focus in the field of plasmas in and in contact with liquids was on glow discharge electrolysis (Hickling and Ingram 1964) and the study of breakdown of dielectric liquids for high-voltage switching (Martin et al. 1996). These works were followed by a strong emphasis on environmental driven research exploiting the fact that plasmas in and in contact with liquids are rich sources of reactive species, such as •OH, O• and H2O2, and UV radiation (Sato et al. 1996). Plasmas are, in fact, a form of advanced oxidation technology enabling the breakdown of organic and inorganic compounds in water (Foster et al. 2012). Many studies on microsecond pulsed discharges in water have addressed these topics (Šunka et al. 1999).

The field of analytical chemistry often uses plasma devices to prepare samples or as a sampling process for the analyses of solutions. These techniques are typically based on glow discharges with liquid electrodes (Webb and Hieftje 2009), inductively coupled plasmas (Rosen and Hieftje 2004) and a variety of corona, dielectric barrier discharges and glow discharges as ionization

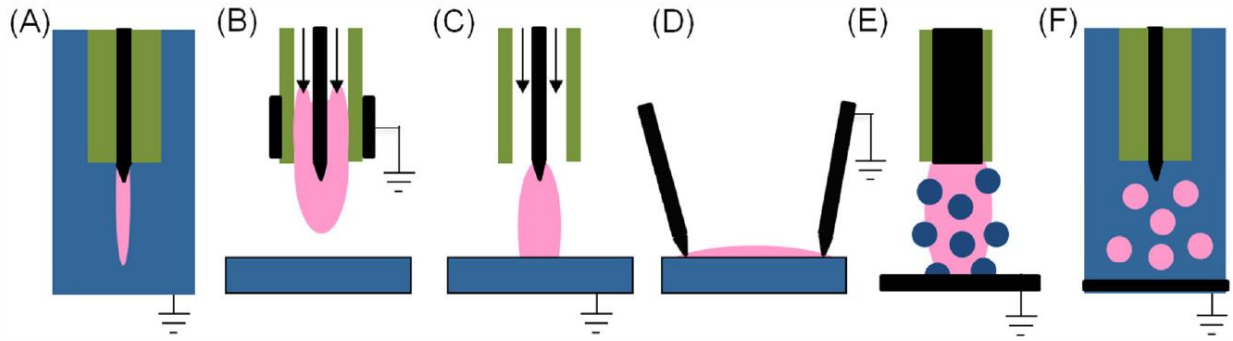

Figure 6.7. Schematic of different discharges used in plasma–liquid interactions: (A) direct discharge in liquid, (B)–(D) gas phase discharges and (E) and (F) multiphase discharges. In more detail: (B) plasma jet without direct contact with liquid, (C) gas phase plasma with liquid electrode, (D) surface discharge, (E) gas phase plasma with dispersed liquid phase (aerosols) and (F) discharges in bubbles. Blue = liquid, pink = plasma, green = dielectric, black = metal electrodes (Bruggeman et al. 2016).

sources for mass spectrometry (Smoluch et al. 2016). The emphasis in these uses of plasmas is typically not to intentionally transfer reactivity from the plasma into the liquid for the purposes of making a more reactive liquid. The plasma community has greatly benefited from this work. The topics addressed in this manuscript build on this knowledge base produced by the analytical chemistry community. However, the focus here is on plasma–liquid interactions and particularly on the physical and chemical mechanisms leading to complex feedback between the plasma and liquid at the plasma–liquid interface resulting in reactivity in the liquid. During the last 15 years, the focus of research on the interactions of plasmas with liquids has broadened to address a variety of application areas, including electrical switching (Martin et al. 1996), analytical chemistry (Webb and Hieftje 2009; Smoluch et al. 2016), environmental remediation (water treatment and disinfection) (Foster et al. 2012), material synthesis (nanoparticles) (Mariotti et al. 2012), material processing (photoresist removal, plasma-polishing, polymer functionalization) (Friedrich et al. 2008; Ishijima et al. 2013), chemical synthesis (H2O2, H2) (Bruggeman and Leys 2009), sterilization and medical applications (plasma induced wound healing, tissue ablation, blood coagulation, lithotripsy) (Sato et al. 1996; Fridman et al. 2008)]. These exciting opportunities have challenged the plasma community with multidisciplinary scientific questions. In addition to specialized review articles, two broader reviews focusing on the applications and the physics of plasmas in and in contact with liquids, have been published (Locke et al. 2005; Bruggeman and Leys 2009).

Plasmas interacting with liquids: classification of conditions

Similar to gas-phase plasmas, plasma–liquid systems can be classified based on the method of generation or configurations. However, the type of interactions with liquid is of particular importance to plasma–liquid systems because it highly influences the plasma properties. One such classification scheme is:

- Direct liquid phase discharges
- Gas phase plasmas producing reactivity in the liquid
    - Without direct contact/electrical coupling with the liquid
    - With direct contact/electrical coupling with the liquid (liquid electrode)
    - At the plasma liquid interphase (surface discharges)
- Multiphase plasmas including
    - Gas phase plasmas with dispersed liquid phase (aerosols)

- Gas phase plasmas dispersed in the gas phase (bubbles) in liquid While many other classifications can be considered, this scheme stresses the different kinds of interactions of plasmas which in turn emphasize differences in plasma generation and heat, mass and species transport. Although this review is far from exhaustive, it provides insights on the different types of plasmas in and in contact with liquids (Bruggeman et al. 2016).

6.6. synthesis parameters and results

6.6.1. Synthesis of CNTs

The CNTs synthesis process and principles using FC-CVD is explained above in details and the reactor we have used is shown in figure 3.24 and figure 6.1. The ferrocene ($C_{10}H_{10}Fe$) was used as a source of Fe, which represents the catalyst with a flow of 130 sccm, Methane (CH_4) was the carbon source with a flow of 160 sccm, and thiophene (C_4H_4S) was the source of S that will promote the growth of nanotubes by preventing the agglomeration of Fe nanoparticles by encapsulating them. with a flow of 90 sccm. Also, we used H_2 with a flow of 1350 sccm which has the same rule of NH_3 in the PECVD process to reduce the formation of amorphous carbon. The process was carries out at temperature 1230 °C. This process usually either produce CNTs or just produce a cloud of gases if the parameters aren't adjusted well which makes it easy to know at the moment if we have CNTs or no. Figure 6.7. Shows how the CNTs mat looks when extracted from the tubular reactor.

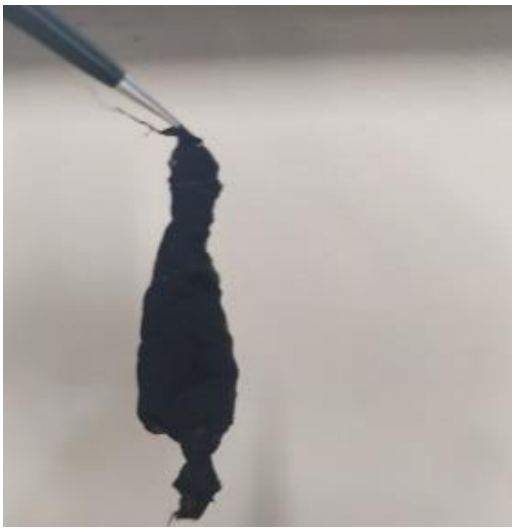

Figure 6.8. CNTs mat obtained by FC-CVD process

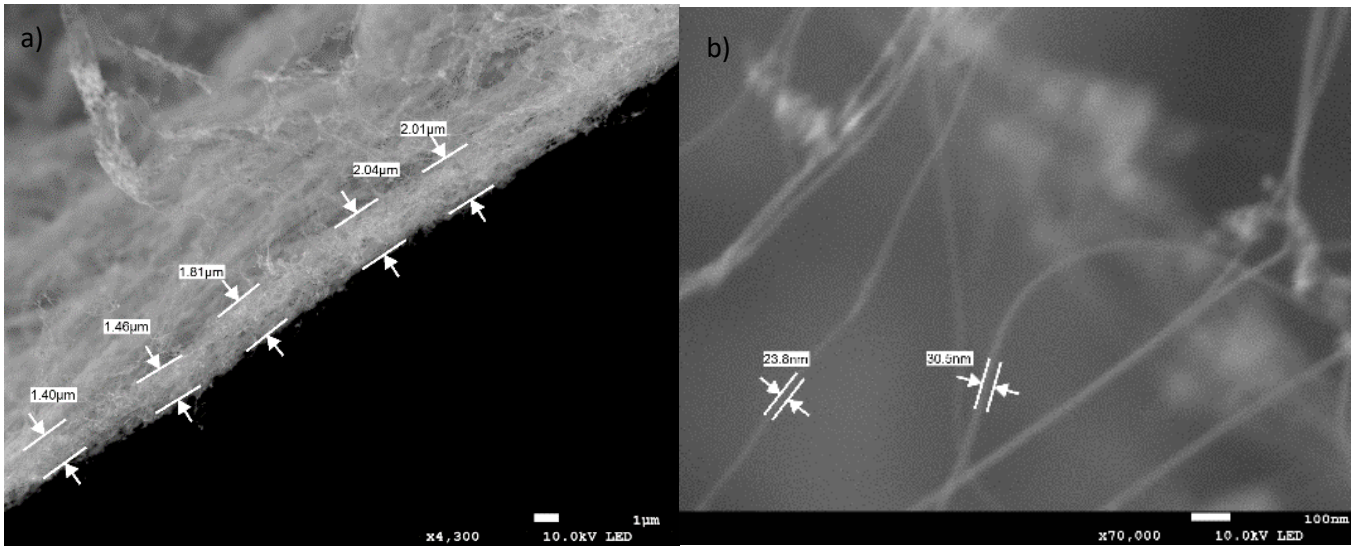

Figure 6.9. FE-SEM images of CNTs ribbons obtained by FC-CVD. a) shows the thickness of the CNTs mat and b) shows the diameter of the nanotubes.

Using FE-SEM, we could see the thickness of the mat (ribbon), which was in the range between 1.40 µm and 2.01 µm. Also it was possible to measure the diameter of the nanotubes by SEM, which was in the range of 20-30 nm.

The EDS spectrum shows that the CNTs are still containing the Fe and S that were used during the process (Figure 6.10), which was proved again with the EDS-HRTEM mapping of a single tube (Figure 6.11)

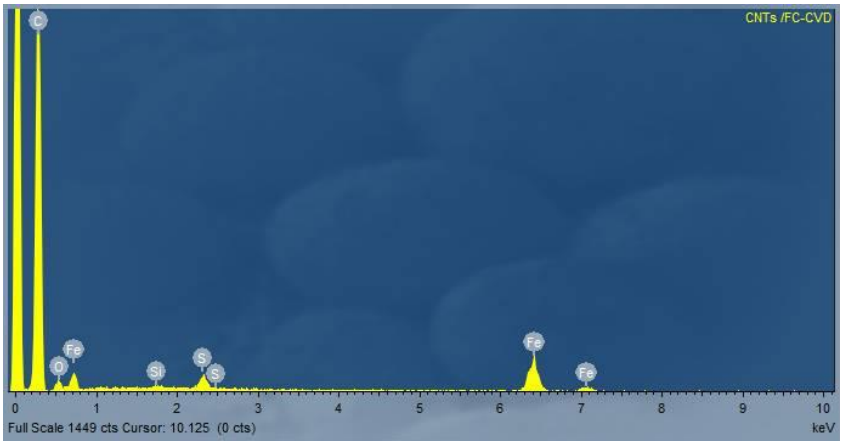

Figure 6.10. EDS of the obtained CNTs using FC-CVD

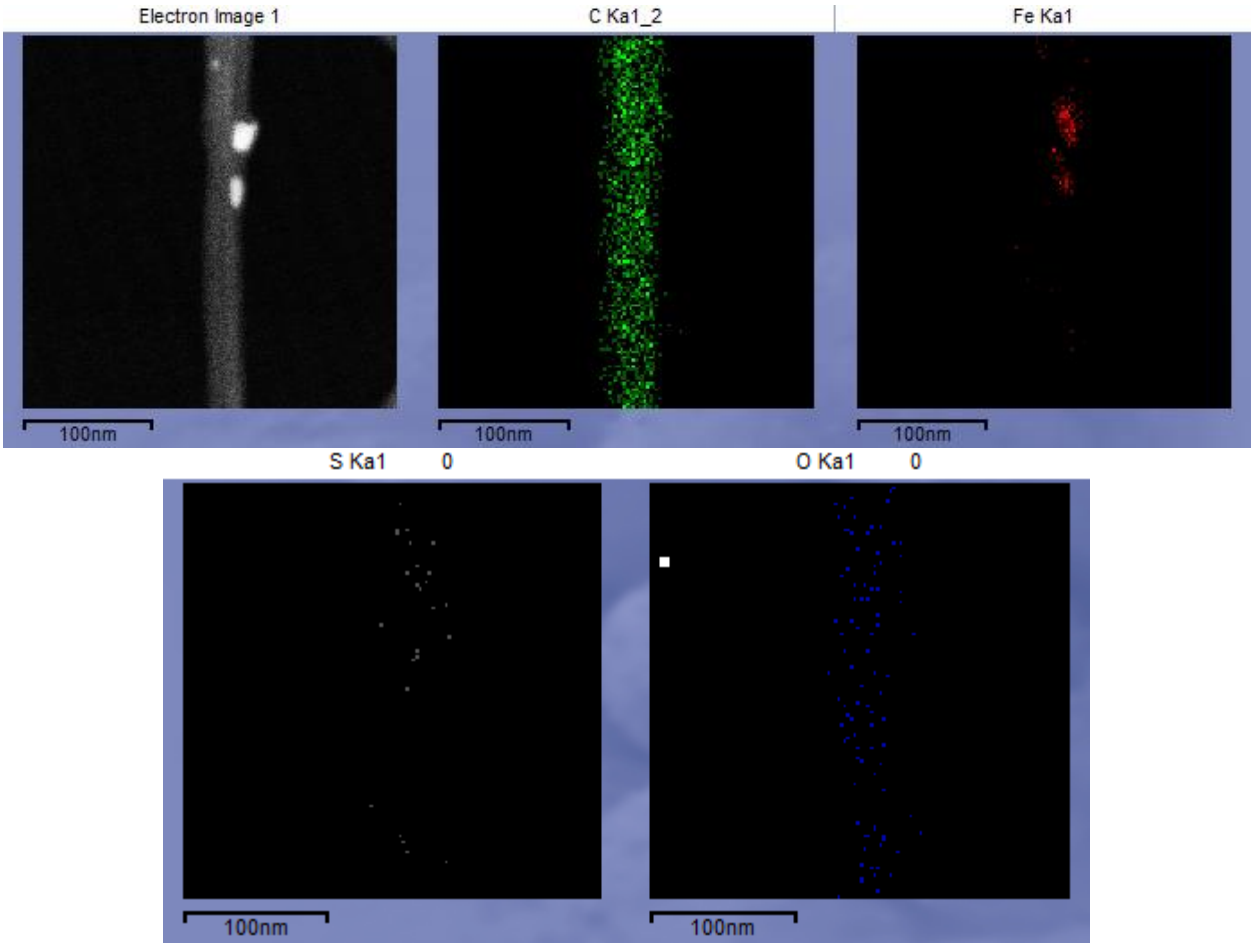

Figure 6.11. Mapping analysis of the obtained CNTs using EDS-HRTEM.

Raman Spectroscopy was used to evaluate the quality of CNTs which shows the two characteristic bands, the tangential stretching G mode (1500-1600cm^{-1}) and the D mode (1330-1360 cm^{-1}) (Korneva 2008) (see Figure 6.12). In addition, multi wall carbon nanotubes (MWCNTs) present a band in the range 1617 to 1625 cm^{-1} called D'-band that corresponds to defects on the side walls of CNTs (Lehman et al. 2011). D'-band is related also with disordered graphitic lattice. These bands are activated by defects due to the breaking of the crystal symmetry that relax the Raman selection rules (Merlen et al. 2017). This band is existed which means that we have multi-layers CNTs. The D band, like the D'-band, is a double resonance Raman mode which can be attributed to the presence of disordered graphitic lattice (Düngen et al. 2017), double resonance effects in sp^2 carbon and other defects (Osswald et al. 2007; Lehman et al. 2011). Following the deconvolution process presented by (Sadezky et al. 2005) in Raman spectra we didn't find the

D'' band which is related to the amorphous carbon and normally exists at 1500 cm^{-1}. The crystalline size L_a was found high, comparing with the other nanotubes we obtained before, for this crystalline structure, which was 5.84 nm.

In figure 6.12 it is also possible to distinguish three strong bands that are close to 2D (G') band. In the literature these 2D sub-bands are denominated D+D'', D+D' and 2D' and are found at 2460, 2940 and 3230 cm^{-1}, respectively (Merlen et al. 2017). The number and origin of the 2D sub-bands have been understood for multilayer graphene (Ferrari et al. 2006) in the framework of the double resonance mechanism and more complex things can occur such as folding (Podila et al. 2012), misorientation (Poncharal et al. 2008), and stacking faults that can modify the intensities and shape (Merlen et al. 2017). In our case these bands can be attributed to the few number of walls of the CNTs. G, 2D and 2D sub-bands are sensitive to defect density in the MWCNTs, including the ones related to tube diameter and number of walls (Antunes et al. 2007).

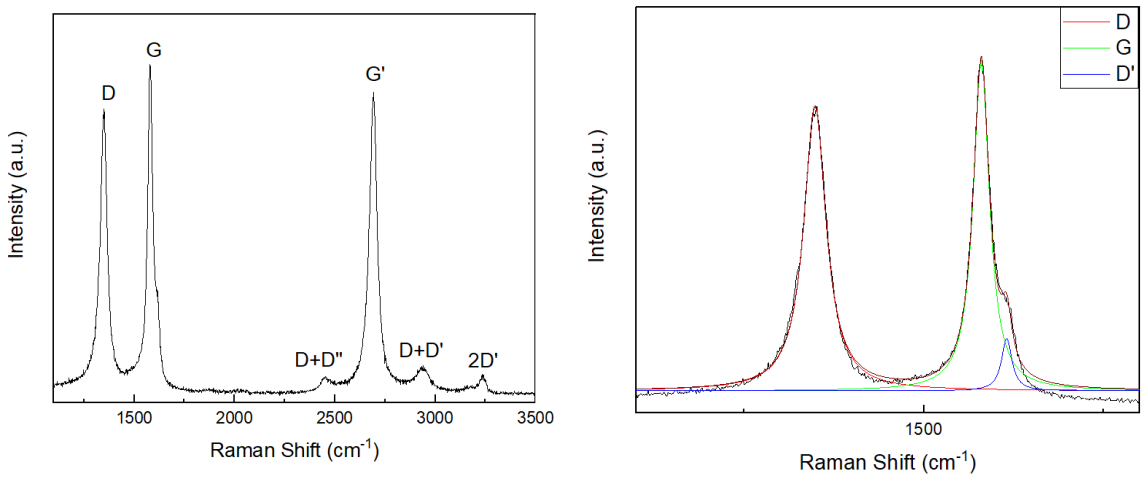

Figure 6.12. Raman spectroscopy of the CNTs showing D, G, D', and G' bands.

		D	G	D'	I_D/I_G	L_a (nm)
CNTs	Position (cm^{-1})	1348.32 ± 0.76	1579.9 ± 0.62	1615.23 ± 2.95	0.86	5.84
	FWHM (cm^{-1})	37.66 ± 2.2	27.51 ± 1.98	17.55 ± 9.75		
	Intensity (a.u.)	25.2 ± 1.82	29.27 ± 2.73	4.65 ± 3.39		

Table 6.1. Data of the distinguished Raman spectrum peaks of CNTs.

6.6.2. Synthesis of NiO_x

NiO_x nanoparticles were synthesized using the plasma-liquid interaction process which is explained previously. The synthesis parameters were improved by the group where this work was done. The process (Figure 6.13) in considered a very simple one comparing with the other methodologies to obtain nanoparticles.

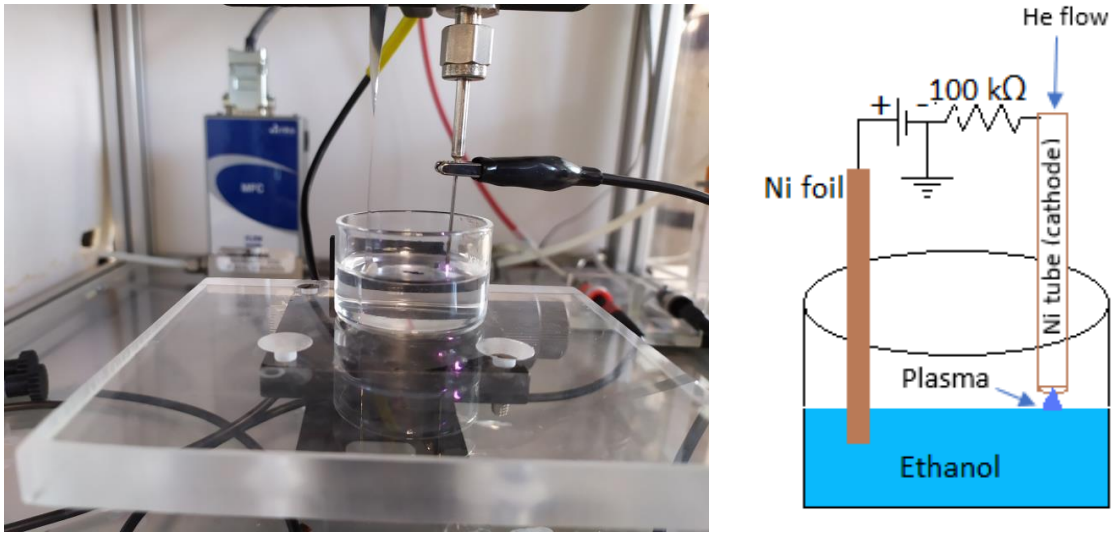

Figure 6.13. Image and schematic of the plasma interaction with ethanol during the synthesis process of NiO_x nanoparticles.

The process depends on flowing noble gas in a conductive tube to be located just on top of the liquid (without touching) and emerging the foil of the metal we need to synthesis its oxide nanoparticle in the same liquid. The process depends on applying high DC potential between the tube where the Ar flows and the emerged foil. The current will not be high at the beginning but must be limited to a specific maximum value. When the plasma is ignited, the metal will start to decompose, therefore the resistance will decrease which will allow the increase of current. If we don't stop the process when the current reached to its adjusted maximum, the voltage will start to decrease.

This process is very critical to many parameters that must be concerned:

1- Maximum current

2- Applied voltage

3- conductivity of the electrolyte

4- immersed area of the cathode (metal foil) in the electrolyte.

5- The gas flow in the capillary.

6- The distance between the metal foil and the capillary.

We achieved the process in 15 ml of ethanol as we used a Ni capillary and a Ni foil. The distance was kept between the foil and the capillary at 1.5 cm. 1.5 cm^2 was immerged in the ethanol and the voltage adjusted at 3 kV. Once the current reached its maximum which was 5 mA, the voltage started to decrease. The voltage value reached to 1.8kV after 45 min. of starting the process. During the process, the Ar flow was set at 50 sccm. The nanoparticles of NiO_x where characterized by TEM where their majority have a spherical shape of about 5 nm dimater (Figure 6.14).

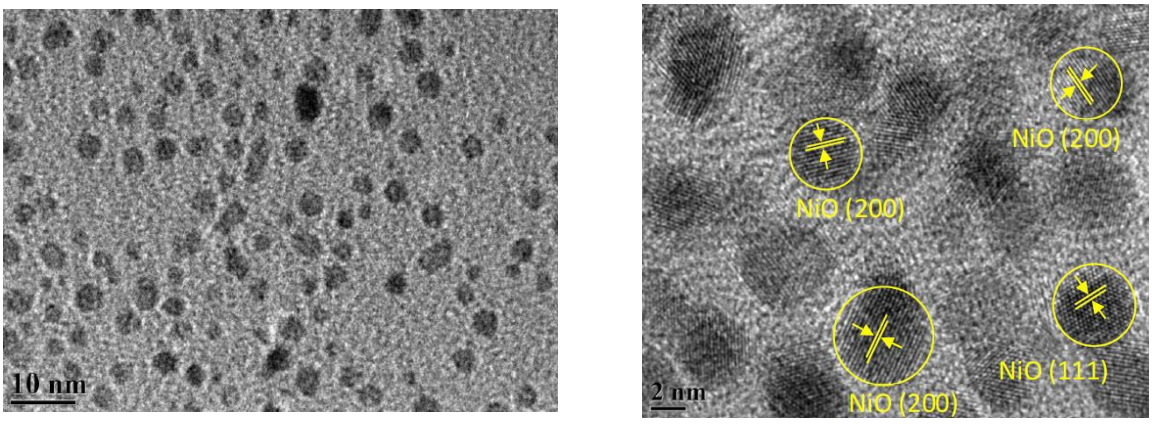

Figure 6.14. TEM images of the NiO_2 nanoparticles obtained by plasma-liquid interaction process.

6.6.3. Electrochemical characterization

Foe electrochemical characterization, the obtained CNTs were dispersed in pure ethanol and in the solution of NiO_2 nanoparticles to compare the characteristics of each method. They were sprayed on graphite paper to support the minimum weight of CNTs. Using cyclic voltammetry we could find the capacitance of the CNTs alone, and when it is dispersed in the nanoparticles solution (Figure 6.15). Four samples were tested by CV using 1 M of Na_2SO_4 to compare the capacitance of the CNTs and NiO_x. The first sample is the Papyesx® substrate to find its capacitance before adding any other material. The second sample is CNTs that is dispersed in ethanol. The third sample is the NiO_x nanoparticles, and the forth is the CNTs that are dispersed in the NiO_x nanoparticles. The second, third and forth samples are sprayed on Papyex® substrate to study the improvement in the capacitance. We found that the capacitance tendency is increasing with the nanotubes. The areal specific capacitance values for the samples of Papyex®, NiO_x, CNTs, and CNTs+NiO_x were 21.53, 26.77, 31.21 and 80.56 mF/cm^2, respectively, at scan rate 10 mV/s (Figure 6.16). The ESR has increased when we add more material to the Papyex substrate which is logical because of the addition of the resistance of the added materials. It was noticed by comparing the ESR of CNTs and NiO_x when each of them was used alone that it is higher for the NiO_x (Figure 6.17).

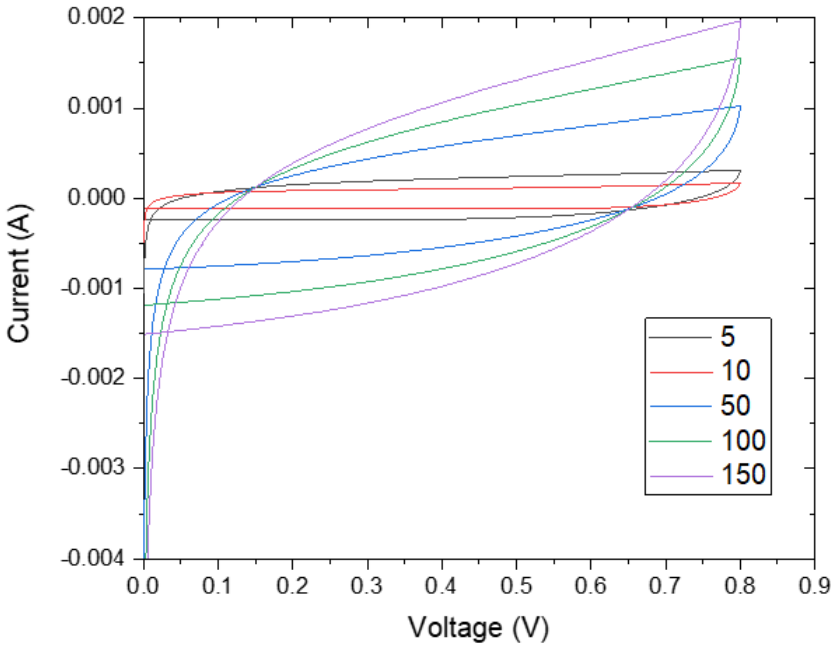

Figure 6.15. Cyclic voltammetry of CNTs and NiO_x nanoparticles mixture at different scan rates

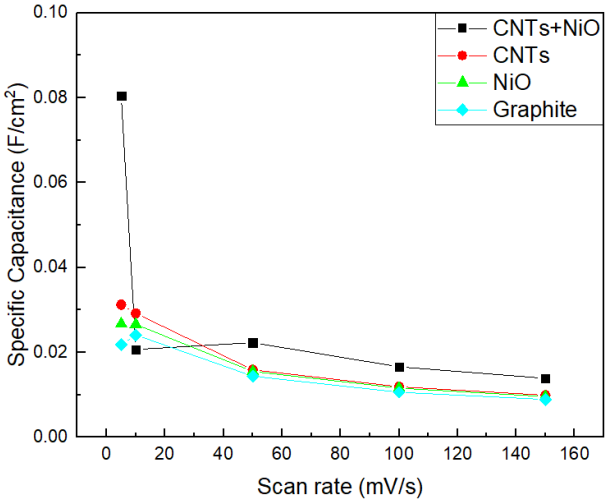

Figure 6.16. Areal specific capacitance of Papyex® substrate only and with NiO_x, CNTs, NiO_x+CNTs.

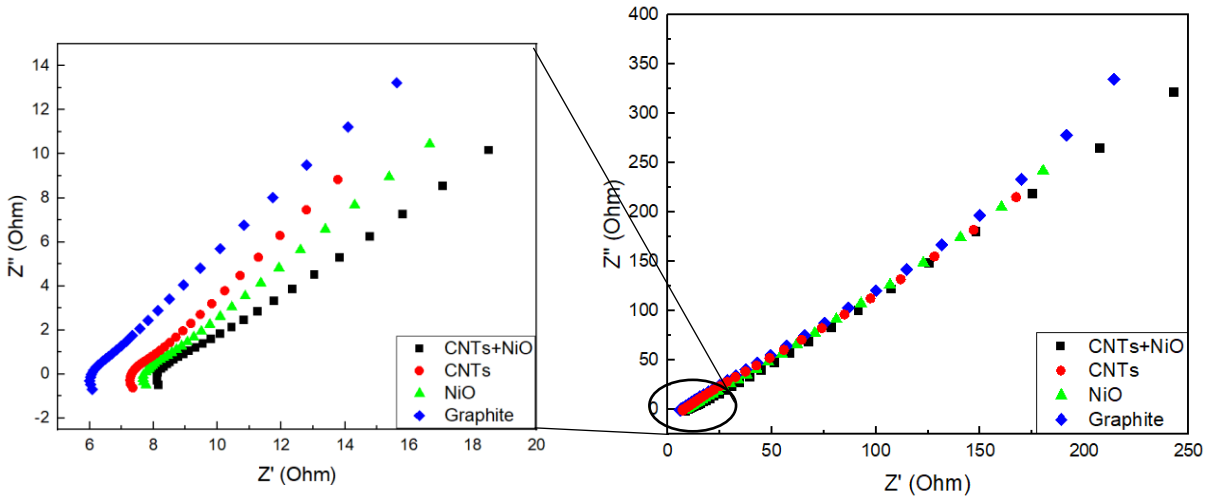

Figure 6.17. Impedance spectra of Papyex®, NiO_x, CNTs, NiO_x+CNTs.

This methodology could look for instance no different from the previous ones as we needed a substrate at the end but the difference is the remarkable quality of the CNTs that we could obtain without the difficulty of taking into account the substrate obstacles during the growth. In addition, this process ensure the continuous production of CNTs which makes it scalable, therefore, suitable for a wide field of industry.

6.7. Conclusions

The synthesis of carbon nanotubes was achieved in a tubular furance reactor using the Ferrocene as a source of Fe, which will represent the catalyst for the growth of CNTs inside the tube without the need of the substrate. The process was carried out under temperature of 1230 °C. The thiophene was used as a source of S, which plays an important role to encapsulate the Fe nanoparticles tp prevent their agglomeration. High S/Fe molar flow produces mult walls CNTs while it can be reduced to obtaine lower layers reaching to DWCNTs. According to recent inversitagations, CNTs obtained by FC-CVD can give higher electrical and thermal conductivity due to its high density in addition to the high strength and Modulus if we compare it with the other methods. SEM and TEM images showed that the CNTs ribbon has a thickness ranges between 1.40 µm and 2.01 µm and a tube diameter between 20 and 30 nm. CNTs are crystalline as Raman spectroscopy shows a strong G' band, low I_D/I_G= 0.86 and crystalline size 5.84 nm.

NiO_x nanoparticle were synthesized by plasma-liquid interaction process using 15 ml of ethanol, and a Ni foil emerged while a capillary with Ar flow is placed just over the solution to obtain plasma after applying high DC potential. The nanoparticles size was about 5 nm with different shapes with a majority of spherical.

To benefit from the electrochemical properties of CNTs and NiO_x nanoparticles, The electrochemical characterization of CNTs dispersed in the solution where the nanoparticles were synthesized to give higher specific capacitance than each one alone. The Specific capacitance of the mixture was found 80.56 mF/cm^2 at scan rate 5 mV/s.

Conclusions

According to the main purpose of the thesis for improving the synthesis parameters of carbon nanotubes and hybrid nanostructures on flexible and conductive substrates, we have shown that the obtained results have a great potential for applications as flexible electrodes for supercapacitors. The diversity of these technologies and nanomaterials also open other future developments of electrodes for batteries, sensors, photo and electrocatalysis.

- Three methodologies have been followed to obtain the CNTs:
  1- Synthesis of CNTs on Papyex ® graphite substrate using plasma enhanced chemical vapor deposition (PECVD).
  2- Synthesis of CNTs directly on SS310 stainless steel using the catalyst elements of the alloy itself using PECVD.
  3- Synthesis of CNTs without substrate in a furnace tubular reactor using floating catalyst CVD (FC-CVD).

- CNTs were successfully synthesized over high flexible Papyex® substrate. Thickness of the Fe catalyst thin film, PECVD temperature, and the growth time are the three parameters that have been optimized in the synthesis process. The parameters we finally selected were using 2.5 nm of catalyst thin film and 700°C PECVD temperature for 15 min. The obtained CNTs are 2 µm long with an average diameter of 60 nm. The CNTs were functionalized by O_2 plasma for different times to modify their structure and morphology to allow the diffusion of ions through the porous nanotubes.

- These CNTs were used as a support for the growth of GNWs using inductively coupled plasma CVD (ICP-CVD) leading to a hybrid carbon nanostructure allowing the increase of the surface area. CNTs and the hybrid carbon nanostructure were used to deposit MnO_2 electrochemically to use them as electrodes for supercapacitors. The highest capacitance was obtained after the deposition of MnO_2 for 10 min as the further deposition blocks the porosity of the carbon nanostructure. The capacitance increased from 11.4 mF/cm^2 to 115.8 mF/cm^2 for CNTs, and from 9.42 to 121.7 mF/cm^2 for the hybrid structure at scan rate 5 mV/s.

- The second methodology we followed was the use of SS310 substrate to directly grow CNTs on it without the need of additional catalyst using PECVD process after reduction. The annealing time and the PECVD temperature were optimized using Box-Wilson experimental design. The reduction was achieved at 680°C temperature using H_2 plasma to remove the native oxide layer from the surface of SS310. Both, the reduction and PECVD were achieved in one continuous process without the need for prior grinding or polishing. The parameters desired by the experimental design are 1010 s of ramp annealing time and PECVD at 700°C.

- The obtained CNTs were about 3.0 µm long with a diameter 71 nm. EDS-HRTEM mapping showed that two elements (catalysts) contributed in the growth of the nanotubes, Fe and Ni. As in the previous methodology, we used the CNTs to be decorated with GNWs to increase the specific capacitance. Again, MnO_2 was deposited electrochemically on the obtained structure to increase the specific capacitance from 12.0 to 128.2 µF/cm^2. The ESR of these samples were in the range between 0.5 and 3.75Ω

- The third methodology of CNTs synthesis is without substrate using FC-CVD process in a tubular furnace reactor. This process allowed the continuous growth of CNTs, which makes it scalable and suitable for a wide field of industries, in addition to the high quality of CNTs produced by this technique.

- The process was achieved at a temperature of 1230°C using CH_4 as a C source, $C_{10}H_{10}Fe$ as a catalyst source (Fe), and C_4H_4S as a promoter to prevent the agglomeration of catalyst nanoparticles by encapsulating them. The thickness of the obtained CNTs ribbons ranges between 1.4 and 2.0 µm and the tube diameter between 20 and 30 nm. CNTs are crystalline as Raman spectroscopy shows a strong G' band, low I_D/I_G= 0.86 and crystalline size 5.8 nm.

- NiO_x nanoparticles were synthesized using plasma-liquid interaction process to be used together with the obtained CNTs from the FC-CVD process as a substrate for supercapacitors. The nanoparticles size was about 5 nm with different shapes with a majority being spherical.

- When the carbon nanotubes were dispersed in the solution containing NiO_x, the electrochemical properties improve, and the specific capacitance of the composite increases up to 81 mF/cm^2 at scan rate 5 mV/s.

APPENDIX

	Substrate	File	Catalyst															PECVD					
			source	Target	Previous vacuum Pa	Ar sccm	Pressure mbar	time s	Deposition rate nms	Power W	Vbias V	H2 sccm	P mbar	Ramp time s	Hold time s	Tfinal C	NH3 sccm	C2H2 sccm	P mbar	RF W	Vbias V_2	Deposition time s
20L16b.pdf	SS304+Ni+Ti+AlN	20L16b.txt	RF	Fe	2.8*10^-4	128	0.0194	25	0.04	60	98	100	2	799	120	671	100	50	1	50	354	1200
20L16c.pdf	SS304+Ni+Ti+AlN	20L16c.txt	RF	Fe	3.5*10^-4	128	0.0194	25	0.04	60	94	100	2	799	120	671	100	50	1	50		1200
01C18a (PECVD-CNTs-Si wafer).pdf	Si	01C18a.txt	RF	Fe	4.2*10^-4	135	0.0202	64 (3nm)	0.047	60	1.01338 4321	100	2	750	120	680	100	50	1	50	-398V	900
19A17a.pdf	SS304+Ni+Ti+AlN	19A17a.txt	RF	Fe	1.4*10^-4	128	0.0194	50	0.04	60	99	100	2	675	120	700	100	50	1	50	349	1200
01J18a (PECVD-test).pdf	Si	01J18a.txt	RF	Fe	6.5*10^-4	135	0.021	75	0.04	60	-123	100	2	750	120	680	100	50	1	50	-1.0235	600
01J18b (WACVD-test).pdf	Si	01J18b.txt	RF	Fe	6.6*10^-4	135	0.021	25	0.04	60	0.99346 9388	100	2	750	120	600/730	100	50	1			300
19A17b.pdf	Si	19A17b.txt	RF	Fe	3*10^-4	128	0.0194	62	0.04	60	97	100	2	750	120	680	100	50	1	50	356	900
19A17c.pdf	Si	19A17c.txt	RF	Fe	3.8*10^-4	128	0.0195	75	0.04	60	98.1	100	2	750	120	680	100	50	1	50	369	900
02C17b.pdf	SS+Ni+Ti+AlN	02C17b.txt	RF	Fe	3.8*10^-4	128	0.0199	40	0.026	60	-96	100	2	750	120	680	100	50	1	50	367	900
20A17a.pdf	Si	20A17a.txt	RF	Fe	2.1*10^-4	128	0.0195	81	0.04	60	97.2	100	2	750	120	680	100	50	1	50	384	900
02D18a (SS304+CNTs).pdf	SS304	02D18a.txt										100	2	750	120	680	100	50	1	50	-407	600
23A17c-Fe calibration.pdf	Glass	23A17c.txt	RF	Fe	2.9*10^-4	128	0.0197	900		60	106.1											
24A17a.pdf	SS304+Ni+Ti+AlN	24A17a.txt	RF	Fe	3.3*10^-4	128	0.0193	90	0.04	60	106.3	100	2	675	90	700	100	50	1	50	349	1200
25A17a-Fe calibration.pdf	Glass	25A17a.txt	RF	Fe	2.6*10^-4	128	0.0197	300		60	106.3											
25A17b-Fe calibration.pdf	Glass	25A17b.txt	RF	Fe	2.6*10^-4	128	0.0197	1500		60	103.7											
02G18a (WACVD).pdf	Al2O3 grid/Si/SiO/Al2O3	02g18a.txt	RF	Fe	4.1*10^-4	135	0.021	35	0.04	60	-124.5	100	2	750	120	600 (730)	100	50	1			1800
30A17a-Fe calibration.pdf	Glass	30A17a.txt	RF	Fe	2.7*10^-4	128	0.0194	1800		70	106.5											
30A17b-Fe calibration.pdf	Glass	30A17b.txt	RF	Fe	2.9*10^-4	128	0.0194	1200		70	106.3											
30A17c-Fe calibration.pdf	Glass	30A17c.txt	RF	Fe	2.5*10^-4	128	0.0195	600		70	107.5											
13B17c-Fe calibration.pdf	Glass	13B17c.txt	RF	Fe	3.4*10^-4	128	0.0195	3600		70	-110.5											
02J18f (SS304+DLC-test).pdf	SS304	02J18f.txt	RF	Fe	5.4*10^-4	135	0.021	75 (3nm)	0.04	60	-0.99248 7479											
02K17a (Al2O3-Grid).pdf	Al2O3	02K17a.txt	RF	Fe	3.7*10^-4	67 (128)	0.02	85	0.047	60	-105.5	100	2	750	120	600	100	50	1			1800
02K17b (Ash).pdf	SS mesh+AlN	02K17b.txt	RF	Fe	6.2*10^-4	128 (66 H2 line)	0.0201	64	0.047	60	-105	100	2	750	120	680	100	50	1	50		900
13B17d-Fe calibration.pdf	Glass	13B17d.txt	RF	Fe	3.4*10^-4	128	0.0195	2400		70	-106.2											
15B17a-cleaning Fe target.pdf	Glass	15B17a.txt	RF	Fe	2.9*10^-4	128	0.0194	1200		60	100.3											
03C17a.pdf	SS+Ni+Ti+AlN	03C17a.txt	RF	Fe	3.8*10^-4	128	0.0202 (90sccm)	40	0.026	60	100	100	2	750	120	680	100	50	1	50	332	900
15B17d.pdf	Si	15B17d.txt	RF	Fe	2.5*10^-4	128	0.0194	77	0.026	60	97.9	100	2	750	120	680	100	50	1	50	364	900
16B17a.pdf	Si	16B17a.txt	RF	Fe	2.3*10^-4	128	0.0194	39	0.026	60	98.7	100	2	750	120	680	100	50	1	50	372	900
03D18a (SS304+CNTs).pdf	SS304	03D18a.txt										100	2	750	120	680	100	50	1			600
17B17a (H2O Plasma).pdf	Si	17B17a.txt	RF	Fe	2.3*10^-4	128	0.0194	62	0.04	60	-100	100	2	750	120	680	100	50	1	50	354	900
20B17a.pdf	Si	20B17a.txt	RF	Fe	3.4*10^-4	128	0.0194	77	0.026	60	98.8	100	2	750	120	680	100	50	1	50	398-404	900
03G18a (WACVD).pdf	Al2O3 grid/Si/Al2O3	03g18a.txt	RF	Fe	4.4*10^-4	135	0.021	25	0.04	60	-124.6	100	2	750	120	600 (730)	100	50	1			1800
03K17a(Ash).pdf	SS mesh+AlN	03K17a.txt	RF	Fe	4.8*10^-4	128 (66 H2 line)	0.0201	64	0.047	60	1.00756 859	100	2	750	120	680	100	50	1	60	1.0059 2	900
03K17b(ICMAB).pdf	Si+G-SS304+AlN	03K17a.txt	RF	Fe	5.9*10^-4	128 (66 H2 line)	0.0201	64	0.047	60	1.00096 432	100	2	750	120	680	100	50	1	60	-350	600
03K17c(Ash).pdf	SS mesh+Al2O3	03K17c.txt	RF	Fe	5.9*10^-4	128 (66 H2 line)	0.0201	64	0.047	60	1.00290 1354	100	2	750	120	680	100	50	1	50	-310	900
20B17b (N2 Plasma).pdf	Si	20B17b.txt	RF	Fe	2.3*10^-4	128	0.0201	62		60	99.2	100	2	750	120	680	100	50	1	50	404-394	900
21B17a.pdf	Si	21B17a.txt	RF	Fe	2.4*10^-4	128	0.0199	39	0.026	60	97.7	100	2	750	120	680	100	50	1	50	393-	900
22B17a.pdf	Si	22B17a.txt	RF	Fe	2.4*10^-4	128	0.0199	39	0.026	60	99	100	2	750	120	680	100	50	1	50	398	900
23B17a.pdf	SS+Ni+Ti+AlN	23B17a.txt	RF	Fe	2.4*10^-4	128	0.0199	62	0.026	60	98.9	100	2	750	120	680	100	50	1	50	385	900
23B17c.pdf	SS+Ni+Ti+AlN	23B17c.txt	RF	Fe	3.5*10^-4	128	0.0199	62	0.026	60	97.7	100	2	750	120	715	100	50	1	50	359	900
27B17a.pdf	SS+Ni+Ti+AlN	27B17a.txt	RF	Fe	2.1*10^-4	128	0.0199	62	0.026	60	102.5	100	2	750	120	730	100	50	1	50	359	900
27B17b.pdf	SS+SS thin film	27B17b.txt	RF	Fe	3.2*10^-4	128	0.0199	62	0.026	60	100.7	100	2	750	120	700	100	50	1	50	357	900
27B17c.pdf	Si	27B17c.txt	RF	Fe	3.4*10^-4	128	0.0199	62	0.026	60	97.4	100	2	750	120	680	100	50	1	50	377-404	900
03e18b (WACVD).pdf	Si	27d18b.txt	RF	Fe	4.5*10^-4	135	0.0206	25	0.04	60	-118	100	2	750	120	600 (730)	100	50	1			1800
28B17a (27B17a).pdf	SS+Ni+Ti+AlN	28B17a.txt	RF	Fe	4.2*10^-4	128						100	2	750	120	730	100	50	1	50	344	900
01C17a.pdf	SS+SS	01C17a.txt	RF	Fe	1.7*10^-4	128	0.0167	62	0.026	60	97.7	100	2	750	120	680	100	50	1	50	370	900
04G18a (WACVD).pdf	Al2O3 grid/Si/Al2O3	04g18a.txt	RF	Fe	3.9*10^-4	135	0.021	50	0.04	60	-124.6	100	2	750	120	600 (730)	100	50	1			1800
04G18b (WACVD).pdf	Al2O3 grid/Si/Al2O3	04g18a.txt	RF	Fe	4.3*10^-4	135	0.021	75	0.04	60	-122.2	100	2	750	120	600 (730)	100	50	1			1800
02C17a.pdf	Si	02C17a.txt	RF	Fe	2.1*10^-4	128	0.0167	62	0.026	60	99.4-98.5	100	2	750	120	680	100	50	1	50	370	900
04J17a (Al2O3).pdf	Al2O3	04J17a.txt	RF	Al	2.7*10^-4	12.1 (17)	0.0043	600	0.016	120	-102											
04J17a (Al2O3-Grid).pdf	Al2O3	04J17a.txt	RF	Fe	3.5*10^-4	67 (128)	0.0198	90s / 4nm	0.047	60	-99	100	2	750	120	600	100	50	1			900
04J17b (Shahzad).pdf	Si+Al2O3+Ni	04J17b.txt			3.5*10^-4							50	0.5	1200	300	680	100	50	1	50	322	900

	Substrate	File	Catalyst														PECVD					
			source	Target	Previous vacuum Pa	Ar sccm	Pressure mbar	time s	Deposition rate nms	Power W	Vbias V	H2 sccm	P mbar	Ramp time s	Hold time s	Tfinal C	NH3 sccm	C2H2 sccm	P mbar	RF W	Vbias V_2	Deposition time s
03C17b.pdf	SS+Ni+Ti+AlN	03C17b.txt	RF	Fe	3.9*10^-4	128	0.0202 (90sccm)	40	0.026	60	99	100	2	750	120	700	100	50	1	50	344-352	900
05C17a.pdf	SS+Ni+Ti+AlN	05C17a.txt	RF	Fe	2.2*10^-4	128	0.0202 (90sccm)	40	0.026	60	99.7	100	2	750	120	715	100	50	1	50	350-363	900
05C17b.pdf	SS+Ni+Ti+AlN	05C17b.txt	RF	Fe	3.5*10^-4	128	0.0199 (90sccm)	40	0.026	60	99.7	100	2	750	120	730	100	50	1	50	381-374	900
07C17a.pdf	SS+Ni+Ti+AlO2	07C17a.txt	RF	Fe	1.9*10^-4	128	0.0199 (90sccm)	40	0.026	60	-99.9	100	2	750	120	680	100	50	1	50	351-374	900
07C17b.pdf	SS+Ni+Ti+AlO2	07C17b.txt	RF	Fe	3.7*10^-4	128	0.0199 (90sccm)	40	0.026	60	99.3	100	2	750	120	700	100	50	1	50	341-354	900
07C17c.pdf	SS+Ni+Ti+AlO2	07C17c.txt	RF	Fe	3.6*10^-4	128	0.0199 (90sccm)	40	0.026	60	97.8	100	2	750	120	730	100	50	1	50	354	900
08C17a.pdf	SS+Ni+Ti+AlO2	08C17a.txt	RF	Fe	3.6*10^-4	128	0.0199 (90sccm)	40	0.026	60	99.4	100	2	750	120	730	100	50	1	50	361	900
08C17c.pdf	SS+Ni+Ti+TaN	08C17c.txt	RF	Fe	3.3*10^-4	128	0.0199 (90sccm)	62	0.026	60	98.4	100	2	750	120	700	100	50	1	50	354-360	900
09C17a.pdf	SS+Ni+Ti+TaN	09C17a.txt	RF	Fe	2.0*10^-4	128	0.0199 (90sccm)	62	0.026	60	98.4	100	2	650	120	715	100	50	1	50	362	900
09C17b.pdf	SS+Ni+Ti+AlN	09C17b.txt	RF	Fe	2.6*10^-4	128	0.0199	62	0.026	60	97.9	100	2	750	120	680	100	50	1	50	367	900
10C17a.pdf	Si	10C17a.txt	RF	Fe	2.4*10^-4	128	0.0201	62		60	97.9	100	2	750	120	680	100	50	1	50	355	900
10C17b.pdf	SS+gradientSS+AlN	10C17b.txt	RF	Fe	3.4*10^-4	128	0.0199	62	0.026	60	96.8	100	2	750	120	680	100	50	1	50	-344	900
05C18c (graphite sheet).pdf	graphite sheet	05c18a.txt	RF	Fe	4.50E-04	135	0.0202	64	0.0383	60	-105.2	100	2	750	120	680	100	50	1	50	-387	900
14C17a.pdf	SS+Ni+Ti+AlN	14C17a.txt	RF	Fe	2.6*10^-4	128	0.0199	62	0.04	60	99.4	100	2	750	120	680	100	50	1	50	363	900
14C17b.pdf	SS+Ni+Ti+AlN	14C17b.txt	RF	Fe	3.8*10^-4	128	0.0199	62	0.04	60	97	100	2	750	120	680	100	50	1	50	363	900
15C17a.pdf	SS+Ni+Ti+AlN	15C17a.txt	RF	Fe	3.8*10^-4	128	0.0199	62	0.04	60	98.3	100	2	750	120	715	100	50	1	50	370-358	900
15C17b.pdf	SS+SSgradient+AlN	15C17b.txt	RF	Fe	2.5*10^-4	128	0.0199	62	0.04	60	-98	100	2	750	120	730	100	50	1	50	370-329	900
05G18a (WACVD).pdf	Al2O3 grid	05g18a.txt	RF	Fe	4.6*10^-4	135	0.021	50	0.04	60	-124.6	100	2	750	120	600 (730)	100	50	1			1800
17C17a.pdf	Si	16C17a.txt	RF	Fe	2.0*10^-4	128	0.0199	62	0.04	60	100.5	100	2	750	120	700	100	50	1	50	-335	1200
27C17a.pdf	Si+Al2O3	27C17a.txt	RF	Fe	3.0*10^-4	128	0.0199	50	0.026	60	98.4	100	2	750	120	700	100	50	1	50		1800
29C17a.pdf	Si+gradient SS304+AlN	29C17a.txt	RF	Fe	2.5*10^-4	128	0.0199	62	0.04	60	98	100	2	750	120	680						
29C17b.pdf	Si+gradient SS304+AlN	29C17b.txt	RF	Fe	5.0*10^-4	128	0.0199	62	0.04	60	96.5	100	2	750	120	700						
05K18a (copper+DLC+test).pdf	Copper	05K18a.txt			3.3*10^-4																	
03D17a.pdf	Si+gradient SS304+AlN	03D17a.txt	RF	Fe	4.6*10^-4	128	0.0201	50	0.04	60	97.2	100	2	750	120	730	100	50	1			1800
05D17a.pdf	Cu+graphene	05D17a.txt	RF	Fe	4.0*10^-4	128	0.0201	62	0.04	60	97.5											
05D17b.pdf	Cu	05D17b.txt	RF	Fe	3.4*10^-4	128	0.0201	62	0.04	60	97.2	100	2	750	120	680						
05D17c.pdf	Cu+graphene	05D17c.txt	RF	Fe	3.5*10^-4	128	0.0201	62	0.04	60	98	100	2	750	120	680						
06D17a.pdf	Si+Al2O3	06D17a.txt	RF	Fe	3.1*10^-4	128	0.0201	50	0.04	60	99.5	100	2	750	120	600	100	50	1	-	-	1800
06D18a (SS304+CNTs).pdf	SS304	06D18a.txt			7.6*10^-4							100	2	750	120	730	100	50	1	50	1.01828	600
06E19a-SS304+GSS304+AlN.pdf	SS+SSgradient+AlN	06E19a.txt	RF	Fe	4.7*10^-4	128	0.0199	83 (2.5nm)	0.03	60	-0.994163424	100	2	750	120	730	100	50	1	50	1.02222	900
06E19b-SS304+GSS304+AlN.pdf	SS+SSgradient+AlN	06E19b.txt	RF	Fe	3.3*10^-4	128	0.0199	83 (2.5nm)	0.03	60	-0.997002997	100	2	750	120	730	100	50	1	50	1.00847	900
07D17a.pdf	Si+Al2O3	07D17a.txt	RF	Fe	2.4*10^-4	128	0.0201	50	0.04	60	97.3	100	2	750	120	600	100	50	1	-	-	1800
06J17a (Al2O3).pdf	Al2O3	06J17a.txt	RF	Al	2.7*10^-4	12.1 (17)	0.0043	600	0.016	120	-94											
06J17a (Al2O3-Grid).pdf	Al2O3	06J17a.txt	RF	Fe	3.4*10^-4	67 (128)	0.0198	64s / 3nm	0.047	60	-105	100	2	750	120	600	100	50	1			900
06K18a (copper+DLC+test).pdf	Copper	06K18a.txt			3.3*10^-4																	
07D17b.pdf	Si+Al2O3	07D17b.txt	RF	Fe	3.5*10^-4	128	0.0201	38	0.04	60	95.4	100	2	750	120	600	100	50	1	-	-	1800
10D17a.pdf	Si+Al2O3	10D17a.txt	RF	Fe	3.0*10^-4	128	0.0201	25	0.04	60	97.6	100	2	750	120	600	100	50	1	-	-	1800
10D17b.pdf	Si+Al2O3	10D17b.txt	RF	Fe	3.5*10^-4	128	0.0201	50	0.04	60	98.6	100	2	750	120	600	100	50	1	-	-	1800
19D17a.pdf	Si	10D17b.txt	RF	Al	2.8*10^-4	8.6 (via H2)	0.0203		0.04	120	-187									-	-	
11D17a.pdf	Si+Al2O3	11D17a.txt	RF	Fe	2.2*10^-4	128	0.0201	13	0.04	60	98.7	100	2	750	120	600	100	50	1	-	-	1800
20D17a.pdf	Cu+graphene	20D17b.txt	RF	Al	2.8*10^-4	8.6 (via H2)	0.0203		0.04	120	-187									-	-	
23D17a (Depth profile XPS).pdf	SS+gradientSS+AlN	23D17a.txt	RF	Fe	3.9*10^-4	128 (90 H2 line)	0.0201	62	0.04	60	97.5	100	2	750	120	680	100	50	1			1200
25D17a.pdf	Cu+graphene	25D17a.txt	RF	Al	1.8*10^-4	8.6 (via H2)	0.0033	318	0.04	120	-182.4	100	2	750	120	650	100	50	1	-	-	600
27D17a.pdf	Cu+graphene	27D17a.txt	RF	Al	1.8*10^-4	8.6 (via H2)	0.0033	318	0.04	120	-183.7	100	2	750	120	650	100	50	1	-	-	600
28D17a.pdf	Cu+graphene	28D17a.txt	RF	Al	1.8*10^-4	8.6 (via H2)	0.0033	318	0.04	120	-183.7	100	2	750	120	650	100	50	1	-	-	600
02F17a-Al calibration.pdf	Glass	02F17a.txt	RF	Al	2.4*10^-4	42(via H2)	0.01	1800		120	-120.9									-		
02F17b-Al2O3 calibration.pdf	Glass	02F17b.txt	RF	Al	2.4*10^-4	8.6(via H2)	0.0034	2700		120	-106.9									-		

	Substrate	File	Catalyst															PECVD					
			source	Target	Previous vacuum Pa	Ar sccm	Pressure mbar	time s	Deposition rate nms	Power W	Vbias V	H2 sccm	P mbar	Ramp time s	Hold time s	Tfinal C	NH3 sccm	C2H2 sccm	P mbar	RF W	Vbias V_2	Deposition time s
02F17c-AlN calibration.pdf	Glass	02F17c.txt	RF	Al	3.3*10^-4	5.6(via H2)	0.0031	2700		120	-128.6									-		
22F17a (similar 15B17d).pdf	Si	22f17a.txt	RF	Fe	4.1*10^-4	128(90 via H)	0.0194	77	0.04	60	100.7	100	2	750	120	680	100	50	1	50	333	900
23F17a (similar 16B17a).pdf	Si	23F17a.txt	RF	Fe	2.3*10^-4	128 (90 via H2)	0.0194	39	0.026	60	97.1	100	2	750	120	680	100	50	1	50	332	900
26F17a (similar 16B17a).pdf	Si	26F17a.txt	RF	Fe	2.3*10^-4	128 (90 via H2)	0.0194	39	0.026	60	94.9	100	2	750	120	680	100	50	1	50	332	900
27F17a (Fe calibration)-new target.pdf	Glass	27F17a.txt	RF	Fe	4.3*10^-4	128 (90 H2 line)	0.0203	600		60	-102											
27F17b (similar 21D17g) WACVD.pdf	SS+gradientSS9+AlN	27F17b.txt	RF	Fe	4.1*10^-4	128 (90 H2 line)	0.0206	62	0.04	60	-101.2	100	2	750	120	600	100	50	1			1200
07e18a (WACVD).pdf	Si	07e18a.txt	RF	Fe	2.6*10^-4	135	0.0218	25	0.04	60	-125.6	100	2	750	120	600 (730)	100	50	1			1800
29F17a (calibration Al).pdf	Glass	29F17a.txt	RF	Al	3.7*10^-4	40 (58)	0.0101	600		120	-123.1											
29F17b (Al2O3 calibration).pdf	Glass	29F17b.txt	RF	Al	3.8*10^-4	37 (51)	0.0109	600		120	-88.5											
08C17b.pdf	SS+Ni+Ti+TaN	08C17b.txt	RF	Fe	3.5*10^-4	128	0.0199 (90sccm)	62	0.026	60	96.3	100	2	750	120	680	100	50	1	50	355	900
30F17a (similar 21D17g) WACVD.pdf	SS+gradientSS+AlN	30F17a.txt	RF	Fe	4.2*10^-4	128 (90 H2 line)	0.0206	55	0.0445	60	-104.3	100	2	750	120	600	100	50	1			1200
30F17b (similar 21D17g) WACVD.pdf	SS+gradientSS+AlN	30F17b.txt	RF	Fe	4.6*10^-4	128 (90 H2 line)	0.0206	55	0.0445	60	-102.7	100	2	750	120	600	100	50	1			1200
08J18a (SS304+DLC+CNTs).pdf	SS304	08J18a.txt	RF	Fe	5.4*10^-4	135	0.021	75 (3nm)	0.04	60	1.01322 314	100	2	750	120	680	100	50	1	50	1.0370 4	600
03G17a (similar 21D17g) WACVD.pdf	SS+gradientSS+AlN	03G17a.txt	RF	Fe	3.7*10^-4	128 (90 H2 line)	0.0202	55	0.0445	60	-103.5	100	2	750	120	600	100	50	1			1200
03G17b (similar 21D17g) WACVD.pdf	SS+gradientSS+AlN	03G17b.txt	RF	Fe	3.8*10^-4	128 (90 H2 line)	0.0202	55	0.0445	60	-101.3	100	2	750	120	600	100	50	1			1200
09A18a (graphite sheet).pdf	graphite sheet	09A18a.txt	RF	Fe	5.9*10^-4	135	0.021	64 (3nm)	0.047	60	- 1.01252 4085	100	2	750	120	600	100	50	1	50	-382	600
05G17a (similar 21D17g) WACVD.pdf	SS+gradientSS+AlN	05G17a.txt	RF	Fe	2.9*10^-4	128 (90 H2 line)	0.0202	55	0.0445	60	-96.8	100	2	750	120	600	100	50	1			1200
06G17a (similar 21D17g) WACVD.pdf	SS+gradientSS+AlN	05G17a.txt	RF	Fe	2.8*10^-4	128 (90 H2 line)	0.0202	55	0.0445	60	-99.5	100	2	750	120	600	100	50	1			1200
07G17a (similar 21D17g) WACVD.pdf	SS+gradientSS+AlN	07G17a.txt	RF	Fe	3.9*10^-4	128 (90 H2 line)	0.0202	55	0.0445	60	-98.5	100	2	750	120	600	100	50	1			1200
09D18a (ref 15C17b)(SS304+GSS304+AlN).pdf	SS+SSgradient+AlN	09D18a.txt	RF	Fe	4.7*10^-4	135	0.0199	78 (3nm)	0.0383	60	1.00482 6255	100	2	750	120	730	100	50	1	50	1.0641	900
09G18a (SS304)(Surface morphology	XPS	XRD).pdf	Success									Without diffusion barrier and catalyst										
09G18b (SS304)(Surface morphology	XPS	XRD).pdf	Success									Without diffusion barrier and catalyst										
09G18c (SS304)(Surface morphology	XPS	XRD).pdf	Success									Without diffusion barrier and catalyst										
09G18d (SS304)(Surface morphology	XPS	XRD).pdf	Success									Without diffusion barrier and catalyst										
09G19a (SS304+CNTs)-Ref(04L18c).pdf	SS304	09G19a.txt			1.0*10^-4							100	1	900	620	500/730	100	50	1	50	-324	1800
09G19b (SS304+CNTs)-Ref(04L18c).pdf	SS304	09G19b.txt			1.8*10^-4							100	1	900	620	500/780	100	50	1	50	- 0.0026	1800
09G19c (SS304+CNTs)-Ref(04L18c).pdf	SS304	09G19c.txt			4.3*10^-4							100	1	900	620	500/780	100	50	1	50	0.8753 3	1800
09G19d (SS304+CNTs)-Ref(04L18c).pdf	SS304	09G19d.txt			5.0*10^-4							100	1	900	620	500/780	100	50	1	50	0.9185 8	1800
10G17a (similar 16B17a) PECVD.pdf	Si (cuarter)	10G17a.txt	RF	Fe	3.0*10^-4	128 (90 via H2)	0.0194	35	0.045	60	97.6	100	2	750	120	680	100	50	1	50	317	900
10G17b (similar 16B17a) PECVD.pdf	Si	10G17b.txt	RF	Fe	3.9*10^-4	128 (90 via H2)	0.0194	35	0.045	60	100	100	2	750	120	680	100	50	1	50	323	900
11G17a (similar 16B17a) PECVD.pdf	Si	11G17a.txt	RF	Fe	3.5*10^-4	128 (90 via H2)	0.0194	35	0.045	60	99.9	100	2	750	120	680	100	50	1	50	329	900
12G17a (WACVD).pdf	Si	12G17a.txt	RF	Fe	3.5*10^-4	128	0.0201	45	0.045	60	100.2	100	2	750	120	600	100	50	1	-	-	1800
13G17a (WACVD).pdf	Si(cuarter)	13G17a.txt	RF	Al	3.1*10^-4	8.6 (12.5)	0.0033	227	0.044	120	-107											
13G17b (WACVD).pdf	Si(cuarter)	13G17b.txt	RF	Al	4.2*10^-4	8.6 (12.5)	0.0033	635	0.044	120	-107	100	2	750	120	600	100	50	1			1800
17G17a (WACVD).pdf	Si(cuarter)	17G17a.txt	RF	Al	3.7*10^-4	8.6 (12.5)	0.0033	635	0.044	120	-100	100	2	750	120	600	100	50	1			1800
19G17a (WACVD).pdf	Si	18G17a.txt	RF	Al	3.5*10^-4	8.6 (12.5)	0.033	635	0.044	120	-103.3	100	2	750	120	600	100	50	1			1800
09e18a (WACVD).pdf	Si+Al2O3	09e18a.txt	RF	Fe	5.3*10^-4	135	0.0203	15	0.04	60	-121.5	100	2	750	120	600 (730)	100	50	1			1800
09e18b (WACVD).pdf	Si+Al2O3	09e18a.txt	RF	Fe	5.3*10^-4	135	0.0203	15	0.04	60	-121.5	100	2	750	120	600 (730)	100	50	1			1800
10A18a (graphite sheet).pdf	graphite sheet	10a18a.txt	RF	Fe	6.6*10^-4	135	0.021	64 (3nm)	0.047	60	- 0.99530 0752	100	2	750	120	600	100	50	1	50	-378	600

	Substrate	File	Catalyst														PECVD					
			source	Target	Previous vacuum Pa	Ar sccm	Pressure mbar	time s	Deposition rate nms	Power W	Vbias V	H2 sccm	P mbar	Ramp time s	Hold time s	Tfinal C	NH3 sccm	C2H2 sccm	P mbar	RF W	Vbias V_2	Deposition time s
10A18b (SS304+DLC).pdf	SS304	10a18b.txt	RF	Fe	6.7*10^-4	135	0.021	64 (3nm)	0.047	60	-1.012464046	100	2	750	120	600	100	50	1	50	1.03022	600
20G17a (WACVD).pdf	Si	20G17a.txt	RF	Al	2.9*10^-4	8.6 (12.5)	0.033	635	0.044	120	-106.7	100	2	750	120	600	100	50	1			600
20G17b (WACVD).pdf	Si	20G17a.txt	RF	Al	2.9*10^-4	8.6 (12.5)	0.033	635	0.044	120	-106.5	100	2	750	120	600	100	50	1			600
27G17a (Al2O3-Grid).pdf	Al2O3	27G17a.txt	RF	Fe	2.8*10^-4	90 (128)	0.02	90	0.044	60	-100.7	100	2	750	120	600	100	50	1			1800
28G17a (Al2O3-Grid).pdf	Al2O3	28G17a.txt	RF	Fe	4.3*10^-4	90 (128)	0.02	23	0.044	60	-100.7	100	2	750	120	600	100	50	1			1800
30H17a (similar 16B17a) PECVD.pdf	Si (cuarter)	30H17a.txt	RF	Fe	3.0*10^-4	128 (90 via H2)	0.0194	35	0.045	60	97.6	100	2	750	120	680	100	50	1	50	317	900
09I17a (similar 16B17a) PECVD.pdf	Si	08I17a.txt	RF	Fe	3.0*10^-4	128 (90 via H2)	0.0211	35	0.045	60	99.9	100	2	750	120	680	100	50	1	50	329	900
10G18a (SS304+CNTs).pdf	SS304	10g18a			4.2*10^-4							100	2	750	120	730	100	50	1	50	1.00957	600
10G18b (WACVD).pdf	Al2O3 grid and Al2O3 grid/Si/Al2O3	10g18b.txt	RF	Fe	4.6*10^-4	135	0.021	37.5	0.04	60	-124.6	100	2	750	120	600 (730)	100	50	1			1800
10G19a (SS304+CNTs)-Ref(04L18c).pdf	SS304	10G19a.txt			5.0*10^-4							100	1	900	620	500/780	100	50	1	50	0.91858	1800
10G19b (SS304+CNTs)-Ref(04L18c).pdf	SS304	10G19b.txt			1.8*10^-4							100	1	900	620	500/780	100	50	1	50	0.98982	1800
10G19c (SS304+CNTs).pdf	SS304	10G19c.txt			3.3*10^-4							100	1	900	620	500/780	100	50	1	50	0.96692	1800
10G19d (SS304+CNTs).pdf	SS304	10G19d.txt			6.0*10^-4							100	1	900	620	500/780	100	50	1	50	-0.0028	1800
10I18a (SS304+CNTs).pdf	SS304	10I18a.txt			3.5*10^-4							100	2	750	120	730	100	50	1	50	1.01205	600
10J17a (Al2O3).pdf	Al2O3	10J17a.txt	RF	Al	1.9*10^-4	12.1 (17)	0.0043	600	0.016	120	-97											
10J17a (Al2O3-Grid).pdf	Al2O3	10J17a.txt	RF	Fe	5.5*10^-4	67 (128)	0.0198	64s / 3nm	0.047	60	-105	100	2	750	120	600	100	50	1			900
12I17a (Al2O3-Grid).pdf	Al2O3	12I17a.txt	RF	Fe	2.8*10^-4	66 (128)	0.02	90	0.044	60	-100.7	100	2	750	120	600	100	50	1			3600
10J18b (SS304+DLC+CNTs).pdf	SS304	10J18b.txt	RF	Fe	5.6*10^-4	135	0.021	75 (3nm)	0.04	60	1.012437811	100	2	750	120	680	100	50	1	50	0.97756	600
15I17b (WACVD on copper).pdf	Cu	15I17b.txt	RF	Fe	4.2*10^-4	66 (128)	0.0202	45	0.044	60	-107	100	2	750	120	600	100	50	1			900
17I17a (similar15B17d).pdf	Si	17I17a.txt	RF	Fe	4.1*10^-4	128(90 via H)	0.0194	77	0.04	60	109.5	100	2	750	120	680	100	50	1	50	333	900
18I17a (Al2O3-Grid).pdf	Al2O3	18I17a.txt	RF	Fe	2.8*10^-4	66 (128)	0.02	90	0.044	60	-100.7	100	2	750	120	600	100	50	1			3600
19I17a (Al2O3-Grid).pdf	Al2O3	19I17a.txt	RF	Fe	2.8*10^-4	66 (128)	0.02	90	0.044	60	-99.7	100	2	750	120	600	100	50	1			3600
19I17b (similar 16B17a).pdf	Si	19I17b.txt	RF	Fe	3.5*10^-4	128 (90 via H2)	0.0194	35	0.045	60	100.4	100	2	750	120	680	100	50	1	50	329	900
20I17a (similar 16B17a).pdf	Si	20I17a.txt	RF	Fe	3.5*10^-4	128 (67 via H2)	0.0194	35	0.045	60	100.4	100	2	750	120	680	100	50	1	54	333	900
10e18a (WACVD).pdf	Si+Al2O3	10e18a.txt	RF	Fe	3.8*10^-4	135	0.0205	10	0.04	60	-121.5	100	2	750	120	600 (730)	100	50	1			1800
10e18b (WACVD).pdf	Si+Al2O3	10e18b.txt	RF	Fe	3.7*10^-4	135	0.0205	12.5	0.04	60	-121.5	100	2	750	120	600 (730)	100	50	1			1800
20I17b (Shahzad).pdf	Si & Cu+Al2O3+Ni (two substrates)	20I17b.txt										100	2	750	300 (with plasma)	600	100	50	1			900
21I17a (Al2O3-Grid).pdf	Al2O3	21I17a.txt	RF	Fe	2.8*10^-4	66 (128)	0.02	90	0.044	60	-99.7	100	2	750	120	600	100	50	1			3600
22I17a (Fe calibration).pdf	Glass	21I17a.txt	RF	Fe	3.5*10^-4	128 (66 via H2)	0.0194	600		60	100.4											
22I17b (Al calibration).pdf	Glass	21I17b.txt	RF	Al	3.5*10^-4	128 (44 via H2)	0.0103	300		60	100.4											
22I17c (Al2O3 calibration).pdf	Glass	21I17c.txt	RF	Al	3.5*10^-4	(18 via H2)	0.0061	1800		90	84.9											
11G18a (WACVD).pdf	Al2O3 grid/Si/Al2O3	11g18a.txt	RF	Fe	5.0*10^-4	135	0.021	50	0.04	60	-123.6	100	2	750	120	600 (730)	100	50	1			1800
29I17a (Al2O3-Grid).pdf	Al2O3	29I17a.txt	RF	Fe	2.8*10^-4	66 (128)	0.02	85	0.047	60	-99.7	100	2	750	120	600	100	50	1			3600
02J17a (Al2O3-Grid).pdf	Al2O3	02J17a.txt	RF	Fe	3.5*10^-4	66 (128)	0.0219	106s / 5nm	0.047	60	-99.9	100	2	750	120	600	100	50	1			2100
02J17b (Shahzad).pdf	Si+Al2O3+Ni & Cu+Al2O3+Ni	02J17b.txt			3.5*10^-4							50	0.5	1200	300	680	100	50	1	50	322	900
02J17c (Al2O3-Grid).pdf	Al2O3	02J17c.txt	RF	Fe	3.5*10^-4	66 (128)	0.0219	106s / 5nm	0.047	60	-98.3	100	2	750	120	600	100	50	1			900
02J17d (similar15B17d).pdf	Si	02J17d.txt	RF	Fe	3.9*10^-4	128(66 via H)	0.0194	64s/ 3nm	0.047	60	98.1	100	2	750	120	680	100	50	1	50	333	900
11J17a (similar15B17d).pdf	Si+AlN	11J17a.txt	RF	Fe	3.0*10^-4	128(66 via H)	0.0194	64s/ 3nm	0.047	60	108	100	2	750	120	680	100	50	1	50	333	900
11e18a (WACVD).pdf	Si+Al2O3	11e18a.txt	RF	Fe	3.7*10^-4	135	0.0205	17.5	0.04	60	-122.6	100	2	750	120	600 (730)	100	50	1			1800
11J17b (similar15B17d).pdf	Si+AlN	11J17b.txt	RF	Fe	3.0*10^-4	128(66 via H)	0.0194	64s/ 3nm	0.047	60	105	100	2	750	120	680	100	50	1	50	322	900
17J17a (similar15B17d).pdf	Si+AlN	17J17a.txt	RF	Fe	3.0*10^-4	128(66 via H)	0.0194	64s/ 3nm	0.047	60	104.7	100	2	750	120	680	100	50	1	50	322	900
19J17a (Ash).pdf	SS	19J17a.txt	RF	Fe	4.7*10^-4	128 (66 H2 line)	0.0201	53	0.047	60	-104.9	100	2	750	120	600	100	50	1			1800
20J17a (Ash).pdf	SS	20J17a.txt	RF	Fe	4.7*10^-4	128 (66 H2 line)	0.0201	85	0.047	60	-105.8	100	2	750	120	600	100	50	1			1800
23J17a (Ash).pdf	SS	23J17a.txt	RF	Fe	1.9*10^-4	128 (66 H2 line)	0.0201	32	0.047	60	-106.2	100	2	750	120	600	100	50	1			1800

	Substrate	File	Catalyst															PECVD					
			source	Target	Previous vacuum Pa	Ar sccm	Pressure mbar	time s	Deposition rate nms	Power W	Vbias V	H2 sccm	P mbar	Ramp time s	Hold time s	Tfinal C	NH3 sccm	C2H2 sccm	P mbar	RF W	Vbias V_2	Deposition time s
12D17a (calibration Al).pdf	Glass	12D17a.txt	RF	Al	1.9*10^-4	42 (58)	0.0103	600		120	-190											
12D17b (calibration Al2O3).pdf	Glass	12D17b.txt	RF	Al	2.8*10^-4	37 (51)	0.0109	600		120	-184											
12D17c (calibration Al2O3).pdf	Glass	12D17c.txt	RF	Al	2.8*10^-4	37 (51)	0.0107	600		120	-180											
12D17c.pdf	Si+Al2O3	10D17b.txt	RF	Fe	2.8*10^-4	128	0.0203	50	0.04	60	-97	100	2	750	120	600	100	50	1.0132	-	-	1800
12D18a (WACVD).pdf	Si	12d18a.txt	RF	Fe	6.5*10^-4	135	0.0202	64	0.0383	60	-103.2	100	2	750	120	600 (730)	100	50	1			900
12D18b (WACVD).pdf	Si	12d18b.txt	RF	Fe	5.5*10^-4	135	0.0203	64	0.0383	60	-104	100	2	750	120	600 (730)	100	50	1			900
26J17a (Shahzad).pdf	Si	26J17a.txt	RF	Fe	2.7*10^-4	128(66 via H)	0.0208	64s/ 3nm	0.047	60	-106.6	100	2	750	120	680	100	50	1	50	-334	300
12F18b (WACVD).pdf	Si+Al2O3	12f18a.txt	RF	Fe	4.8*10^-4	135	0.0225	20	0.04	60	-119.7	100	2	750	120	600 (730)	100	50	1			1800
31J17a (Shahzad).pdf	Cu	31J17a.txt	RF	Fe	2.7*10^-4	128(66 via H)	0.0208	64s/ 3nm	0.047	60	-106.6	100	2	750	120	680	100	50	1	50	-310	900
12G18a (SS304)(Surface morphology	XPS	XRD).pdf	Success	Decapado uniforme								Without diffusion barrier and catalyst										
12G18b (SS304)(Surface morphology	XPS	XRD).pdf	Success	decapado poco uniforme								Without diffusion barrier and catalyst										
12G18c (SS304)(Surface morphology	XPS	XRD).pdf	Success	decapado poco uniforme								Without diffusion barrier and catalyst										
12G18d (WACVD).pdf	Al2O3 grid/Si/Al2O3	11g18a.txt	RF	Fe	5.0*10^-4	135	0.021	50	0.04	60	-123.6	100	2	750	120	600 (730)	100	50	1			1800
03K17d (Ash).pdf	SS mesh+Al2O3	03K17d.txt	RF	Fe	4.7*10^-4	67 (128)	0.02	64	0.047	60	-107	100	2	750	120	600	100	50	1			1800
11A18a (graphite sheet).pdf	graphite sheet	11a18a.txt	RF	Fe	3.6*10^-4	135	0.021	64 (3nm)	0.047	60	-106.3	100	2	750	120	680	100	50	1	50	-534	600
11A18b (graphite sheet).pdf	graphite sheet	11a18b.txt	RF	Fe	3.6*10^-4	135	0.021	64 (3nm)	0.047	60	-107.7	100	2	750	120	680	100	50	1	50	-483/-	600
12A18a (graphite sheet).pdf	graphite sheet	12a18a.txt	RF	Fe	3.8*10^-4	135	0.021	64 (3nm)	0.047	60	-104.8	100	2	750	120	680	100	50	1	50	-392/	600
14A18a (graphite sheet).pdf	graphite sheet	14a18a.txt	RF	Fe	3.8*10^-4	135	0.021	64 (3nm)	0.047	60	1.00753 2957	100	2	750	120	680	100	50	1	50	-392/	600
15A18a (Si).pdf	Si	15a18a.txt	RF	Fe	3.8*10^-4	135	0.0202	64 (3nm)	0.047	60	1.00568 1818	100	2	750	120	680	100	50	1		-392/	900
29A18a (graphite sheet).pdf	graphite sheet	29a18a.txt	RF	Fe	3.2*10^-4	135	0.021	64 (3nm)	0.047	60	1.01224 1055	100	2	750	120	680 (730 CVD)	100	50	1			900
31A18a (graphite sheet).pdf	graphite sheet	31a18a.txt	RF	Fe	3.0*10^-4	135	0.021	64 (3nm)	0.047	60	1.01229 8959	100	2	750	120	680	100	50	1	50	- 393V/ 380V	900
13B17a.pdf	Si	13B17a.txt	RF	Fe	3.2*10^-4	128	0.0194	200	0.015	60	102	100	2	750	120	680	100	50	1	50	397	900
13B17b.pdf	Si	13B17b.txt	RF	Fe	4.7*10^-4	128	0.0194	233	0.015	60	101.3	100	2	750	120	680	100	50	1	50	378	900
31A18b (graphite sheet).pdf	graphite sheet	31a18b.txt	RF	Fe	3.0*10^-4	135	0.0205	43 (2nm)	0.047	60	1.00477 5549	100	2	750	120	680 (730 CVD)	100	50	1	50	- 393V/ 380V	900
05B18a (IBEC).pdf	Si	05b18a.txt	RF	Fe	2.6*10^-4	135	0.0202	64 (3nm)	0.047	60	-105.3	100	2	750	120	680	100	50	1		-387/	900
05B18b (IBEC).pdf	Si	05b18b.txt	RF	Fe	3.7*10^-4	135	0.0202	64 (3nm)	0.047	60	1.01620 591	100	2	750	120	680	100	50	1		-394	900
06B18a (graphite sheet+AlO2).pdf	graphite sheet	06b18a.txt	RF	Fe	3.2*10^-4	135	0.0202	64 (3nm)	0.047	60	1.00657 277	100	2	750	120	680	100	50	1	50	-398V	900
07B18a (graphite sheet+AlO2).pdf	graphite sheet	07b18a.txt	RF	Fe	2.3*10^-4	135	0.0202	64 (3nm)	0.047	60	-106.7	100	2	750	120	630 (730)	100	50	1	50	-398V	900
13C17a.pdf	SS+gradientSS+Al N	13C17a.txt	RF	Fe	3.4*10^-4	128	0.0199	62	0.026	60	-98	100	2	750	120	700	100	50	1	50	-352	900
13C17b.pdf	SS+Ni+Ti+AlN	13C17b.txt	RF	Fe	2.8*10^-4	128	0.0199	62	0.026	60	-98	100	2	750	120	700	100	50	1	50	-380	900
13C17c.pdf	SS+Ni+Ti+AlN	13C17c.txt	RF	Fe	2.8*10^-4	128	0.0199	62	0.04	60	-96.5	100	2	750	120	680	100	50	1	50	-380	900
13C18a (SS304+DLC+CNTs)(WACVD).pdf	SS304	13C18a.txt	RF	Fe	3.9*10^-4	135	0.021	78 (3nm)	0.0383	60	- 1.01725 791	100	2	750	120	600/730	100	50	1			600
13E19a-SS304+CNTs (H2O plasma).pdf	SS+CNTs	13E19a.txt			3.4*10^-4																	
13F18a (WACVD).pdf	Si+Al2O3	13f18a.txt	RF	Fe	4.7*10^-4	135	0.0207	25	0.04	60	-121.8	100	2	750	120	600 (730)	100	50	1			1800
13F18b (WACVD).pdf	Si+Al2O3	13f18b.txt	RF	Fe	4.8*10^-4	135	0.021	25	0.04	60	-121.8	100	2	750	120	600 (730)	100	50	1			1800
08B18a (WACVD).pdf	Si	08b18a.txt	RF	Fe	4*10^-4	135	0.0202	64 (3nm)	0.047	60	-101.8	100	2	750	120	600 (730)	100	50	1	50	-398V	900
13G17b (Al2O3).pdf	Si	13G17b.txt	RF	Al	4.2*10^-4	8.6 (12.5)	0.0033	635	0.016	120	-105											
12B18a (WACVD).pdf	Si	12b18a.txt	RF	Fe	3.2*10^-4	135	0.0202	64 (3nm)	0.047	60	-105.3	100	2	750	120	600 (730)	100	50	1	50	-398V	900
13I17c (test-Si).pdf	Si	13I17c.txt	RF	Fe	4.7*10^-4	65 (128)	0.019	45	0.044	60	-107	100	2	750	120	600	100	50	1	50	-344	900
13B18a (WACVD).pdf	Si	13b18a.txt	RF	Fe	2.6*10^-4	135	0.0202	64 (3nm)	0.047	60	-106.6	100	2	750	120	600 (730)	100	50	1	50	-398V	900
13K18a (Copper+SS-nucleation study).pdf	Copper+SS304	13K18a.txt			3.1*10^-4							100	2	750	120	730						
13K18b (Copper+SS+CNTs).pdf	Copper+SS304	13K18b.txt			4.8*10^-4							100	2	750	120	730	100	50	2	50	-380	900
21B18a (graphite sheet).pdf	graphite sheet	21b18a.txt	RF	Fe	2.60E-04	135	0.0202	64	0.0383	60	-104.5	100	2	750	120	680	100	50	1	50	-380/-	1800
22B18a (graphite sheet).pdf	graphite sheet	22b18a.txt	RF	Fe	2.60E-04	135	0.0202	64	0.0383	60	-104.7	100	2	750	120	600/730	100	50	1			900

	Substrate	File	Catalyst															PECVD					
			source	Target	Previous vacuum Pa	Ar sccm	Pressure mbar	time s	Deposition rate nms	Power W	Vbias V	H2 sccm	P mbar	Ramp time s	Hold time s	Tfinal C	NH3 sccm	C2H2 sccm	P mbar	RF W	Vbias V_2	Deposition time s
02C18a (WACVD).pdf	Si	02c18a.txt	RF	Fe	2.6*10^-4	135	0.0202	64	0.0383	60	-108.1	100	2	750	120	600 (730)	100	50	1			900
05C18a (WACVD).pdf	Si	05c18a.txt	RF	Fe	4.5*10^-4	135	0.0202	64	0.0383	60	-106.5	100	2	750	120	600 (730)	100	50	1			150
05C18b (WACVD).pdf	Si	05c18b.txt	RF	Fe	3.4*10^-4	135	0.0202	64	0.0383	60	-105.6	100	2	750	120	600 (730)	100	50	1			150
09C18a (WACVD).pdf	Si	09C18a.txt	RF	Fe	3.3*10^-4	135	0.0202	64s	0.0383	60	-104.9	100	2	750	120	600/730	100	50	1			150
16D18a (Cleaning Fe target).pdf	Glass	16d18a.txt	RF	Fe	5.5*10^-4	135	0.0207	300		60	-123.7											
16D18b (Fe calibration).pdf	Glass	16d18b.txt	RF	Fe		135		1800	0.04	60												
14B18a (Fe callibration).pdf	glass (PREMIERE, Ted Pella) 1"X1"	14b18a.txt	RF	Fe	3.3*10^-4	135	0.0202	600 (~33nm)	0.0383	60	-105.6											
23D18a (PECVD).pdf	Si	23d18a.txt	RF	Fe	3.6*10^-4	135	0.0203	75	0.04	60	-122.9	100	2	750	120	680	100	50	1	50		900
23D18b (PECVD).pdf	SS	23d18b.txt	RF	Fe	4.8*10^-4	135	0.0203	75	0.04	60	-120.5	100	2	750	120	600 (730)	100	50	1	50	387	1800
23D18c (WACVD).pdf	Si	23d18c.txt	RF	Fe	4.8*10^-4	135	0.0203	62	0.04	60	-119.8	100	2	750	120	600 (730)	100	50	1	50	387	1800
14F18a (WACVD).pdf	Si+Al2O3	14f18a.txt	RF	Fe	6.4*10^-4	135	0.021	25	0.04	60	-121.8	100	2	750	120	600 (730)	100	50	1			1800
14I18a (SS304+CNTs).pdf	SS304	14i18a.txt			6.5*10^-4							100	2	750	120	730	100	50	1	50	1.03765	600
08e18a (WACVD).pdf	Si+Al2O3	08e18a.txt	RF	Fe	2.8*10^-4	135	0.0206	25	0.04	60	-120.2	100	2	750	120	600 (730)	100	50	1			1800
14K18a (Copper+SS+CNTs).pdf	Copper+SS304	14K18a.txt			2.5*10^-4							100	2	750	120	730	100	50	1	50	1.03359	900
14K18b (Copper+SS+CNTs).pdf	Copper+SS304	14K18b.txt			4.9*10^-4							100	2	750	120	730	100	50	1	50	1.08527	900
14K18c (Copper+SS+CNTs).pdf	Copper+SS304	14K18c.txt			5.0*10^-4							100	2	750	120	730	100	50	1	50	1.03819	900
02e18a (PECVD).pdf	Graphite	02e18a.txt	RF	Fe	1.7*10^-4	135	0.021	75	0.04	60	-122.5	100	2	750	120	680	100	50	1	50	371	900
11F18a (PECVD).pdf	Graphite	11f18a.txt	RF	Fe	4.8*10^-4	135	0.0203	75	0.04	60	-121.2	100	2	750	120	680	100	50	1	50	385	900
12F18a (PECVD).pdf	Graphite	12f18a.txt	RF	Fe	4.2*10^-4	135	0.0203	62	0.04	60	-122.3	100	2	750	120	680	100	50	1	50	385	900
04I18a (SS304+CNTs).pdf	SS304	04i18a.txt			8.6*10^-4							100	2	750	120	730	100	50	1	50	0.96606	600
14e18a (WACVD).pdf	Si+Al2O3	11e18a.txt	RF	Fe	2.8*10^-4	135	0.0205	17.5	0.04	60	-122.6	100	2	750	120	600 (730)	100	50	1			1800
05I18a (SS304+CNTs).pdf	SS304	05i18a.txt			8.6*10^-4							100	2	750	120	730	100	50	1	50	0.96606	600
05I18b (SS304+CNTs).pdf	SS304	05i18b.txt			4.7*10^-4							100	2	750	120	730	100	50	1	50	1.01015	600
15B17b-Fe calibration.pdf	Glass	15B17b.txt	RF	Fe	3.5*10^-4	128	0.0195	1200		60	98											
15B17c-Fe calibration.pdf	Glass	15B17c.txt	RF	Fe	3.7*10^-4	128	0.0197	1200+1200		60	97											
05I18c (SS304+CNTs).pdf	SS304	05i18c.txt			8.8*10^-4							100	2	750	120	730	100	50	1	50	1.02538	900
15B18a (graphite sheet).pdf	graphite sheet	15b18a.txt	RF	Fe	4.3*10^-4	135	0.0205	64	0.0383	60	1.004775549	100	2	750	120	680 (730 CVD)	100	50	1	50	-393V/380V	900
05I18d (SS304+CNTs).pdf	SS304	05i18d.txt			6.8*10^-4							100	2	750	120	730	100	50	1	50	-378	600
07I18a (SS304+CNTs).pdf	SS304	07i18a.txt			7.4*10^-4							100	2	750	120	730	100	50	1	50	-401	600
07I18b (SS304+CNTs).pdf	SS304	07i18b.txt			7.4*10^-4							100	2	750	120	730	100	50	1	50	-401	600
17I18b (PECVD).pdf	Si	17i18b.txt	RF	Fe	4.4*10^-4	135	0.021	75	0.04	60	-121.3	100	2	750	120	680	100	50	1	50	-401	1800
15C17c.pdf	Si	15C17c.txt	RF	Fe	4.6*10^-4	128	0.0199	62	0.04	60	-95.5	100	2	750	120	680	100	50	1	50	370-329	900
15F18a (WACVD).pdf	Si+Al2O3	15f18a.txt	RF	Fe	4.8*10^-4	135	0.021	25	0.04	60	-120.3	100	2	750	120	600 (730)	100	50	1			1800
15I17a (test-Si).pdf	Si	15i17a.txt	RF	Fe	4.2*10^-4	66 (128)	0.0202	45	0.044	60	-116	100	2	750	120	600	100	50	1	50	-303	900
18I18b (SS304+CNTs).pdf	SS304	18i18b.txt			5.5*10^-4							100	2	750	120	730	100	50	1	50	0.99525	600
15J18a (SS304+DLC+CNTs).pdf	SS304	15j18a.txt																				
15J18b (SS304+CNTs).pdf	SS304	15j18b.txt										100	2	750	120	680	100	50	1	50	1.04381	600
19I18a (SS304+CNTs).pdf	SS304	19i18a.txt			4.5*10^-4							100	2	750	120	730	100	50	1	50	-410	600
21I18a (SS304+CNTs).pdf	SS304	21i18c.txt			4.0*10^-4							100	2	750	120	730	100	50	1	40	1.29861	600
25I18a (SS304+CNTs).pdf	SS304	25i18c.txt			3.8*10^-4							100	2	750	120	730	100	50	1	40	1.02895	600
15e18a (WACVD).pdf	Al2O3	15e18a.txt	RF	Fe	2.6*10^-4	135	0.0203	15	0.04	60	-121.5	100	2	750	120	600 (730)	100	50	1			1800
26I18a (SS304+CNTs).pdf	SS304	26i18a.txt			4.9*10^-4							100	2	750	120	650	100	50	1	55	-408	600
26I18b (SS304+CNTs).pdf	SS304	26i18b.txt			4.9*10^-4							100	2	750	120	730	100	50	1	55	1.04926	600
26I18c (SS304+CNTs).pdf	SS304	26i18c.txt			4.9*10^-4							100	2	750	120	730	100	50	1	55	1	600
16B17b.pdf	Si	16B17b.txt	RF	Fe	3.5*10^-4	128	0.0194	62	0.04	60	-97	100	2	750	120	680	100	50	1	50	374-384	900
27I18a (SS304+CNTs).pdf	SS304	26i18c.txt			4.9*10^-4							100	2	750	120	650	100	50	1	60	-414	600
16C17a.pdf	Si	16C17a.txt	RF	Fe	3.2*10^-4	128	0.0199	62	0.04	60	-99	100	2	750	120	700	100	50	1	50	-335	1200
09J18a (Graphite).pdf	Graphite	09J18a.txt	RF	Fe	3.2*10^-4	135	0.021	13 (0.5nm)	0.04	60	0.996747967	100	2	750	120	700	100	50	1	60	1.0273	900
09J18b (Graphite).pdf	Graphite	09J18b.txt	RF	Fe	3.2*10^-4	135	0.021	25 (1nm)	0.04	60	0.941223833	100	2	750	120	700	100	50	1	60	1.00948	900

	Substrate	File	Catalyst														PECVD					
			source	Target	Previous vacuum Pa	Ar sccm	Pressure mbar	time s	Deposition rate nms	Power W	Vbias V	H2 sccm	P mbar	Ramp time s	Hold time s	Tfinal C	NH3 sccm	C2H2 sccm	P mbar	RF W	Vbias V_2	Deposition time s
16G18d (WACVD).pdf	Al2O3 grid/Si/Al2O3	16g18a.txt	RF	Fe	4.8*10^-4	135	0.021	40	0.04	60	-124.5	100	2	750	120	600 (730)	100	50	1			1800
09J18c (Graphite).pdf	Graphite	09J18c.txt	RF	Fe	4.1*10^-4	135	0.021	38 (1.5nm)	0.04	60	1.00324412	100	2	750	120	700	100	50	1	60	-427/-	900
16J17a (Al2O3).pdf	SS304 (grid)	16J17a.txt	RF	Al	1.9*10^-4	12.1 (17)	0.0043	1250	0.016	120	-93											
16J17a (SS304-Grid).pdf	SS304 (grid)	16J17a.txt	RF	Fe	5.5*10^-4	67 (128)	0.0198	64s / 3nm	0.047	60	-104.7	100	2	750	120	600	100	50	1	50	-389	900
09J18d (Graphite).pdf	Graphite	09J18d.txt	RF	Fe	3.9*10^-4	135	0.021	50 (2nm)	0.04	60	0.99675 0609	100	2	750	120	700	100	50	1	60	1.0071 9	900
09J18e (Graphite).pdf	Graphite	09J18e.txt	RF	Fe	4.6*10^-4	135	0.021	63 (2.5nm)	0.04	60	0.99173 5537	100	2	750	120	700	100	50	1	60	1.0095 5	900
10J18a (Graphite).pdf	Graphite	10J18a.txt	RF	Fe	3.3*10^-4	135	0.021	75 (3nm)	0.04	60	0.99682 035	100	2	750	120	700	100	50	1	60	1.0317 1	900
15J18c (SS304+CNTs).pdf	SS304	15J18c.txt										100	2	750	120	680	100	50	1	50	1.0080 6	600
16J18a (SS304+CNTs).pdf	SS304	16J18a.txt										100	2	750	120	680	100	50	1	50	1.0341 5	600
16J18b (Graphite).pdf	Graphite	16J18b.txt	RF	Fe	4.7*10^-4	135	0.021	50 (2nm)	0.04	60	0.96104 9285	100	2	750	120	600	100	50	1	60	1.0102 3	900
16J18c (Graphite).pdf	Graphite	16J18c.txt	RF	Fe	3.7*10^-4	135	0.021	50 (2nm)	0.04	60	0.98251 1924	100	2	750	120	650	100	50	1	60	0.9975 3	900
16e18a (WACVD).pdf	Si con Al2O3	16e18a.txt	RF	Fe	3.4*10^-4	135	0.0205	15	0.04	60	-121.3	100	2	750	120	600 (730)	100	50	1			1800
16e18b (WACVD).pdf	Si+Al2O3	16e18b.txt	RF	Fe	4.1*10^-4	135	0.0205	17.5	0.04	60	-122.6	100	2	750	120	600 (730)	100	50	1			1800
16J18d (Graphite).pdf	Graphite	16J18d.txt	RF	Fe	4.1*10^-4	135	0.021	50 (2nm)	0.04	60	0.99182 3385	100	2	750	120	750	100	50	1	60	1.0410 6	900
17B17b.pdf	Si	17B17b.txt	RF	Fe	2.3*10^-4	128	0.0194	39	0.026	60	98.7	100	2	750	120	680	100	50	1	50	-381	900
18J18f (SS304+CNTs).pdf	SS304	18J18f.txt	RF	Fe	3.9*10^-4	135	0.0209	50 (2nm)	0.04	60	-121.3	100	2	750	120	730	100	50	1	50	-393/-	600
19J18a (SS304+CNTs).pdf	SS304	19J18a.txt	RF	Fe	4.1*10^-4	135	0.0209	75 (3nm)	0.04	60	-113.4	100	2	750	120	730	100	50	1	50	-383/-	600
17G17b (Al2O3-Grid).pdf	Al2O3	17G17b.txt	RF	Fe	5.1*10^-4	90 (128)	0.02	45	0.044	60	-100.7	100	2	750	120	600	100	50	1			1800
17G18a (WACVD).pdf	Al2O3 grid/Si/Al2O3	17g18a.txt	RF	Fe	4.2*10^-4	135	0.021	50	0.04	60	-124.9	100	2	750	120	730	100	50	1			1800
17G18b (WACVD).pdf	Al2O3 grid/Si/Al2O3	17g18b.txt	RF	Fe	4.7*10^-4	135	0.021	50	0.04	60	-124.9	100	2	750	120	730	100	50	1			1800
21J18a (SS304+CNTs).pdf	SS304	21J18a.txt	RF	Fe	3.7*10^-4	135	0.0209	75 (3nm)	0.04	60	-117.7	100	2	750	120	730	100	50	1	50	-383/-	600
17I18a (SS304+CNTs).pdf	SS304	17I18a.txt			5.8*10^-4							100	2	750	120	730	100	50	1	45	1.0052 9	600
22J18c (Graphite).pdf	Graphite	22J18c.txt	RF	Fe	3.5*10^-4	135	0.021	50 (2nm)	0.04	60	0.99199 3595	100	2	750	120	750	100	50	1	50	1.0510 8	600
17I18c (SS304)(Surface morphology study).pdf	SS304	17I18cht																				
17I18d (SS304)(Surface morphology study).pdf	SS304	17I18dht																				
22J18d (Graphite).pdf	Graphite	22J18d.txt	RF	Fe	4.2*10^-4	135	0.021	50 (2nm)	0.04	60	0.99428 5714	100	2	750	120	750	100	50	1	60	1.0404 8	600
17J17a (AlN).pdf	Si wafer	17J17a.txt	RF	Al	2.6*10^-4	12.1 (17)	0.0043	1250	0.016	120	-93											
22J18e (Graphite).pdf	Graphite	22J18e.txt	RF	Fe	4.3*10^-4	135	0.021	50 (2nm)	0.04	60	0.98935 2989	100	2	750	120	750	100	50	1	60	1.0279 1	1200
23J18a (SS304+CNTs).pdf	SS304	23J18a.txt	RF	Fe	3.8*10^-4	135	0.0209	75 (3nm)	0.04	60	-123	100	2	750	120	730	100	50	1	50	-417/-	600
17e18a (SS304+DLC+CNTs)+H2O plasma.pdf	SS304	17E18a.txt	RF	Fe	3.5*10^-4	135	0.021	75 (3nm)	0.04	60	1.00158 3531	100	2	750	120	680	100	50	1	50	1.0102	600
23J18b (Graphite).pdf	Graphite	23J18a.txt	RF	Fe	4.2*10^-4	135	0.021	50 (2nm)	0.04	60	0.99105 6911	100	2	750	120	750	100	50	1	60	1.0581 4	300
23J18c (SS304+CNTs).pdf	SS304	23J18c.txt	RF	Fe	2.9*10^-4	135	0.0209	50 (2nm)	0.04	60	0.99352 7508	100	2	750	120	730	100	50	1	70	1.0239 7	600
23J18d (Graphite-ICMAB).pdf	Graphite	23J18d.txt	RF	Fe	4.3*10^-4	135	0.021	50 (2nm)	0.04	60	0.98855 2739	100	2	750	120	750	100	50	1	60	-0.0025	900
01G19a test.pdf	Graphite	24J18b.txt	RF	Fe	4.1*10^-4	135	0.021	50 (2nm)	0.04	60	-122.9.5/-124.2	100	2	750	120	750	100	50	1	60	1.0363 2	900
18D17a (Al2O3).pdf	Glass	12D17c.txt	RF	Al	2.8*10^-4	37 (51)	0.0107	600		120	-182											
18D17a.pdf	Si+Al2O3	10D17b.txt	RF	Fe	2.8*10^-4	128	0.0203	50	0.04	60	-98.2	100	2	750	120	600	100	50	1.0132	-	-	1800
18D18a (SS304+CNTs).pdf	SS304	18D18a.txt			5.9*10^-4							100	2	750	120	730	100	50	1	50	1.0410 3	600
18D18b (SS304+CNTs).pdf	SS304	18D18b.txt			5.9*10^-4							100	2	750	120	730	100	50	1	50	1.0259 7	600
18D18c (SS304+CNTs).pdf	SS304	18D18c.txt			5.9*10^-4							100	2	750	120	730	100	50	1	50	1.0337 7	600
18F18a (WACVD).pdf	Back of Si+Al2O3	18f18a.txt	RF	Fe	4.4*10^-4	135	0.0225	25	0.04	60	-120.2	100	2	750	120	600 (730)	100	50	1			1800
24J18a (Graphite-ICMAB).pdf	Graphite	24J18a.txt	RF	Fe	3.7*10^-4	135	0.021	50 (2nm)	0.04	60	0.98888 0064	100	2	750	120	750	100	50	1	60	-0.0025	900
18G17a (Al2O3).pdf	SS304+G SS304	18G17a.txt	RF	Al	2.7*10^-4	12.1 (17)	0.0043	600	0.016	120	-102											
18G17a (WACVD).pdf	SS304+G SS304+Al2O3	18G17a.txt	RF	Al	3.6*10^-4	90 (128)	0.02	45	0.044	60	-101	100	2	750	120	600	100	50	1			1800
18G17b (Al2O3).pdf	SS304+G SS304	18G17a.txt	RF	Al	2.7*10^-4	8.6 (12.5)	0.0033	600	0.016	120	-102											

	Substrate	File	Catalyst															PECVD					
			source	Target	Previous vacuum Pa	Ar sccm	Pressure mbar	time s	Deposition rate nms	Power W	Vbias V	H2 sccm	P mbar	Ramp time s	Hold time s	Tfinal C	NH3 sccm	C2H2 sccm	P mbar	RF W	Vbias V_2	Deposition time s
18G17b (WACVD).pdf	SS304+G SS304+Al2O3	18G17a.txt	RF	Al	3.5*10^-4	8.6 (12.5)	0.033	635	0.044	120	-101	100	2	750	120	600	100	50	1			1800
24J18b (Graphite-ICMAB).pdf	Graphite	24J18b.txt	RF	Fe	4.1*10^-4	135	0.021	50 (2nm)	0.04	60	-122.9.5/ -124.2	100	2	750	120	750	100	50	1	60	1.03632	900
18I18a (SS304+CNTs).pdf	SS304	18I18a.txt			5.5*10^-4							100	2	750	120	730	100	50	1	50	0.99525	600
24J18c (Graphite-ICMAB).pdf	Graphite	24J18c.txt	RF	Fe	4.5*10^-4	135	0.021	50 (2nm)	0.04	60	0.99262 2951	100	2	750	120	750	100	50	1	60	1.01591	900
18J17a (Al2O3).pdf	SS304 (grid)	16J17a.txt	RF	Al	1.9*10^-4	12.1 (17)	0.0043	1250	0.016	120	-93											
18J17a (SS304-Grid).pdf	SS304 (grid)	16J17a.txt	RF	Fe	5.5*10^-4	67 (128)	0.0198	64s / 3nm	0.047	60	-104.7	100	2	750	120	600	100	50	1	50	-389	900
18J18a (quartz+DLC+callibration).pdf	Quarz	18J18a.txt			5.0*10^-4																	
18J18b (quartz+DLC+callibration).pdf	Quartz	18J18b.txt			4.7*10^-4																	
18J18c (quartz+DLC+callibration).pdf	Quartz	18J18c.txt			4.8*10^-4																	
18J18d (quartz+DLC+callibration).pdf	Quartz	18J18d.txt			3.9*10^-4																	
18J18e (quartz+DLC+callibration).pdf	Quartz	18J18e.txt			3.0*10^-4																	
25J18a (SS304+CNTs).pdf	SS304	25J18a.txt	RF	Fe	2.6*10^-4	135	0.0207	50 (2nm)	0.04	60	0.98946 5154	100	2	750	120	730	100	50	1	50	-0.2544	600
10K18a (SS304+CNTs).pdf	SS304	10k18a.txt			8.0*10^-4							100	2	750	120	730	100	50	1	50	1.00922	300
10K18b (SS304+CNTs).pdf	SS304	10k18b.txt			9.5*10^-4							100	2	750	120	730	100	50	1	50	1.02123	600
12K18a (SS304+CNTs).pdf	SS304	12k18a.txt			8.5*10^-4							100	2	750	120	730	100	50	1	50	1.00744	1800
18b19b (Graphite).pdf	Graphite	18b19b.txt	RF	Fe	4.6*10^-4	128	0.0202	67 (2nm)	0.03	60	1.00190 1141	100	2	750	120	750	100	50	1	50	-361	900
18b19c (Graphite).pdf	Graphite	18b19c.txt	RF	Fe	3.6*10^-4	128	0.0202	67 (2nm)	0.03	60	-105.2	100	2	750	120	750	100	50	1	60	-418	900
18e18a (WACVD).pdf	Si+Al2O3	18e18b.txt	RF	Fe	4.1*10^-4	135	0.0205	15	0.04	60	-123.3	100	2	750	120	600 (730)	100	50	1			1800
18e18b (WACVD).pdf	Si+Al2O3	18e18b.txt	RF	Fe	4.4*10^-4	135	0.0205	15	0.04	60	-122.2	100	2	750	120	600 (730)	100	50	1			1800
12K18b (SS304+CNTs).pdf	SS304	12k18b.txt			6.9*10^-4							100	2	750	120	730	100	50	1	50	-407	1200
22K18a (SS304+CNTs).pdf	SS304	22k18a.txt			6.9*10^-4							100	2	750	120	730	100	50	1	50	-0.0026	1800
26K18a (SS304+CNTs).pdf	SS304	26k18a.txt			4.2*10^-4							100	1	900	200	730	100	50	1	50	1.04557	1800
26K18b (SS304+CNTs).pdf	SS304	26k18b.txt			4.1*10^-4							100	1	900	620	730	100	50	1	50	1.01285	1200
27K18a (SS304+CNTs).pdf	SS304	27k18a.txt			4.2*10^-4							100	1	900	620	680	100	50	1	50	-403/	1800
27K18b (SS304+CNTs).pdf	SS304	27k18b.txt			4.2*10^-4							100	1	900	620	600/730	100	50	1	50	0.98565	1800
19B18a (graphite sheet).pdf	graphite sheet	19b18a.txt	RF	Fe	3.5*10^-4	135	0.0202	64	0.0383	60	-103.6	100	2	750	120	680	100	50	1	50	-377	900
19B18b (graphite sheet).pdf	graphite sheet	19b18a.txt	RF	Fe	5.70E-04	135	0.0202	64	0.0383	60	-102.3	100	2	750	120	680	100	50	1	50	-378	900
28K18a (SS304+CNTs).pdf	SS304	28k18a.txt			2.3*10^-4							100	1	900	620	500/730	100	50	1	50	1.01653	1800
30K18a (SS304+CNTs).pdf	SS304	30k18a.txt			2.7*10^-4							100	1	900	620	500/730	100	50	1	50	1.01493	1800
03L18a (SS304+CNTs).pdf	SS304	03L18a.txt			2.8*10^-4							100	1	900	620	500/730	100	50	1	50	1.00489	1800
19C19a (SS304)(reduction-OES).pdf	SS304	19c19aht																				
19D17a (Al2O3).pdf	Glass	19D17b.txt	RF	Al	2.8*10^-4	8.6 (12.5)	0.0033	900	0.016	120	-185											
03L18b (SS304+CNTs).pdf	SS304	03L18b.txt			6.1*10^-4							100	1	900	620	500/730	100	50	1	50	1.04489	1800
19F18a (SS304+CNTs).pdf	SS304	19F18a.txt			7.6*10^-4							100	2	750	120	730	100	50	1	50	1.01408	600
19F18b (SS304+CNTs).pdf	SS304	19F18b.txt			5.9*10^-4							100	2	750	120	730	100	50	1	50	1.01408	600
04L18a (SS304+CNTs).pdf	SS304	04L18a.txt			3.7*10^-4							100	1	900	620	500/730	100	50	1	50	1.01759	1800
19G18a (WACVD).pdf	Al2O3 grid/Si/Al2O3	19g18a.txt	RF	Fe	4.1*10^-4	135	0.021	63	0.04	60	-122	100	2	750	120	600(900)	100	50	1			1800
04L18b (SS304+CNTs).pdf	SS304	04L18b.txt			3.2*10^-4							100	1	900	620	500/730	100	50	1	50	1.02872	1800
04L18c (SS304+CNTs).pdf	SS304	04L18c.txt			6.8*10^-4							100	1	900	620	500/730	100	50	1	50	0.97	1800
07L18a (SS316+CNTs).pdf	SS316	07L18a.txt			2.8*10^-4							100	1	900	620	730	100	50	1	50	1.02993	1800
19I18b (SS304+CNTs).pdf	SS304	19I18b.txt			6.7*10^-4							100	2	750	120	730	100	50	1	45	1.01519	600
19I18c (SS304+CNTs).pdf	SS304	19I18c.txt			7.2*10^-4							100	2	750	120	730	100	50	1	40	1	600
19I18d (SS304+CNTs).pdf	SS304	19I18d.txt			6.9*10^-4							100	2	750	120	730	100	50	1	35	0.88136	600
19J17a (Al2O3-Grid).pdf	Al2O3	19J17a.txt	RF	Fe	4.0*10^-4	90 (128)	0.02	85	0.047	60	-103.5	100	2	750	120	600	100	50	1			1800
07L18b (SS316+CNTs).pdf	SS316	07L18b.txt			3.5*10^-4							100	1	900	620	600/730	100	50	1	50	1.0402	1800
07L18c (SS316+CNTs).pdf	SS316	07L18c.txt			3.5*10^-4							100	1	900	620	500/730	100	50	1	50	0.99485	1800
19L16a.pdf	SS304+Ni+Ti+AlN	19L16a.txt	RF	Fe	1.3*10^-4	128	0.0193	25	0.04	60	97	100	2	500	120	600	100	50	1	50	342	1200

	Substrate	File	Catalyst														PECVD					
			source	Target	Previous vacuum Pa	Ar sccm	Pressure mbar	time s	Deposition rate nms	Power W	Vbias V	H2 sccm	P mbar	Ramp time s	Hold time s	Tfinal C	NH3 sccm	C2H2 sccm	P mbar	RF W	Vbias V_2	Deposition time s
10L18a (SS316+CNTs).pdf	SS316	10L18a.txt			2.7*10^-4							100	1	900	620	500/730	100	50	1	50	1.01768	1800
10L18b (SS316+CNTs).pdf	SS316	10L18b.txt			5.1*10^-4							100	1	750	120	730	100	50	1	50	-403/-	1800
10L18c (SS316+CNTs).pdf	SS316	10L18c.txt			5.1*10^-4							100	1	750	120	500/730	100	50	1	50	1.00969	1800
12L18a (SS316+CNTs).pdf	SS316	12L18a.txt			2.3*10^-4							100	1	750	120	600/730	100	50	1	50	-389/-	1800
12L18b (SS316+CNTs).pdf	SS316	12L18b.txt			5.7*10^-4							100	1	750	120	600/730	100	50	1	50	-0.0025	1800
20A17b.pdf	Si	20A17b.txt	RF	Fe	2.5*10^-4	128	0.0195	87	0.04	60	96.7	100	2	750	120	680	100	50	1	50	372	900
19L18a (SS304+CNTs).pdf	SS304	19L18a.txt			5.1*10^-4							100	1	750	120	730	100	50	1	50	1.05598	1800
14a19a (Fe Calibration).pdf	Glass	14a19a.txt	RF	Fe	3.7*10^-4	128	0.0206	600		60	-106.2/											
20C17a.pdf	SS+SSgradient+AlN	20C17a.txt	RF	Fe	3.3*10^-4	128	0.0199	62	0.026	60	-97.6	100	2	750	120	700	100	50	1	50	-334	1200
20C17b.pdf	SS+SSgradient+AlN	20C17b.txt	RF	Fe	4.5*10^-4	128	0.0199	62	0.026	60	-95.6	100	2	750	120	700	100	50	1	50	-325	1200
20C18a (SS304+DLC+CNTs).pdf	SS304	20C18a.txt	RF	Fe	2.0*10^-4	135	0.021	78 (3nm)	0.0383	60	-1.004784689	100	2	750	120	680	100	50	1	50	1.03581	600
16a19a (SS316+CNTs).pdf	SS316	16a19a.txt			2.6*10^-4							100	1	750	120	600/730	100	50	1	50	-396/	1800
20F18a (SS304+CNTs).pdf	SS304	20F18a.txt			4.9*10^-4							100	2	750	120	730	100	50	1	50	1.02528	600
20F18b (SS304+CNTs).pdf	SS304	20F18b.txt			5.5*10^-4							100	2	750	120	730	100	50	1	60	1.01093	600
20F18c (SS304+CNTs).pdf	SS304	20F18c.txt			7.5*10^-4							100	2	750	120	730	100	50	1	60	1.0068	600
18a19a (SS316+CNTs).pdf	SS316	18a19a.txt			2.2*10^-4							100	1	750	120	600/730	100	50	1	50	-0.0024	1800
22a19a (SS304+CNTs).pdf	SS304	22a19a.txt			2.9*10^-4							100	1	750	620	500/730	100	50	1	50	1.08696	1800
20G18a (WACVD).pdf	Al2O3 grid/Si/Al2O3	20g18a.txt	RF	Fe	4.1*10^-4	135	0.0225	63	0.04	60	-124.5	100	2	750	120	730	100	50	1			1800
22a19b (SS304+CNTs).pdf	SS304	22a19b.txt			2.9*10^-4							100	1	900	620	730	100	50	1	50	1.09499	1800
22a19c (SS304+CNTs).pdf	SS304	22a19c.txt			2.9*10^-4							100	1	900	620	500/730	100	50	1	50	1.06286	1800
20I18a (SS304+CNTs).pdf	SS304	20I18a.txt			4.9*10^-4							100	2	750	120	730	100	50	1	40	0.99468	600
23a19a (SS304+CNTs).pdf	SS304	23a19a.txt			2.9*10^-4							100	1	900	620	500/730	100	50	1	50	1.01554	1800
20L16a.pdf	SS304+Ni+Ti+AlN	20L16a.txt	RF	Fe	1.5*10^-4	128	0.0194	25	0.04	60	98	100	2	500	120	600	100	50	1	50	357	1200
23a19b (SS304+CNTs).pdf	SS304	23a19b.txt			4.0*10^-4							100	1	900	620	500	100	50	1	50	1.01554	1800
23a19c (SS304+CNTs).pdf	SS304	23a19c.txt			4.0*10^-4							100	1	900	620	500/730	100	50	1	50	0.97701	1800
23a19d (SS304+CNTs).pdf	SS304	23a19d.txt			4.4*10^-4							100	1	900	620	500/730	100	50	1	50	0.96438	1800
28a19a (Graphite).pdf	Graphite	28a19a.txt	RF	Fe	2.0*10^-4	128	0.021	50 (1.5nm)	0.03	60	1.004642526	100	2	750	120	750	100	50	1	60	1.04082	900
21C19a (SS304)(reduction-OES).pdf	SS304	21c19aht																				
21C19b (SS304)(reduction-OES).pdf	SS304	21c19bht																				
21C19c (SS304)(reduction-OES).pdf	SS304	21c19cht																				
21D17a (Depth profile XPS).pdf	SS+gradientSS+AlN	21D17a.txt	RF	Fe	2.5*10^-4	128 (90 H2 line)	0.0201	62	0.04	60	-96.9	100	2	750	120	680	100	0	0			
21D17b (Depth profile XPS).pdf	SS+gradientSS+AlN	21D17b.txt	RF	Fe	4.7*10^-4	128 (90 H2 line)	0.0201	62	0.04	60	-99.5	100	2	750	120	680						
21D17c (Depth profile XPS).pdf	SS+gradientSS+AlN	21D17c.txt	RF	Fe	3.9*10^-4	128 (90 H2 line)	0.0201	62	0.04	60	-99.3	100	2	750	120	700						
21D17d (Depth profile XPS).pdf	SS+gradientSS+AlN	21D17d.txt	RF	Fe	3.7*10^-4	128 (90 H2 line)	0.0201	62	0.04	60	-99.4	100	2	750	120	715						
21D17e (Depth profile XPS).pdf	SS+gradientSS+AlN	21D17e.txt	RF	Fe	3.4*10^-4	128 (90 H2 line)	0.0202	62	0.04	60	-99.1											
21D17f (Depth profile XPS).pdf	SS+gradientSS+AlN	21D17f.txt	RF	Fe	3.3*10^-4	128 (90 H2 line)	0.0201	62	0.04	60	-97.9	100	2	750	120	730						
21D17g (Depth profile XPS).pdf	SS+gradientSS+AlN	21D17g.txt	RF	Fe	4.7*10^-4	128 (90 H2 line)	0.0201	62	0.04	60	-98	100	2	750	120	600	100	50	1			1200
21F18a (SS304+CNTs).pdf	SS304	21F18a.txt			5.1*10^-4							100	2	750	120	730	100	50	1	50	1.02273	600
21F18b (SS304+DLC+CNTs).pdf	SS304	21F18b.txt	RF	Fe	4.9*10^-4	135	0.21	75	0.04	60	1.004269855	100	2	750	120	730	100	50	1	50	1.00504	600
21G17a (Al2O3-Grid).pdf	Al2O3	21G17a.txt	RF	Fe	4.7*10^-4	90 (128)	0.02	45	0.044	60	-100.7	100	2	750	120	600	100	50	1			1800
28a19b (Graphite).pdf	Graphite	28a19b.txt	RF	Fe	3.3*10^-4	128	0.021	67 (2nm)	0.03	60	1.00095057	100	2	750	120	750	100	50	1	65	1.02222	900
28a19c (Graphite).pdf	Graphite	28a19c.txt	RF	Fe	4.3*10^-4	128	0.021	67 (2nm)	0.03	60	1.005581395	100	2	750	120	750	100	50	1	80	1.0988	900
28a19d (Graphite).pdf	Graphite	28a19d.txt	RF	Fe	5.5*10^-4	128	0.021	83 (2.5nm)	0.03	60	1.005581395	100	2	750	120	750	100	50	1	80	1.0988	900
05b19a (Graphite).pdf	Graphite	05b19a.txt	RF	Fe	2.3*10^-4	128	0.021	67 (2nm)	0.03	60	1.010456274	100	2	750	120	750	100	50	1	60	-426/-	900

	Substrate	File	Catalyst														PECVD					
			source	Target	Previous vacuum Pa	Ar sccm	Pressure mbar	time s	Deposition rate nms	Power W	Vbias V	H2 sccm	P mbar	Ramp time s	Hold time s	Tfinal C	NH3 sccm	C2H2 sccm	P mbar	RF W	Vbias V_2	Deposition time s
05b19b (Graphite).pdf	Graphite	05b19b.txt	RF	Fe	2.1*10^-4	128	0.021	67 (2nm)	0.03	60	1.025689819	100	2	750	120	750	100	50	1	60	-0.0027	900
06b19a (Graphite).pdf	Graphite	06b19a.txt	RF	Fe	2.1*10^-4	128	0.0199	67 (2nm)	0.03	60	0.996303142	100	2	750	120	750	100	50	1	60	-0.0026	900
06b19b (Graphite).pdf	Graphite	06b19b.txt	RF	Fe	4.9*10^-4	128	0.0202	67 (2nm)	0.03	60	1.005714286	100	2	750	120	750	100	50	1	60	0.99754	900
22F17b (similar 21D17g) WACVD.pdf	SS+gradientSS+AlN	22F17b.txt	RF	Fe	4.7*10^-4	128 (90 H2 line)	0.0201	62	0.04	60	-97.3	100	2	750	120	600	100	50	1			1200
08b19a (SS304+CNTs).pdf	SS304	08b19a.txt			2.1*10^-4							100	1	900	620	500/730	100	50	1	50	0.96438	1800
13b19a (SS304+CNTs).pdf	SS304	13b19a.txt			2.4*10^-4							100	1	900	620	500/730	100	50	1	50	1.01944	1800
13b19b (SS304+CNTs).pdf	SS304	13b19b.txt			4.1*10^-4							100	1	900	620	500/730	100	50	1	50	0.98133	1800
13b19c (Cu wire).pdf	Cu wire coveredwith Ni	13b19c.txt			3.7*10^-4							100	1	900	620	500/730	100	50	1	50	0.98133	1800
13b19d (Graphite).pdf	Graphite	13b19d.txt	RF	Fe	3.1*10^-4	128	0.0202	67 (2nm)	0.03	60	1.009182736	100	2	750	120	750	100	50	1	60	-430/-	900
22J18a (SS304+DLC+CNTs).pdf	SS304	22J18a.txt	RF	Fe	5.2*10^-4	135	0.021	75 (3nm)	0.04	60	0.998348472	100	2	750	120	680	100	50	1	50	-380	600
22J18b (SS304+CNTs).pdf	SS304	22J18b.txt			4.9*10^-4							100	2	750	120	650	100	50	1	60	-414	600
27b19c (Cu wire).pdf	Cu wire coveredwith Ni	27c19c.txt			3.7*10^-4							100	1	900	620	500/730	100	50	1	50	0.98133	1800
14b19a (Graphite).pdf	Graphite	14b19a.txt	RF	Fe	2.3*10^-4	128	0.0202	67 (2nm)	0.03	60	1.001867414	100	2	750	120	750	100	50	1	60	-430/-	900
14b19b (Si+Al2O3).pdf	Si+Al2O3	14b19b.txt	RF	Fe	2.8*10^-4	128	0.0202	34 (1nm)	0.03	60	-105.4	100	2	750	120	600/730	100	50	1			900
15b19a (Si+Al2O3).pdf	Si+Al2O3	15b19a.txt	RF	Fe	2.8*10^-4	128	0.0202	34 (1nm)	0.03	60	-106.8	100	2	750	120	600/730	100	50	1			900
22K18b (SS304+CNTs).pdf	SS304	22k18b.txt			2.7*10^-4							100	2	750	500	730	100	50	1	50	1.02828	1800
15b19b (Si+Al2O3).pdf	Si+Al2O3	15b19b.txt	RF	Fe	3.2*10^-4	128	0.0201	34 (1nm)	0.03	60	-106.4	100	2	750	120	600/730	100	50	1			900
18b19a (Si+Al2O3).pdf	Si+Al2O3	15b19b.txt	RF	Fe	2.3*10^-4	128	0.0199	34 (1nm)	0.03	60	-106.5	100	2	750	120	600/730	100	50	1			900
19b19a (Graphite).pdf	Graphite+Al2O3	19b19a.txt	RF	Fe	2.2*10^-4	128	0.0202	67 (2nm)	0.03	60	-111.1	100	2	750	120	600/750	100	50	1			1800
21b19a (Si+Al2O3).pdf	Si+Al2O3	21b19a.txt	RF	Fe	2.3*10^-4	128	0.0199	34 (1nm)	0.03	60	-104.2	100	2	750	120	600/730	100	25	1			900
22b19a (Graphite).pdf	Graphite	22b19a.txt	RF	Fe	2.3*10^-4	128	0.0202	67 (2nm)	0.03	60	-104.7	100	2	750	120	750	100	50	1	60	-407/-	900
22b19b (Graphite).pdf	Graphite	22b19b.txt	RF	Fe	2.3*10^-4	128	0.0202	67 (2nm)	0.03	60	-104.9	100	2	750	120	750	100	50	1	60	1.0201	900
23b19a (Graphite).pdf	Graphite	23b19a.txt	RF	Fe	2.3*10^-4	128	0.0202	67 (2nm)	0.03	60	-103.3	100	2	750	120	750	100	50	1	60	-409/-	900
23b19b (Graphite).pdf	Graphite	23b19b.txt	RF	Fe	4.6*10^-4	128	0.0202	67 (2nm)	0.03	60	-105.4	100	2	750	120	750	100	50	1	60	-409/-	900
25b19a (Graphite).pdf	Graphite	25b19a.txt	RF	Fe	2.9*10^-4	128	0.0202	67 (2nm)	0.03	60	-106.2	100	2	750	120	750	100	50	1	60	-414/-	900
23A17a-Fe calibration.pdf	Glass	23A17a.txt	RF	Fe	2.5*10^-4	128	0.0195	600		60	106.1											
23A17a.pdf	Si	20A17b.txt	RF	Fe	2.5*10^-4	128	0.0195	87	0.04	60	96.7	100	2	750	120	680	100	50	1	50	372	900
23A17b-Fe calibration.pdf	Glass	23A17b.txt	RF	Fe	2.5*10^-4	128	0.0194	900		60	106.2											
25b19b (Graphite).pdf	Graphite	25b19b.txt	RF	Fe	4.2*10^-4	128	0.0202	67 (2nm)	0.03	60	-104.3	100	2	750	120	750	100	50	1	60	1.07143	900
23A17d.pdf	SS304+Ni+Ti+AlN	23A17d.txt	RF	Fe	2.9*10^-4	128	0.0193	90	0.04	60	105.5	100	2	675	120	700	100	50	1	50	396	1200
23A18a (SS304+DLC).pdf	SS304	23a18a.txt	RF	Fe	4.3*10^-4	135	0.021	64 (3nm)	0.047	60	-1.008797654	100	2	750	120	680	100	50	1	50	1.03093	600
25b19c (Graphite).pdf	Graphite	25b19c.txt	RF	Fe	3.6*10^-4	128	0.0202	67 (2nm)	0.03	60	-104	100	2	750	120	750	100	50	1	60	-408	900
23B17b.pdf	SS+Ni+Ti+AlN	23B17b.txt	RF	Fe	4.5*10^-4	128	0.0199	62	0.026	60	-96	100	2	750	120	700	100	50	1	50	367	900
25b19d (Graphite).pdf	Graphite	25b19d.txt	RF	Fe	4.1*10^-4	128	0.0202	67 (2nm)	0.03	60	-104.9	100	2	750	120	750	100	50	1	60	-413	900
23C18a (SS304+G-SS304+CNTs).pdf	SS304+G-SS304+AlN	23C18a.txt	RF	Fe	2.5*10^-4	135	0.0202	78 (3nm)	0.0383	60	1.01047619	100	2	750	120	730	100	50	1	50	0.99256	900
25b19e (Graphite).pdf	Graphite	25b19e.txt	RF	Fe	3.9*10^-4	128	0.0202	67 (2nm)	0.03	60	-103.1	100	2	750	120	750	100	25	1	60	1.01	900
25b19f (Graphite).pdf	Graphite	25b19f.txt	RF	Fe	4.1*10^-4	128	0.0202	67 (2nm)	0.03	60	-104.8	100	2	750	120	750	100	12	1	60	-418	900
25b19g (Graphite).pdf	Graphite	25b19g.txt	RF	Fe	4.1*10^-4	128	0.0202	67 (2nm)	0.03	60	-105.1	100	2	750	120	750	100	12	1	60	1.0829	900
26b19a (Graphite).pdf	Graphite	26b19a.txt	RF	Fe	2.2*10^-4	128	0.0202	67 (2nm)	0.03	60	-105.6	100	2	750	120	750	100	12	1	60	1.0829	1800
23D19a-SS304+GSS304+AlN (ref.15C17b PECVD).pdf	SS+SSgradient+AlN	23D19a.txt	RF	Fe	2.5*10^-4	128	0.0199	67 (2nm)	0.03	60	0.990384615	100	2	750	120	730	100	50	1	50	370-329	900
23D19b-SS304+GSS304+AlN (ref.15C17b PECVD).pdf	SS+SSgradient+AlN	23D19b.txt	RF	Fe	3.4*10^-4	128	0.0199	67 (2nm)	0.03	60	-106.8	100	2	750	120	730	100	50	1	50	1.10942	900
23D19c (Glass+SS304+callibration).pdf	Glass	23d19c.txt			5.7*10^-4																	
26b19b (Graphite).pdf	Graphite	26b19b.txt	RF	Fe	4.2*10^-4	128	0.0202	67 (2nm)	0.03	60	-104.8	100	2	750	120	750	100	50	1	60	1.0829	900
23F17b (similar 21D17g) WACVD.pdf	SS+gradientSS+AlN	23F17b.txt	RF	Fe	5.5*10^-4	128 (90 H2 line)	0.0206	62	0.04	60	-95.9	100	2	750	120	600	100	50	1			1200

	Substrate	File	Catalyst														PECVD					
			source	Target	Previous vacuum Pa	Ar sccm	Pressure mbar	time s	Deposition rate nms	Power W	Vbias V	H2 sccm	P mbar	Ramp time s	Hold time s	Tfinal C	NH3 sccm	C2H2 sccm	P mbar	RF W	Vbias V_2	Deposition time s
23F17c (similar 21D17g) WACVD.pdf	SS+gradientSS	23F17c.txt	RF	Fe	5.3*10^-4	128 (90 H2 line)	0.0206	62	0.04	60	-95.5	100	2	750	120	600	100	50	1			1200
26b19c (Graphite).pdf	Graphite	26b19c.txt	RF	Fe	3.6*10^-4	128	0.0202	67 (2nm)	0.03	60	-103	100	2	750	120	750	100	12	1	60	-401	900
27b19a (Graphite).pdf	Graphite	27b19a.txt	RF	Fe	2.6*10^-4	128	0.0202	67 (2nm)	0.03	60	-106.4	100	2	750	120	750	100	60	1	60	1.05128	900
27b19b (Graphite).pdf	Graphite	27b19b.txt	RF	Fe	2.6*10^-4	128	0.0202	67 (2nm)	0.03	60	-105.2	100	2	750	120	750	100	60	2	60	1.33663	900
25C19a (SS316+CNTs).pdf	SS316	25c19a.txt			2*10^-4							100	1	750	120	600/730	100	50	1	50	-0.0025	1800
26c19a (Graphite).pdf	Graphite	26c19a.txt	RF	Fe	2.3*10^-4	128	0.0202	67 (2nm)	0.03	60	-11.9	100	2	750	120	750	100	12	1	60	-440	900
28C19b (SS316+CNTs).pdf	SS316	28c19b.txt			2.2*10^-4							100	1	750	120	600/730	100	50	1	50	-0.0025	1800
23K18a (SS304+CNTs).pdf	SS304	23k18a.txt			4.6*10^-4							100	1	900	120	730	100	50	1	50	-0.0026	1800
23K18b (SS304+CNTs).pdf	SS304	23k18b.txt			5.5*10^-4							100	1	900	120	730	100	50	1	50	1.02993	1800
28c19a (Graphite).pdf	Graphite	28c19a.txt	RF	Fe	2.4*10^-4	128	0.0202	67 (2nm)	0.03	60	-109.4	100	2	750	120	750	100	12	1	56	-404	900
02D19a (SS316+CNTs).pdf	SS316	02D19a.txt			2.0*10^-4							100	1	750	120	630/780	100	50	1	50	0.90824	1800
04d19a (Cu wire).pdf	Cu wire coveredwith Ni	04d19a.txt			3.2*10^-4							100	1	900	620	500/730	100	50	1	50	0.98133	1800
06d19a (SS304+CNTs).pdf	SS304	06d19a.txt			3.0*10^-4							100	1	900	120	500/730	100	50	1	50	1.01571	1800
06d19b (SS304+CNTs).pdf	SS304	06d19b.txt			3.9*10^-4							100	1	900	120	500/730	100	50	1	50	1.01571	1800
03d19a (SS304+CNTs).pdf	SS304	03d19a.txt			3.1*10^-4							100	1	900	620	500/730	100	50	1	50	0.98133	1200
03d19b (SS304+CNTs).pdf	SS304	03d19b.txt			3.1*10^-4							100	1	900	620	500/730	100	50	1	50	1.00785	1800
03d19c (SS304+CNTs).pdf	SS304	03d19c.txt			3.3*10^-4							100	1	900	120	500/730	100	50	1	50	1.01571	1800
26d19a (Cu wire).pdf	Cu wire coveredwith Ni	26d19a.txt			2.4*10^-4							100	1	900	620	500/730	100	50	1	50	0.98133	1800
23e18a (WACVD).pdf	Si+Al2O3	23e18a.txt	RF	Fe	1.7*10^-4	135	0.0205	15	0.04	60	-122.4	100	2	750	120	600 (730)	100	50	1			1800
23e18b (WACVD).pdf	Si+Al2O3	23e18b.txt	RF	Fe	3.9*10^-4	135	0.0211	15	0.04	60	-122.1	100	2	750	120	600 (730)	100	50	1			1800
26d19b (Cu wire).pdf	Cu wire coveredwith Ni	26d19b.txt			2.4*10^-4							100	1	900	620	500/730	100	50	1	50	0.98133	1800
24A18a (graphite sheet+DLC) Arevik.pdf	graphite sheet	24a18a.txt			3.5*10^-4																	
26d19c (Cu wire)-1.pdf	Cu wire coveredwith Ni	26d19c.txt			2.4*10^-4							100	1	900	620	500/730	100	50	1	50	0.98133	1800
24D18a (WACVD).pdf	Si	24d18a.txt	RF	Fe	3.4*10^-4	135	0.0205	62	0.04	60	-121	100	2	750	120	600 (730)	100	50	1	50	387	1800
24D19a-SS304+GSS304+AlN (ref.15C17b PECVD).pdf	SS+SSgradient+AlN	24D19a.txt	RF	Fe	2.7*10^-4	128	0.0199	83 (2.5nm)	0.03	60	-0.985968195	100	2	750	120	730	100	50	1	50	1.01796	900
24D19b-SS304+GSS304+AlN (ref.15C17b PECVD).pdf	SS+SSgradient+AlN	24D19b.txt	RF	Fe	5.6*10^-4	128	0.0199	83 (2.5nm)	0.03	60	-0.997090204	100	2	750	120	730	100	50	1	50	1	900
24D19c-SS304+GSS304+AlN (ref.15C17b PECVD).pdf	SS+SSgradient+AlN	24D19c.txt	RF	Fe	5.1*10^-4	128	0.0199	83 (2.5nm)	0.03	60	-0.993110236	100	2	750	120	730	100	50	1	50	0.98011	900
24D19d-SS304+GSS304+AlN (ref.15C17b PECVD).pdf	SS+SSgradient+AlN	24D19d.txt	RF	Fe	5.1*10^-4	128	0.0199	83 (2.5nm)	0.03	60	-1.006849315	100	2	750	120	730	100	50	1	50	1.01913	900
24D19e-SS304+GSS304+AlN (ref. 21D17g WACVD).pdf	SS+gradientSS+AlN	24D19e.txt	RF	Fe	4.3*10^-4	128	0.0201	67 (2nm)	0.03	60	0.994146341	100	2	750	120	600	100	50	1			1800
24J17a (H2O Plasma)-IBEC.pdf	Si	24J17a.txt	RF	Fe	4.8*10^-4	67 H2 line (128)	0.0203	64 (3nm)	0.047	60	-106.4	100	2	750	120	680	100	50	1	50	354	900
26d19c (Cu wire).pdf	Cu wire coveredwith Ni	26d19b.txt			2.4*10^-4							100	1	900	620	500/730	100	50	1	50	0.98133	1800
14b19a (Fe Calibration).pdf	Glass	07J19a.txt	RF	Fe	9.8*10^-5	128	0.0202	67 (2nm)	0.03	60	-107.3											
Copia de 14b19a (Fe Calibration).pdf	Glass	07J19a.txt	RF	Fe	9.8*10^-5	128	0.0202	67 (2nm)	0.03	60	-107.3											
15k19a-Si.pdf	Si	15k19a.txt	RF	Fe	3.9*10^-5	128	0.0199	75	0.033	60	-110/	100	2	750	120	680	100	50	1	50	-374	900
24a19a (SS304+CNTs).pdf	SS304	24a19a.txt			2.2*10^-4							100	1	780	620	650/730	100	50	1	50	1.10149	1800
24a19b (SS304+CNTs).pdf	SS304	24a19b.txt			2.9*10^-4							100	1	780	1200	650/730	100	50	1	50	1.01397	1800
24a19c (SS304+CNTs).pdf	SS304	24a19c.txt			3.4*10^-4							100	1	780	200/500/500	650/650	100	50	1	50	0.98108	1800
24e18a (WACVD).pdf	Si+Al2O3	24e18a.txt	RF	Fe	2.7*10^-4	135	0.021	50	0.04	60	0.995106036	100	2	750	120	600 (730)	100	50	1			1800
24e18b (WACVD).pdf	Si+Al2O3	24e18b.txt	RF	Fe	3.6*10^-4	135	0.021	25	0.04	60	-121.3	100	2	750	120	600 (730)	100	50	1			1800
15k19b-Si.pdf	Si	15k19b.txt	RF	Fe	1.6*10^-4	128	0.0199	75	0.033	60	-111.2/	100	2	750	120	680	100	50	1	50	-1.0559	900
18k19a-Si.pdf	Si	18k19a.txt	RF	Fe	1.1*10^-4	128	0.0199	95	0.033	60	-110.2	100	2	750	120	680	100	50	1	50	-1.0553	900

	Substrate	File	Catalyst														PECVD					
			source	Target	Previous vacuum Pa	Ar sccm	Pressure mbar	time s	Deposition rate nms	Power W	Vbias V	H2 sccm	P mbar	Ramp time s	Hold time s	Tfinal C	NH3 sccm	C2H2 sccm	P mbar	RF W	Vbias V_2	Deposition time s
18k19b (Graphite).pdf	Graphite	18k19a.txt	RF	Fe	3.8*10^-4	128	0.0202	67 (2nm)	0.03	60	-108.9	100	2	750	120	750	100	50	1	60	-1.0677	900
18k19c-Si.pdf	Si	18k19c.txt	RF	Fe	1.3*10^-4	128	0.0199	100	0.033	60	-109.1	100	2	750	120	680	100	50	1	50	-1.0553	900
25D19a-SS304+GSS304+AlN (H2O Plasma 23D19b)-SEM-RAMAN.pdf	SS+SSgradient+AlN+Fe+CNTs	25D19a.txt	RF	Fe	3.4*10^-4	128	0.0199	67 (2nm)	0.03	60	-106.8	100	2	750	120	730	100	50	1	50	1.10942	900
25D19b-SS304+GSS304+AlN (WACVD).pdf	SS+gradientSS+AlN	25D19a.txt	RF	Fe	5.9*10^-4	128	0.0201	67 (2nm)	0.03	60	1.015369837	100	2	750	120	600	100	50	1			600
25F18a (WACVD).pdf	Back of Si+Al2O3	18f18a.txt	RF	Fe	4.4*10^-4	135	0.0225	25	0.04	60	-120.2	100	2	750	120	600 (730)	100	50	1			1800
19k19a-Si.pdf	Si	19k19a.txt	RF	Fe	7.9*10^-5	128	0.0199	100	0.033	60	-110.3	100	2	750	120	680	100	50	1	50	-398	900
25J17a (similar15B17d)-ICMAB.pdf	Si+AlN	25J17a.txt	RF	Fe	3.4*10^-4	128(66 via H)	0.0208	64s/3nm	0.047	60	-108.3	100	2	750	120	680	100	50	1	50	-334	900
22k19a (Graphite).pdf	Graphite	22k19a.txt	RF	Fe	1.1*10^-4	128	0.0202	67 (2nm)	0.03	60	-108	100	2	750	120	750	100	50	1	60	-1.0401	900
25J18b (SS304+DLC+CNTs).pdf	SS304	25J18b.txt	RF	Fe	4.3*10^-4	135	0.021	50 (2nm)	0.04	60	0.994854202	100	2	750	120	680	100	50	1	50	1.045955	600
25J18c (SS304+DLC+CNTs).pdf	SS304	25J18c.txt																				
25J18d (SS304+DLC+CNTs).pdf	SS304	25J18d.txt	RF	Fe	5.2*10^-4	135	0.021	75 (3nm)	0.04	60	0.998348472	100	2	750	120	680	100	50	1	50	-380	600
25J18e (SS304+DLC+CNTs).pdf	SS304	25J18e.txt	RF	Fe	2.7*10^-4	135	0.021	50 (2nm)	0.04	60	0.998312236	100	2	750	120	680	100	50	1	50	1.061455	600
25a19a (SS304+CNTs).pdf	SS304	25a19a.txt			2.1*10^-4							100	1	780	1200	650/730	100	50	1	50	1.0431	1800
22k19b (Graphite).pdf	Graphite	22k19b.txt	RF	Fe	2.4*10^-4	128	0.0202	67 (2nm)	0.03	60	-107.8	100	2	750	120	750	100	50	1	60	-404/	900
22k19c (Graphite).pdf	Graphite	22k19c.txt	RF	Fe	2.4*10^-4	128	0.0202	67 (4nm)		60	-0.981078524	100	2	750	120	750	100	50	1	60	-1.0978	900
22k19d (Graphite).pdf	Graphite	22k19d.txt	RF	Fe	3.9*10^-4	128	0.0202	67 (4nm)		60	-106.4	100	2	750	120	750	100	50	1	60	-1.0734	900
29k19a (Graphite).pdf	Graphite	29k19a.txt	RF	Fe	3.9*10^-4	128	0.0202	74	0.03	60	-108.5	100	2	750	120	750	100	50	1	60	-407/	900
30k19a (Graphite).pdf	Graphite	30k19a.txt	RF	Fe	1.8*10^-4	128	0.0202	81	0.03	60	-109.2	100	2	750	120	750	100	50	1	60	-1.1194	900
03L19a (Graphite).pdf	Graphite	03L19a.txt	RF	Fe	5.8*10^-5	128	0.0202	60	0.03	60	-0.99009009	100	2	750	120	750	100	50	1	60	-365/	900
03L19b (Graphite).pdf	Graphite	03L19b.txt	RF	Fe	1.4*10^-4	128	0.0202	60	0.03	60	-109.5	100	2	750	120	780	100	50	1	60	-0.0032	900
25e18a (WACVD).pdf	Si+Al2O3	25e18a.txt	RF	Fe	4.4*10^-4	135	0.0213	25	0.04	60	-120.3	100	2	750	120	600 (730)	100	50	1			1800
26B18a (Glass+DLC+callibration).pdf	Glass	26b18a.txt			6.7*10^-4																	
26B18b (Glass+DLC+callibration).pdf	Glass	26b18b.txt			3.2*10^-4																	
26D18a (WACVD).pdf	Si	26d18a.txt	RF	Fe	2.1*10^-4	135	0.0203	62	0.04	60	-121.5	100	2	750	120	600 (730)	100	50	1	50	387	1800
11L19a-SS304+GSS304+AlN (ref.15C17b PECVD).pdf	SS+SSgradient+AlN	11L19a.txt	RF	Fe	2.0*10^-4	128	0.0199	83 (2.5nm)	0.03	60	-107.5	100	2	750	120	730	100	50	1	55(80 on the meter)	-286	900
26F17b (Fe calibration)-old target.pdf	Glass	27F17b.txt	RF	Fe	4.6*10^-4	128 (90 H2 line)	0.0203	900		60	-93.8											
26F17c (Fe calibration)-old target.pdf	Glass	27F17c.txt	RF	Fe	4.8*10^-4	128 (90 H2 line)	0.0207	1800		60	-95.3, -94.5											
11L19b-Cleaning RF head.pdf	SS+SSgradient+AlN	11L19b.txt	RF	RF head	2.0*10^-4	50	1	600		40	0.304568528											
11L19c-SS304+GSS304+AlN (ref.15C17b PECVD).pdf	SS+SSgradient+AlN	11L19c.txt	RF	Fe	2.2*10^-4	128	0.0199	83 (2.5nm)	0.03	60	-109.9	100	2	750	120	730	100	50	1	50(70 on the meter)	-310	900
12L19a-SS304+GSS304+AlN (ref.15C17b PECVD).pdf	SS+SSgradient+AlN	11L19c.txt	RF	Fe	1.8*10^-4	128	0.0199	83 (2.5nm)	0.03	60	-106.5	100	2	750	120	730	100	50	1	50(70 on the meter)	-314/	900
12L19a (Graphite).pdf	Graphite	12L19a.txt	RF	Fe	1.6*10^-4	128	0.0191	67 (4nm)		60	-108.1	100	2	750	120	750	100	50	1	65	-338/	900
13L19a-SS304+GSS304+AlN (ref.15C17b PECVD).pdf	SS+SSgradient+AlN	13L19c.txt	RF	Fe	1.4*10^-4	128	0.0199	83 (2.5nm)	0.03	60	-108.9	100	2	750	120	730	100	50	1	50(70 on the meter)	-314/	900
13L19b (Graphite).pdf	Graphite	13L19a.txt	RF	Fe	2.1*10^-4	128	0.0191	67 (3nm)		60	-108.2	100	2	750	120	750	100	50	1	65	-1.1786	900
13L19c (Graphite).pdf	Graphite	13L19c.txt	RF	Fe	3.7*10^-4	128	0.0191	67 (3nm)		60	-108.2	100	2	750	120	750	100	50	1	6 (real 90)	-309	900
16L19a (Fe calibration).pdf	Glass	16L19a.txt	RF	Fe		128	0.0191	3600 (104.4nm)	0.029	60 (80W real)												
17L19a-SS304+GSS304+AlN (ref.15C17b PECVD).pdf	SS+SSgradient+AlN	17L19a.txt	RF	Fe	1.1*10^-4	128	0.019	86 (2.5nm)	0.029	60	-0.991674376	100	2	750	120	730	100	50	1	70(100 on the	-344/	900

	Substrate	File	Catalyst														PECVD					
			source	Target	Previous vacuum Pa	Ar sccm	Pressure mbar	time s	Deposition rate nms	Power W	Vbias V	H2 sccm	P mbar	Ramp time s	Hold time s	Tfinal C	NH3 sccm	C2H2 sccm	P mbar	RF W	Vbias V_2	Deposition time s
																				meter)		
17L19b-SS304+GSS304+AlN (ref.15C17b PECVD).pdf	SS+SSgradient+AlN	17L19b.txt	RF	Fe	1.1*10^-4	128	0.019	86 (2.5nm)	0.029	60	-0.995309568	100	2	750	120	750	100	50	1	70(100 on the meter)	-320	900
18L19a-SS304+GSS304+AlN (ref.15C17b PECVD).pdf	SS+SSgradient+AlN	18L19a.txt	RF	Fe	1.3*10^-4	128	0.019	86 (2.5nm)	0.029	60	-0.995366080	100	2	750	120	770	100	50	1	70(100 on the meter)	-362	900
19L19a-SS304+GSS304+AlN (ref.15C17b PECVD).pdf	SS+SSgradient+AlN	18L19a.txt	RF	Fe	1.1*10^-4	128	0.019	86 (2.5nm)	0.029	60	-107	100	2	750	120	700	100	50	1	70(100 on the meter)	-362	900
24A20a (Graphite).pdf	Graphite	24A20a.txt	RF	Fe	7.4*10^-5	128	0.0193	67 (3nm)		60	-107.3	100	2	750	120	750	100	50	1	6 (real 90)	46/66/280/264	900
29A20a (Graphite).pdf	Graphite	29A20a.txt	RF	Fe	2.4*10^-4	128	0.0193	67 (3nm)		60	-108.6	100	2	750	120	680	100	50	1	60	-410	900
30A20a (Graphite).pdf	Graphite	30A20a.txt	RF	Fe	4.3*10^-4	128	0.0193	73 (3nm)		60	-106.4	100	2	750	120	680	100	50	1	50	-390	900
30A20b (SS310).pdf	SS310	30A20b.txt	RF		2.1*10^-4							100	2	750	180	500-730	100	50	1	50	0.98272	1800
31A20a (SS310).pdf	SS310	31A20a.txt	RF		1.1*10^-4							100	2	750	180	600-730	100	50	1	50	0.97543	1800
31A20b (SS310).pdf	SS310	31A20b.txt	RF		3.2*10^-4							100	2	750	180	730-730	100	50	1	50	-399/	1800
31A20c (SS310).pdf	SS310	31A20c.txt	RF		2.3*10^-4							100	2	750	180	557-730	100	50	1	50	1.00752	1800
01B20a (SS310).pdf	SS310	01B20a.txt	RF		1.1*10^-4							100	2	750	180	680-680	100	50	1	50	-1	1800
03B20a (SS310).pdf	SS310	03B20a.txt	RF		3.8*10^-4							100	2	750	120	600-730	100	50	1	50	0.98985	1800
04B20a (SS310).pdf	SS310	04B20a.txt	RF		1.5*10^-4							100	2	750	180	500						
27D18a (WACVD).pdf	Si	26d18a.txt	RF	Fe	4.4*10^-4	135	0.0206	40	0.04	60	-120.1	100	2	750	120	600 (730)	100	50	1	50	387	1800
27D18b (WACVD).pdf	Si	27d18b.txt	RF	Fe	4.5*10^-4	135	0.0206	25	0.04	60	-118	100	2	750	120	600 (730)	100	50	1			1800
04B20b (SS310).pdf	SS310	04B20b.txt	RF		2.4*10^-4							100	2	750	180	730						
05B20a (SS310).pdf	SS310	05B20a.txt	RF		1.8*10^-4							100	2	750	180	680						
27F17c (similar 21D17g) WACVD.pdf	SS+gradientSS+AlN	27F17c.txt	RF	Fe	5.5*10^-4	128 (90 H2 line)	0.0206	62	0.04	60	-101.5	100	2	750	120	600	100	50	1			1200
05B20b (SS310).pdf	SS310	05B20b.txt	RF		1.9*10^-4							100	2	750	180	680						
27I17a (DLC).pdf	Glass	27i17a.txt			3.4*10^-4												40			100	-508	600
27I17b (DLC).pdf	Glass	27i17b.txt			4.4*10^-4												50 (mfc 80)			120	-1114	600
27I17c (DLC).pdf	SS304+G-SS304+AlN	27i17c.txt			3.4*10^-4												50 (mfc 80)			120	-1145	600
27I17d (DLC).pdf	SS304+G-SS304+AlN	27i17d.txt			3.4*10^-4												40 (mfc 64.7)			100	-1223	600
06B20a (SS310).pdf	SS310	06B20a.txt	RF		8.2*10^-5							100	2	750	180	557						
07B20a (SS310).pdf	SS310	07B20a.txt	RF		1.9*10^-4							100	2	750	180	600						
07B20b (SS310).pdf	SS310	07B20b.txt	RF		2.0*10^-4							100	2	750	180	730						
12B20a (SS310).pdf	SS310	12B20a.txt	RF		1.4*10^-4							100	2	900	180	680/700	100	50	1	50	397/409	1800
12B20b (SS310).pdf	SS310	12B20b.txt	RF		2.2*10^-4							100	2	800	180	680/715	100	50	1	50	414/418	1800
12B20c (SS310).pdf	SS310	12B20c.txt	RF		2.2*10^-4							100	2	1000	180	680/715	100	50	1	50	406/412	1800
13B20a (SS310).pdf	SS310	13B20a.txt	RF		2.2*10^-4							100	2	760	180	680/750	100	50	1	50	416/418	1800
13B20b (SS310).pdf	SS310	13B20b.txt	RF		2.8*10^-4							100	2	900	180	680/750	100	50	1	50	415/405	1800
14B20a (SS310).pdf	SS310	14B20a.txt	RF		6.5*10^-5							100	2	1040	180	680/750	100	50	1	50	408	1800
28B18a (SS304+DLC+CNTs).pdf	SS304	28b18a.txt	RF	Fe	4.0*10^-4	135	0.021	64 (3nm)	0.047	60	-1.010496183	100	2	750	120	680	100	50	1	50	1.03093	600
28B18b (SS304+DLC+CNTs).pdf	SS304	28b18b.txt	RF	Fe	5.5*10^-4	135	0.021	64 (3nm)	0.047	60	-101.2	100	2	750	120	680	100	50	1	50	-367	600
28B18c (SS304+DLC+CNTs).pdf	SS304	28b18c.txt	RF	Fe	3.7*10^-4	135	0.021	64 (3nm)	0.047	60	-1.009871668	100	2	750	120	680	100	50	1	50	1.00985	600
28B18d (SS304+DLC+CNTs).pdf	SS304	28b18d.txt	RF	Fe	3.6*10^-4	135	0.021	78 (3nm)	0.0383	60	-1.008571429	100	2	750	120	680	100	50	1	50	1	600

	Substrate	File	Catalyst														PECVD					
			source	Target	Previous vacuum Pa	Ar sccm	Pressure mbar	time s	Deposition rate nms	Power W	Vbias V	H2 sccm	P mbar	Ramp time s	Hold time s	Tfinal C	NH3 sccm	C2H2 sccm	P mbar	RF W	Vbias V_2	Deposition time s
15B20a (SS310).pdf	SS310	15B20a.txt	RF		1.9*10^-4							100	2	800	180	680/785	100	50	1	50	0.9448 3	1800
15B20b (SS310).pdf	SS310	15B20b.txt	RF		2.2*10^-4							100	2	1000	180	680/785	100	50	1	50	0.9557 1	1800
16B20a (SS310).pdf	SS310	16B20a.txt	RF		1.7*10^-4							100	2	900	180	680/800	100	50	1	50	0.9211 7	1800
18B20a (SS310).pdf	SS310	18B20a.txt	RF		5.6*10^-5							100	2	900	180	680/800	100	50	1	40	0.9634 1	1800
18B20b (SS310).pdf	SS310	18B20b.txt	RF		9.1*10^-5							100	2	900	180	680/800	100	50	1	60	0.9132 3	1800
18B20c (SS310).pdf	SS310	18B20c.txt	RF		2.2*10^-4							100	2	700	180	680						
18B20d (SS310).pdf	SS310	18B20d.txt	RF		1.7*10^-4							100	2	1040	180	680						
19B20a (SS310).pdf	SS310	19B20a.txt	RF		1.3*10^-4							100	2	1000	180	680						
19B20b (SS310).pdf	SS310	19B20b.txt	RF		1.8*10^-4							100	2	900	180	680						
19B20c (SS310).pdf	SS310	19B20c.txt	RF		1.8*10^-4							100	2	760	180	680						
18F20a (SS310).pdf	SS310	18F20a.txt	RF		2.5*10^-4							100	2	1040	180	680/750	100	50	1	50	0.9715 8	1800
22F20a (SS310).pdf	SS310	22F20a.txt	RF		1.1*10^-4							100	2	1040	180	680/750	100	50	1	50	0.9848 9	1800
22F20b (SS310).pdf	SS310	22F20b.txt	RF		3.0*10^-4							100	2	1040	180	680/750	100	50	1	50	0.9376 5	1800
08G20a (SS310).pdf	SS310	08G20a.txt	RF		7.0*10^-5							100	2	1040	180	680/750	100	50	1	50	0.9087 7	1800
11I20a (SS310).pdf	SS310	11I20a.txt	RF		2.4*10^-4							100	2	1040	180	680/750	100	50	1	50	0.8801 6	1800
12I20a (SS310).pdf	SS310	12I20a.txt	RF		1.2*10^-4							100	2	1040	180	680/750	100	50	1	25	-0.0018	1800
16I20a (SS310).pdf	SS310	16I20a.txt	RF		9.6*10^-5							100	2	1040	180	680/750	100	50	1	50	-397/	1800
29I20a (SS310).pdf	SS310	29I20a.txt	RF		6.1*10^-5							100	2	1040	180	680/700	100	50	1	50	0.9923 7	1800
29I20b (SS310).pdf	SS310	29I20b.txt	RF		6.1*10^-5							100	2	1040	180	680/730	100	50	1	50	0.9873 7	1800
29I20c (SS310).pdf	SS310	29I20c.txt	RF		1.4*10^-4							100	2	1040	180	680/780	100	50	1	50	0.9593 9	1800
30I20a (SS310).pdf	SS310	30I20a.txt	RF		1.0*10^-4							100	2	1040	180	680/720	100	50	1	50	0.9898 7	1800
30I20b (Graphite).pdf	Graphite	30I20b.txt	RF	Fe	1.7*10^-4	136	0.0193	67 (2nm)		60	-108.2	100	2	750	120	680	100	50	1	50 (real 80)	0.9534 9	900
30I20c (Graphite).pdf	Graphite	30I20c.txt	RF	Fe	2.5*10^-4	136	0.0193	67 (2nm)		60	-106.3	100	2	750	120	730	100	50	1	50 (real 80)	0.9898 7	900
01J20a (Graphite).pdf	Graphite	01J20a.txt	RF	Fe	1.6*10^-4	136	0.0193	67 (2nm)		60	-105.3	100	2	750	120	700	100	50	1	50 (real 80)	0.9974 1	900
29a19a (SS304+CNTs).pdf	SS304	29a19a.txt			3.6*10^-4							100	1	780	200/500/500	650/680	100	50	1	50	1.0027 8	1800
29a19b (SS304+CNTs).pdf	SS304	29a19b.txt			2.8*10^-4							100	1	780	200/500/500	650/730	100	50	1	50	1.1375	1800
29a19c (SS304+CNTs).pdf	SS304	29a19c.txt			3.3*10^-4							100	1	780	620	650/730	100	50	1	50	1.0771 5	1800
09J20a (SS310).pdf	SS310	09J20a.txt	RF		1.8*10^-4							100	2	1040	180	680/680	100	50	1	50	-390/-	1800
13J20a (SS310).pdf	SS310	13J20a.txt	RF		1.4*10^-4							100	2	1040	180	680/700	100	50	1	50	1	1800
14J20a (SS310)-.pdf	SS310	14J20a.txt	RF		9.4*10^5							100	2	1040	180	680/720	100	50	1	50	1	1800
16J20a (SS310).pdf	SS310	16J20a.txt	RF		2.7*10^-4							100	2	1040	180	680/720	100	50	1	50	-395/-	1800
23J20a (SS310).pdf	SS310	23J20a.txt	RF		2.7*10^-4							100	2	1040	180	680/720	100	50	1	50	-412	1800
26J20a (SS310).pdf	SS310	26J20a.txt	RF		7.3*10^-5							100	2	1040	180	650/690	100	50	1	50	0.9948 1	1800
30C17a.pdf	Si+gradient SS304+AlN	30C17a.txt	RF	Fe	4.7*10^-4	128	0.0201	62	0.04	60	-98.5	100	2	750	120	715						
26J20b (SS310).pdf	SS310	26J20b.txt	RF		2.2*10^-4							100	2	1040	180	670/710	100	50	1	50	0.9527 4	1800
27J20a (SS310).pdf	SS310	27J20a.txt	RF		9.6*10^-5							100	2	1040	180	660/700	100	50	1	50	0.9151 8	1800
27J20b (SS310).pdf	SS310	27J20b.txt	RF		9.6*10^-5							100	2	1040	180	660/700	100	50	1	50	0.9151 8	1800
28J20a (SS310).pdf	SS310	28J20a.txt	RF		8.3*10^-5							100	2	1040	180	650/690	100	50	1	50	-372/-	1800
28J20b (SS310).pdf	SS310	28J20b.txt	RF		1.2*10^-4							100	2	1040	180	680/720	100	50	1	50	-385/-	1800
29J20a (SS310).pdf	SS310	29J20a.txt	RF		1.1*10^-4							100	2	1040	180	680/720	100	50	1	50	-385/-	1800
30J17a (similar15B17d)-ICMAB.pdf	Si+AlN	30J17a.txt	RF	Fe	3.4*10^-4	128(66 via H)	0.0208	64s/ 3nm	0.047	60	-108.1	100	2	750	120	680	100	50	1	50	-334	1200
29J20b (SS310).pdf	SS310	29J20b.txt	RF		1.8*10^-4							100	2	1040	180	680/720	100	50	1	50	1.0487 1	1800
29J20c (SS310).pdf	SS310	29J20c.txt	RF		1.7*10^-4							100	2	1040	180	680/720	100	50	1	50	1.0197 2	2120
23K20a (SS310).pdf	SS310	23K20a.txt	RF		9.6*10^-5							100	2	1040	180	680/720	100	50	1	50	1.0197 2	2120
23K20b (SS310).pdf	SS310	23K20b.txt	RF		1.3*10^-4							100	2	1040	180	680/720	100	50	1	50	0.9466 7	2120

	Substrate	File	Catalyst														PECVD					
			source	Target	Previous vacuum Pa	Ar sccm	Pressure mbar	time s	Deposition rate nms	Power W	Vbias V	H2 sccm	P mbar	Ramp time s	Hold time s	Tfinal C	NH3 sccm	C2H2 sccm	P mbar	RF W	Vbias V_2	Deposition time s
23K20c (SS310).pdf	SS310	23K20c.txt	RF		2.3*10^-4							100	2	1040	180	665/705	100	50	1	50	0.97714	1800
24K20a (SS310).pdf	SS310	24K20a.txt	RF		9.6*10^-5							100	2	1040	180	670/710	100	50	1	50	-360/-	1800
26J20a (Graphite).pdf	Graphite	26J20a.txt	RF	Fe	1.6*10^-4	136	0.0193	67 (2nm)		60	-105.3	100	2	750	120	700	100	50	1	50 (real 80)	0.99741	900
31C17a.pdf	Si+gradient SS304+AlN	31C17a.txt	RF	Fe	4.2*10^-4	128	0.0201	62	0.04	60	-96.6	100	2	750	120	730						
09L19a-SS304+GSS304+AlN (ref.15C17b PECVD).pdf	SS+SSgradient+AlN	09L19a.txt	RF	Fe	7.1*10^-5	128	0.0199	83 (2.5nm)	0.03	60	-109.4/	100	2	750	120	730	100	50	1	50 (70	-1.62	900
31a19a (SS304+CNTs).pdf	SS304	31a19a.txt			2.1*10^-4							100	1	780	200/500/500	650/730	100	50	1	50	1.03377	1800
10L19a-SS304+GSS304+AlN (ref.15C17b PECVD).pdf	SS+SSgradient+AlN	10L19a.txt	RF	Fe	5.7*10^-5	128	0.0199	83 (2.5nm)	0.03	60	-107.6	100	2	750	120	730	100	50	1		-286	900

Bibliography

Abbas, G., Papakonstantinou, P., Iyer, G. R. S., Kirkman, I. W., & Chen, L. C. (2007). Substitutional nitrogen incorporation through rf glow discharge treatment and subsequent oxygen uptake on vertically aligned carbon nanotubes. *Physical Review B - Condensed Matter and Materials Physics*, *75*(19). https://doi.org/10.1103/PHYSREVB.75.195429/FIGURES/10/MEDIUM

Active Motive. (2020). EpiShear Probe Sonicator. Retrieved October 5, 2021, from https://www.activemotif.com/catalog/719/epishear-probe-sonicator

Adamska, M., & Narkiewicz, U. (2017). Fluorination of Carbon Nanotubes − A Review. *Undefined*, *200*, 179–189. https://doi.org/10.1016/J.JFLUCHEM.2017.06.018

Akhtar, K., Ali Khan, S., Khan, S. B., & Asiri, A. M. (2018). Scanning Electron Microscopy: Principle and Applications in Nanomaterials Characterization. In *Handbook of Materials Characterization* (pp. 111–145). https://doi.org/10.1007/978-3-319-92955-2_3

Al-Dmour, E. (2020). *Fundamentals of Vacuum Physics and Technology*. 1–21. Retrieved from http://arxiv.org/abs/2006.01464

Albella, J. M. (2018). *Capas delgadas y modificación superficial de materiales*. Consejo Superior de Investigaciones Científicas.

Alemán, B., Reguero, V., Mas, B., & Vilatela, J. J. (2015). Strong Carbon Nanotube Fibers by Drawing Inspiration from Polymer Fiber Spinning. *ACS Nano*, *9*(7), 7392–7398. https://doi.org/10.1021/ACSNANO.5B02408/SUPPL_FILE/NN5B02408_SI_002.MPG

Alyamani, A., & Lemine, O. (2012). FE-SEM characterization of some nanomaterial, INTECH Open Access Publisher. *Intech*, (1), 463–472.

Amade, R., Alshaikh, I., Musheghyan-Avetisyan, A., & Bertran-Serra, E. (2021). Enhanced capacitance of manganese oxide driven by hierarchically structured carbon nanotube-carbon nanowall composite. *Surface and Coatings Technology*, *428*, 127885. https://doi.org/10.1016/J.SURFCOAT.2021.127885

Amade, R., Muyshegyan-Avetisyan, A., González, J. M., del Pino, A. P., György, E., Pascual, E., … Serra, E. B. (2019). Super-capacitive performance of manganese dioxide/graphene nano-walls electrodes

deposited on stainless steel current collectors. *Materials*, *12*(3), 1–13. https://doi.org/10.3390/ma12030483

An, J., Zhan, Z., & Zheng, L. (2017). Controllable Synthesis of Carbon Nanotubes. *Industrial Applications of Carbon Nanotubes*, 1–45. https://doi.org/10.1016/B978-0-323-41481-4.00001-0

Anders, A. (2011). Discharge physics of high power impulse magnetron sputtering. *Surface and Coatings Technology*, *205*(SUPPL. 2), S1–S9. https://doi.org/10.1016/j.surfcoat.2011.03.081

Antunes, E. F., Lobo, A. O., Corat, E. J., & Trava-Airoldi, V. J. (2007). Influence of diameter in the Raman spectra of aligned multi-walled carbon nanotubes. *Carbon*, *45*(5), 913–921. https://doi.org/10.1016/J.CARBON.2007.01.003

Antunes, E. F., Lobo, A. O., Corat, E. J., Trava-Airoldi, V. J., Martin, A. A., & Veríssimo, C. (2006). Comparative study of first- and second-order Raman spectra of MWCNT at visible and infrared laser excitation. *Carbon*, *44*(11), 2202–2211. https://doi.org/10.1016/J.CARBON.2006.03.003

Arenal, R., Löthman, P., Picher, M., Than, T., Paillet, M., & Jourdain, V. (2012). Direct evidence of atomic structure conservation along ultra-long carbon nanotubes. *Journal of Physical Chemistry C*, *116*(26), 14103–14107. https://doi.org/10.1021/JP212540N/SUPPL_FILE/JP212540N_SI_003.PDF

Arnold, M. S., Green, A. A., Hulvat, J. F., Stupp, S. I., & Hersam, M. C. (2006). Sorting carbon nanotubes by electronic structure using density differentiation. *Nature Nanotechnology 2006 1:1*, *1*(1), 60–65. https://doi.org/10.1038/nnano.2006.52

Asher, S. A. (2012). UV Resonance Raman Spectroscopy for Analytical, Physical, and Biophysical Chemistry. *Analytical Chemistry*, *65*(4), 201A-210A. https://doi.org/10.1021/AC00052A715

Avetisyan, A. M. (2019a). *Synthesis and characterization of multilayer graphene nanostructures*. University of Barcelona.

Avetisyan, A. M. (2019b). *Synthesis and characterization of multilayer graphene nanostructures*.

Bachilo, S. M., Balzano, L., Herrera, J. E., Pompeo, F., Resasco, D. E., & Weisman, R. B. (2003). Narrow (n,m)-distribution of single-walled carbon nanotubes grown using a solid supported catalyst. *Journal of the American Chemical Society*, *125*(37), 11186–11187. https://doi.org/10.1021/JA036622C

Bai, J., Zhong, X., Jiang, S., Huang, Y., & Duan, X. (2010). Graphene nanomesh. *Nature Nanotechnology 2010 5:3*, *5*(3), 190–194. https://doi.org/10.1038/nnano.2010.8

Baker, R. T. K., Yates, D. J. C., & Dumesic, J. A. (1982). FILAMENTOUS CARBON FORMATION OVER IRON SURFACES. *ACS Symposium Series*, *20*, 1–21. https://doi.org/10.1021/BK-1983-0202.CH001

Balandin, A. A. (2011). Thermal properties of graphene and nanostructured carbon materials. *Nature Materials 2011 10:8*, *10*(8), 569–581. https://doi.org/10.1038/nmat3064

Ban, S., Zhang, J., Zhang, L., Tsay, K., Song, D., & Zou, X. (2013). Charging and discharging electrochemical supercapacitors in the presence of both parallel leakage process and electrochemical decomposition of solvent. *Electrochimica Acta*, *Complete*(90), 542–549. https://doi.org/10.1016/J.ELECTACTA.2012.12.056

Barretoa, J. C. G., Tita, D. L., & Orlandi, M. O. (2019). Quim. Nova,. *Quim. Nova*, *42*(4), 447–452. https://doi.org/10.21577/0100-4042.20170353

Baughman, R. H., Zakhidov, A. A., & De Heer, W. A. (2002). Carbon nanotubes - The route toward applications. *Science*, *297*(5582), 787–792. https://doi.org/10.1126/SCIENCE.1060928

Béguin, F., Presser, V., Balducci, A., & Frackowiak, E. (2014). Carbons and electrolytes for advanced supercapacitors. *Advanced Materials*, *26*(14), 2219–2251. https://doi.org/10.1002/adma.201304137

Behera, A., Mallick, P., & Mohapatra, S. S. (2020). Nanocoatings for anticorrosion. *Corrosion Protection at the Nanoscale*, 227–243. https://doi.org/10.1016/b978-0-12-819359-4.00013-1

Bell, M S, Teo, B. K., & Milne, W. I. (2007). Factors determining properties of multi-walled carbon nanotubes/fibres deposited by PECVD. *J. Phys. D: Appl. Phys*, *40*, 2285–2292. https://doi.org/10.1088/0022-3727/40/8/S07

Bell, Martin S., Teo, K. B. K., Lacerda, R. G., Milne, W. I., Hash, D. B., & Meyyappan, M. (2006). Carbon nanotubes by plasma-enhanced chemical vapor deposition. *Pure and Applied Chemistry*, *78*(6), 1117–1125. https://doi.org/10.1351/PAC200678061117/MACHINEREADABLECITATION/RIS

Berg, S., & Katardjiev, I. V. (1994). Modelling of bias sputter deposition processes. *Surface and Coatings Technology*, *68–69*(C), 325–331. https://doi.org/10.1016/0257-8972(94)90181-3

Bertin, E. P. (1975). *Principles and Practice of X-Ray Spectrometric Analysis*. Springer US.

Bertóti, I., Mohai, M., & László, K. (2015). Surface modification of graphene and graphite by nitrogen plasma: Determination of chemical state alterations and assignments by quantitative X-ray

photoelectron spectroscopy. *Carbon*, *84*(1), 185–196. https://doi.org/10.1016/J.CARBON.2014.11.056

Bethune, D. S., Klang, C. H., De Vries, M. S., Gorman, G., Savoy, R., Vazquez, J., & Beyers, R. (1993). Cobalt-catalysed growth of carbon nanotubes with single-atomic-layer walls. *Nature 1993 363:6430*, *363*(6430), 605–607. https://doi.org/10.1038/363605a0

Bokobza, L., Bruneel, J.-L., & Couzi, M. (2015). Raman Spectra of Carbon-Based Materials (from Graphite to Carbon Black) and of Some Silicone Composites. *C 2015, Vol. 1, Pages 77-94*, *1*(1), 77–94. https://doi.org/10.3390/C1010077

Bondeson, D. (2007). *Biopolymer-based Nanocomposites: Processing and Properties-PhD Thesis*.

Brabazon, D., & Raffer, A. (2000). Advanced Characterization Techniques for Nanostructures. In W. Ahmed & M. J. Jackson (Eds.), *Emerging nanotechnologies for manufacturing* (first edition). William Andrew.

Brad, A. J., & Faulkner, L. R. (2001). Electrochemcical Methods : Fundamentals and Applications. In *Physics* (2nd ed.). Retrieved from http://elib.tu-darmstadt.de/tocs/95069577.pdf

Brown, B., Parker, C. B., Stoner, B. R., & Glass, J. T. (2011). Growth of vertically aligned bamboo-like carbon nanotubes from ammonia/methane precursors using a platinum catalyst. *Carbon*, *49*(1), 266–274. https://doi.org/10.1016/J.CARBON.2010.09.018

Bruggeman, P. J., Kushner, M. J., Locke, B. R., Gardeniers, J. G. E., Graham, W. G., Graves, D. B., … Zvereva, G. (2016). Plasma-liquid interactions: A review and roadmap. *Plasma Sources Science and Technology*, *25*(5). https://doi.org/10.1088/0963-0252/25/5/053002

Bruggeman, P., & Leys, C. (2009). Non-thermal plasmas in and in contact with liquids. *Journal of Physics D: Applied Physics*, *42*(5), 053001. https://doi.org/10.1088/0022-3727/42/5/053001

Burgess, S., Li, X., & Holland, J. (2013). High spatial resolution energy dispersive X-ray spectrometry in the SEM and the detection of light elements including lithium - 2013 - Wiley Analytical Science. *Microsc. Anal.*, S8–S13. Retrieved from https://analyticalscience.wiley.com/do/10.1002/micro.620/full/

Camp Jr, C. H., & Cicerone, M. T. (2015). Chemically sensitive bioimaging with coherent Raman scattering. *Nature Photonics 2015 9:5*, *9*(5), 295–305. https://doi.org/10.1038/nphoton.2015.60

Cavendifli, H., & Read June, E. A. S. (1785). XXIII. Experiments on air. *Philosophical Transactions of the Royal Society of London*, *75*, 372–384. https://doi.org/10.1098/RSTL.1785.0023

Chambers, A., Fitch, R. K., & Halliday, B. S. (1998). Basic vacuum technology. In *Vacuum*.

Che, Y., Wang, C., Liu, J., Liu, B., Lin, X., Parker, J., … Zhou, C. (2012). Selective synthesis and device applications of semiconducting single-walled carbon nanotubes using isopropyl alcohol as feedstock. *ACS Nano*, *6*(8), 7454–7462. https://doi.org/10.1021/NN302720N/SUPPL_FILE/NN302720N_SI_001.PDF

Chen, C., Liang, B., Ogino, A., Wang, X., & Nagatsu, M. (2009). Oxygen functionalization of multiwall carbon nanotubes by microwave-excited surface-wave plasma treatment. *Journal of Physical Chemistry C*, *113*(18), 7659–7665. https://doi.org/10.1021/JP9012015

Chen, C., Ogino, A., Wang, X., & Nagatsu, M. (2010). Plasma treatment of multiwall carbon nanotubes for dispersion improvement in water. *Applied Physics Letters*, *96*(13), 131504. https://doi.org/10.1063/1.3377007

Chen, R. J., Franklin, N. R., Kong, J., Cao, J., Tombler, T. W., Zhang, Y., & Dai, H. (2001). Molecular photodesorption from single-walled carbon nanotubes. *Applied Physics Letters*, *79*(14), 2258. https://doi.org/10.1063/1.1408274

Chen, T., & Dai, L. (2013). Carbon nanomaterials for high-performance supercapacitors. *Materials Today*, *16*(7–8), 272–280. https://doi.org/10.1016/J.MATTOD.2013.07.002

Chen, Y., & Zhang, J. (2011). *Diameter controlled growth of single-walled carbon nanotubes from SiO 2 nanoparticles*. https://doi.org/10.1016/j.carbon.2011.04.016

Chen, Y., & Zhang, J. (2014). Chemical Vapor Deposition Growth of Single-Walled Carbon Nanotubes with Controlled Structures for Nanodevice Applications. *Accounts of Chemical Research*, *47*(8), 2273–2281. https://doi.org/10.1021/AR400314B

Cheng, H. M., Li, F., Su, G., Pan, H. Y., He, L. L., Sun, X., & Dresselhaus, M. S. (1998). Large-scale and low-cost synthesis of single-walled carbon nanotubes by the catalytic pyrolysis of hydrocarbons. *Applied Physics Letters*, *72*(25), 3282–3284. https://doi.org/10.1063/1.121624

Cheng, J.-X., & Xie, X. S. (2003). Coherent Anti-Stokes Raman Scattering Microscopy: Instrumentation, Theory, and Applications. *Journal of Physical Chemistry B*, *108*(3), 827–840. https://doi.org/10.1021/JP035693V

Cheng, M., Wang, B. W., Hou, P. X., Li, J. C., Zhang, F., Luan, J., … Cheng, H. M. (2018). Selective growth of

semiconducting single-wall carbon nanotubes using SiC as a catalyst. *Carbon*, *135*, 195–201. https://doi.org/10.1016/J.CARBON.2018.04.047

Cheng, S., Yang, L., Chen, D., Ji, X., Jiang, Z. jie, Ding, D., & Liu, M. (2014). Phase evolution of an alpha MnO2-based electrode for pseudo-capacitors probed by in operando Raman spectroscopy. *Nano Energy*, *9*, 161–167. https://doi.org/10.1016/j.nanoen.2014.07.008

Collon, P. (2008). *Introduction to vacuum gauges Vacuum Gauges*.

Conder, J., Fic, K., & Matei Ghimbeu, C. (2019). Supercapacitors (electrochemical capacitors). In *Char and Carbon Materials Derived from Biomass: Production, Characterization and Applications*. https://doi.org/10.1016/B978-0-12-814893-8.00010-9

Conrad. (2020). Ultrasonic Cleaners. Retrieved October 5, 2021, from https://www.conrad.com/o/ultrasonic-cleaners-0601120

Conroy, D., Moisala, A., Cardoso, S., Windle, A., & Davidson, J. (2010). Carbon nanotube reactor: Ferrocene decomposition, iron particle growth, nanotube aggregation and scale-up. *Chemical Engineering Science*, *65*(10), 2965–2977. https://doi.org/10.1016/J.CES.2010.01.019

Corain, B., Schmid, G., & Toshima, N. (2008). Metal Nanoclusters in Catalysis and Materials Science: The Issue of Size Control. In *Metal Nanoclusters in Catalysis and Materials Science: The Issue of Size Control*. Elsevier.

Costa, P. M. F. J., & Ferreira, P. J. (2016). In Situ TEM of Carbon Nanotubes. In *Hitachi Review* (Vol. 65). Springer.

Cruden, B. A., & Meyyappan, M. (2005). Characterization of a radio frequency carbon nanotube growth plasma by ultraviolet absorption and optical emission spectroscopy. *Journal of Applied Physics*, *97*(8). https://doi.org/10.1063/1.1865315

Cuxart, M. G., Šics, I., Goñi, A. R., Pach, E., Sauthier, G., Paradinas, M., … Pellegrin, E. (2017). Inductively coupled remote plasma-enhanced chemical vapor deposition (rPE-CVD) as a versatile route for the deposition of graphene micro- and nanostructures. *Carbon*, *117*, 331–342. https://doi.org/10.1016/J.CARBON.2017.02.067

Dai, L. (2006). *Carbon nanotechnology : recent developments in chemistry, physics, materials science and device applications*. Elsevier.

Dasgupta, K., Joshi, J. B., Singh, H., & Banerjee, S. (2014). Fluidized bed synthesis of carbon nanotubes: Reaction mechanism, rate controlling step and overall rate of reaction. *AIChE Journal*, *60*(8), 2882–2892. https://doi.org/10.1002/AIC.14482

Datsyuk, V., Kalyva, M., Papagelis, K., Parthenios, J., Tasis, D., Siokou, A., … Galiotis, C. (2008). *Chemical oxidation of multiwalled carbon nanotubes*. 833–840. https://doi.org/10.1016/j.carbon.2008.02.012

Deghiedy, N. M., Yousif, N. M., Hosni, H. M., & Balboul, M. R. (2022). Silver-modified electrodes based on amorphous MnO2/ carbon nanotube: Multicomponent approach to enhance the performance of supercapacitors. *Journal of Physics and Chemistry of Solids*, *161*, 110445. https://doi.org/10.1016/J.JPCS.2021.110445

Dervishi, E., Li, Z., Watanabe, F., Xu, Y., Saini, V., Biris, A. R., & Biris, A. S. (2009). Thermally controlled synthesis of single-wall carbon nanotubes with selective diameters. *Journal of Materials Chemistry*, *19*(19), 3004–3012. https://doi.org/10.1039/B822469B

Devia, D. M., Rodriguez-Restrepo, L. V, & Restrepo-Parra, E. (2015). Methods Employed in Optical Emission Spectroscopy Analysis: a Review. *Ingeniería y Ciencia*, *11*(21), 239–267. https://doi.org/10.17230/ingciencia.11.21.12

Dimentions. (2021). No Title. Retrieved from https://app.dimensions.ai/discover/publication

Drescher, D., & Kneipp, J. (2012). Nanomaterials in complex biological systems: insights from Raman spectroscopy. *Chemical Society Reviews*, *41*(17), 5780–5799. https://doi.org/10.1039/C2CS35127G

Dresselhaus, M. S., Jorio, A., Hofmann, M., Dresselhaus, G., & Saito, R. (2010). Perspectives on Carbon Nanotubes and Graphene Raman Spectroscopy. *Nano Letters*, *10*(3), 751–758. https://doi.org/10.1021/NL904286R

Düngen, P., Prenzel, M., Stappen, C. Van, Pfänder, N., Heumann, S., Schlögl, R., … Schlögl, R. (2017). Investigation of Different Pre-Treated Multi-Walled Carbon Nanotubes by Raman Spectroscopy. *Materials Sciences and Applications*, *8*(8), 628–641. https://doi.org/10.4236/MSA.2017.88044

Ebbesen, T. W., & Ajayan, P. M. (1992). Large-scale synthesis of carbon nanotubes. *Nature 1992 358:6383*, *358*(6383), 220–222. https://doi.org/10.1038/358220a0

Eliezer, S., & Eliezer, Y. (2001). *The Four State of Matter*.

Enoki, T., Kobayashi, Y., & Fukui, K. I. (2007). Electronic structures of graphene edges and nanographene.

Http://Dx.Doi.Org/10.1080/01442350701611991, *26*(4), 609–645. https://doi.org/10.1080/01442350701611991

Falcao, E. H. L., & Wudl, F. (2007). Carbon allotropes: beyond graphite and diamond. *Journal of Chemical Technology & Biotechnology*, *82*(6), 524–531. https://doi.org/10.1002/JCTB.1693

Fantini, C., Jorio, A., Souza, M., Strano, M. S., Dresselhaus, M. S., & Pimenta, M. A. (2004). Optical Transition Energies for Carbon Nanotubes from Resonant Raman Spectroscopy: Environment and Temperature Effects. *Physical Review Letters*, *93*(14), 147406. https://doi.org/10.1103/PhysRevLett.93.147406

Ferrari, A. C., Meyer, J. C., Scardaci, V., Casiraghi, C., Lazzeri, M., Mauri, F., … Geim, A. K. (2006). Raman spectrum of graphene and graphene layers. *Physical Review Letters*, *97*(18), 187401. https://doi.org/10.1103/PHYSREVLETT.97.187401/FIGURES/3/MEDIUM

Ferreira, F. V., Franceschi, W., Menezes, B. R. C., Biagioni, A. F., Coutinho, A. R., & Cividanes, L. S. (2019). Synthesis, Characterization, and Applications of Carbon Nanotubes. *Carbon-Based Nanofillers and Their Rubber Nanocomposites: Carbon Nano-Objects*, 1–45. https://doi.org/10.1016/B978-0-12-813248-7.00001-8

Fitzgerald, R., Keil, K., & Heinrich, K. F. (1968). Solid-state energy-dispersion spectrometer for electron-microprobe x-ray analysis. *Science*, *159*(814), 528–530. https://doi.org/10.1126/SCIENCE.159.3814.528

Flahaut, E., Govindaraj, A., Peigney, A., Laurent, C., Rousset, A., Nagesa Ramachandra Rao, C., & R Synthesis, C. N. (1999). Synthesis of single-walled carbon nanotubes using binary (Fe, Co, Ni) alloy nanoparticles prepared in situ by the reduction of oxide solid solutions Open Archive TOULOUSE Archive Ouverte (OATAO). *Chemical Physics Letters*, *300*, 236–242. https://doi.org/10.1016/S0009-2614(98)01304-9ï

Foroughi, J., Mitew, T., Ogunbona, P., Raad, R., & Safaei, F. (2016). Smart Fabrics and Networked Clothing: Recent developments in CNT-based fibers and their continual refinement. *IEEE Consumer Electronics Magazine*, *5*(4), 105–111. https://doi.org/10.1109/MCE.2016.2590220

Foster, J., Sommers, B. S., Gucker, S. N., Blankson, I. M., & Adamovsky, G. (2012). Perspectives on the interaction of plasmas with liquid water for water purification. *IEEE Transactions on Plasma Science*, *40*(5 PART 1), 1311–1323. https://doi.org/10.1109/TPS.2011.2180028

Fridman, A. (2008). *Plasma Chemistry*.

Fridman, G., Friedman, G., Gutsol, A., Shekhter, A. B., Vasilets, V. N., & Fridman, A. (2008). Applied Plasma Medicine. *Plasma Processes and Polymers*, *5*(6), 503–533. https://doi.org/10.1002/PPAP.200700154

Friedrich, J. F., Mix, R., Schulze, R. D., Meyer-Plath, A., Joshi, R., & Wettmarshausen, S. (2008). New Plasma Techniques for Polymer Surface Modification with Monotype Functional Groups. *Plasma Processes and Polymers*, *5*(5), 407–423. https://doi.org/10.1002/PPAP.200700145

Fujii, S., Tanaka, T., Miyata, Y., Suga, H., Naitoh, Y., Minari, T., … Kataura, H. (2009). Performance enhancement of thin-film transistors by using high-purity semiconducting single-wall carbon nanotubes. *Applied Physics Express*, *2*(7). https://doi.org/10.1143/APEX.2.071601

Gaines, J. R. (2019). *Introduction to vacuum Science and System Design*. Kurt J. Lesker.

GAJENDRASING, G. K. (2020). *STUDY ON PLASMA EMISSION BEHAVIOR DURING PLASMA ELECTROLYTIC OXIDATION (PEO) ON MAGNESIUM ALLOY*. Tokushima University.

Ganesan, K., Ghosh, S., Gopala Krishna, N., Ilango, S., Kamruddin, M., & Tyagi, A. K. (2016). A comparative study on defect estimation using XPS and Raman spectroscopy in few layer nanographitic structures. *Physical Chemistry Chemical Physics*, *18*(32), 22160–22167. https://doi.org/10.1039/C6CP02033J

Gao, T., Fjellvåg, H., & Norby, P. (2009). A comparison study on Raman scattering properties of alpha- and beta-MnO2. *Analytica Chimica Acta*, *648*(2), 235–239. https://doi.org/10.1016/J.ACA.2009.06.059

Garcia-Martinez, J., Li, K., & Davis, M. E. (n.d.). *Mesoporous zeolites : preparation, characterization and applications*. Weinheim: Wiley.

García Cespedez, J. (2008). *Nanotubos de carbono: síntesis , caracterización y aplicaciones*.

Gil Min, B., Gi Chae, H., Minus, M. L., & Kumar, S. (2020). Polymer/carbon nanotube composite fibers-An overview. *Transworld Research Network*, *37*(2), 43–73.

Gill, W. D., & Kay, E. (2004). Efficient Low Pressure Sputtering in a Large Inverted Magnetron Suitable for Film Synthesis. *Review of Scientific Instruments*, *36*(3), 277. https://doi.org/10.1063/1.1719553

Girard-Lauriault, P. L., Illgen, R., Ruiz, J. C., Wertheimer, M. R., & Unger, W. E. S. (2012). Surface functionalization of graphite and carbon nanotubes by vacuum-ultraviolet photochemical reactions. *Applied Surface Science*, *258*(22), 8448–8454. https://doi.org/10.1016/J.APSUSC.2012.03.012

Glocker, D. A., Shah, S. I., & Westwood, W. D. (William D. (2018). *Handbook of thin film process technology : reactive sputtering*. CRC Press.

Goldstein, J., Newbury, D. E., Joy, D. C., Lyman, C. E., Echlin, P., Lifshin E., … Michael, J. R. (2003). Scanning Electron Microscopy and X-ray microanalysis. In *Springer Science* (3rd ed.). https://doi.org/10.1007/978-1-4615-0215-9

Goldstein, Joseph, Joy, D. C., & LastNameRoming Jr., A. D. (1986). *Principles of Analytical Electron Microscopy | Joseph Goldstein | Springer*. Retrieved from https://www.springer.com/gp/book/9780306423871

Gouadec, G., Colomban, P., Raman Spectroscopy, P. C., & Gouadec, G. (2007). Raman Spectroscopy of Nanomaterials: How Spectra Relate to Disorder, Particle Size and Mechanical Properties. *Progress in Crystal Growth and Characterization of Materials*, *53*(1), 1–56. https://doi.org/10.1016/j.pcrysgrow.2007.01.001ï

Graphenea. (2020). The Price Of Graphene – Graphenea. Retrieved December 15, 2021, from https://www.graphenea.com/pages/graphene-price#.YbnMk72ZOUk

Grüneis, A., Kramberger, C., Grimm, D., Gemming, T., Rümmeli, M. H., Barreiro, A., … Büchner, B. (2006). Eutectic limit for the growth of carbon nanotubes from a thin iron film by chemical vapor deposition of cyclohexane. *Chemical Physics Letters*, *425*(4–6), 301–305. https://doi.org/10.1016/J.CPLETT.2006.05.057

Gspann, T. S., Juckes, S. M., Niven, J. F., Johnson, M. B., Elliott, J. A., White, M. A., & Windle, A. H. (2017). High thermal conductivities of carbon nanotube films and micro-fibres and their dependence on morphology. *Carbon*, *114*, 160–168. https://doi.org/10.1016/J.CARBON.2016.12.006

Gubkin, J. (1887). Electrolytische Metallabscheidung an der freien Oberfläche einer Salzlösung. *Annalen Der Physik*, *268*(9), 114–115. https://doi.org/10.1002/ANDP.18872680909

Gudmundsson, J. T. (2020). Physics and technology of magnetron sputtering discharges. *Plasma Sources Science and Technology*, *29*(11). https://doi.org/10.1088/1361-6595/abb7bd

Guo, L., Shanov, V., & Singh, R. N. (2005). Growth of Carbon Nanotubes by Microwave Plasma Chemical Vapor Deposition (MPCVD). *Ceramic Transactions*, *159*, 175–183. https://doi.org/10.1002/9781118407158.CH19

Gupta, T. (2017). Carbon: The black, the gray and the transparent. *Carbon: The Black, the Gray and the Transparent*, 1–319. https://doi.org/10.1007/978-3-319-66405-7

Han, G., He, J., Fukuyama, S., & Yokogawa, K. (1998). Effect of strain-induced martensite on hydrogen environment embrittlement of sensitized austenitic stainless steels at low temperatures. *Acta Materialia*, *46*(13), 4559–4570. https://doi.org/10.1016/S1359-6454(98)00136-0

Han, Z. J., Tay, B. K., Shakerzadeh, M., & Ostrikov, K. (2009). Superhydrophobic amorphous carbon/carbon nanotube nanocomposites. *Applied Physics Letters*, *94*(22), 223106. https://doi.org/10.1063/1.3148667

Han, Z., Tay, B., Tan, C., Shakerzadeh, M., & Ostrikov, K. (2009). Electrowetting control of Cassie-to-Wenzel transitions in superhydrophobic carbon nanotube-based nanocomposites. *ACS Nano*, *3*(10), 3031–3036. https://doi.org/10.1021/NN900846P/SUPPL_FILE/NN900846P_SI_001.PDF

Harutyunyan, A. R., Tokune, T., & Mora, E. (2005). Liquid as a required catalyst phase for carbon single-walled nanotube growth. *Applied Physics Letters*, *87*(5), 051919. https://doi.org/10.1063/1.2005395

Harutyunyan, Avetik R., Chen, G., Paronyan, T. M., Pigos, E. M., Kuznetsov, O. A., Hewaparakrama, K., … Sumanasekera, G. U. (2009). Preferential growth of single-walled carbon nanotubes with metallic conductivity. *Science*, *326*(5949), 116–120. https://doi.org/10.1126/SCIENCE.1177599/SUPPL_FILE/HARUTYUNYAN.SOM.PDF

Harvey, D. (2001). Electrochemical Methods. In *Analytical Chemistry* (pp. 667–781). Retrieved from https://chem.libretexts.org/Bookshelves/Analytical_Chemistry/Analytical_Chemistry_2.1_(Harvey)/11%3A_Electrochemical_Methods

He, M., Chernov, A. I., Fedotov, P. V., Obraztsova, E. D., Sainio, J., Rikkinen, E., … Krause, A. O. I. (2010). Predominant (6,5) single-walled carbon nanotube growth on a copper-promoted iron catalyst. *Journal of the American Chemical Society*, *132*(40), 13994–13996. https://doi.org/10.1021/JA106609Y/SUPPL_FILE/JA106609Y_SI_001.PDF

Hendra, P. J., & Vear, C. J. (1970). Laser Raman spectroscopy. A review. *Analyst*, *95*(1129), 321–342. https://doi.org/10.1039/AN9709500321

Hernadi, K., Fonseca, A., Nagy, J. B., Bernaerts, D., & Lucas, A. A. (1996). Fe-catalyzed carbon nanotube formation. *Carbon*, *34*(10), 1249–1257. https://doi.org/10.1016/0008-6223(96)00074-7

Herziger, F., Tyborski, C., Ochedowski, O., Schleberger, M., & Maultzsch, J. (2014). Double-resonant la phonon scattering in defective graphene and carbon nanotubes. *Physical Review B - Condensed Matter and Materials Physics*, *90*(24), 245431. https://doi.org/10.1103/PHYSREVB.90.245431/FIGURES/3/MEDIUM

Herzing, A. A., Richter, L. J., & Anderson, I. M. (2010). 3D nanoscale characterization of thin-film organic photovoltaic device structures via spectroscopic contrast in the TEM. *Journal of Physical Chemistry C*, *114*(41), 17501–17508. https://doi.org/10.1021/JP105883P

Hickling, A., & Ingram, M. D. (1964). Contact glow-discharge electrolysis. *Transactions of the Faraday Society*, *60*(0), 783–793. https://doi.org/10.1039/TF9646000783

Hiramatsu, M., Mitsuguchi, S., Horibe, T., Kondo, H., Hori, M., & Kano, H. (2013). Fabrication of carbon nanowalls on carbon fiber paper for fuel cell application. *Japanese Journal of Applied Physics*, *52*(1 PART2), 01AK03. https://doi.org/10.7567/JJAP.52.01AK03/XML

Hnatiuc, E., Astanei, D., Ursache, M., Hnatiuc, B., & Brisset, J. L. (2012). A review over the cold plasma reactors and their applications. *EPE 2012 - Proceedings of the 2012 International Conference and Exposition on Electrical and Power Engineering*, 497–502. https://doi.org/10.1109/ICEPE.2012.6463884

Hodoroaba, V. D. (2019). Energy-dispersive X-ray spectroscopy (EDS). In *Characterization of Nanoparticles: Measurement Processes for Nanoparticles*. https://doi.org/10.1016/B978-0-12-814182-3.00021-3

Hofmann, S., Ducati, C., Robertson, J., & Kleinsorge, B. (2003). Low-temperature growth of carbon nanotubes by plasma-enhanced chemical vapor deposition. *Applied Physics Letters*, *83*(1), 135. https://doi.org/10.1063/1.1589187

Honeychuck, R. V. (1996). Science of Fullerenes and Carbon Nanotubes By M. S. Dresselhaus (MIT), G. Dresselhaus (MIT), and P. C. Eklund (University of Kentucky). Academic Press: San Diego. 1996, xviii + 965 pp. ISBN 0-12-221820-5. *Journal of the American Chemical Society*, *118*(37), 8987–8987. https://doi.org/10.1021/JA965593L

Hopwood, J., Guarnieri, C. R., Whitehair, S. J., & Cuomo, J. J. (1998). Langmuir probe measurements of a radio frequency induction plasma. *Journal of Vacuum Science & Technology A: Vacuum, Surfaces, and Films*, *11*(1), 152. https://doi.org/10.1116/1.578282

Hou, C., Li, T., Zhang, Z., Chang, C., & An, L. (2022). Nickel-cobalt layered double hydroxide hollow nanocages anchored on carbon nanotubes as electrode for supercapacitors. *Materials Letters*, *309*, 131361. https://doi.org/10.1016/J.MATLET.2021.131361

Hsu, Y. K., Chen, Y. C., Lin, Y. G., Chen, L. C., & Chen, K. H. (2011). Reversible phase transformation of MnO2 nanosheets in an electrochemical capacitor investigated by in situ Raman spectroscopy. *Chemical Communications (Cambridge, England)*, *47*(4), 1252–1254. https://doi.org/10.1039/C0CC03902K

Hussain, S., Amade, R., Jover, E., & Bertran, E. (2012). Functionalization of carbon nanotubes by water plasma. *Nanotechnology*, *23*(38), 385604. https://doi.org/10.1088/0957-4484/23/38/385604

Hussain, Shahzad. (2014). *Carbon Nanotubes Deposited by Hot Wire Plasma CVD and water assisted CVD for Energetic and Environmental Applications.*

Hussain, Shahzad, Amade, R., Boyd, A., Musheghyan-Avetisyan, A., Alshaikh, I., Martí-Gonzalez, J., … Bertran-Serra, E. (2021). Three-dimensional Si / vertically oriented graphene nanowalls composite for supercapacitor applications. *Ceramics International*, *47*(15), 21751–21758. https://doi.org/10.1016/j.ceramint.2021.04.190

Hussain, Shahzad, Amade, R., Jover, E., & Bertran, E. (2013). Water plasma functionalized CNTs/MnO2 composites for supercapacitors. *The Scientific World Journal*, *2013*, 1–9. https://doi.org/10.1155/2013/832581

Hussain, Shahzad, Amade, R., Jover, E., & Bertran, E. (2015). Growth and Plasma Functionalization of Carbon Nanotubes. *Journal of Cluster Science*, *26*(2), 315–336. https://doi.org/10.1007/s10876-015-0862-1

Hussain, Shahzad, Amade, R., Moreno, H., & Bertran, E. (2014). RF-PECVD growth and nitrogen plasma functionalization of CNTs on copper foil for electrochemical applications. *Diamond and Related Materials*, *49*(December), 55–61. https://doi.org/10.1016/j.diamond.2014.08.006

Hussain, Shahzad, Kovacevic, E., Amade, R., Berndt, J., Pattyn, C., Dias, A., … Bertran-Serra, E. (2018). Plasma synthesis of polyaniline enrobed carbon nanotubes for electrochemical applications. *Electrochimica Acta*, *268*, 218–225. https://doi.org/10.1016/J.ELECTACTA.2018.02.112

Hussein, R. O. (2010). *Study on electrolytic plasma discharging behavior and its influence on the plasma electrolytic oxidation coatings*.

Hye, R. B., Lim, H., Hyun, J. S., & Hee, C. C. (2007). A Synthesis of High Purity Single-Walled Carbon Nanotubes from Small Diameters of Cobalt Nanoparticles by Using Oxygen-Assisted Chemical Vapor Deposition Process. *Bulletin of the Korean Chemical Society*, *28*(11), 2056–2060. https://doi.org/10.5012/BKCS.2007.28.11.2056

Iijima, S. (1991a). Helical microtubules of graphitic carbon. *Nature 1991 354:6348*, *354*(6348), 56–58. https://doi.org/10.1038/354056a0

Iijima, S. (1991b). Helical microtubules of graphitic carbon. *Nature 1991 354:6348*, *354*(6348), 56–58. https://doi.org/10.1038/354056a0

Iijima, S., Brabec, C., Maiti, A., & Bernholc, J. (1998). Structural flexibility of carbon nanotubes. *The Journal of Chemical Physics*, *104*(5), 2089. https://doi.org/10.1063/1.470966

Iijima, S., & Ichihashi, T. (1993). Single-shell carbon nanotubes of 1-nm diameter. *Nature*, *363*(6430), 603–605. https://doi.org/10.1038/363603A0

Ishijima, T., Nosaka, K., Tanaka, Y., Uesugi, Y., Goto, Y., & Horibe, H. (2013). A high-speed photoresist removal process using multibubble microwave plasma under a mixture of multiphase plasma environment. *Applied Physics Letters*, *103*(14), 142101. https://doi.org/10.1063/1.4823530

ISO. (2015). ISO/TS 80004-1:2015(en), Nanotechnologies — Vocabulary — Part 1: Core terms. Retrieved December 15, 2021, from https://www.iso.org/obp/ui/#iso:std:iso:ts:80004:-1:ed-2:v1:en

iTecTec. (2021). Impedance matching network and power transfer to the load – iTecTec. Retrieved November 4, 2021, from https://itectec.com/electrical/electronic-impedance-matching-network-and-power-transfer-to-the-load/

Janas, D., & Koziol, K. K. (2016). Carbon nanotube fibers and films: Synthesis, applications and perspectives of the direct-spinning method. *Nanoscale*, *8*(47), 19475–19490. https://doi.org/10.1039/C6NR07549E

Javed, Y., Ali, K., Akhtar, K., Jawaria, M., Hussain, I., Ahmad, G., & Arif, T. (2018). TEM for Atomic-Scale Study: Fundamental, Instrumentation, and Applications in Nanotechnology. In *Handbook of Materials Characterization*. https://doi.org/10.1007/978-3-319-92955-2

Jhang, S. H., Craciun, M. F., Schmidmeier, S., Tokumitsu, S., Russo, S., Yamamoto, M., … Strunk, C. (2011). Stacking-order dependent transport properties of trilayer graphene. *Physical Review B - Condensed*

Matter and Materials Physics, *84*(16), 161408. https://doi.org/10.1103/PHYSREVB.84.161408/FIGURES/4/MEDIUM

Ji, X., Zhang, W., Li, X., Yu, H., & Dong, H. (2017). A novel hybrid method combining ASP with PECVD for in-situ low temperature synthesis of vertically aligned carbon nanotube films. *Diamond and Related Materials*, *77*, 16–24. https://doi.org/10.1016/J.DIAMOND.2017.05.008

Jones, R. R., Hooper, D. C., Zhang, L., Wolverson, D., & Valev, V. K. (2019). Raman Techniques: Fundamentals and Frontiers. *Nanoscale Research Letters 2019 14:1*, *14*(1), 1–34. https://doi.org/10.1186/S11671-019-3039-2

Jorio, A., Pimenta, M. A., Filho, A. G. S., Samsonidze, G. G., Swan, A. K., Ünlü, M. S., … Dresselhaus, M. S. (2003). Resonance Raman Spectra of Carbon Nanotubes by Cross-Polarized Light. *Physical Review Letters*, *90*(10), 107403. https://doi.org/10.1103/PhysRevLett.90.107403

Jorio, A., Saito, R., Dresselhaus, G., & Dresselhaus, M. S. (2004). Determination of nanotubes properties by Raman spectroscopy. *Philosophical Transactions of the Royal Society of London. Series A: Mathematical, Physical and Engineering Sciences*, *362*(1824), 2311–2336. https://doi.org/10.1098/RSTA.2004.1443

Jousten, K. (2016). *Handbook of Vacuum Technology* (2nd ed.). Retrieved from https://www.wiley.com/en-us/Handbook+of+Vacuum+Technology%2C+2nd+Edition-p-9783527413386

JS, K., T, L., BW, R., ML, T., MR, A., WE, K., … GH, C. (2008). Imaging of transient structures using nanosecond in situ TEM. *Science (New York, N.Y.)*, *321*(5895), 1472–1475. https://doi.org/10.1126/SCIENCE.1161517

Julien, C., & Massot, M. (2002). Spectroscopic studies of the local structure in positive electrodes for lithium batteries. *Physical Chemistry Chemical Physics*, *4*(17), 4226–4235. https://doi.org/10.1039/B203361E

Julien, C., Massot, M., Baddour-Hadjean, R., Franger, S., Bach, S., & Pereira-Ramos, J. P. (2003). Raman spectra of birnessite manganese dioxides. *Solid State Ionics*, *159*(3–4), 345–356. https://doi.org/10.1016/S0167-2738(03)00035-3

Jung, Y., Cho, Y. S., Lee, J. W., Oh, J. Y., & Park, C. R. (2018). How can we make carbon nanotube yarn

stronger? *Composites Science and Technology*, *166*, 95–108. https://doi.org/10.1016/J.COMPSCITECH.2018.02.010

Jurečka, S., Imamura, K., Matsumoto, T., & Kobayashi, H. (2018). Investigation of morphological and optical properties of nanostructured layers formed by the SSCT etching of silicon. *Applied Surface Science*, *461*, 72–77. https://doi.org/10.1016/J.APSUSC.2018.08.099

Kaech, A. (2013). An Introduction To Electron Microscopy Instrumentation, Imaging and Preparation. *Center for Microscopy and Image Analysis*, 1–26. Retrieved from http://www.zmb.uzh.ch/static/bio407/assets/Script_AK_2014.pdf

Kalbacova, M., Broz, A., Kromka, A., Babchenko, O., & Kalbac, M. (2021). Controlled oxygen plasma treatment of single-walled carbon nanotube films improves osteoblast cells attachment and enhances their proliferation. *Carbon*, *49*(9), 2926–2934. https://doi.org/10.1016/j.carbon.2011.02.069

Kalha, C., Fernando, N. K., Bhatt, P., Johansson, F. O. L., Lindblad, A., Rensmo, H., … Regoutz, A. (2021). Hard x-ray photoelectron spectroscopy: A snapshot of the state-of-the-art in 2020. *Journal of Physics Condensed Matter*, *33*(23). https://doi.org/10.1088/1361-648X/abeacd

Kang, L. X., Li, D., Yong, Z. Z., Zhang, X. H., & Li, Q. (2017). Growth of Aligned Carbon Nanotubes and Their Applications. *Industrial Applications of Carbon Nanotubes*, 381–403. https://doi.org/10.1016/B978-0-323-41481-4.00013-7

Ke, Q., & Wang, J. (2016). Graphene-based materials for supercapacitor electrodes – A review. *Journal of Materiomics*, *2*(1), 37–54. https://doi.org/10.1016/J.JMAT.2016.01.001

KEIDAR, M., & BEILIS, I. I. (2018). PLASMA ENGINEERING. In *Plasma Engineering*.

keyence. (2019). Introduction to Roughness. Retrieved September 10, 2021, from https://www.keyence.com/ss/products/microscope/roughness/surface

Kiamahalleh, M. V., Zein, S. H. S., Najafpour, G., Sata, S. A., & Buniran, S. (2012). Multiwalled carbon nanotubes based nanocomposites for supercapacitors: A review of electrode materials. *Nano*, *7*(2), 1–27. https://doi.org/10.1142/S1793292012300022

Kieser, B., Phillion, R., Smith, S., & Mccartney, T. (2011). The Application of Industrial Scale Ultrasonic Cleaning To Heat exchangers. *Heat Exchanger Fouling and Cleaning - 2011*, *2011*(1961), 336–338.

Retrieved from www.heatexchanger-fouling.com

Kim, S. H. (2014). Protection of accelerator hardware: RF systems. *2014 Joint International Accelerator School: Beam Loss and Accelerator Protection, Proceedings*, *002*(November 2014), 361–376. https://doi.org/10.5170/CERN-2016-002.361

Kirkland, A., & Young, N. (2012). *MicroscopyandAnalysis | 25th Anniversary Issue*.

Kong, D., Xiao, Z., Gao, Y., Zhang, X., Guo, R., Huang, X., … Zhi, L. (2019). Sp2-carbon dominant carbonaceous materials for energy conversion and storage. *Materials Science and Engineering: R: Reports*, *137*, 1–37. https://doi.org/10.1016/J.MSER.2018.10.001

Korneva, G. (2008). *Functionalization Of carbon nanotubes*. Retrieved from https://idea.library.drexel.edu/islandora/object/idea%3A2797

Koshino, M. (2009). Interlayer screening effect in graphene multilayers with ABA and ABC stacking. *Physical Review B - Condensed Matter and Materials Physics*, *81*(12). https://doi.org/10.1103/PhysRevB.81.125304

Kowalczyk, D., Brzeziński, S., Makowski, T., & Fortuniak, W. (2015). Conductive hydrophobic hybrid textiles modified with carbon nanotubes. *Applied Surface Science*, *PA*(357), 1007–1014. https://doi.org/10.1016/J.APSUSC.2015.09.132

Krishnan, A., Dujardin, E., Ebbesen, T. W., Yianilos, P. N., & Treacy, M. M. J. (1998). Young's modulus of single-walled nanotubes. *Physical Review B*, *58*(20), 14013. https://doi.org/10.1103/PhysRevB.58.14013

Kroto, H. W., Heath, J. R., O'Brien, S. C., Curl, R. F., & Smalley, R. E. (1985). C60: Buckminsterfullerene. *Nature 1985 318:6042*, *318*(6042), 162–163. https://doi.org/10.1038/318162a0

Krstulović, N., Labazan, I., Miloević, S., Cvelbar, U., Vesel, A., & Mozeti, M. (2006). Optical emission spectroscopy characterization of oxygen plasma during treatment of a PET foil. *Journal of Physics D: Applied Physics*, *39*(17), 3799. https://doi.org/10.1088/0022-3727/39/17/014

Kumar, J. (2018). Photoelectron Spectroscopy: Fundamental Principles and Applications. In *Handbook of Materials Characterization* (pp. 435–495). https://doi.org/10.1007/978-3-319-92955-2

Kumar, M., & Ando, Y. (2010). Chemical vapor deposition of carbon nanotubes: a review on growth mechanism and mass production. *Journal of Nanoscience and Nanotechnology*, *10*(6), 3739–3758.

https://doi.org/10.1166/JNN.2010.2939

Landau, L. D., & Lifshitz, E. M. (1980). *Statistical physics*. Retrieved from https://ia600702.us.archive.org/22/items/ost-physics-landaulifshitz-statisticalphysics/LandauLifshitz-StatisticalPhysics.pdf

Lebrón-Colón, M., Meador, M. A., Lukco, D., Sol, F., Santos-Pérez, J., & McCorkle, L. S. (2011). Surface oxidation study of single wall carbon nanotubes. *Nanotechnology*, *22*(45). https://doi.org/10.1088/0957-4484/22/45/455707

Lee, D. S., Kim, D. W., Kim, H. S., Lee, S. W., Jhang, S. H., Park, Y. W., & Campbell, E. E. B. (2005). Extraction of semiconducting CNTs by repeated dielectrophoretic filtering. *Applied Physics A: Materials Science and Processing*, *80*(1), 5–8. https://doi.org/10.1007/S00339-004-2992-4

Lehman, J. H., Terrones, M., Mansfield, E., Hurst, K. E., & Meunier, V. (2011). Evaluating the characteristics of multiwall carbon nanotubes. *Carbon*, *49*(8), 2581–2602. https://doi.org/10.1016/J.CARBON.2011.03.028

Lekawa-Raus, A., Patmore, J., Kurzepa, L., Bulmer, J., & Koziol, K. (2014). Electrical Properties of Carbon Nanotube Based Fibers and Their Future Use in Electrical Wiring. *Advanced Functional Materials*, *24*(24), 3661–3682. https://doi.org/10.1002/ADFM.201303716

Lens, M. (2009). Use of fullerenes in cosmetics. *Recent Patents on Biotechnology*, *3*(2), 118–123. https://doi.org/10.2174/187220809788700166

Lepró, X., Lima, M. D., & Baughman, R. H. (2010). Spinnable carbon nanotube forests grown on thin, flexible metallic substrates. *Carbon*, *48*(12), 3621–3627. https://doi.org/10.1016/J.CARBON.2010.06.016

Li, H., Zhou, B., Lin, Y., Gu, L., Wang, W., Fernando, K. A. S., … Sun, Y. P. (2004). Selective Interactions of Porphyrins with Semiconducting Single-Walled Carbon Nanotubes. *Journal of the American Chemical Society*, *126*(4), 1014–1015. https://doi.org/10.1021/JA037142O

Li, Y., He, Y., Qiu, J., Zhao, J., Ye, Q., Zhu, Y., & Mao, J. (2018). Enhancement of Pitting Corrosion Resistance of Austenitic Stainless Steel Through Deposition of Amorphous/Nanocrystalline Oxy-nitrided Phases by Active Screen Plasma Treatment. *Materials Research*, *21*(6), 20170697. https://doi.org/10.1590/1980-5373-MR-2017-0697

Li, Y. L., Kinloch, I. A., & Windle, A. H. (2004). Direct Spinning of Carbon Nanotube Fibers from Chemical Vapor Deposition Synthesis. *Science*, *304*(5668), 276–278. https://doi.org/10.1126/SCIENCE.1094982/SUPPL_FILE/PAP.PDF

Li, Y., Xu, G., Zhang, H., Li, T., Yao, Y., Li, Q., & Dai, Z. (2015). Alcohol-assisted rapid growth of vertically aligned carbon nanotube arrays. *Carbon*, *91*, 45–55. https://doi.org/10.1016/J.CARBON.2015.04.035

Lieberman, M. A. (Michael A. ., & Lichtenberg, A. J. (2005). *Principles of plasma discharges and materials processing*. Retrieved from https://www.wiley.com/en-us/Principles+of+Plasma+Discharges+and+Materials+Processing%2C+2nd+Edition-p-9780471720010

Lin, M., Tan, J. P. Y., Boothroyd, C., Loh, K. P., Tok, E. S., & Foo, Y. L. (2006). Direct observation of single-walled carbon nanotube growth at the atomistic scale. *Nano Letters*, *6*(3), 449–452. https://doi.org/10.1021/nl052356k

Liu, B., Wu, F., Gui, H., Zheng, M., & Zhou, C. (2017). Chirality-Controlled Synthesis and Applications of Single-Wall Carbon Nanotubes. *ACS Nano*, *11*(1), 31–53. https://doi.org/10.1021/ACSNANO.6B06900

Lloyd, G. E. (1987). Atomic number and crystallographic contrast images with the SEM: a review of backscattered electron techniques. *Mineralogical Magazine*, *51*(359), 3–19. https://doi.org/10.1180/minmag.1987.051.359.02

Locke, B. R., Sato, M., Sunka, P., Hoffmann, M. R., & Chang, J. S. (2005). Electrohydraulic Discharge and Nonthermal Plasma for Water Treatment. *Industrial and Engineering Chemistry Research*, *45*(3), 882–905. https://doi.org/10.1021/IE050981U

Loiseau, a. A., & Gavillet, a. J. (n.d.). *Nucleation and growth of SWNT: TEM studies of the role of the catalyst - EM consulte*. Retrieved from https://www.em-consulte.com/article/19010/resume/nucleation-and-growth-of-swnt-tem-studies-of-the-r

Lolli, G., Zhang, L., Balzano, L., Sakulchaicharoen, N., Tan, Y., & Resasco, D. E. (2006). Tailoring (n,m) Structure of Single-Walled Carbon Nanotubes by Modifying Reaction Conditions and the Nature of the Support of CoMo Catalysts. *Journal of Physical Chemistry B*, *110*(5), 2108–2115. https://doi.org/10.1021/JP056095E

Lu, J. P. (1997). Elastic properties of single and multilayered nanotubes. *Journal of Physics and Chemistry of Solids*, *58*(11), 1649–1652. https://doi.org/10.1016/S0022-3697(97)00045-0

Lui, C. H., Li, Z., Chen, Z., Klimov, P. V., Brus, L. E., & Heinz, T. F. (2011). Imaging stacking order in few-layer graphene. *Nano Letters*, *11*(1), 164–169. https://doi.org/10.1021/NL1032827

Maeda, Y., Takano, Y., Sagara, A., Hashimoto, M., Kanda, M., Kimura, S. ichi, … Nagase, S. (2008). Simple purification and selective enrichment of metallic SWCNTs produced using the arc-discharge method. *Carbon*, *46*(12), 1563–1569. https://doi.org/10.1016/J.CARBON.2008.06.057

Mallet-Ladeira, P., Puech, P., Toulouse, C., Cazayous, M., Ratel-Ramond, N., Weisbecker, P., … Monthioux, M. (2014). A Raman study to obtain crystallite size of carbon materials: A better alternative to the Tuinstra-Koenig law. *Carbon*, *80*(1), 629–639. https://doi.org/10.1016/j.carbon.2014.09.006

Manos, D. M., & Flamm, D. L. (1989). *Plasma etching : an introduction*. Academic Press.

Mantzaris, N. V., Gogolides, E., Boudouvis, A. G., Rhallabi, A., & Turban, G. (1998). Surface and plasma simulation of deposition processes: CH4 plasmas for the growth of diamondlike carbon. *Journal of Applied Physics*, *79*(7), 3718. https://doi.org/10.1063/1.361205

Marchi, C. S., San, C., & Somerday, M. B. P. (2020). *Technical Reference on Hydrogen Compatibility of Materials Austenitic Stainless Steels: Type 304 & 304L (code 2101)*.

Mariotti, D., Patel, J., Švrček, V., & Maguire, P. (2012). Plasma–Liquid Interactions at Atmospheric Pressure for Nanomaterials Synthesis and Surface Engineering. *Plasma Processes and Polymers*, *9*(11–12), 1074–1085. https://doi.org/10.1002/PPAP.201200007

Marquardt, N. (1999). *CAS - CERN Accelerator School : Vacuum Technology : Snekersten, Denmark 28 May - 3 Jun 1999* (S. Turner, Ed.). https://doi.org/10.5170/CERN-1999-005

Matsumura, H., Umemoto, H., Gleason, K. K., & Schropp, R. E. I. (2019). *Catalytic Chemical Vapor Deposition : Technology and Applications of Cat-CVD*. Retrieved from https://www.wiley.com/en-us/Catalytic+Chemical+Vapor+Deposition%3A+Technology+and+Applications+of+Cat+CVD-p-9783527818662

Mattox, D. M. (2010). The “Good” Vacuum (Low Pressure) Processing Environment. In *Handbook of Physical Vapor Deposition (PVD) Processing*. https://doi.org/10.1016/b978-0-8155-2037-5.00003-4

Maultzsch, J., Telg, H., Reich, S., & Thomsen, C. (2005). Radial breathing mode of single-walled carbon

nanotubes: Optical transition energies and chiral-index assignment. *Physical Review B*, *72*(20), 205438. https://doi.org/10.1103/PhysRevB.72.205438

Mcmahon, G. (2007). Instrumentation A Guide to Laboratory , Miniaturized Instruments. *Analytical Instrumentation*.

Mehmood, F., Kamal, T., & Ashraf, U. (2018). *Generation and Applications of Plasma (An Academic Review)*. https://doi.org/10.20944/preprints201810.0061.v1

mekanizmalar. (2012). Roots Pump Two Lobe. Retrieved November 3, 2021, from https://www.youtube.com/watch?v=_-fwWrFLiyY&ab_channel=mekanizmalar

Merlen, A., Buijnsters, J. G., & Pardanaud, C. (2017). A Guide to and Review of the Use of Multiwavelength Raman Spectroscopy for Characterizing Defective Aromatic Carbon Solids: from Graphene to Amorphous Carbons. *Coatings 2017, Vol. 7, Page 153*, *7*(10), 153. https://doi.org/10.3390/COATINGS7100153

Meyyappan, M., Delzeit, L., Cassell, A., & Hash, D. (2003). Carbon nanotube growth by PECVD: a review. *Plasma Sources Science and Technology*, *12*(2), 205. https://doi.org/10.1088/0963-0252/12/2/312

MIT. (2021). Carbon nanotube-based sensor can detect SARS-CoV-2 proteins | MIT News | Massachusetts Institute of Technology. Retrieved December 16, 2021, from https://news.mit.edu/2021/carbon-nanotube-covid-detect-1026

Miyata, T., Nagao, T., Watanabe, D., Kumagai, A., Akutagawa, K., Morita, H., & Jinnai, H. (2021). Nanoscale Stress Distribution in Silica-Nanoparticle-Filled Rubber as Observed by Transmission Electron Microscopy: Implications for Tire Application. *ACS Applied Nano Materials*, *4*(5), 4452–4461. https://doi.org/10.1021/acsanm.1c00009

Miyata, Y., Maniwa, Y., & Kataura, H. (2005). Selective Oxidation of Semiconducting Single-Wall Carbon Nanotubes by Hydrogen Peroxide. *Journal of Physical Chemistry B*, *110*(1), 25–29. https://doi.org/10.1021/JP055692Y

MKS. (2021). *MASS FLOW TECHNOLOGY*. Retrieved from https://www.mksinst.com/mam/celum/celum_assets/mks/resources/MassFlowTechnology-TechNote.pdf?0

Moisala, A., Nasibulin, A. G., & Kauppinen, E. I. (2003). The role of metal nanoparticles in the catalytic

production of single-walled carbonnanotubes—a review. *Journal of Physics: Condensed Matter*, *15*(42), S3011. https://doi.org/10.1088/0953-8984/15/42/003

Moreno, H. A., Hussain, S., Amade, R., & Bertran, E. (2014). Growth and functionalization of CNTs on stainless steel electrodes for supercapacitor applications. *Materials Research Express*, *1*(3). https://doi.org/10.1088/2053-1591/1/3/035050

Mouawad, B., Soueidan, M., Fabregue, D., Buttay, C., Allard, B., Bley, V., … Fabrègue, D. (2012). Application of the Spark Plasma Sintering Technique to Low-Temperature Copper Bonding. *Institute of Electrical and Electronics Engineers*, (4), 553–560. https://doi.org/10.1109/TCPMT.2012.2186453ï

Msi-pse. (2021). How Sputtering Works. Retrieved November 8, 2021, from http://www.msi-pse.com/magnetron_sputtering.htm

National Academies of Sciences, E. and M. (2021). Plasma Science: Enabling Technology, Sustainability, Security, and Exploration. *Plasma Science*, 1–432. https://doi.org/10.17226/25802

Novoselov, K. S., Geim, A. K., Morozov, S. V., Jiang, D., Zhang, Y., Dubonos, S. V., … Firsov, A. A. (2004). Electric field effect in atomically thin carbon films. *Science (New York, N.Y.)*, *306*(5696), 666–669. https://doi.org/10.1126/SCIENCE.1102896

O'Hanlon, J. F. (2003). A User's Guide to Vacuum Technology. In *A User's Guide to Vacuum Technology*. https://doi.org/10.1002/0471467162

Odom, T. W., Huang, J. L., Kim, P., & Lieber, C. M. (1998). Atomic structure and electronic properties of single-walled carbon nanotubes. *Nature 1998 391:6662*, *391*(6662), 62–64. https://doi.org/10.1038/34145

Ohring, M. (2002). Front Matter. *Materials Science of Thin Films*, iii. https://doi.org/10.1016/b978-0-12-524975-1.50018-5

Olympus. (2020). Introduction to Confocal Microscopy. Retrieved September 10, 2021, from https://www.olympus-lifescience.com/en/microscope-resource/primer/techniques/confocal/confocalintro/

Osswald, S., Havel, M., & Gogotsi, Y. (2007). Monitoring oxidation of multiwalled carbon nanotubes by Raman spectroscopy. *Undefined*, *38*(6), 728–736. https://doi.org/10.1002/JRS.1686

Paillet, M., Parret, R., Sauvajol, J. L., & Colomban, P. (2018). Graphene and related 2D materials: An

overview of the Raman studies. *Journal of Raman Spectroscopy*, *49*(1), 8–12. https://doi.org/10.1002/JRS.5295

Palomar. (2021). The Importance of DC Self-Bias Voltage in Plasma Applications. Retrieved November 4, 2021, from https://www.palomartechnologies.com/blog/the-importance-of-dc-self-bias-voltage-in-plasma-applications

Pantoja-Suárez, F. (2019). Carbon nanotubes grown on stainless steel for supercapacitor applications.

Paradise, M., & Goswami, T. (2007). Carbon nanotubes – Production and industrial applications. *Materials & Design*, *28*(5), 1477–1489. https://doi.org/10.1016/J.MATDES.2006.03.008

Pardanaud, C., Martin, C., & Roubin, P. (2014). Multiwavelength Raman spectroscopy analysis of a large sampling of disordered carbons extracted from the Tore Supra tokamak. *Vibrational Spectroscopy*, *70*, 187–192. https://doi.org/10.1016/J.VIBSPEC.2013.12.004

Parkansky, N., Boxman, R. L., Alterkop, B., Zontag, I., Lereah, Y., & Barkay, Z. (2004). Single-pulse arc production of carbon nanotubes in ambient air. *Journal of Physics D: Applied Physics*, *37*(19), 2715. https://doi.org/10.1088/0022-3727/37/19/015

Payling, R., & Larkins, P. (2000). *Optical emission lines of the elements*. Wiley.

Pethe, A. (2021). *Probe sonicator*. Retrieved from https://www.slideshare.net/AnilPethe/probe-sonicator

Pimenta, M. A., Hanlon, E. B., Marucci, A., Corio, P., Brown, S. D. M., Empedocles, S. A., … Dresselhaus, M. S. (2000). The anomalous dispersion of the disorder-induced and the second-order Raman Bands in Carbon Nanotubes. *Brazilian Journal of Physics*, *30*(2), 423–427. https://doi.org/10.1590/S0103-97332000000200026

Pirard, S. L., Douven, S., & Pirard, J. P. (2017). Large-scale industrial manufacturing of carbon nanotubes in a continuous inclined mobile-bed rotating reactor via the catalytic chemical vapor deposition process. *Frontiers of Chemical Science and Engineering 2017 11:2*, *11*(2), 280–289. https://doi.org/10.1007/S11705-017-1635-1

PJ, P., MC, B., MJ, M., & M, D. G. (2011). Diffraction contrast STEM of dislocations: imaging and simulations. *Ultramicroscopy*, *111*(9–10), 1483–1487. https://doi.org/10.1016/J.ULTRAMIC.2011.07.001

Prasek, J., Drbohlavova, J., Chomoucka, J., Hubalek, J., Jasek, O., Adam, V., & Kizek, R. (2011). Methods for

carbon nanotubes synthesis—review. *Journal of Materials Chemistry*, *21*(40), 15872–15884. https://doi.org/10.1039/C1JM12254A

Pu, S., Gong, C., & Robertson, A. W. (2020). Liquid cell transmission electron microscopy and its applications. *Royal Society Open Science*, *7*(1). https://doi.org/10.1098/rsos.191204

Rahmayeni, Alfina, A., Stiadi, Y., Lee, H. J., & Zulhadjri. (2019). Green synthesis and Characterization of ZnO-$CoFe_2O_4$ Semiconductor Photocatalysts Prepared Using Rambutan (*Nephelium lappaceum* L.) Peel Extract. *Materials Research*, *22*(5). https://doi.org/10.1590/1980-5373-MR-2019-0228

Ram, S., Ward, E. S., & Ober, R. J. (2006). Beyond Rayleigh's criterion: A resolution measure with application to single-molecule microscopy. *Proceedings of the National Academy of Sciences of the United States of America*, *103*(12), 4457–4462. https://doi.org/10.1073/pnas.0508047103

Ramić, B. D., Stojanac, I. L., Drobac, M. R., Kantardžić, I. R., Maletin, A. Z., Cvjetićanin, M. T., … Petrović, L. M. (2021). Application of Scanning Electron Microscopy in the observation of dentin-adhesive interface. *Microscopy Research and Technique*, *84*(4), 602–607. https://doi.org/10.1002/jemt.23618

Rangan, S., Schulze, H. G., Vardaki, M. Z., Blades, M. W., Piret, J. M., & Turner, R. F. B. (2020). Applications of Raman spectroscopy in the development of cell therapies: state of the art and future perspectives. *Analyst*, *145*(6), 2070–2105. https://doi.org/10.1039/C9AN01811E

Rao, C. N. R., & Govindaraj, A. (2011). *Nanotubes and Nanowires*. https://doi.org/10.1039/9781849732840

Ravula, S., Baker, S. N., Kamath, G., & Baker, G. A. (2015). Ionic liquid-assisted exfoliation and dispersion: stripping graphene and its two-dimensional layered inorganic counterparts of their inhibitions. *Nanoscale*, *7*(10), 4338–4353. https://doi.org/10.1039/C4NR01524J

Rawat, P. S., Srivastava, R. C., Dixit, G., & Asokan, K. (2020). Structural, functional and magnetic ordering modifications in graphene oxide and graphite by 100 MeV gold ion irradiation. *Vacuum*, *182*, 109700. https://doi.org/10.1016/J.VACUUM.2020.109700

Reilly, W. M., & Obara, C. J. (2021). Advances in Confocal Microscopy and Selected Applications. *Methods in Molecular Biology*, *2304*, 1–35. https://doi.org/10.1007/978-1-0716-1402-0_1

Reimer, L., & Kohl, H. (2008). *Transmission Electron Microscopy - Physics of Image Formation | Ludwig Reimer | Springer*. Retrieved from https://www.springer.com/gp/book/9780387400938

Rinolfi, L. (2016). *Technology & Applications of Particle Accelerators*. Retrieved from https://indico.cern.ch/event/471931/contributions/1149828/attachments/1228618/1799927/Presentat_JUAS_2016_course_2.pdf

Robertson, J. (2002). Diamond-like amorphous carbon. *Materials Science and Engineering: R: Reports*, *37*(4–6), 129–281. https://doi.org/10.1016/S0927-796X(02)00005-0

Robertson, J. (2006). Amorphous carbon. *Http://Dx.Doi.Org/10.1080/00018738600101911*, *35*(4), 317–374. https://doi.org/10.1080/00018738600101911

Rosen, A. L., & Hieftje, G. M. (2004). Inductively coupled plasma mass spectrometry and electrospray mass spectrometry for speciation analysis: applications and instrumentation. *Spectrochimica Acta Part B: Atomic Spectroscopy*, *59*(2), 135–146. https://doi.org/10.1016/J.SAB.2003.09.004

Rosenauer, A., Krause, F. F., Müller, K., Schowalter, M., & Mehrtens, T. (2014). Conventional Transmission Electron Microscopy Imaging beyond the Diffraction and Information Limits. *Physical Review Letters*, *113*(9), 096101. https://doi.org/10.1103/PhysRevLett.113.096101

Rosenberg, E., & Weis, M. (1983). *Chapter 5 Introduction to Electron Microscopy*. 59–66.

Roth, J. (1983). *Chemical sputtering*. https://doi.org/10.1007/3-540-12593-0_3

Roy, D., Kanojia, S., Mukhopadhyay, K., & Eswara Prasad, N. (2021). Analysis of carbon-based nanomaterials using Raman spectroscopy: principles and case studies. *Bulletin of Materials Science*, *44*(1), 1–9. https://doi.org/10.1007/s12034-020-02327-9

Roychaudhuri, R., Acharyya, D., & Bhattacharyya, P. (2018). Morphological evolution of MnO2 based nanostructures by tuning the reaction time. *2018 International Symposium on Devices, Circuits and Systems, ISDCS 2018*, *4*, 1–4. https://doi.org/10.1109/ISDCS.2018.8379628

Ruelle, B. (2010). *Functionalization of carbon nanotubes via plasma post-discharge surface treatment: Implication as nanofiller in polymeric matrices*. Retrieved from https://www.yumpu.com/en/document/view/21863636/functionalization-of-carbon-nanotubes-via-plasma-post-discharge-

Ruess, G., & Vogt, F. (1948). Höchstlamellarer Kohlenstoff aus Graphitoxyhydroxyd. *Monatshefte Für Chemie Und Verwandte Teile Anderer Wissenschaften 1998 78:3*, *78*(3), 222–242. https://doi.org/10.1007/BF01141527

Rümmeli, M. H., Schäffel, F., Kramberger, C., Gemming, T., Bachmatiuk, A., Kalenczuk, R. J., … Pichler, T. (2007). Oxide-Driven Carbon Nanotube Growth in Supported Catalyst CVD. *Journal of the American Chemical Society*, *129*(51), 15772–15773. https://doi.org/10.1021/JA0779405

Sadezky, A., Muckenhuber, H., Grothe, H., Niessner, R., & Pöschl, U. (2005). Raman microspectroscopy of soot and related carbonaceous materials: Spectral analysis and structural information. *Carbon*, *43*(8), 1731–1742. https://doi.org/10.1016/J.CARBON.2005.02.018

Sagar, K. V., Goutam, B., Chandra, K. V., & Chary, S. N. (2021). Analysis of double walled carbon nanotube structured badminton racket. *AIP Conference Proceedings*, *2327*. https://doi.org/10.1063/5.0039426

Saito, R., Dresselhaus, G., & Dresselhaus, M. S. (1998). Physical Properties of Carbon Nanotubes R. Saito;G. Dresselhaus;M. S. Dresselhaus: Amazon.es: Libros. Retrieved December 15, 2021, from https://www.amazon.es/Physical-Properties-Carbon-Nanotubes-1998-07-23/dp/B01K0RHU14

Saito, R., Hofmann, M., Dresselhaus, G., Jorio, A., & Dresselhaus, M. S. (2011). Raman spectroscopy of graphene and carbon nanotubes. *Advances in Physics*, *60*(3), 413–550. https://doi.org/10.1080/00018732.2011.582251

Sanchez-Valencia, J. R., Dienel, T., Gröning, O., Shorubalko, I., Mueller, A., Jansen, M., … Fasel, R. (2014). Controlled synthesis of single-chirality carbon nanotubes. *Nature 2014 512:7512*, *512*(7512), 61–64. https://doi.org/10.1038/nature13607

Sant'Anna, C., Campanati, L., Gadelha, C., Lourenço, D., Labati-Terra, L., Bittencourt-Silvestre, J., … De Souza, W. (2005). Improvement on the visualization of cytoskeletal structures of protozoan parasites using high-resolution field emission scanning electron microscopy (FESEM). *Histochemistry and Cell Biology*, *124*(1), 87–95. https://doi.org/10.1007/s00418-005-0786-1

Sasaki, T., Sawada, H., Hosokawa, F., Kohno, Y., Tomita, T., Kaneyama, T., … Suenaga, K. (2010). Performance of low-voltage STEM/TEM with delta corrector and cold field emission gun. *Journal of Electron Microscopy*, *59*(S1), S7–S13. https://doi.org/10.1093/JMICRO/DFQ027

Sato, M., Ohgiyama, T., & Clements, J. S. (1996). Formation of chemical species and their effects on microorganisms using a pulsed high-voltage discharge in water. *IEEE Transactions on Industry Applications*, *32*(1), 106–112. https://doi.org/10.1109/28.485820

Savvides, N., & Window, B. (1998). Unbalanced magnetron ion-assisted deposition and property modification of thin films. *Journal of Vacuum Science & Technology A: Vacuum, Surfaces, and Films*, *4*(3), 504. https://doi.org/10.1116/1.573869

Schneider, R. (2011). Energy-Dispersive X-Ray Spectroscopy (EDXS). *Surface and Thin Film Analysis: A Compendium of Principles, Instrumentation, and Applications, Second Edition*, 293–310. https://doi.org/10.1002/9783527636921.ch18

Seah, M. P. (2012a). An accurate and simple universal curve for the energy-dependent electron inelastic mean free path. *Surface and Interface Analysis*, *44*(4), 497–503. https://doi.org/10.1002/SIA.4816

Seah, M. P. (2012b). Simple universal curve for the energy-dependent electron attenuation length for all materials. *Surface and Interface Analysis*, *44*(10), 1353–1359. https://doi.org/10.1002/SIA.5033

Sens. (2021). What is the working principle of the Pirani gauge? Retrieved November 3, 2021, from https://sens4.com/pirani-working-principle.html

Shahil, K. M. F., & Balandin, A. A. (2012). Thermal properties of graphene and multilayer graphene: Applications in thermal interface materials. *Solid State Communications*, *152*, 1331–1340. https://doi.org/10.1016/j.ssc.2012.04.034

Shard, A. G. (2020). X-ray photoelectron spectroscopy. In *Characterization of Nanoparticles: Measurement Processes for Nanoparticles*. https://doi.org/10.1016/B978-0-12-814182-3.00019-5

Shishkovsky, I. V., & Lebedev, P. N. (2011). Chemical and physical vapor deposition methods for nanocoatings. *Nanocoatings and Ultra-Thin Films*, 57–77. https://doi.org/10.1533/9780857094902.1.57

Smoluch, M., Mielczarek, P., & Silberring, J. (2016). Plasma-based ambient ionization mass spectrometry in bioanalytical sciences. *Mass Spectrometry Reviews*, *35*(1), 22–34. https://doi.org/10.1002/MAS.21460

Spence, J. C. H. (2017). *High-resolution electron microscopy* (Fourth edi). Oxford Scholarship Online.

Srivastava, S. K., Vankar, V. D., & Kumar, V. (2006). Growth and microstructures of carbon nanotube films prepared by microwave plasma enhanced chemical vapor deposition process. *Thin Solid Films*, *515*(4), 1552–1560. https://doi.org/10.1016/J.TSF.2006.05.009

St Croix, C. M., Shand, S. H., & Watkins, S. C. (2005). Confocal microscopy: comparisons, applications, and

problems. *BioTechniques*, *39*(6 Suppl). https://doi.org/10.2144/000112089

Stankovich, S., Dikin, D. A., Dommett, G. H. B., Kohlhaas, K. M., Zimney, E. J., Stach, E. A., … Ruoff, R. S. (2006). Graphene-based composite materials. *Nature 2006 442:7100*, *442*(7100), 282–286. https://doi.org/10.1038/nature04969

Stillahn, J. M., Trevino, K. J., & Fisher, E. R. (2008). Plasma Diagnostics for Unraveling Process Chemistry. *Http://Dx.Doi.Org/10.1146/Annurev.Anchem.1.031207.112953*, *1*(1), 261–291. https://doi.org/10.1146/ANNUREV.ANCHEM.1.031207.112953

Stopar, K., Drobne, D., Eler, K., & Bartol, T. (2016). Citation analysis and mapping of nanoscience and nanotechnology: identifying the scope and interdisciplinarity of research. *Scientometrics*, *106*(1), 563–581. https://doi.org/10.1007/s11192-015-1797-x

Suga, S., & Sekiyama, A. (2021). *Photoelectron spectroscopy : bulk and surface electronic structures* (2nd ed., Vol. 176). Springer Series in Optical Sciences.

Sullivan, J. P., Robertson, J., Zhou, O., Allen, T. B., & Coll, B. F. (2000). Amorphous and Nanostructured Carbon. *Materials Research Society Symposium Proceedings*, *593*. Retrieved from www.cambridge.org

Sun, Y. P., Fu, K., Lin, Y., & Huang, W. (2002). Functionalized Carbon Nanotubes: Properties and Applications. *Accounts of Chemical Research*, *35*(12), 1096–1104. https://doi.org/10.1021/AR010160V

Šunka, P., Babický, V., Člupek, M., Lukeš, P., Šimek, M., Schmidt, J., & Černák, M. (1999). Generation of chemically active species by electricaldischarges in water. *Plasma Sources Science and Technology*, *8*(2), 258. https://doi.org/10.1088/0963-0252/8/2/006

Szybowicz, M., Nowicka, A. B., & Dychalska, A. (2018). Characterization of carbon nanomaterials by raman spectroscopy. In *Characterization of Nanomaterials: Advances and Key Technologies*. https://doi.org/10.1016/B978-0-08-101973-3.00001-8

T. H. MartinA, H. Guenther, & M. Kristiansen. (1996). J. C. Martin on Pulsed Power. In *J. C. Martin on Pulsed Power*. https://doi.org/10.1007/978-1-4899-1561-0

Tafwidli, F., & Kang, Y. B. (2017). Thermodynamic modeling of Fe-C-S ternary system. *ISIJ International*, *57*(5), 782–790. https://doi.org/10.2355/ISIJINTERNATIONAL.ISIJINT-2016-672

Tan, P., An, L., Liu, L., Guo, Z., Czerw, R., Carroll, D. L., … Guo, H. (2002). Probing the phonon dispersion relations of graphite from the double-resonance process of Stokes and anti-Stokes Raman scatterings in multiwalled carbon nanotubes. *Physical Review B*, *66*(24), 245410. https://doi.org/10.1103/PhysRevB.66.245410

Tessonnier, J. P., & Su, D. S. (2011). Recent Progress on the Growth Mechanism of Carbon Nanotubes: A Review. *ChemSusChem*, *4*(7), 824–847. https://doi.org/10.1002/CSSC.201100175

Thostenson, E. T., Ren, Z., & Chou, T. W. (2001). Advances in the science and technology of carbon nanotubes and their composites: a review. *Composites Science and Technology*, *61*(13), 1899–1912. https://doi.org/10.1016/S0266-3538(01)00094-X

Toncu, D. C. (2016). Optical Emission Spectroscopy Investigation of Direct Current Micro-plasma for Carbon Structures Growth. *Advanced Surface Engineering Materials*, 495–515. https://doi.org/10.1002/9781119314196.ch11

Touati, K. A., Chenini, K., & Meftah, M. T. (2020). Stark-zeeman broadening of spectral line shapes in magnetized plasmas. *Atoms*, *8*(4), 1–9. https://doi.org/10.3390/atoms8040091

Tougaard, S. (2019). Surface analysis | X-ray Photoelectron Spectroscopy. In *Encyclopedia of Analytical Science*. https://doi.org/10.1016/B978-0-12-409547-2.00527-8

Tran, T. Q., Headrick, R. J., Bengio, E. A., Myo Myint, S., Khoshnevis, H., Jamali, V., … Pasquali, M. (2017). Purification and Dissolution of Carbon Nanotube Fibers Spun from the Floating Catalyst Method. *ACS Applied Materials and Interfaces*, *9*(42), 37112–37119. https://doi.org/10.1021/ACSAMI.7B09287

Treacy, M. M. J., Ebbesen, T. W., & Gibson, J. M. (1996). Exceptionally high Young's modulus observed for individual carbon nanotubes. *Nature 1996 381:6584*, *381*(6584), 678–680. https://doi.org/10.1038/381678a0

Ulloa, E. (2013). *[PDF] Fullerenes and their Applications in Science and Technology* . Retrieved from https://nanopdf.com/download/fullerenes-and-their-applications-in-science-and-technology_pdf

Varshney, D., Weiner, B. R., & Morell, G. (2010). Growth and field emission study of a monolithic carbon nanotube/diamond composite. *Carbon*, *48*(12), 3353–3358. https://doi.org/10.1016/J.CARBON.2010.05.025

Vashishtha, N., & Sapate, S. (2018). Effect of Experimental Parameters on Wear Response of Thermally

Sprayed Carbide Based Coatings. *Materials Research*, *22*(1), 20180475. https://doi.org/10.1590/1980-5373-MR-2018-0475

Vempati, R. K., Hess, T. R., & Cocke, D. L. (1996). *Chapter 12 X-Ray Photoelectron Spectroscopy*. (5), 357–375.

Venezuela, P., Lazzeri, M., & Mauri, F. (2011). Theory of double-resonant Raman spectra in graphene: Intensity and line shape of defect-induced and two-phonon bands. *Physical Review B - Condensed Matter and Materials Physics*, *84*(3), 035433. https://doi.org/10.1103/PHYSREVB.84.035433/FIGURES/29/MEDIUM

Vernon-Parry, K. D. (2000). Scanning Electron Microscopy : An introduction. *Analysis*, *13*(4), 40–44.

Vigolo, B., Vincent, B., Eschbach, J., Bourson, P., Marêché, J.-F., McRae, E., … Rouxel, D. (2009). Multiscale Characterization of Single-Walled Carbon Nanotube/Polymer Composites by Coupling Raman and Brillouin Spectroscopy. *Journal of Physical Chemistry C*, *113*(41), 17648–17654. https://doi.org/10.1021/JP903960F

Vilatela, J. J., & Windle, A. H. (2012). A Multifunctional yarn made of carbon nanotubes. *Journal of Engineered Fibers and Fabrics*, *7*(3), 23–28. https://doi.org/10.1177/155892501200702S04

Vizireanu, S., Stoica, S. D., Luculescu, C., Nistor, L. C., Mitu, B., & Dinescu, G. (2010). Plasma techniques for nanostructured carbon materials synthesis. A case study: carbon nanowall growth by low pressure expanding RF plasma. *Plasma Sources Science and Technology*, *19*(3). https://doi.org/10.1088/0963-0252/19/3/034016

Voiry, D., Shin, H. S., Loh, K. P., & Chhowalla, M. (2018). Low-dimensional catalysts for hydrogen evolution and CO2 reduction. *Nature Reviews Chemistry 2018 2:1*, *2*(1), 1–17. https://doi.org/10.1038/s41570-017-0105

Vorburger, T. V., Song, J., Petraco, N., & Lilien, R. (2019). Emerging technology in comparisons. In *Forensic Firearm Examination*. https://doi.org/10.1016/b978-0-12-814539-5.00015-0

Voutou, B., & Stefanaki, E. (2008). *Electron Microscopy: The basics*.

Waits, R. K. (1998). Planar magnetron sputtering. *Journal of Vacuum Science and Technology*, *15*(2), 179. https://doi.org/10.1116/1.569451

Walkup, R. E., Saenger, K. L., & Selwyn, G. S. (1998). Studies of atomic oxygen in O2+CF4 rf discharges by

two-photon laser-induced fluorescence and optical emission spectroscopy. *The Journal of Chemical Physics*, *84*(5), 2668. https://doi.org/10.1063/1.450339

Wang, J. N., Luo, X. G., Wu, T., & Chen, Y. (2014). High-strength carbon nanotube fibre-like ribbon with high ductility and high electrical conductivity. *Nature Communications 2014 5:1*, *5*(1), 1–8. https://doi.org/10.1038/ncomms4848

Wang, Y. (2012). *MANGANESE DIOXIDE BASED COMPOSITE ELECTRODES FOR ELECTROCHEMICAL SUPERCAPACITORS*.

Wasa, K., & Hayakawa, S. (2003). Low Pressure Sputtering System of the Magnetron Type. *Review of Scientific Instruments*, *40*(5), 693. https://doi.org/10.1063/1.1684039

Webb, M. R., & Hieftje, G. M. (2009). Spectrochemical Analysis by Using Discharge Devices with Solution Electrodes. *Analytical Chemistry*, *81*(3), 862–867. https://doi.org/10.1021/AC801561T

Weller, L., Smail, F. R., Elliott, J. A., Windle, A. H., Boies, A. M., & Hochgreb, S. (2019). Mapping the parameter space for direct-spun carbon nanotube aerogels. *Carbon*, *146*, 789–812. https://doi.org/10.1016/j.carbon.2019.01.091

Wen, J. M., Evans, J. W., Bartelt, M. C., Burnett, J. W., & Thiel, P. A. (1996). Coarsening Mechanisms in a Metal Film: From Cluster Diffusion to Vacancy Ripening. *Physical Review Letters*, *76*(4), 652. https://doi.org/10.1103/PhysRevLett.76.652

Weston, G. F. (1985). Ultrahigh Vacuum Practice. In *Ultahigh Vac Pract*. https://doi.org/10.1049/ep.1986.0046

Westwood, W. D. (2018). Reactive Sputtering: Introduction and General Discussion. In *Handbook of Thin Film Process Technology* (p. A5.0:1-A5.1:10). https://doi.org/10.1201/9781351072786-2

Window, B., & Savvides, N. (1998). Charged particle fluxes from planar magnetron sputtering sources. *Journal of Vacuum Science & Technology A: Vacuum, Surfaces, and Films*, *4*(2), 196. https://doi.org/10.1116/1.573470

Wu, A., Li, X., Yang, J., Du, C., Shen, W., & Yan, J. (2017). Upcycling Waste Lard Oil into Vertical Graphene Sheets by Inductively Coupled Plasma Assisted Chemical Vapor Deposition. *Nanomaterials 2017, Vol. 7, Page 318*, *7*(10), 318. https://doi.org/10.3390/NANO7100318

Wu, Y., Yang, B., Zong, B., Sun, H., Shen, Z., & Feng, Y. (2004). Carbon nanowalls and related materials.

Journal of Materials Chemistry, *14*(4), 469–477. https://doi.org/10.1039/B311682D

Xu, B., Kaneko, T., Shibuta, Y., & Kato, T. (2017). Preferential synthesis of (6,4) single-walled carbon nanotubes by controlling oxidation degree of Co catalyst. *Scientific Reports*, *7*(1). https://doi.org/10.1038/S41598-017-11712-0

Xu, Y., Dervishi, E., Biris, A. R., & Biris, A. S. (2011). Chirality-enriched semiconducting carbon nanotubes synthesized on high surface area MgO-supported catalyst. *Materials Letters*, *12*(65), 1878–1881. https://doi.org/10.1016/J.MATLET.2011.03.040

Yadav, M. D., Dasgupta, K., Patwardhan, A. W., & Joshi, J. B. (2017). High Performance Fibers from Carbon Nanotubes: Synthesis, Characterization, and Applications in Composites—A Review. *Industrial and Engineering Chemistry Research*, *56*(44), 12407–12437. https://doi.org/10.1021/ACS.IECR.7B02269

Yadav, M. D., Patwardhan, A. W., Joshi, J. B., & Dasgupta, K. (2019a). Kinetic study of multi-walled carbon nanotube synthesis by thermocatalytic decomposition of methane using floating catalyst chemical vapour deposition. *Chemical Engineering Journal*, *377*, 119895. https://doi.org/10.1016/J.CEJ.2018.09.056

Yadav, M. D., Patwardhan, A. W., Joshi, J. B., & Dasgupta, K. (2019b). Selective synthesis of metallic and semi-conducting single-walled carbon nanotube by floating catalyst chemical vapour deposition. *Diamond and Related Materials*, *97*(January), 107432. https://doi.org/10.1016/j.diamond.2019.05.017

Yang, D., & Ionescu, M. I. (2017). Metal Oxide–Carbon Hybrid Materials for Application in Supercapacitors. *Metal Oxides in Supercapacitors*, 193–218. https://doi.org/10.1016/B978-0-12-810464-4.00008-5

Yang, F., Wang, X., Zhang, D., Qi, K., Yang, J., Xu, Z., … Li, Y. (2015). Growing Zigzag (16,0) Carbon Nanotubes with Structure-Defined Catalysts. *Journal of the American Chemical Society*, *137*(27), 8688–8691. https://doi.org/10.1021/JACS.5B04403/SUPPL_FILE/JA5B04403_SI_001.PDF

Yang, J., Esconjauregui, S., Sugime, H., Makaryan, T., Hallam, T., Duesberg, G. S., & Robertson, J. (2014). Comparison of carbon nanotube forest growth using AlSi, TiSiN, and TiN as conductive catalyst supports. *Physica Status Solidi (B) Basic Research*, *251*(12), 2389–2393. https://doi.org/10.1002/PSSB.201451162

Yang, N., Yang, D., Zhang, G., Chen, L., Liu, D., Cai, M., & Fan, X. (2018). The Effects of Graphene Stacking

on the Performance of Methane Sensor: A First-Principles Study on the Adsorption, Band Gap and Doping of Graphene. *Sensors 2018, Vol. 18, Page 422*, *18*(2), 422. https://doi.org/10.3390/S18020422

Yu, A., Chabot, V., & Zhang, J. (2013). *electrochemical double-layer capacitors for energy storage and conversion*.

Yu, L., Shearer, C., & Shapter, J. (2016). Recent Development of Carbon Nanotube Transparent Conductive Films. *Chemical Reviews*, *116*(22), 13413–13453. https://doi.org/10.1021/ACS.CHEMREV.6B00179

Yu, M. F., Kowalewski, T., & Ruoff, R. S. (2000). Investigation of the Radial Deformability of Individual Carbon Nanotubes under Controlled Indentation Force. *Physical Review Letters*, *85*(7), 1456. https://doi.org/10.1103/PhysRevLett.85.1456

Yu, Y., Cui, C., Qian, W., Xie, Q., Zheng, C., Kong, C., & Wei, F. (2013). Carbon nanotube production and application in energy storage. *Asia-Pacific Journal of Chemical Engineering*, *8*(2), 234–245. https://doi.org/10.1002/APJ.1701

Yuan, X.-Z. (Riny), Song, C., Wang, H., & Zhang, J. (2010). *Electrochemical Impedance Spectroscopy in PEM Fuel Cells Fundamentals and Applications*.

Zhao, Q., Xu, Z., Hu, Y., Ding, F., & Zhang, J. (2016). Chemical vapor deposition synthesis of near-zigzag single-walled carbon nanotubes with stable tube-catalyst interface. *Science Advances*, *2*(5). https://doi.org/10.1126/SCIADV.1501729

Zheng, J. P., Huang, J., & Jow, T. R. . (1997). The Limitations of Energy Density for Electrochemical Capacitors. *J. Electrochem. Soc.*, *144*(6), 2026–2031. https://doi.org/10.1149/1.1837738

Zheng, M., & Diner, B. A. (2004). Solution Redox Chemistry of Carbon Nanotubes. *Journal of the American Chemical Society*, *126*(47), 15490–15494. https://doi.org/10.1021/JA0457967

Zheng, M., Jagota, A., Semke, E. D., Diner, B. A., McLean, R. S., Lustig, S. R., … Tassi, N. G. (2003). DNA-assisted dispersion and separation of carbon nanotubes. *Nature Materials 2003 2:5*, *2*(5), 338–342. https://doi.org/10.1038/nmat877

Zhou, W., Apkarian, R., Wang, Z. L., & Joy, D. (2007). Fundamentals of scanning electron microscopy (SEM). In *Scanning Microscopy for Nanotechnology: Techniques and Applications* (pp. 1–40). https://doi.org/10.1007/978-0-387-39620-0_1

Zoican Loebick, C., Podila, R., Reppert, J., Chudow, J., Ren, F., Haller, G. L., … Pfefferle, L. D. (2010). Selective synthesis of subnanometer diameter semiconducting single-walled carbon nanotubes. *Journal of the American Chemical Society*, *132*(32), 11125–11131. https://doi.org/10.1021/JA102011H/SUPPL_FILE/JA102011H_SI_001.PDF

Trajectory of the author

EDUCATION

2014-2016	**Master of Nanoscience and Nanotechnology** Master Thesis: Optimization of Carbon nanotubes for Supercapacitor Applications	Universitat de Barcelona
2009-2013	**Bachelor of Physics** Graduation Project: Fabrication of Dye Sensitized solar cells using natural dyes.	The Islamic University of Gaza

WORK EXPERIENCE

Sep. 2017 - Feb. 2020	**Teaching Assistant** Laboratories of electromagnetism and nanoscience subjects for bachelor and master students.	Universitat de Barcelona
Sep. 2013 – Aug. 2014	**Teaching Assistant** Discussion classes on physics courses and laboratories of general physics for the bachelor students	The Islamic University of Gaza

PREVIOUS STAYS IN RESEARCH CENTERS

Research institute	Department of Applied Physics, Faculty of Physics, FEMAN Group, Institute of Nanoscience and Nanotechnology, Universitat de Barcelona.
Location	Barcelona, Spain
Year	2015
Duration	6 months
Research line	Supercapacitors and carbon based materials

Research institute	Nanotechnology and Integrated Bioengineering Center (NNIBEC), Mariotti Research Group, Ulster University.
Location	Northern Ireland, United Kingdom
Year	2019
Duration	3 months
Research line	Carbon and metal oxide materials for supercapacitors

MATERIAL PRODUCTION TECHNIQUES

Technique	Chemical vapor deposition (CVD) and its related processes: PECVD, WACVD, FC-CVD, and ICP-CVD.
Technique	Magnetron sputtering physical vapor deposition (PVD).
CNTs reactor	A reactor prepared for high vacuum processes and provided with RF. Available for plasma treatments, PECVD, and RF-sputtering
GNWs reactor	A reactor prepared for vacuum processes using inductively coupled plasma (ICP).
Thin films reactor	A reactor used for thin films RF- and pulsed DC-sputtering for thin films deposition.
Plasma-Liquid interaction	A set-up for oxide nanoparticles synthesis.

CHARACTERIZATION TECHNIQUES

Scanning electron microscopy (SEM), transmission electron spectroscopy (TEM), energy-dispersive X-ray spectroscopy (EDX), atomic force microscopy (AFM), Raman Spectroscopy, X-ray photoelectron spectroscopy (XPS), and Profilometer.

PUBLICATIONS IN JOURNALS (https://orcid.org/0000-0001-7333-1503)

Authors	Roger Amade, **Islam Alshaikh**, Arevik Mucheghyan-Avetisyan and Enric Bertran-Serra
Title	Enhanced capacitance of manganese oxide driven by hierarchically structured carbon nanotube-carbon nanowall composite.
Journal	Surface and Coatings Technology
DOI	https://doi.org/10.1016/j.surfcoat.2021.127885
Year	2021

Authors	Hussain S., Amade R., Boyd A., Musheghyan-Avetisyan A., **Alshaikh I.**, Martí -Gonzalez J., Pascual E., Meenan B. J. and Bertran-Serra E.
Title	Three-dimensional Si/vertically oriented graphene nanowalls composite for supercapacitor applications.
Journal	Ceramic International
DOI	10.1016/j.ceramint.2021.04.190
Year	2020

Authors Yu P., Coll M., Amade R., **Alshaikh I.**, Pantoja-Suárez F., Pascual E., Andújar J. L. and Serra E. B.
Title Homogeneous Fe_2O_3 coatings on carbon nanotube structures for supercapacitors.
Journal Dalton Transactions
DOI 10.1039/c9dt04908h
Year 2020

Authors Albert Queraltó, Ángel Pérez del Pino, Constantin Logofatu , Angela Datcu , Roger Amade, **Islam Alshaikh**, Enric Bertran, Iuliana Urzica and Eniko Gyorgy.
Title MAPLE synthesis of reduced graphene oxide/silver nanocomposite electrodes: Influence of target composition and gas ambience
Journal Journal of Alloys and Compounds
DOI https://doi.org/10.1016/j.jallcom.2017.08.052
Year 2017

Authors A Pérez del Pino, E György, **I Alshaikh**, F Pantoja-Suárez, J L Andújar, E Pascual, R Amade and E Bertran-Serra.
Title Laser-driven coating of vertically aligned carbon nanotubes with manganese oxide from metal organic precursors for energy storage.
Journal Nanotechnology
DOI https://doi.org/10.1088/1361-6528/aa81b1
Year 2017

Authors Sofyan A. Taya , Taher M. El-Agez1, Monzir S. Abdel-Latif, Hatem S. El-Ghamri, Amal Y. Batniji and **Islam R. El-Sheikh**.
Title Fabrication of Dye-Sensitized Solar Cells Using Dried Plant Leaves
Journal International Journal of Renewable Energy
Year 2014

PUBLICATIONS IN CONFERENCES AND CONGRESSES

Authors **I. Alshaikh**, R. Amade-Rovira and E. Bertran-Serra.
Title Direct Growth of Carbon Nanotubes on Stainless Steel by Plasma Enhanced Chemical Vapour Deposition.
Participation Poster
Conference IN2UB annual meeting
Place Barcelona-Telematic
Date October 2021

Authors **Islam Alshaikh**, Roger Amade-Rovira and Enric Bertran-Serra.
Title Specific Capacitance Enhancement of MnO_2 on Graphene-Carbon Nanotubes hybrid structure on Stainless Steel Electrodes.
Participation Poster
Conference Graphene Week
Place Telematic
Date September 2021

Authors **Islam Alshaikh**, Ruairi McGlynn, Paul Brunet, Roger Amade Rovira, Enric Bertran-Serra, and Davide Mariotti.

Title Synthesis of Carbon Nanotubes at Atmospheric Pressure for Supercapacitor Applications.
Participation Poster
Conference Nanospain 2020
Place Telematic
Date September 2020

Authors **Islam Alshaikh**, Roger Amade, Fernando Pantoja-Suárez and Enric Bertran-Serra.
Title Vertically Aligned Carbon Nanotubes grown on Graphite Paper Electrodes for Highly Flexible Supercapacitors.
Participation Oral presentation
Conference Nanospain 2019
Place Barcelona, Spain
Date May 2019

Authors Fernando Pantoja-Suárez, **Islam Alshaikh**, Joan Martí- González, Arevik Musheghyan Avetisyan, Roger Amade, José Luis Andujar, Esther Pascual and Enric Bertran-Serra
Title Carbon-based materials growth process effect on 304 stainless steel substrates
Participation Poster
Conference Nanospain 2019
Place Barcelona, Spain
Date May 2019

Authors Arevik Musheghyan-Avetisyan, R. Amade, J. Marti-González, J-L. Andújar, E. Pascual,F. Pantoja, **I. Alshaikh** and E. Bertran-Serra
Title Bottom up mechanism that describes the graphene nanowalls synthesis by inductively coupled plasma chemical vapor deposition
Participation Oral presentation
Conference Applied Nanotechnology and nanoscience international conference 2018
Place Berlin, Germany
Date Octuber 2018

Authors	Arevik Musheghyan-Avetisyan, J. Marti-Gonzalez, F. Pantoja, **I. Alshaikh**, S. Hussain, R. Amade, J-L. Andújar, E. Pascual and E. Bertran-Serra
Title	Study of the morphology effect of carbon nanostructures on the electrochemical performance of EDLC
Participation	Poster
Conference	Surface functionalisation of materials for high added value applications 2018
Place	Barcelona, Spain
Date	2018

Authors	Amade R., Musheghyan-Avetisyan A., Martí-González J, Pantoja-Suárez F., **Alshaikh I**, Hussain S., Andújar J.L., Pascual E., Bertran E., Pérez del Pino A. and György E.
Title	Growth and electrochemical characterization of graphene nanowalls and carbon nanotubes
Participation	Poster
Conference	Advanced Materials 2018
Place	Zürich, Switzerland
Date	September 2018

Authors	J. Marti-Gonzalez, F. Pantoja, A. Musheghyan-Avetisyan, **I. Alshaikh**, R. Amade, J.L. Andújar, E. Pascual and E. Bertran-Serra
Title	Synthesis and characterization of graphene nanowalls / carbon nanotubes hybrid nanostructures
Participation	Poster
Conference	TNT2018
Place	Lecce, Italy
Date	September 2018

Authors	Pantoja-Suárez, F.; **Alshaikh, I.**; Amade, R.; Andújar, J.L.; Pascual, E. and Bertran-Serra, E.
Title	Surface analysis of gradient stainless steel buffer layer to support aluminum nitride diffusion barrier for carbon nanotubes growth.
Participation	Poster
Conference	Trends in Nanotechnology International Conference (TNT2017)
Place	Dresden, Germany
Date	June 2017

Authors	Arevik Musheghyan-Avetisyan, R. Amade, J. Marti-González, J-L. Andújar, E. Pascual,F. Pantoja, **I. Alshaikh** and E. Bertran-Serra.
Title	Direct growth of vertically oriented graphene nanowalls on multiple substrates by Low Temperature Plasma-Enhanced Chemical Vapor Deposition
Participation	Oral presentation
Conference	Trends in Nanotechnology International Conference (TNT2017)
Place	Dresden, Germany
Date	June 2017

Authors Pantoja-Suárez, F.; **Alshaikh, I.**; Amade, R.; Andújar, J.L.; Pascual, E. and Bertran-Serra, E.
Title Gradient stainless steel buffer layer to support aluminium nitride diffusion barrier for carbon nanotubes growth.
Participation Poster
Conference 26th International Conference on Metallurgy and Materials (Metal 2017)
Place Brno, Czech Republic
Date May 2017

Authors Arevik Musheghyan-Avetisyan, R. Amade, J. Marti-González, J-L. Andújar, E. Pascual, F. Pantoja, **I. Alshaikh** and E. Bertran-Serra
Title Direct growth of vertically oriented graphene nanowalls on multiple substrates by Low Temperature Plasma-Enhanced Chemical Vapor Deposition
Participation Oral presentation
Conference European Graphene Forum-EGF2017; Smart Material and Surfaces-SMS EUROPE
Place Paris, France
Date April 2017

Authors Enric Bertran-Serra, A. Musheghyan-Avetisyan, F. Pantoja-Suarez**, I. Alshaikh**, J. Martí-González, S. Chaitoglou, R. Amade, JL Andújar, E. Pascual
Title New carbon based nanostructures grown by chemical vapor deposition
Participation Oral presentation
Conference World congress and Expo on Nanotechnology and Materials Science
Place Barcelona, Spain
Date April 2017

Authors Pantoja-Suárez, F.; **Alshaikh, I.**; Amade, R.; Andújar, J.L.; Pascual, E. and Bertran, E.
Title Thin AlN diffusion barrier for carbon nanotubes growth over stainless steel substrate.
Participation Poster
Conference IN2UB annual meeting
Place Barcelona
Date January 2017

Authors Arevik Musheghyan-Avetisyan, R. Amade, J. Marti-González, J-L. Andújar, E. Pascual, F. Pantoja, **I. Alshaikh** and E. Bertran-Serra
Title Low temperature Inductively Coupled Plasma Chemical Vapor Deposition of vertically oriented graphene nanowalls
Participation Poster
Conference IN2UB annual meeting
Place Barcelona, Spain
Date January 2017

PARTICIPATION IN RESEARCH PROJECTS

Project: Textile Competence Center Vorarlberg 2 (TCCV2)
Research Team:
Enric Bertran Serra (IP1)
Roger Amade Rovira (IP2)
Islam Alshaikh (Collaborator Contract)
COMET-Competence Centers Excellent Technologies (COMET PROJECTS) of The Austrian Research Promotion Agency (FFGAT) .
Program: 82FFG - The Austrian Research Promotion Agency (FFG)
UE code: FFG 882502
start date: 01/04/2021 **end date :** 31/03/2025
Tipology: FPM International Project, first level

Project: Electrodos híbridos para almacenamiento de energía avanzado: hacia un futuro sostenible (ESTORE)
Research Team:
Enric Bertran Serra (IP1)
Roger Amade Rovira (IP2)
Frank Güell Vila (Researcher)
Jose Luis Andujar Bella (Researcher)
Stefanos Chaitoglou (Postdoctoral researcher)
Islam Alshaikh (PhD student)
Call: Convocatòria d'ajuts del Programa Estatal d'Investigació, Desenvolupament i Innovació Orientada als reptes de la Societat. Modalitat Reptes , Ministerio de Ciencia e Innovación (MICINN)**.**
Institution: UB
Program: Programa Nacional de Energía
Official code: PID2020-116612RB-C32
Start date: 01/09/2021 **End date:** 31/08/2024
Key words: 003060 - Almacenamiento de energía / 070450 - supercondensadores / 070451 - electrodos híbridos nanoestructurados / 038629 - Grafeno / 228030 - Nanotubos de carbono

Project: Síntesis de CNS (VACNTs y GNWs) en cintas metálicas flexibles y estudio de sus propiedades electroquímicas tras la funcionalización con materiales compuestos de óxido metálico (ADHES)
Research Team:
Enric Bertran Serra (Investigador Principal)
Esther Pascual Miralles (Coinvestigador Principal)
Jose Luis Andujar Bella (Investigador Secundario)
Roger Amade Rovira (Investigador Secundario)
Victor Manuel Freire Soler (Equipo de trabajo)
Stefanos Chaitoglou (PhD student)
Arevik Musheghyan Avetisyan (PhD student)
Fernando Pantoja Suárez (PhD student)
Islam Alshaikh (PhD student)
Joan Martí González (PhD student)
Call: Convocatòria d'ajuts del Programa Estatal d'Investigació, Desenvolupament i Innovació Orientada als reptes de la Societat. Modalitat Projectes I+D+I, Ministerio de Economia y Competitividad (MEC).
Institution: UB
Program: Programa Nacional de Energía
Official Code: ENE2017-89210-C2-2-R
Star date: 01/01/2018 **End date:** 31/12/2020
Unesco codes: 331200 - Tecnología de Materiales / 332200 - Tecnología Energética (Ver 2212.03 y 5312.05)
Keywords: 054971 - CNTs / 054972 - GNWs / 004855 - Óxidos metálicos / 010442 - ICP / 015952 – CVD

Resum de la tesi

Actualment, la Nanotecnologia està tenint un impacte en pràcticament tots els aspectes de la vida humana. És una tecnologia transformadora que ha influït i continuarà en l'electrònica i la informàtica, la medicina, els materials i la fabricació, la catàlisi, l'energia i el transport. Ha canviat la manera d'utilitzar els materials en el futur, millorant la seva durabilitat i reactivitat. Tenim moltes oportunitats per fer que les coses siguin més petites, més lleugeres i més fortes. Els materials de carboni són un dels principals materials que els científics han estudiat intensament les seves propietats durant les últimes tres dècades per les seves notables propietats, que encara s'estan investigant i s'estan descobrint noves propietats i aplicacions fins al moment. Els nanotubs de carboni (CNT) i el grafè són els principals materials de carboni investigats i més importants des del seu descobriment. El primer descobriment de CNT va ser l'any 1991 pel Dr. Sumio Iijima on eren nanotubs de carboni de paret múltiple (MWCNT) ja que els podia produir al seu laboratori en condicions estables. Dos anys més tard, el mateix científic va poder descobrir els primers CNT de paret única (SWCNT). Una dècada més tard, la revolució del grafè va començar quan el professor Andre Geim i el professor Constantine Novoselov van poder obtenir una sola capa de grafè separant els fragments de grafit repetidament fins a obtenir una capa de carboni d'un àtom de gruix. De fet, atès que s'ha avançat la tecnologia per produir CNT i grafè a escala industrial, es poden trobar en nombroses aplicacions, com ara polímers de reforç, que actuen com a bastides per al creixement artificial de teixits, utilitzant-los en molts dispositius sensors com ara com a elèctrics, òptics i biològics, fabricant els components d'elèctrodes de bateries i supercondensadors de nova generació. Els CNT i el grafè són suports ideals per a altres materials, especialment quan es combinen amb materials d'alta capacitat. Investigadors i empreses de tot el món estan dedicant esforços importants a desenvolupar elèctrodes amb disseny tridimensional a escala nanomètrica i una gran superfície específica. Aquesta tesi se centra en l'optimització dels paràmetres de síntesi de CNTs utilitzant diferents metodologies per obtenir els CNTs sobre substrats conductors i flexibles i sense substrat per utilitzar-los com a elèctrodes per a supercondensadors. Els CNT s'han estudiat per separat, combinats amb nanowalls de grafè (GNW) i combinats amb MnO_2 per augmentar la capacitat tant com sigui possible. Totes les metodologies de síntesi de CNT i GNW són processos relacionats amb CVD.

Les tecnologies estudiades també ofereixen una diversitat de mètodes de producció de nanomaterials, que obren altres desenvolupaments futurs tals com elèctrodes flexibles per a

supercondensadors i bateries, sensors, foto i electrocatàlisi, i altres desenvolupaments com biosensors per a roba intel·ligent.

Capítol 1-Introducció

Aquest capítol tracta alguns principis bàsics de la nanociència i la nanotecnologia. Els materials de carboni prenen la resta del capítol a partir dels al·lòtrops de carboni, explicant amb detall conceptes sobre nanotubs de carboni, les seves propietats, tècniques de síntesi, mecanisme de creixement i l'efecte dels gasos catalitzadors i precursors en el creixement. A continuació, s'explica breument la història i els conceptes del grafè, a més de la seva estructura i propietats tèrmiques i mecàniques.

Capítol 2 – Tècniques de caracterització

Les tècniques de caracterització utilitzades durant aquesta tesi es descriuen amb detall en aquest capítol. Es van realitzar diferents mesures espectroscòpiques, elèctriques i electroquímiques per caracteritzar els materials de carboni que hem sintetitzat, així com la seva aplicació com a elèctrodes per a dispositius supercondensadors. En aquest capítol, també es presenten les descripcions de les tècniques de microscòpia electrònica i d'anàlisi de superfícies utilitzades per a la caracterització composicional, estructural i morfològica de les mostres.

Capítol 3 – Conceptes i configuracions experimentals.

Aquest capítol és el nucli per a la capacitat d'imaginar com es va dur a terme el treball del material de síntesi durant la tesi. Cobreix amb detall els conceptes del sistema de buit i els possibles recursos de gas dins de les cambres de buit, els conceptes de plasma i els processos relacionats de deposició física de vapor (PVD) i deposició de vapor químic (CVD). S'expliquen els tres reactors que hem utilitzat per sintetitzar els materials de carboni. En particular, les seves parts (principi de funcionament, bombes, vacuòmetres, etc...) i la importància de cada peça per a un ús exitós i segur de les cambres. Finalment, també es va explicar una tècnica de plasma atmosfèric per a la síntesi de nanopartícules metàl·liques.

Capítol 4 – Síntesi de composites basats en carboni sobre substrats Papyex® altament flexibles

En aquest capítol, es presenta l'optimització dels paràmetres de creixement dels CNTs alineats verticalment (VACNT) i dels seus compostos GNWs sobre substrats de grafit Papyex® mitjançant CVD millorat per plasma (PECVD) i CVD de plasma acoblat inductivament (ICP-CVD) per utilitzar-los. com elèctrodes per a supercondensadors. Els paràmetres es van optimitzar un per un incloent la funcionalització del plasma de la mostra. Les mostres es van caracteritzar mitjançant diferents tècniques microscòpiques, espectroscòpiques i de raigs X. Les propietats electroquímiques dels CNT i les estructures híbrides de carboni es van investigar abans i després de l'electrodeposició de MnO_2.

Capítol 5 – Síntesi de compostos basats en carboni directament sobre aliatges flexibles SS310

En aquest capítol, hem estudiat el creixement de CNT directament sobre aliatges d'acer inoxidable SS310 utilitzant les partícules de catalitzador presents al propi substrat en un únic procés continu mitjançant PECVD. L'optimització dels paràmetres del procés es va dur a terme mitjançant el disseny experimental de Box-Wilson. Els CNT obtinguts es van decorar amb escates de GNW per augmentar la seva superfície específica. La morfologia i les propietats dels compostos CNTs i CNTs-GNWs es van caracteritzar mitjançant diferents tècniques microscòpiques i espectroscòpiques. Es va dipositar diòxid de manganès sobre l'estructura obtinguda i se'n van estudiar les propietats electroquímiques.

Capítol 6 – Síntesi de nanotubs de carboni i nanopartícules d'òxid metàl·lic a pressió atmosfèrica.

Aquest és l'últim capítol de resultats, que presentarà una tècnica diferent per al creixement de CNT. La síntesi de CNT es va fer sense substrat mitjançant un catalitzador flotant CVD (FC-CVD). Aquesta tècnica permet la síntesi contínua (escalable) de CNT a pressió atmosfèrica en un entorn d'oxigen lliure dins d'un reactor de forn tubular. En aquest capítol es presenta una altra tècnica per a la síntesi de nanopartícules d'òxid metàl·lic anomenada interacció plasma-líquid. Mitjançant aquesta tècnica es van sintetitzar diferents òxids metàl·lics però només vam utilitzar NiO2. Mitjançant aquestes tècniques podríem obtenir una estructura híbrida de CNTs i nanopartícules

de NiO_2. Tots dos es van caracteritzar per tècniques microscòpiques i espectroscòpiques per finalment utilitzar-los per a aplicacions electroquímiques. La major part d'aquest treball es va dur a terme durant una estada curta a la Universitat d'Ulster - Irlanda del Nord.

Conclusions

L'exposició dels resultats i la discussió s'ha completat amb una llista de conclusions derivades dels principals resultats i assoliments de la tesi.